The University of Adelaide

Department of Mechanical Engineering

The Generation of Large-Scale Structures by Jet Precession

Ph.D. Thesis

David Scott Nobes

December 1997

Abstract

Research at the University of Adelaide into mixing has resulted in the development of several geometric configurations of jet nozzle, which enhance large-scale structure in the flow through jet precession. One of these, the fluidic precessing jet (FPJ) nozzle, has proven significant benefits in industrial gas flames. Precession is used to describe the motion of a vector, which defines the jet (i.e., nozzle exit velocity). The vector is inclined to the nozzle's geometric axis and rotates about that axis. An analogous mechanical precessing jet (MPJ) nozzle has been developed as a tool to allow a fundamental investigation the effects of precession on the mixing field of a well-defined simple jet of a circular cross section. The MPJ nozzle enables independent variation of the angle of inclination of a simple round jet from the nozzle axis and the rotational speed of the nozzle about the axis.

The present work investigates the effects of precession on the scalar mixing field. The hypothesis that precession acts to modify the length scales of mixing throughout the flow is argued. It is demonstrated that there are distinct regions within the flow, each of which has different mixing characteristics. Within the near field the precession of the helical footprint of the emerging jet dominates the flow. In the far field the flow develops into self-similar behavior. The transition region links the near field and far field flow regions. Mixing in the transition and far fields of the flow field is dominated by a length-scale, which is larger than the length-scale of a non-precessing jet at comparable location.

The ability of four dimensionless variables to characterize the flow are compared: the Reynolds number, $V_o d / \nu$, the Strouhal number, $f.d / V_o$, a dimensionless strain rate, $(f.d / V_o).\sin\phi$, and a modified Strouhal number, $V_o/(f.r_h)$, based on half the diameter of the helical footprint of the emerging jet. Extensive data sets have been collected for a parametric analysis into the effects of these parameters on the scalar mixing field. It is shown that the dimensionless strain rate characterizes the near field flow region best, but the helix diameter is important in the transition region.

A planar, laser imaging technique has been developed to provide both qualitative and quantitative characterization of the flow. The mixture field of a passive conserved scalar quantity, which marks the jet fluid, has been determined from planar Mie scattering in air. This technique has been validated by an investigation of a simple round jet, which represents a limiting case of a precessing jet. The data have been processed to determine the concentration statistics, the scalar dissipation and the spatial correlation results from measurements extending well into the far field, up to 100 jet throat diameters. The data provides comparative information about the spread, mixing decay rate and integral length-scale of the flows.

The results of the study confirm that the dimensionless strain rate is the most influential of the four parameters in the near field. The Strouhal number gives good characterization also, but only for a fixed deflection angle of the jet. The deflection angle also has a significant effect but of less importance than the Strouhal number. Reynolds number is seen to have a negligible effect for those values investigated. Statistics of the mixture field show significant variations in axial and radial decay. They are dependent mostly on the Strouhal number.

Measurements of the integral length-scale of the flow, via the two point spatial correlation, show that with increasing Strouhal number the integral length-scale is increased dramatically. This signifies the generation of much larger structures within the transition region of the jet and in the far field. Measurements of scalar dissipation and probability density function show that with increasing Strouhal number there is an increase in the scalar gradient in the far field. Mixing characteristics are modified as a result of large scale engulfment of fluid and the importance of shear in the mixing process is reduced relative to the non-precessing case.

It is concluded that the hypotheses are well supported by the experimental data and together provide a logical description of the dominant features of the complex mixing field associated with jet precession.

Contents

Notation

Abbreviations

FPJ	Fluidic precessing jet nozzle
MPJ	Mechanical precessing jet nozzle
NO_x	Oxides of Nitrogen
PDF	Probability Density Function
PJ	Precessing Jet
SO_x	Oxides of Sulfur

Variable Quantities

C	Instantaneous fluid concentration	
C_o	Concentration at nozzle exit	
$\overline{C}$	Mean fluid concentration	
C'	Fluctuating fluid concentration	
d	Jet exit diameter	(m)
d_p	Typical particle diameter	(m)
D	Molecular diffusion coefficient	
f	Frequency of precession	(Hz)
f	Frequency	(Hz)
i	indexing variable	
J	Thrust	($kg.m.s^{-2}$)
J_o	Momentum flux of the jet	($kg.m.s^{-2}$)
L	Flow length scale	m

$\dot{m}_o$	jet mass flux at the exit	($kg.s^{-1}$)
N	Number of samples	
r	Radial coordinate	(m)
r_h	helix radius	(m)
r_o	nozzle radius, normalizing length scale	(m)
r_e	momentum or equivalent radius	(m)
R	Radius, in spherical coordinates	(m)
R_Λ	Correlation coefficient of the jet concentration fluctuations	
t	Time	(s)
U	Bulk mean fluid velocity	(m/s)
V	Bulk mean fluid velocity	(m/s)
x	Stream-wise (axial) coordinate	
x	Cross-stream coordinate	
y	Cross-stream coordinate - in the image plane	
z	Axial Component	
z_0	Virtual origin of the jet concentration measurements	
Φ	Scalar dissipation $= 2D\nabla^2 C$	
ε	Kinetic energy dissipation rate	
λ_b	Batchelor micro-scale $= \left(\frac{\varepsilon}{\nu D}\right)^{-\frac{1}{4}}$	
λ_k	Kolmogorov micro-scale $= \left(\frac{\varepsilon}{\nu^3}\right)^{-\frac{1}{4}}$	
λ_T	Taylor micro-scale	
Λ	Integral length scale	
ν	Kinematic viscosity of a fluid	($kg.s^{-2}$)

ϕ Angle of the jet exiting the MPJ nozzle

ϕ_p Measured angle to the point of interest

θ Phase angle of precession

ρ Fluid density $(kg.m^{-3})$

σ density ratio

χ Dimensionless axial component

η Dimensionless radial component

Non-dimensional Parameters

Re Reynolds number $= \frac{V_o d}{\nu}$

St Strouhal number of precession of the MPJ nozzle $= \frac{fd}{V_o}$

St.sinϕ Dimensionles strain rate

$1/St_m$ Modified Strouhal number, $V_o/f.r$, in the form of a Rossby number

Subscripts

t_o Initial time.

Δt Time step

0 Denotes quantity at the source

∞ Denotes quantity in the far-field/ambient

i,j Denotes quantity at a given pixel

x,y Denotes quantity at a given geometric point

Statement of Originality

The material in this thesis is original and has not been submitted or accepted for the award of a degree or diploma at any other university and to the best of my knowledge and belief, the thesis contains no material previously published or written by another person except where due reference is made in the text of the thesis.

David S. Nobes

Permission to Copy

The author consents to the thesis being made available for loan and photocopying provided that the thesis is accepted for the award of the degree.

David S. Nobes

Acknowledgment

This experience of a lifetime has been made possible by the efforts, enthusiasm and support of many people. The supervisors of the project, Dr Graham J. Nathan and Professor R.E. (Sam) Luxton have provided unbounded enthusiasm and inspiration which have had a profound influence on this document. Serious debate, enlightening humor, and unreserved support of Dr. Greg J.R Newbold and Dr. Zeyad T. Alwahabi have made this project not only successful but a truly significant experience.

The experimental equipment and facilities have been made available through the shared resources of the Combustion Group in the Department of Mechanical Engineering and the Department of Chemical Engineering. During the course of this project each team member of the group has freely made time for valuable discussions and project participation, particularly by Dr. Gerald Schneider, Mr. Neil Smith, Associate Professor K.D. King and Dr. J. Mi..

The work that is presented here has made use of new experimental facilities and diagnostic techniques that have been established through the efforts of the technical staff in the Department of Mechanical Engineering and the Department of Chemical Engineering. The contributions made by all the technical staff, in particular Mr. Silvio de Ieso, Mr. Graham Kelly, Mr. Bruce Ide and Mr. Brian Mulcay. The academic, clerical and technical staff of the Department of Mechanical Engineering are all deserving of my thanks.

This project has been made possible by the financial support provided by the Australian Research Council Collaborative Grant scheme, and the industrial partner, Fuel and Combustion Technology (FCT).

Thank you.

David S. Nobes

19th of December 1997

1 INTRODUCTION

1.1 INDUSTRIAL BURNERS : *THE MOTIVATION*

1.1.1 Background on the use of burners in industry

Combustion processes have been in the past and will continue for the foreseeable future to be the prime source of energy for modern society. In the process of combustion, the energy, which is stored in the chemical structure of the fuel and air, is released and converted to heat. In turn, the heat generated can be used directly in industrial processes or can be further converted to electricity. Essential building materials such as cement, lime, glass, and steel require high temperature during their manufacture. Such high temperature processes are a significant part of the total energy used in industry today.

In addition to carbon dioxide (CO_2) and, in poorly designed or operated plant, carbon monoxide (CO), the burning of fossil fuels with air adds to atmospheric levels of water vapor and the oxides of nitrogen, collectively referred to as NO_x. All of the above gases are "greenhouse" gases which are now concluded to be contributing to global warming (IPCC, 1995). In the atmosphere NO_x and SO_x, which is also produced during combustion when sulphur is present in the fuel, react with water vapor in the atmosphere to form acids. These acids cause severe damage to stonework, metals, forests and crops, amongst other things. The environmental impact of "greenhouse" gas emissions and "acid rain" have brought the rate of consumption of fossil fuels under increased scrutiny. The need to decrease fuel consumption and emission levels, without decreasing (and ideally increasing) the throughput of production plant, while at the same time improving the quality of the product, has stimulated interest in the design of burners which can be optimized to match the requirements of the process they are serving.

1.1.1.1 The environment in which combustion occurs.

The environment in which combustion occurs in many industrial processes can be harsh, requiring the combustion equipment to be very robust. The fuel for the process is typically introduced into the combustion environment via a nozzle. Air for the combustion reaction is typically introduced into the combustion chamber as a co-flow around the fuel nozzle or as a cross flow and can significantly influence the mixing process. The walls of the chamber are usually refractory lined for materials processing, but can be lined with heat exchange surfaces for chemical process industries so that, in both cases, the combustion is confined. In most applications the flame must not impinge on the confining walls or product. The combustion reaction releases heat and causes volumetric expansion of the gases. The containing walls and the hot product both feed back radiation to the fuel and air mixture and can influence the combustion process significantly. Dust from the product, where present (as in a rotary cement kiln), can provide a heat sink to the flame and can also influence the emissivity of the flame. The geometry of the air and feed ducts, if not carefully designed, can introduce asymmetries into the aerodynamics, which bias the mixing process and hence the heat transfer profile from the flame to the charge. All of the above factors vary with time during the stabilization phase of the process and combine to produce a very complex environment for the combustion of the fuel and the transfer of the released heat to the charge (Moles, 1986).

1.1.1.2 Requirements of a burner.

In those processes which use a rotary kiln, the product quality, fuel consumption, combustion emissions and stability of the operation have all been shown to be dependent on the mixing performance of the burner (Rhine and Tucker, 1991). In the cement industry it has been shown

that the heat flux profile of the combustion reaction has a dominant influence on the location, extent and rate of the clinkering reactions of the cement process (Nathan and Manias, 1995). That is, product quality is dependent on the heat flux profile and hence on the flame produced by the burner. In general the rate at which a given process can be driven and hence the kiln throughput, is dependent on the rate of heat transfer from the heat source to the feed in the area of greatest heat load. The thermal efficiency of the process, and hence the fuel consumption, is then determined by the efficiency of the heat transfer process, which in high temperature processes is dominated by radiation (Sarofim, 1986).

In addition to the primary combustion products, trace elements from the fuel or product can react with oxygen in the high temperature environment to form gaseous compounds. Thus oxides of nitrogen, NO_x, can be derived from fuel bound NO_x when burning coal or oil, but are principally derived from the nitrogen in the air (thermal NO_x) when burning natural gas. Although it is a minor species in terms of volume, NO_x has such a significant effect on the atmosphere that many industrial countries have legislated to limit the quantity that can be released to the atmosphere. These limits are best expressed on a specific basis, that is, per tonne of product. Thus the goal in the development of diffusion flame burners which utilize mixing to control the combustion process is to minimize the NO_x production per unit of fuel burnt and simultaneously to maximize the product throughput per unit of fuel burnt, by maximizing heat transfer.

The function of a burner nozzle is to introduce and mix the fuel into the surrounding combustion air. It should be noted that chemical kinetic rates are much faster than mixing rates and hence combustion in diffusion flames is "mixing controlled". The characteristics of the mixing therefore largely control the shape of the flame and the heat flux profile produced.

The primary aim of the burner design must be to shape the flame and the heat flux profile to satisfy the heat input requirements of the specific process. A second aim must be to achieve mixing of the fuel and air in a manner that allows complete combustion while minimizing NO_x generation. In the past, attention has focused on maximizing combustion intensity to minimize furnace / boiler volume and hence capital cost. This tends to create high temperatures and therefore high NO_x emissions. However recent work by Nathan, Turns and Bandaru (1996) has demonstrated that changes in the mixing characteristics of a jet by precession can simultaneously increase radiant fraction, thereby dropping the characteristic flame temperature, and reduce NO_x emission. While these effects are unambiguously linked to changes in the mixing, the mixing has not been sufficiently quantified to date to explain the benefits adequately. It is this gap in understanding that is addressed by the present work.

1.1.1.3 Burner Design for a Combustion Process.

A basic building block of gas burners, and one that dominated early burner designs, is a high velocity turbulent jet of fuel issuing from a straight pipe. Such a jet utilizes the shear layer to entrain the surrounding air and so produce a combustible mixture. This is the most elementary form of a turbulent jet diffusion flame. The evolution from this elementary design resulted from the need to stabilize these flames, as stability is the most fundamental issue in any continuous combustion operation. A turbulent diffusion flame detaches from the end of a simple turbulent jet nozzle as fuel throughput increases and becomes a "lifted flame". To a first approximation the front of the lifted flame is located where the flame propagation speed equals the local speed of the jet of fuel and entrained air (Kalghatgi, 1984). As the fuel flow increases the flame front moves downstream until either the fuel / air mixture falls below that required for ignition or the rate at which the flame can raise the mixture to ignition temperature becomes insufficient. The flame is then said to 'blow-off'. A detached flame is very unstable and limits

the range over which the process and the flame can be operated. Such "burners" have poor "turn-down" ratio. Another aspect of the diffusion flame is that it is relatively long. The fine scale turbulent mixing generated by intense shear in the jet mixing layers results in high local temperatures and accompanying high levels of thermally generated NO_x (FCT, 1996)

Increased flame stability was achieved by the introduction of a recirculation zone within the fuel jet (Beer and Chigier, 1972). A recirculation zone can be produced by the flow of an annular jet around a bluff body or by the introduction of swirl into the primary jet or the surrounding air, or both. In either case the effects are to increase the rate of mixing by large-scale engulfment of air into the fuel and to recirculate hot combustible products to the root of the flame, both being achieved through the generation of large-scale structures (Syred and Beer, 1974). This causes combustion and heat release to occur closer to the burner. Burners employing this method of flame stabilization are typically used in utility boilers. Related techniques such as flue gas recirculation and combustion staging have been used to reduce NO_x emissions (Smart and Weber, 1989). However the geometry of these burners can be very complicated and combustion staging and flue gas recirculation are not appropriate for use in many types of processes, notably rotary kilns, because of constraints in the design.

1.1.1.4 Summary

The combustion characteristics of a flame are a consequence of the rate and manner of mixing of the fuel and oxidant gas. For diffusion flames the properties of the mixing field are directly related to the geometry of the nozzle and to the aerodynamics of the system. In general, an increase in mixing rate allows for a smaller combustion system and hence lower plant capital cost, but may increase NO_x emissions. The flame produced by a burner nozzle is fundamentally dependent on the mixture field produced by that nozzle. For a given process in a

given plant configuration the burner must be designed to achieve a specific heat release profile to maximize the effective energy transfer to the required sections of the process for best thermal efficiency and fuel consumption. If this is achieved, it is surmised that combustion emissions will be at a minimum (Nathan and Manias, 1995).

1.1.2 Background to the Fluidic Precessing Jet (FPJ) nozzle.

The need to meet the above requirements of a burner has led researchers to investigate the use of enhanced large scale mixing from burner nozzles. There have been investigations into the use of acoustic excitation, such as the pulsed combustor, as well as nozzles that have natural fluid-mechanical excitation. One of these is the flow field generated by a jet that precesses about an axis other than its own geometric axis. The flow fields generated by these nozzles, termed precessing jets (PJ), are the focus of this study.

The Fluidic Precessing Jet (FPJ) nozzle, developed in the Department of Mechanical Engineering in the University of Adelaide, employs a novel fluid dynamic instability discovered by Prof. R.E. Luxton and Dr. G.J. Nathan (Luxton *et al.* 1988). With natural gas as the fuel the unique mixing characteristics of the FPJ result in a flame which is very different from a conventional, axisymmetric jet flame. The flame is shorter and more bulbous, as a result of the very large spreading angle of the jet, is visually yellow and luminous, and has a short stand-off distance (Nathan, 1988) which is almost independent of the flow rate of the jet. High stability of the flame over a wide operating range results in a large turndown ratio (Nathan and Luxton, 1989). The flame in an unconfined environment has been reported to 'puff' somewhat like a pool fire (Newbold, *et al.* 1993a, 1993b, 1998). These authors also demonstrated that the mixing of the jet fluid with the surrounding air is of a substantially larger scale than in a simple

jet and that the characteristic strain rate through the majority of the flame is significantly reduced.

The major benefit of the FPJ in industrial applications is that much less NO_x is generated for a given heat release rate than with a conventional burner. In a controlled experimental facility at a semi-industrial scale of 2 MW, the MPJ nozzle was shown to reduce NO_x emissions by 50% relative to an optimized swirl burner (Nathan, Luxton and Smart, 1992). These reductions were linked to large-scale flow structures that were identified in the flame. In industrial trials firing natural gas, NO_x emission reductions of up to 75% have been achieved (Manias and Nathan, 1993, 1994) with a conservative norm of 30-50% (Nathan and Manias, 1995). The flame can be adjusted easily in service and hence the heat flux profile can be controlled (Rapson, Stokes and Hill, 1995). This has resulted in significant fuel savings, in the order of 3-10% being typical (Nathan and Manias, 1995). Other benefits which are directly important to the running of a kiln also result, such as, increased process stability, ease of light-up, increased flame stability, reduced dust loss and improved product quality. Increased refractory life has also been achieved (Nathan and Manias, 1995).

1.1.3 Description of the Fluidic Precessing Jet (FPJ) nozzle

Initial work on the FPJ revolved around stabilizing the precessing flow mode that occurs within the fluidic chamber and characterizing the frequency of precession. The work of Nathan (1988), Nathan *et al.* (1998), Hill, *et al.* (1992, 1995) and Hill (1998) optimized the geometry of the nozzle for the development of the fluidic instability. Investigation of the external flow field (Newbold, 1998) resolved some detail of the structure of the flow and its influences on the geometry of flames derived from different fuel types. The following

discussion is a brief description of the flow field developed within the nozzle chamber and some comments on recent work on characteristics of the flow field which is generated.

1.1.3.1 The internal flow field of the Fluidic Precessing Jet (FPJ) nozzle.

The FPJ nozzle that produces the precessing jet flow is axisymmetric, does not rotate, has no moving parts, and has no internal or external deflector vanes. Figure 1.1 shows a schematic of the orifice-cavity-orifice configuration of the FPJ nozzle chamber and an interpretation of the motion of the fluid within it. A jet flow enters the chamber through the (small) upstream orifice. Minor variations in the rate of entrainment of cavity fluid into the entering jet cause local asymmetries in the pressure field within the chamber. The resulting force developed by the pressure field deflects the confined jet locally. A positive feedback between the rate of entrainment and the variation in the pressure field causes the jet to deflect further until it reattaches to the inside wall of the chamber (Luxton, 1993). The reattachment length normalized by the step height of the expansion into the chamber, is less than half of that which occurs in other reattachment flows which use smaller expansion ratios (Hill *et al.* 1995; Nathan *et al.* 1997). Reattachment occurs about half way along the chamber. The reattachment point constitutes a positive bifurcation (Luxton, 1993; Nathan and Luxton, 1991d) beyond which the main bulk of the jet continues toward the chamber exit as a wall jet, while a small portion on the inlet side of the stagnation streamline moves upstream towards the inlet.

The deflected jet can reattach on the inner wall of the chamber at any azimuthal location and all positions are equally probable. As with the radial pressure gradient, any azimuthal variation in the entrainment of fluid into the jet will set up an azimuthal pressure gradient. When the chamber dimensions are in the right range, this azimuthal pressure gradient, acting on the point of reattachment, drives the jet around the inside of the chamber wall. The movement of the

reattachment point is also a positive feed back to the azimuthal pressure gradient so reinforcing it.

The bulk of the reattached jet continues toward the exit as a wall jet until it encounters the orifice ("exit lip") at the outlet plane of the nozzle. This causes it to separate and is deflected at a sharp angle toward and across the nozzle axis as it leaves the nozzle chamber. Thus, the emerging jet leaves the nozzle at an angle of about 60° relative to the geometric axis of the nozzle and precesses about that axis.

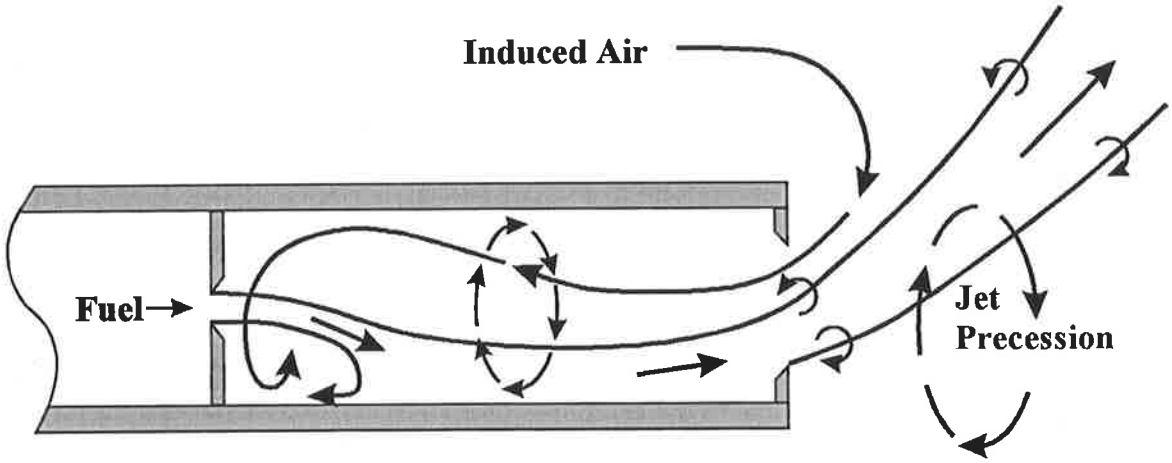

Figure 1.1 A schematic diagram of the fluid motions within an axisymmetric Fluid-mechanical Precessing Jet nozzle.

The angle at which the jet leaves the axisymmetric nozzle and the rate of precession both vary significantly from cycle to cycle (Nathan, 1988). As the jet passes through nozzle exit it does not completely fill the orifice and, because the jet entrains fluid from within the chamber, the chamber pressure is below that of the surroundings (Nathan, 1988). Thus ambient, external fluid is drawn into the chamber. This ambient fluid moves rapidly to the upstream end of the nozzle where it forms a strong swirling flow which 'counterbalances' the angular momentum associated with the jet precession (Luxton, 1993).

1.1.3.2 The external flow field

Flow visualization of the jet flow exiting from the FPJ nozzle is seen to form "large-scale" roller structures in the near field, close to the nozzle. Velocity measurements resolved from a PIV technique indicate that the velocity of the jet fluid is reduced by two orders of magnitude from the velocity at which it enters the chamber within a short distance from the nozzle exit (Newbold *et al.* 1995). The rapid decay in velocity appears to be associated with the generation of the large roller structures. The mixing field of the FPJ, compared with that of a turbulent jet, shows significantly more ambient fluid on the jet centerline (Newbold, 1998).

Visualization of vertically fired, unconfined FPJ flames shows that large-scale buoyant structures dominate the mixing and entrainment of surrounding fluid in the region downstream from the stabilization region and are responsible for the large oscillation in the flame length. Stabilization of the flame occurs upstream from the location where buoyant forces become important so that these large-scale structures are not associated with the flame stabilization mechanism (Newbold, *et al.* 1997). The existence of "thick" reaction zones within the flame stabilization region suggest that laminar flamelet concepts are insufficient to describe the combustion field (Newbold, 1998). Comparison with the instantaneous mixture field structure, determined from cold flow studies only, shows that broad regions that are within the flammability limits of typical hydrocarbon fuels exist in comparable locations to the broad OH images obtained in flames (Newbold, 1998). This implies that a pre-mixed flame stabilization best explains the stabilization mechanism process in FPJ flames (Newbold, 1998).

1.1.3.3 Summary of present knowledge of the Fluidic Precessing Jet (FPJ) flow.

The flow fields generated by the FPJ nozzle are extremely complex and exhibit large cycle-to-cycle variability. The general character of the motion of the jet has been determined from flow visualization, frequency measurements (Hill *et al* 1992; Nathan and Luxton, 1991d) and intuitive logic (Luxton, 1993). The mixing characteristics have been shown qualitatively to differ significantly from simple jet flows and quantitatively to result in dramatically increased jet spreading and initial entrainment (Nathan and Luxton, 1991). The resulting combustion processes are dramatically altered, with increased flame stability, reduced NO_x emissions and increased emissivity in both small open flames and large industrial flames (Manias and Nathan, 1995). There are many questions yet to be answered about the mechanisms by which precession influences combustion. There is little quantitative information about the length scales in the flow, the degree to which jet and ambient fluids are mixed, strain rates or scalar dissipation. The present investigation aims to address these gaps by conducting a fundamental study of the effect of position on the mixing characteristics of a non- reacting jet flow.

1.2 REVIEW OF THE MECHANICAL PRECESSING JET (MPJ).

1.2.1 Background

It has been found difficult to define the exit conditions of the jet that emerges from the fluidic precessing jet (FPJ) nozzle. The diameter, cross-section and velocity profiles of the exiting jet are not clearly defined and exhibit wide variability. These factors have limited the investigation of the external flow field of the FPJ mostly to visualization techniques (Nathan, 1988; Newbold, 1997). The present information is semi-quantitative and interpretation of the data requires, at every stage, a combination of intuition and disciplined logic. To allow a fundamental investigation of the effects of precession on the mixing characteristics of a jet, a nozzle has been designed for which the exit conditions are well defined. It is the flow from this nozzle, which is loosely termed an analogue of the FPJ that is explored in the present thesis. A schematic of the exit tip of the Mechanical Precessing Jet (MPJ) used to generate this flow is shown in Figure 1.2 and a detailed description of the MPJ nozzle is covered in the following sections. The use of this "analogue" allows each of the parameters, namely jet diameter, jet velocity, jet deflection angle, eccentricity and the angular velocity, to be varied independently in a parametric investigation.

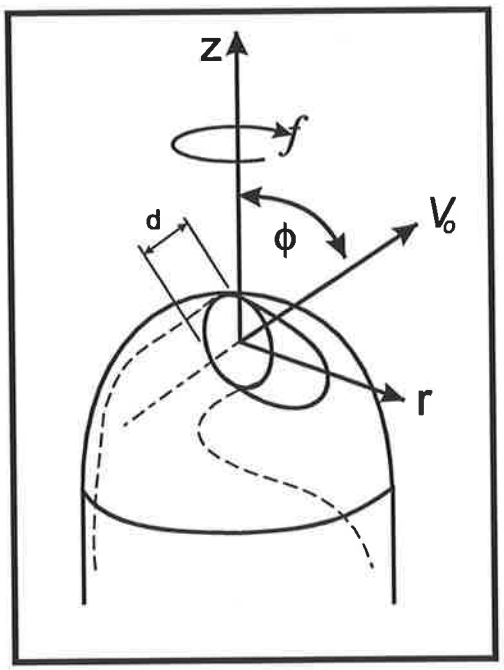

Figure 1.2 A schematic diagram of the rotating tip of the Mechanical Precessing Jet (MPJ) nozzle and associated notation, nozzle exit diameter, d, nozzle exit velocity Vo, nozzle rotation frequency, *f*, and spatial coordinates, z and r.

1.2.2 Previous descriptions of the flow field generated by the Mechanical Precessing Jet (MPJ) nozzle.

Previous work on the effects of precession on the turbulence field of a jet as generated by the MPJ nozzle includes flow visualization, velocity and pressure field measurement and quantification of the global combustion characteristics.

Detailed investigation of the velocity and pressure field produced by the MPJ has shed light on the general shape and turbulence characteristics of the mixing field (Schneider, 1996; Schneider *et al* 1992, 1993, 1994, 1996a, 1996b). A distinct relationship between the rotational frequency of the nozzle tip and the general shape of the flow field has been posed for one fixed deflection angle, $\phi = 45°$ (Schneider, 1996). A Strouhal Number ($St = f.d / V_o$) based on the jet exit velocity, V_o, jet exit diameter, d, and the frequency of rotation, f, is used to define the conditions

of initial jet conditions. For a given exit angle and diameter, the Strouhal number was found to describe the trajectories of the jet flow for a wide range of Reynolds numbers. Analytical investigations have shown that the external flow field is governed by only one dimensionless parameter, this being a combination of Reynolds and Strouhal Number which was deduced to eliminate the length scale from the problem (Luxton, 1993; Luxton *et al* 1995).

Large differences in the character of a precessing jet flow are evident as the precessional Strouhal number is varied, resulting in two broad regimes of precessional flow being defined with a smooth transition between them. For a "low" Strouhal number regime, $St < 0.015$, the flow field displays characteristics which are similar to those of a fully pulsed jet. Vortex structures emanating from the nozzle exit follow a straight line path from the jet origin, resulting in an overall flow which is described by a projected Archimedian spiral of low curvature and is easily recognized at $z/d = 19$. There is negligible asymmetry found in the pressure gradient. Nevertheless there are generally increased Reynolds stresses and velocity decay in this regime.

For the high Strouhal number regime, $St > 0.01$, flow characteristics are found to be dramatically different. A low-pressure region and a recirculation zone are established in the near field on the centre line of the flow. The path of the jet is significantly changed, spiraling out from the nozzle exit around the recirculation zone. The path of "individual" vortex structures in the jet, which appeared to be analogous to "vortex puffs", assume a helical shaped spiral whose radial extent seems to asymptote to a well defined radius within the near field. The jet velocity decays much more rapidly and Reynolds stresses are much higher in the first 10 diameters than in a simple turbulent jet. The far field flow downstream from the

recirculation zone becomes axisymmetric in the both the time-averaged and phase-averaged flows.

1.2.3 Combustion Characteristics

The importance of mixing in determining the global characteristics of a flame has long been recognized in studies of combustion. Examples of global parameters include flame radiation and flame emissions. Combustion models have generally been derived from simple jet flows and the mixing field has therefore been assumed to be self-similar at the point of stabilization. Hence, the flame characteristics of virtually all models assume essentially the same turbulence levels and mixing scales. The use of precession causes dramatic changes in the scales of turbulence and the shear rates for a given nozzle exit diameter, nozzle exit velocity, fuel type and hence heat release rate.

Significant visual differences are evident in the flames produced by an MPJ nozzle as Strouhal number is varied while the fuel exit velocity is kept constant. The two broad regimes found in the investigation of the unreacting field have been found to be relevant in the reacting case. For the low, sub-critical Strouhal number case, the flame is non-luminous, blue and has a shape which resembles an inverted cone where the cone angle is the same as the jet deflection angle, ϕ. The liftoff height of the flame varies with the exit velocity and at high velocities the flame becomes unstable. For the high, super-critical regime, the flame is highly luminous in the visible frequency and bright yellow, deduced to be a consequence of increased soot generation. The liftoff height is an order of magnitude less than that of a non-precessing jet flame and there is a corresponding increase in flame stability (Nathan *et al.* 1995, 1996)

Detailed measurements of radiant fraction, global residence time, emissions, burnout and flame geometry produced by the MPJ nozzle with varying Strouhal number were performed by Nathan *et al.* (1996). The radiant fraction was found to increase with Strouhal number, and to correlate with the visual increase in flame luminosity. NO_x emissions were found to decrease with increasing Strouhal number, for $St > 0.01$ which correlates with the measured increase in global residence time also resulting in the previously mentioned increase in luminosity. There is a measured reduction in flame liftoff height by a factor between 5 and 10 relative to a conventional flame from a simple jet.

1.2.4 A preliminary comparison between the FPJ and the MPJ flows and flames.

A comparison of the flames produced by the high Strouhal number MPJ nozzle and the FPJ nozzle suggests that the two flows are somewhat analogous. Both flames show an increase in flame luminosity and stability and a decrease in NO_x emissions relative to a simple jet flame and their global shape is similar. While detailed in-flame measurements of velocity and mixture fraction are yet to be made, there is sufficient evidence to suggest that changing the scales of turbulence and shear within the combustion region can have a marked effect on the flow. When the MPJ is operated at a similar Strouhal number to the FPJ both turbulent flames have similar global combustion performance (Nathan *et al.* 1996).

Despite the similarities between the MPJ and FPJ flows, there are some differences, which should be considered in assessing how analogous the two flows are. These differences are fundamental and raise questions regarding the absolute relevance of the MPJ as a *full* analogy to the FPJ flow. While the exit conditions from the FPJ can be characterized, they are essentially unknown at a given instant in time and are continually dynamic. By contrast the exit conditions

from the MPJ nozzle are well defined and controlled. It is presently unknown whether this dynamic difference between exit conditions is important. There are also significant differences in the near field of both flows. The jet exiting from the MPJ nozzle, as designed for the present research, is centered on the spinning axis of the nozzle where as for the FPJ the jet emerges away from the geometric centerline (Hill, 1998). The significance of is this eccentricity at the inlet is a possible source of vorticity but the significance is also unknown. The present jet is round at the exit, while the jet emerging from the MPJ nozzle is not. The effects of these differences have also yet to be investigated.

While there are some questions about the degree to which the MPJ flow is truly analogous to the FPJ flow, it does provide an experimental tool that allows good control of all fundamental variables. It can be concluded that the MPJ is a useful tool that provides a fundamental assessment of the effects of precession on the mixing characteristics of a simple jet and is the tool used in this investigation.

1.3 OTHER RELEVANT BACKGROUND

The mixing of two fluids is fundamental to the combustion process in diffusion flames and can be achieved through a variety of mechanisms. Outlined below is summary of the different types of mixing and a discussion of other relevant parameters.

1.3.1 Mixing Processes

1.3.1.1 Molecular Diffusion

The final diffusion process in the mixing of two fluids occurs at the molecular level, which is at a scale smaller than the Kolmogorov scale, the smallest scale of turbulence in the flow (Turns, 1996; Hinze, 1975; Monin and Yaglom, 1972). Combustion is necessarily a molecular level process. Thus in turbulent reacting flows there are two fundamental time scales to consider, a characteristic reaction time and the characteristic time for the fluid to mix to a level where the molecular diffusion process is dominant. The ratio of these two times is known as the Damkohler number (Turns, 1996). The diffusion process is present in all flows and is a function of the Schmidt number, which is the ratio of viscous to diffusive mixing. Other processes can enhance molecular level mixing. Fine scale "turbulent diffusion" and mixing at very large scales are two of these. The importance of each of these processes is discussed below.

1.3.1.2 Turbulence

The time required to mix two fluids to the molecular level can be shortened by an increase in the turbulence intensity of the flow. This increase is sometimes said to be due to turbulent

diffusion, since it can be modeled by an increased diffusion coefficient. However it is strictly a different phenomenon. The turbulence intensity is a measure of the potential for the flow to drive the turbulent diffusion process. The energy in the cascade process, in which energy is transported from the largest scales in the flow to the smallest, is a function of the turbulence intensity in that particular region of the flow. Velocity gradients are the source of turbulence generation and high velocity jets are often used to generate high local turbulence intensity. It should be noted, however, that turbulent intensity is a single valued parameter and does not take into account the scale of the turbulence fluctuations.

Self-similar flows are those in which each of the mean and turbulent fields at any transverse section have a unique distribution when normalized by appropriately chosen local scales. It should be noted that generally most lifted turbulent diffusion flames are stabilized in regions of the flow in which the turbulence parameters are close to self-similar, in at least the mean characteristics.

1.3.1.3 Vortical Motions and Large Scale Flow Structures

Simple jets issuing from nozzles of circular cross section are generally axisymmetric, in a statistical sense, within the azimuthal plane. However the instantaneous structure within the flow is not axisymmetric. The presence of large scale, ordered structures in such flows indicates that the mixing process can be on a scale larger than a characteristic length scale determined statistically, such as the momentum thickness of the shear layer. Flow visualization of simple jets over a range of Reynolds number has identified a range of structures, characterized as being broadly axisymmetric or helical in shape, dependent on the Reynolds number (Crow and Champagne, 1971; Dimotakis *et al*, 1983).

A notable feature of a flow field containing large-scale motions is the presence of coherent structures, defined by Hussain (1986) to be a "connected turbulent fluid mass with instantaneous phase-correlated vorticity over its spatial extent". That is, underlying the random, three-dimensional vorticity that characterizes turbulence, there is a component of "large-scale vorticity", which is instantaneously coherent over the spatial extent of a structure.

Entrainment and mixing of non-turbulent fluid from the ambient background into the turbulent fluid of the jet has been found to be intimately connected with the kinematics of the large-scale structures present (Dimotakis *et al*, 1983). In several investigations of jet flows in water, which has a high Schmidt number, ambient fluid is found on or across the centerline of the jet (Dimotakis *et al*, 1983; Dowling and Dimotakis, 1990). The instantaneous radial profiles of concentration differ considerably from the classical, time-averaged Gaussian profiles measured by single-point techniques (Schefer *et al*, 1994). The instantaneous profiles consist of plateaus of relatively uniform concentration, jet fluid with rapid gradients and uniform regions of ambient fluid. Large-scale structures are also important for the stability of turbulent diffusion flames (Namazian *et al*, 1992) through the increased mixing rate of the fuel. The presence of large-scale motions within flows and their importance in stimulating mixing at their boundaries and hence in providing a good environment for combustion to occur is now a recognized part of combustion fluid mechanics.

1.3.2 Axisymmetric Free Turbulent Jets

1.3.2.1 Introduction

The axisymmetric free turbulent jet is a relatively simple and well investigated free shear flow. It is used as a baseline case for the present investigation since the simple round jet can also be

described as a limiting case of a precessing jet flow, in which the deflection angle is zero and the rotational frequency is zero. An understanding of this limit case is therefore a logical pre-requisite to understanding the MPJ flow. Many investigations of both the vector and scalar fields have been conducted on the "axisymmetric" jet flow. The present investigation will focus on the scalar field of the MPJ for purposes described below, thus discussed here are results only of the scalar field. The scalar field has been measured using both single point and planar Laser Diagnostic Techniques (Mie Scattering, LIF, Raman, Rayleigh Scattering) and by probe analyses. The effects of the Reynolds number (Pitts, 1991a), Schmidt number (Dahm and Dimotakis, 1990), global density (Pitts, 1991a; Richards and Pitts, 1993), and co-flows (Rajaratnam, 1976) on the mixing in an axisymmetric jet have been investigated. Needless to say, the conserved scalar field of such a free jet is well documented. A description of the axisymmetric jet also highlights the terminology and introduces the techniques required for the present investigation.

1.3.2.2 General Features of the Mixture Field in a Free Jet from an Axisymmetric Nozzle.

The general features of the mixing field in the jet flow produced by an axisymmetric nozzle are shown in Figure 1.3. A jet of fluid with a bulk mean velocity, V_o, issues from the nozzle into a quiescent fluid which has zero mean velocity ($V_\infty = 0$). The fluid exiting from the nozzle tip is referred to as the nozzle fluid (which would be fuel in the case of a diffusion flame). Concentration within the mixing fluids can be normalized to be in the range of 0-1. The concentration at the nozzle exit, $C_{o(nozzle)}$ is defined to be 1, and as the distance from the nozzle exit approaches infinity, $C_{\infty(nozzle)}$ approaches a value of 0. The surrounding fluid, also referred to as the ambient, background, reservoir or surrounding fluid, correspondingly has at the nozzle exit a value of $C_{o(ambient)}= 0$, and at infinity, $C_{\infty(ambient)}= 1$. A core region immediately downstream from the nozzle is defined as the region in which the concentration is 100% nozzle

fluid. The pure fluid is diluted by the mixing of the nozzle and ambient fluids. A transition region follows in which turbulent mixing begins. The far field is defined as being the region in which the radial contours of mean and higher order moments of concentration and velocity are self-similar.

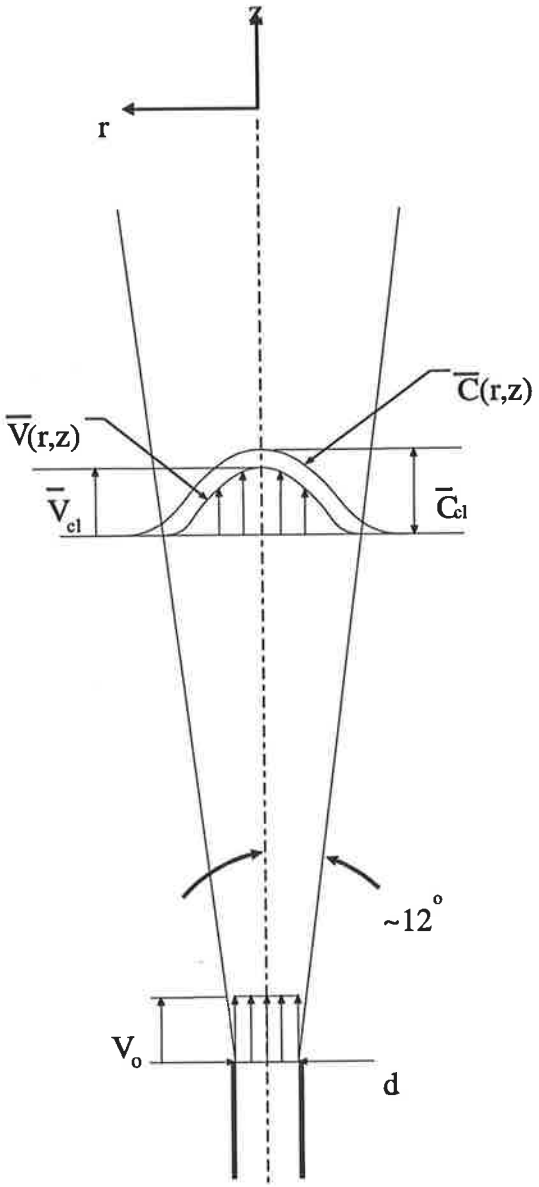

Figure 1.3 The general features of the mean mixing field of a simple, free, round jet. (Abramovich, 1963; Rajaratnam, 1976)

1.3.2.3 The terminology used to describe the scalar field in an axisymmetric jet -

The mixing field generated by a turbulent jet is usually defined in cylindrical coordinates, (z, r,θ), where z, r and θ are respectively, the axial, radial and azimuthal directions. In general, the mean concentration field is symmetrical about the geometric axis of the nozzle. Hence there is no variation of the mean field in the azimuthal direction and the jet-mixing field is axisymmetric in a statistical sense. The mean concentration field in the similarity region is then a function of position; thus $\overline{C} = f\{C(z, r)\}$. Normalization of this field can be carried out by selecting an appropriate length scale in each case. A characteristic transverse scale of the flow is the radius, r_o, of the jet at the exit from the nozzle. This is used as the normalizing length scale in the axial direction; $\chi = z / r_o$. The radial dimension can be normalized using the radial position from the axis of the jet, r, and the distance from the nozzle, z; thus $\eta = r / z$. Radial plots of $\overline{C}(\chi,\eta)/\ \overline{C}(\chi,0)$ versus $\eta = r / z$ have been shown by investigators using a range of techniques to have a distinct, self-similar profile for which all data in the far field collapses onto a single curve (Becker *et al.* 1967(b) (Mie Scattering); Birch *et al.* 1978 (Raman Scattering); Dowling and Dimotakis, 1990 (Rayleigh Scattering); Dahm and Dimotakis 1990 (LIF) and Lockwood and Moneib, 1980 (thermometry)). The axial decay of jet fluid concentration on the centerline of the jet can be plotted in the form of scaled centerline concentration, χ. $\overline{C}(\chi,0)$ verses χ. This plot exhibits an asymptotic behavior in the self-similar region of the jet-mixing field (Becker *et al* 1967(b); Birch *et al* 1978; Dowling and Dimotakis, 1990; Dahm and Dimotakis, 1990 and Lockwood and Moneib, 1980).

The condition of the jet at the exit from the nozzle differs for each of the above experiments. In some experiments the velocity profile at $\chi = 0$ is not specified, but might be assumed to be 'top-hat'. In others it is simply stated to be "top-hat". A truly "top-hat" profile is not possible but

can be closely approximated by the use of a carefully profiled smooth contraction. For nozzles that do not produce a top hat profile, two additional scaling parameters have been introduced to allow comparison between the different exit conditions. The parameters are the virtual origin, z_o, the position of which is a function of the flow, and the effective radius of the jet, r_e, defined by the velocity profile at $\chi = 0$. However the virtual origin can be defined in two ways (Richards and Pitts, 1993). The first being, z_{oJ}, obtained from the spreading rate of the jet, and the second, z_{oY}, obtained from the centerline decay rate which has principally been used in the normalization of jet flows for cases where the jet fluid density differs from the ambient. For an iso-density, jet-reservoir system where the jet inlet velocity profile is 'top-hat', z_{oJ} and z_{oY} have been shown to correspond to the exit plane of the nozzle, ie $z = 0$ (Richards and Pitts, 1993). For systems where there is a density difference between the jet and the ambient fluid there are two distinct virtual origins, each of which is needed to allow proper definition of flow similarity (Richards and Pitts, 1993).

Another concept which has been used to establish the self-similarity of a turbulent jet (Becker *et al.* 1967; Dowling and Dimotakis 1990; Pitts, 1991a; Richards and Pitts, 1993) is to define an effective momentum radius, r_e or diameter, d* given by,

$$d^* = 2r_e = \frac{\dot{m}_o}{(\pi \rho_\infty J_o)^{1/2}}$$

Equation 1.1

where $\dot{m}_o$, is the initial mass flux, J_o is the momentum flux of the jet and ρ_∞ is density of the ambient fluid. Physically, r_e corresponds to the equivalent radius of a jet with a top hat velocity profile, density equal to ρ_∞ and the same $\dot{m}_o$ and J_o as the jet under consideration (Richards and Pitts, 1993).

The rms field can be investigated in a similar manner. The radial profiles have a characteristic 'double hump', with the peaks corresponding to the location of maximum shear stress in the jet. High fluctuations in concentration occur in the region of the peaks, corresponding to the maximum gradient in the mean profile. The ratio of rms to mean concentration is commonly referred to as the unmixedness (Richards and Pitts 1993) and relates to the driving potential for fluids to continue to mix by virtue of concentration differentials. In jet flows the unmixedness approaches an asymptotic behavior as downstream distance increases, although there is significant scattering both within the data sets and between the measured asymptotic values obtained by different researchers (Richards and Pitts 1993).

1.3.2.4 Effect of Reynolds Number

Changing the exit velocity of from a given nozzle changes both the Reynolds number and the momentum of the jet. The Reynolds number $Re = V_o.d / \nu$, based on the exit nozzle diameter, d, exit axial velocity, V_o, and kinematic viscosity of the nozzle fluid, ν, is used to characterize the flow. Pitts (1991b) shows that with increasing Reynolds number there is a downstream shift in the normalized position of the virtual origin. The slope of the normalized curve of the centerline decay of concentration does not change with Reynolds number for fully turbulent jet flows. The location at which the asymptotic value of centerline unmixedness is reached, that is where self-similarity begins, increases with Reynolds number (Pitts, 1991b). The location of the virtual origin is sensitive not only to Reynolds number but also to the inlet velocity and turbulence intensity profiles of the exiting jet (Pitts, 1991b).

1.3.2.5 Effect of Global Density Ratio

A global density ratio is defined as $R_\rho = \rho_o/\rho_\infty$ (Richards and Pitts 1993), where ρ_o is the density of the jet fluid and ρ_∞ the density of the ambient fluid, has been used to investigate the mixture field. For flows which have a variable density, the concentration field (mole fraction), X, is related to the density by:

$$\rho = \rho_\infty(1-X)+\rho_0(X)$$

Equation 1.2

The mixture fraction (mass fraction), Y, can be expressed in terms of mole fraction as

$$Y = \frac{\rho_0 X}{\rho_\infty((1-X)+\rho_0 X)} = \frac{R_\rho X}{1+(R_\rho - 1)X}$$

Equation 1.3

Mass fraction is the appropriate concentration scalar for characterizing mixing in variable density flows (Richards and Pitts, 1993).

Richards and Pitts, (1993) show that if buoyancy and co-flow effects are negligible, the behavior in the far field of the jet is essentially the same as in a constant density jet - ambient fluid system, i.e. R_ρ=1. Centerline decay rate and spreading rate of the jet are independent of the initial density difference and also of velocity profile and turbulence levels. The centerline unmixedness reaches an asymptotic value, and this value compares well with the value reported for a constant density jet. Both the mean and rms radial profiles are self-preserving, in which two virtual origins need to be specified.

1.3.3 Summary

Where possible the present work seeks to maintain consistency with the terminology and methods of presentation that has been used by previous researchers in the field. However, where ambiguity exists about the appropriate normalizing scale, the data is usually presented in a raw form.

1.4 MOTIVATION FOR THE PRESENT RESEARCH PROGRAM.

The chemical reactions in a diffusion flame is mixing rate limited so that a diffusion flame is fundamentally dependent on the mixture field produced by that burner. Visualization of the flow field generated by a PJ flow has shown the structure of turbulence to differ significantly from that of a simple jet. The generation of large-scale structures has been deduced to be important in the enhancement of the combustion for those flames. Optimization of the mixing characteristics and the ability to model these flows requires detailed characterization of the effect of precession. The present project is motivated by this need to quantify in detail the effect of precession on the scale of the flow structures and to characterize the mixture field. The velocity field has been previously investigated, thus a necessary pre-request has been to develop an experimental tool to provide quantitative planar measurement of concentration in jet flows.

A two-dimensional technique to image the mixture field using a laser diagnostic technique has been chosen as the primary experimental tool in the investigation since it can provide whole field characterization of the mixture field. The MPJ nozzle has been chosen to control the flow since it has well characterized initial conditions to shed light on the governing parameters of the flow.

1.4.1 Validation of the Experimental Technique

Although the experimental laser based diagnostic technique used in the investigation is well established, it is new to the Department of Mechanical Engineering of the University of Adelaide. Hence the facility has been validated by comparison with data obtained from a flow

whose characteristics are well documented. For this comparison, concentration measurements in a simple, free, turbulent jet from an axisymmetric nozzle has been selected. In addition to providing validation of the experimental setup, the data has provided new knowledge of simple jet flows since there is limited, quantitative, whole field, two-dimensional, concentration data published in the literature.

1.4.2 Characterization of the Mixing Field of a Precessing Jet Flow

The mixing field generated by an MPJ has been investigated by means of a parametric study in which all fundamental parameters have been varied. Experiments have been performed in an open, unconfined environment. The parametric array of experimental data has allowed the effect of Reynolds Number, Strouhal Number, jet deflection angle and nozzle diameter on the mixture field to be assessed. A large field of view has been chosen to allow local features of the flow to be obtained. The data has been processed to provide a quantitative measure of instantaneous and phase averaged statistics of concentration, scalar dissipation, two-point spatial correlation of the macro mixing length scale and probability density functions of concentration.

1.5 HYPOTHESES

Based on work carried out previously and in preliminary experiments, several key hypotheses are proposed. The hypotheses, outlined below, are supported by argument and quantified by experimental data in subsequent chapters. The key hypotheses are:

1. That the flow field produced by the Mechanical Precessing Jet can be divided into three distinct regions, each characterized by distinctly different flow phenomena, which dominate the mixing. These regions are:
    - **The precessing helix region:** The three dimensional footprint of the instantaneous jet of fluid emerging from the MPJ nozzle is, on average, in the shape of a helix, or spiral. Although, from a Lagrangian perspective, each fluid element continues generally in the direction at which it left the nozzle, the position of the nozzle causes the helical footprint to "precess" with the nozzle, so that the flow is three dimensional in space and is time dependent. The character of this **near field** is found to exist for approximately 2π radians (360°) into the helix, and is referred to as the "precessing helix region".
    - **The limit cycle region:** At the position corresponding to about 2π radians in the helix from the nozzle origin, the helix "collapses" in upon itself and the jet fluid flow becomes more or less uniform about the geometric axis of the nozzle. This region constitutes a **transition** between the precessing helix region and the far field and has features which are characteristic of a "limit cycle". This range of the flow is denoted the limit cycle region.
    - **The far field:** Beyond the limit cycle region the flow evolves toward self-similar turbulence in the far field. However the structure of this far field turbulence is

determined by the upstream flow and differs significantly from the far field of the non-precessing jet flow.

2. Precession influences the properties of the near field, the precessing helix region, by the addition of a "strain rate" generated directly by the rotation of the nozzle. The ratio of the additional strain rate introduced by precession relative to that of the jet without precession, controls to a large measure the shape of the helix, the position of the transition (limit cycle) region and the concentration of fluid within it.
3. Precession causes the transition region to display several characteristics of a limit cycle.
4. The spectrum of length scales within the limit cycle region and the far field region are altered fundamentally by precession in a manner which suppresses fine scale mixing and augments large scale mixing.

1.6 OUTLINE OF THE REMAINDER OF THE THESIS

The present **Introduction** seeks to inform the reader of the history and significance of the precessing jet flow. The motivation for the investigation and the tools used for it are then presented with reference to relevant research on jet flows and combustion and to gaps in present knowledge. The key hypotheses are presented and form the basis of the structure in subsequent chapters. The **Experimental Techniques and Validation** of the experimental method is described in detail in Chapter 2. Details of the experimental method, the method of reducing data and a validation of the technique are presented. The flow chosen for validation is the 'trivial case' of precessing jet flows, a non-precessing jet issuing from an axisymmetric nozzle. The **Developing Region of Mechanical Precessing Jet (MPJ) Flows** is investigated in Chapter 3 using a parametric study of jet exit conditions. A description of the flow field and the parameters used to normalize the flow are presented along with evidence of features that have characteristics of a 'limit cycle'. Statistics of the **Mean and Fluctuating Concentration in the MPJ Flow Field** are presented in Chapter 4. The statistical data are presented in both conventional line plots and in two-dimensional format. **The Effects of Precession on the Macro Mixing Length Scale** is investigated in Chapter 5 through the computation of the Integral Length Scale. In Chapter 6 the **Effect of Precession on Scalar Mixing** is deduced from measurements of scalar dissipation and probability density functions (PDF's). Chapter 7 provides **Conclusions** that draw together and assesses the foregoing evidence for and against the initial hypotheses. Recommendations for future work are also given in Chapter 7.

2. EXPERIMENTAL TECHNIQUES AND VALIDATION

2.1 OVERVIEW

The experimental equipment and techniques used in the present studies of simple and precessing jets are described. The design of the experiment is validated by investigating the scalar mixing field in the well documented, simple axisymmetric jet. The method of calibration of the laser diagnostic system and each correction procedure is described.

2.2 EXPERIMENTAL EQUIPMENT AND TECHNIQUES

2.2.1 Introduction

A planar laser diagnostic technique has been the tool selected for the present investigations of jet flows. This technique has the significant advantage over single point techniques in that it is planar, and the advantage over sampling techniques of being non-intrusive, allowing the remote measurement of the scalar field. The mixture field can be captured both quantitatively and qualitatively, allowing the concentration field to be mapped as a sequence of instantaneous, two-dimensional images.

Flow visualization has been used semi-quantitatively for many years within the controlled environment of a laboratory to describe flow patterns and identify structures in flows (e.g. Hussain and Clark, 1981). Planer laser imaging is a direct evolution of this basic fluid dynamic investigative tool. Techniques which allow quantitative imaging in a two-dimensional plane

include Mie scattering (e.g. Chao *et al*, 1990,1991; Clemens and Mungal, 1991), Raman scattering (e.g. Schefer *et al*, 1994), Rayleigh scattering (e.g. Everest *et al*, 1995) and Planar Laser Induced Fluorescence (PLIF) (e.g. Dimotakis *et al*; 1983, van Cruyningen *et al.* 1990). Fundamental elements of the layout of the experimental apparatus are the same for all of these techniques. The essential ingredients are a sheet of light, produced by a laser beam, suitable optics through which the beam is passed and a detector, which can be a solid-state array or photographic film. The beam produced by the laser generates a signal either by scattering from particles or molecules or by excitation of species within the flow field. The signal is collected by the detector and is stored for processing.

The Mie Scattering technique has been chosen for the present investigation because of its high signal strength, enabling a large flow area to be investigated. Figure 2.1 shows a comparison of the relative signal strengths from an analysis by Eckbreth (1988) of a comparable experiment using the various laser diagnostic techniques. It highlights that the Mie Scattering signal is orders of magnitude larger that other techniques which can be used for planar imaging.

2.2.2 Experimental Technique - Mie Scattering

2.2.2.1 Introduction

The technique of imaging a flow by scattering light from small particles is generally known as Mie Scattering, Lorenz-Mie Scattering or Marker Nephelometry. The feasibility of the technique for use in experimental investigations of flows was initially begun by Rosenwig *et al.* (1961) and further explored by Becker *et al.* (1963, 1969(a) & 1969(b)). A detailed description of the theory and experimental application of the technique is reviewed by Becker (1977). It has been used by researches to investigate the concentration and mixing in round jets (Becker *et al.*

1969(b); Shaungnessy *et al,* 1977, Long *et al.* 1978), coherent structures in jets (Long *et al.* 1981; Chao *et al.* 1990,1991; Clemens and Mungal, 1991), conserved scalar concentration in flames (Kennedy *et al.* 1979), time-resolved, three-dimensional concentration field in a transitional gas jet (Yip *et al.* 1987), reaction zones in flames (Roquemore *et al.* 1986), local extinction of a jet diffusion flame (Takahasi *et al.* 1992) and characterisation droplet/vapor/vortex interactions in a two dimensional shear layer (Hancock *et al.* 1993).

2.2.2.2 Experiment Layout

A pictorial representation of the general arrangement of experimental apparatus for the present experiments is shown in Figure 2.2, highlighting the typical physical arrangement of planar imaging experiments. A light sheet is formed by focusing the laser beam through a long focal length (~1m) spherical lens and then diverging the focusing beam in one dimension with a cylindrical lens. The resulting sheet of laser light is directed through the jet flow. Optics are arranged so that the focus of the long focal length spherical lens is on the center line of the flow field to minimize the thickness of the sheet for optimal spatial resolution. Thus the light sheet bisects the flow field.

The jet stream is seeded with the a marker or particles, which may be liquid droplet (typical minimal droplet sizes are, for water vapor ≈2.0 μm, dioctyl phthalate ≈0.8μm, olive oil ≈0.6μm) or solid particles (Al_2O_3 , TiO_2 , glass beads or sugar particles from < 1μm). The accuracy of the technique for concentration measurements depends strongly on how closely the marker follows the marked fluid. Good accuracy requires that the properties of the marker should not change over the field of measurement and that the effects of drag, evaporation or sublimation, chemical reaction and changes in index of refraction of the marker be negligible. The marker should everywhere in the flow constitute a negligible mass fraction of the fluid and also have a negligible effect on fluid viscosity and density.

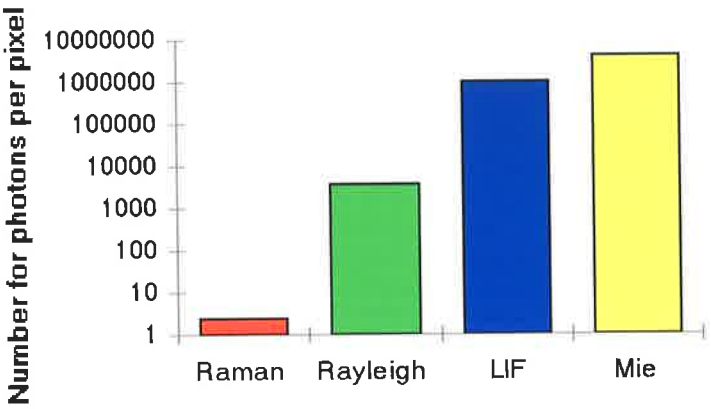

Figure 2.1 A comparison of signal strength for different laser diagnostic techniques (Eckbreth, 1988)

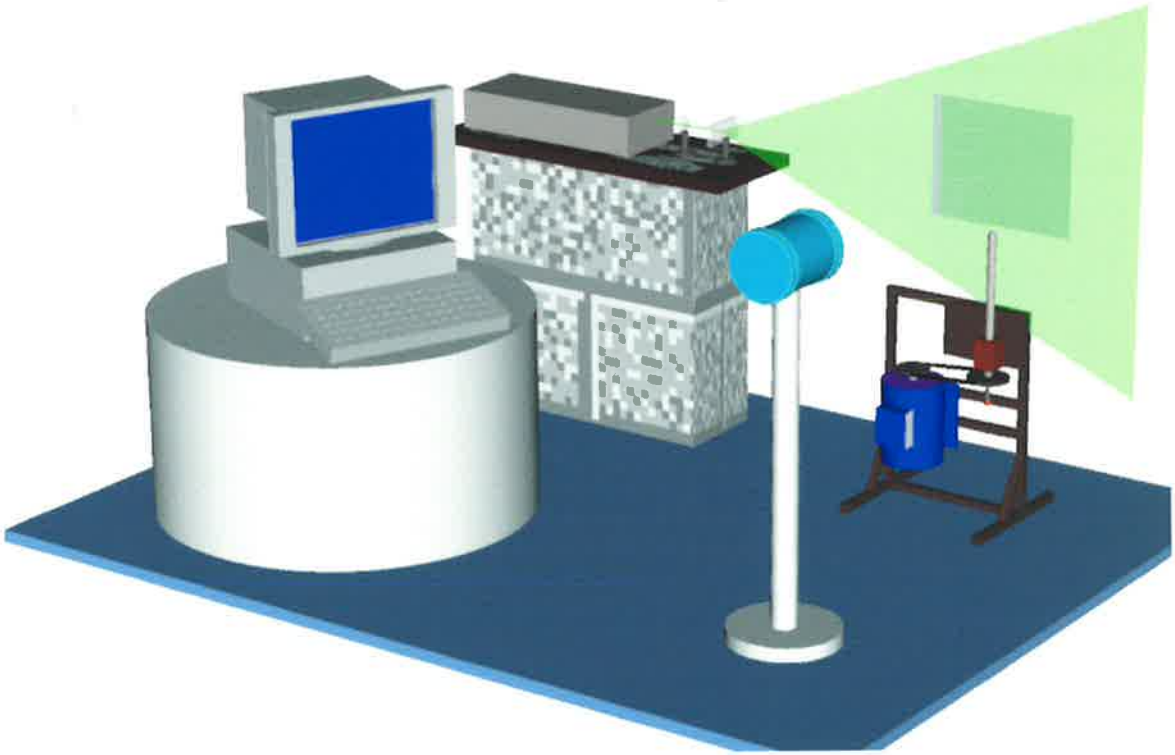

Figure 2.2 A pictorial view of the experimental set-up showing the computer used to control the experiment and store the data, the laser, laser sheet in which the interrogation volume is highlighted, the nozzle and the camera (foreground).

Light, scattered by the particles, is collected by a recording device, either a film or array camera located at right angles to the laser sheet. The collected images can be processed to provide a concentration map of the jet fluid as it mixes with the surrounding ambient fluid. Use of a sufficiently short pulse of the illuminating sheet can eliminate the "integrated" effects common in many flow visualization experiments. The laser used in the present measurements produces a 3 nsec laser pulse which effectively freezes the turbulent motion in each image. The effectively instantaneous images, in digitized format, can then be further processed to provide a range of statistical data.

2.2.2.3 Sources of Error

Three dominant sources of error are associated with the Mie scattering technique described above. These are marker (or particle) inertia, optical attenuation and marker shot noise. Other sources of error, which have been addressed in the literature by others, relate mainly to the influence of specific items of equipment used by those investigators.

Marker Inertia.

The inertial characteristics of the particles used to mark the fluid determine how well the marker follows the flow. Becker *et al.* (1969a) analyzed this problem and calculated the frequencies at which the velocity amplitude response is within a set value can be predicted. As an example Becker *et al.* (1969a) computed estimates of deviation of solid particles of density 1 g/cm^3 for a range of diameter, dp, when moving in a sinusoidal varying air stream at 25 °C at 1 atm. Their analysis gives the frequency, f at which the velocity amplitude at which the response of each particle size differs by 10% from the amplitude of the air stream fluctuation. The results for the Becker *et al* (1969a) analysis are reproduced in Table 2.1. The analysis showed that doubling the viscosity of the fluid doubles the frequency to which the particles can "follow" the air

stream, and doubling the density of the particles, halves it. Essentially, the smaller the particle, the more accurately it will follow the flow.

Table 2.1 A comparison of the dependence of particle diameter, dp to frequency, *f* response (Becker *et al* 1969)

dp (μm)	0.1	0.3	1	3	10
f (kHz) (10% amplitude error)	930	180	22	2.7	0.25

Melling and Whitelaw (1975) used an approximate equation, based on the Stokes equation, to determine the frequency response of particles, typical of those used in laser doppler velocimetry experiments. The equation

$$f \leq \frac{0.4\nu}{d_p^2 \sigma}$$

Equation 2.1

was used to satisfy the criterion : *amplitude of particle oscillation / amplitude of fluid oscillation > 99%*. For air of kinematic viscosity of air, $\nu = 1.5\text{x}10^{-5}$ m^2/s, a typical particle diameter of $d_p = 0.6\text{x}10^{-6}$m and a density ratio of $\sigma = 767$ based on the olive oil used in the present experiments, Equation 2.1 predicts a frequency response of 21.7 kHz. This is much higher than the expected maximum turbulent frequency of interest in the present experiments. The inability of the marker to adequately follow the flow is stated by many authors as the major weakness of the technique.

Optical Path Attenuation.

An error is also introduced by optical path attenuation due to absorption and scattering of the laser beam by particles along the optical path. This occurs both as the laser sheet enters the control volume and as the scattered signal travels towards the detector. For a given path length the beam intensity decreases exponentially with the number of particles in the path. When this

number fluctuates in time, a complex modulation is added to the scattered light field and reaches the detector as noise. Attenuation noise can be minimized by maximizing the available laser power to produce a signal of high intensity and by minimizing the particle concentration to that just necessary to achieve acceptable results.

Marker Shot Noise

Concentration measurement using the Mie scattering technique is based on the "counting" of the number of particles in a control volume. It is this number which is assumed to be proportional to the concentration of the marked fluid. When the size of the control volume is large and the seeded density of the marker is high the fluctuation of the number of particles used to represent a given concentration of marked fluid will vary only minimally compared to the total number of particles. As the size of the control volume or the density of the seeded particles decreases, the fluctuation, as a proportion of the total number, becomes significant. This variation in the number of particles introduces an error in the estimate of the concentration of the marked fluid and is termed, *marker shot noise*.

Marker shot noise imposes a limitation on the spatial resolution of measured concentration. While minimizing the concentration of marker particles helps to provide acceptable optical path attenuation noise, a progressive reduction in the size of the control volume, to increase spatial resolution, also causes the particle population in the control volume to decrease and the ratio of fluctuations in particle numbers to the total particle number to increase. Therefore enhanced spatial resolution is achieved at the expense of increased marker shot noise. Becker (1977) noted that the error introduced by marker shot noise are generally small, however the error is significant for high power light sources and low particle concentrations within the control volume.

2.2.2.4 Data Correction

There are two important corrections to the data that have been applied. The first is to allow the ensemble average of the images to be carried out. The concentration value within each individual image is a function of the laser power in the pulse used to capture that image. If the power of the laser pulses varies between pulses, then each image must be corrected for this pulse-to-pulse power variation. The correction is made by reference to a known concentration of the jet fluid, which occurs in the unmixed core region of the jet immediately following the jet exit. Normalizing each image relative to this reference signal also compensates for any variations in seeding density, which may occur over a time scale that is much longer than the convection time of fluid in the image region.

The second correction required is for variations in the spatial intensity of the light sheet. Ideally a pulse from a pulsed laser is a cylinder of light of constant intensity. In practice, the intensity varies slightly in the radial direction and possibly also in the axial direction. It is the variations in the radial direction, which are of concern here because when the beam is expanded through the cylindrical lens in one dimension the variation will produce a variation of the beam intensity profile across the long axis of the light sheet. A correction for consistent variations in the light sheet is obtained by a calibration of the light sheet using a planar laser induced florescence technique. A glass container (the "Fish Tank") is filled with a uniform concentration of Rhodamine B, a florescent dye which emits orange light when excited with the green, 532 nm of the Nd:YAG to provide intensity maps of the light sheet. Several images are captured by the detector to produce an "average light sheet" profile. A curve is fitted to the profile and then used to generate a correction light sheet correction image. This correction image, a record of the consistent non-uniformities in the light sheet is used to correct each of the data records.

2.2.3 Experimental Equipment

2.2.3.1 General Arrangement of the Experiment

The schematic diagram in Figure 2.3 includes equipment used for both the random and phase referenced collection of images and shows the lines of communication between experimental items. Phase referenced collection of data is a method of collecting images at a constant phase in the rotational (precessional) cycle of the nozzle tip. The figure illustrates that the plane of the incident laser light is perpendicular to the viewing window of the detector. The field of view of the detector is highlighted and can be altered by adjusting the distance between the plane to be imaged and the detector.

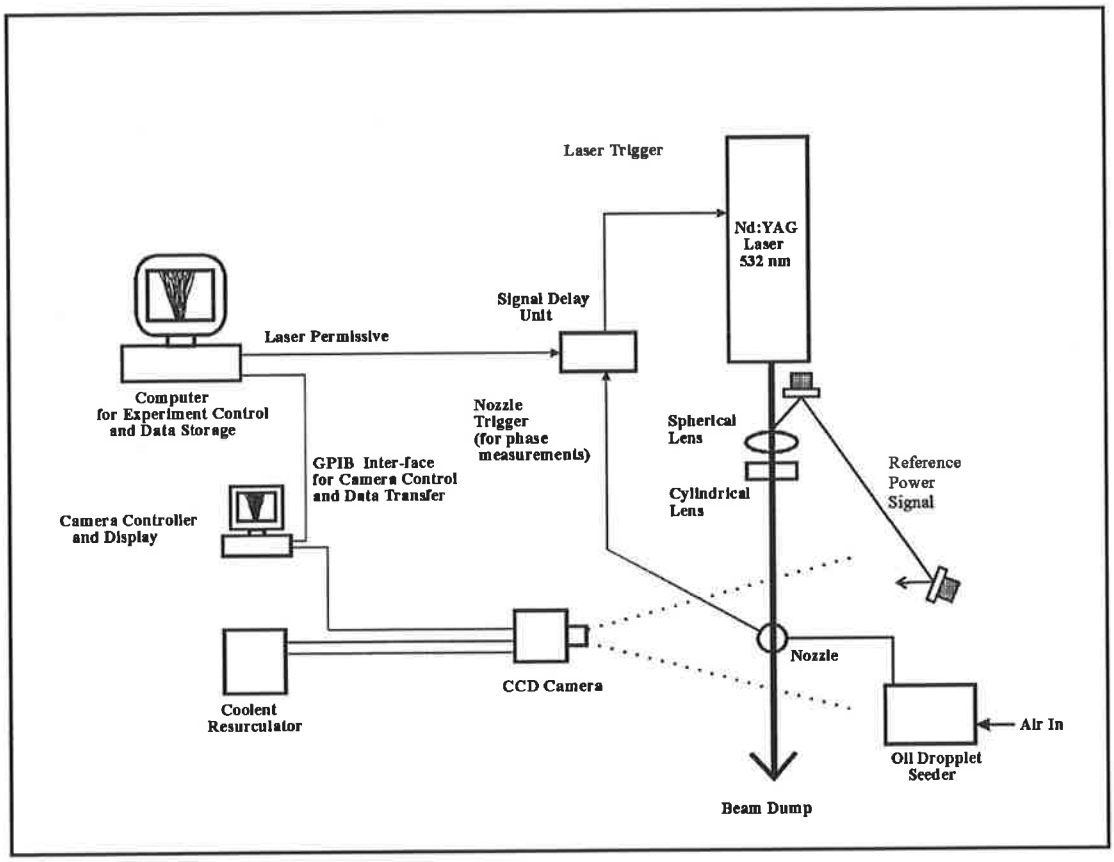

Figure 2.3 Arrangement of experimental equipment used for both the random and phase triggered collection of data.

A pulse of laser light is generated by the Nd:YAG laser when a permissive trigger signal has been received from the computer controlling the experiment. The pulse of light is steered by two mirrors on to the incident beam axis of the experiment. Appropriate optics transform the cylindrical pulse into a light sheet by diverging the beam in one dimension through a cylindrical lens and converging or focusing the beam in the other dimension through a spherical lens. The convergence of the beam increases the spatial resolution and the light intensity in the probe volume. The line of convergence is at the centre of the image window, on the axis of rotation of the nozzle. In the line of convergence the light sheet is approximately 0.25 mm thick.

The light sheet interacts with the flow field and the resulting signal (scattered light), from the image window is captured by the detector. The detector's two-dimensional array of pixels accumulates a charge, which is proportional to the intensity of the signal. Once the image has been collected the array is read out from each pixel individually. An analog-to-digital converter, with 12-bit resolution then converts the signal from each pixel into a digital format. The image is transferred to the control computer via a GPIB interface. The computer is also used to communicate with and control the detector / laser timing sequence.

2.2.3.2 Details of the Experimental Equipment.

The major items of equipment and their performance characteristics are described below.

The Laser

The laser which is used in this investigation is a Neodymium Yttrium Aluminium Gallium (Nd:YAG) laser (Coherent "INFINITY"). The fundamental wavelength of the laser, 1064 nm, is frequency doubled to 532 nm, which is in the visible green region of the spectrum. The

power intensity of the pulse in the radial direction is almost 'top-hat' for the fundamental frequency, which produces a light sheet profile having minimal radial beam intensity variations. The confirmed pulse width is less than 3 nsec. The laser can be controlled externally by a trigger signal and when internally controlled can have a pulse repetition-rate of up to 100 Hz.

The Optics

Specific optics capable of transmitting the high power of this Nd:YAG are used. The mirrors are coated to maximise reflection of the 532 nm beam. The spherical lens has a focal length of 1 or 1.5 m, depending on the spreading angle of the light sheet required. In both cases the lens is sufficiently far from the experiment to avoid flow interference.

The Seeder

A six-jet atomiser (TSI Model 9306) is used both to generate and introduce particles into the jet flow. The number of particles generated is directly proportional to the input pressure to the unit. Between one and six jets can be used to vary the particle concentration and a side bypass of the jet fluid is available to give a continuous range of particle densities. Olive oil is used as the seeding material because it is non-toxic and is readily available. This yields a particle size distribution which peaks close to 0.6 μm as seen in Figure 2.4.

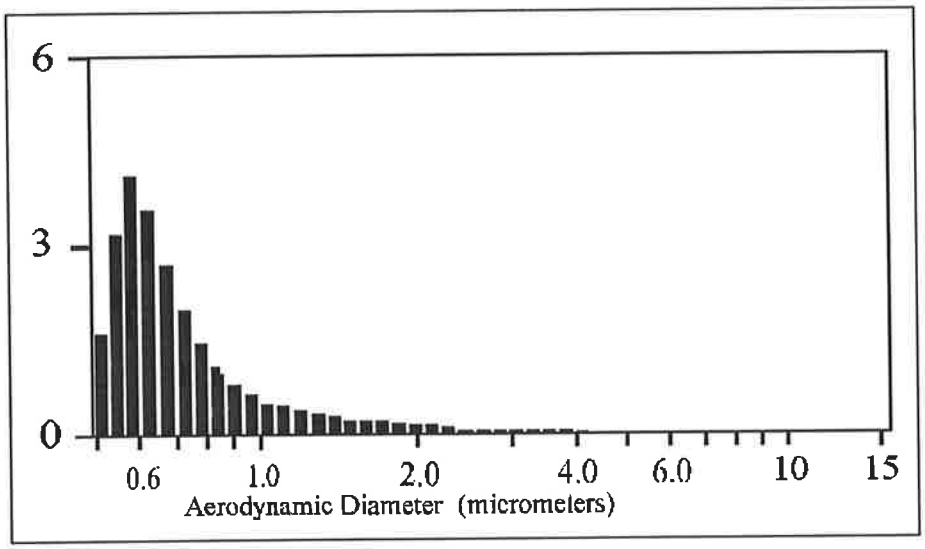

Figure 2.4 Particle size distribution from the oil seeder used in experiments as specified by the manufacturer (TSI, 1997)

The Detector

The two-dimensional detector array is a cooled, slow scan, 'charge coupled device' (CCD) camera (Photometrics STAR 1). It has an image array of 576 x 384 pixels each of which are 23μm square. The chip holding the array is cooled by a thermoelectric cooler so that the camera operates at -45 °C. This feature and the slow read out of the data ensures minimal interference from dark current, electrical and read out noise. The analog-to-digital converter converts the pixel charge, which is linearly proportional to the detected light intensity, to digital format for storage with 12 bit resolution. A given image can then be measured, without scaling, over the range of values, 0 – 4096.

Fluid Flow

Air for the jet is drawn from pressure regulated plant air metered by a rotameter (Fisher and Porter, FP-1/2-27-G-10 tube, ½-GSVT-45A & ½-GSVT-410 floats) with a nominal accuracy of ±2%. Nozzles are mounted approximately 1 m above floor level and jet fluid is vented through a 1m x 1m overhead exhaust hood. The extraction velocity is controllable, and is set to produce a negligible co-flow in the working section. Cross drafts were minimised by keeping all doors and vents in the relatively small laboratory (6m x 7m) closed.

2.2.4 Details of the Experimental Nozzle

Nozzles of two different diameters were used in the present experiments. Each nozzle generates a jet, which emerges on the nozzle axis but is deflected at an angle from that axis. The nozzle can be rotated mechanically about its geometric axis so that the axis of the deflected jet rotates about the axis of rotation (geometric axis) of the nozzle. That is, the jet precesses about the nozzle axis.

2.2.4.1 The Mechanical Precessing Jet (MPJ) nozzle

The larger of the two nozzles used in the present experiments is the same as that used by Schneider (1997). Details of that nozzle and drive mechanism and control can be found in Schneider (1997) and Schneider *et al.* (1997, 1996). This nozzle has an exit diameter of 10 mm. The smaller 3mm exit diameter nozzle described below is constructed in a way which is similar to Schneider's 10 mm nozzle.

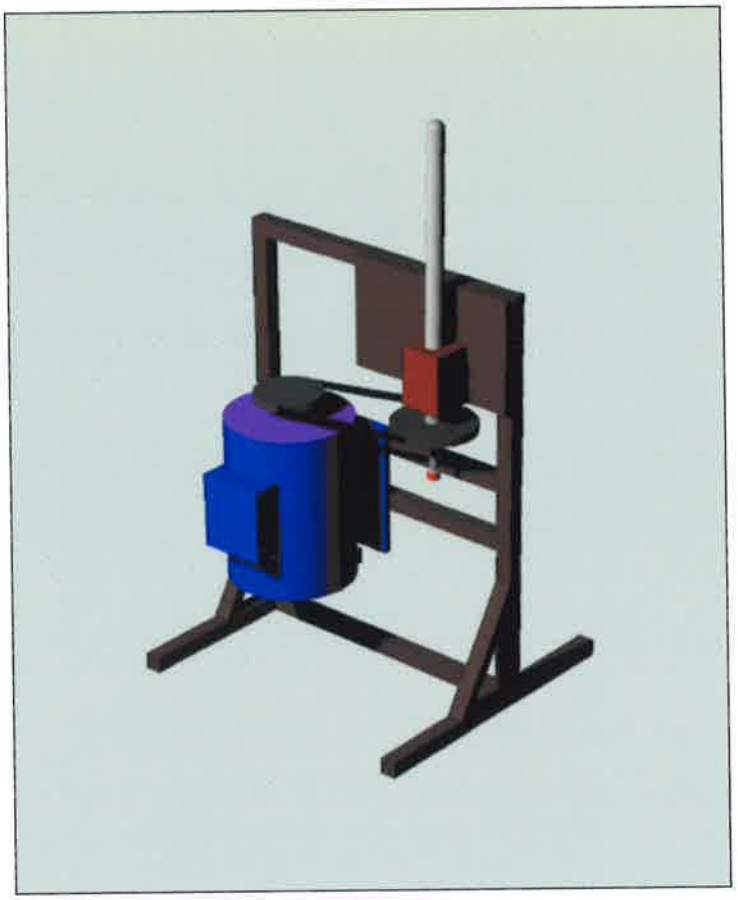

Figure 2.5 An isometric view of the layout of the MPJ nozzle, motor and frame. A shield to avoid disturbances from the motor fan and belt drive, which otherwise would influence flow in the region of the nozzle tip is also used but not shown.

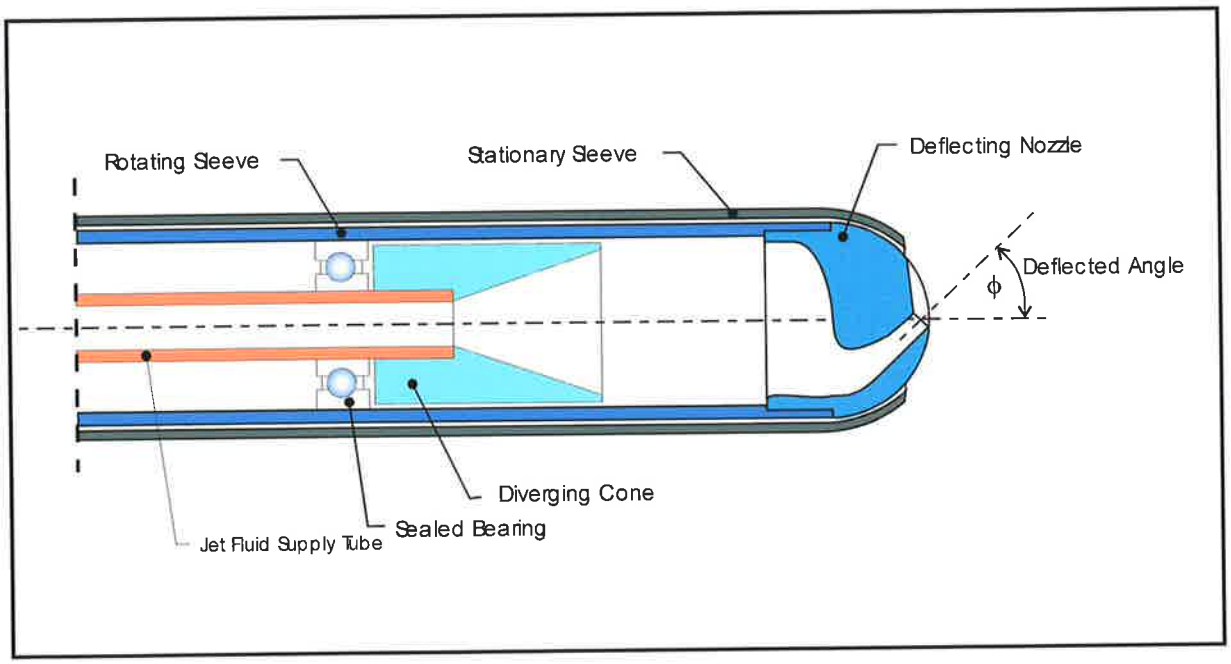

Figure 2.6 A schematic of the internals of MPJ showing a jet fluid supply tube, flow diffuser, exit nozzle, stationary sleeve and the rotating nozzle tube..

An isometric drawing of the 3mm diameter MPJ nozzle, motor and support frame is shown in Figure 2.5. Rotation of the nozzle is provided by the electric motor (ABB 3 Phase CI.FIP 55 IEC34 MT80A19-4 Mk110018-L) to which it is connected by a toothed rubber timing belt. Angular frequency of the motor is controlled by a frequency control unit (ABB ACS 200) which allows the nozzle rotational frequency to be set between zero and 100 Hz, and maintained within ± 0.01 Hz. Air supply to the nozzle is via a 10mm diameter nylon air hose, which is connected to the inner stationary, nozzle feel pipe.

The inner stationary, jet fluid supply tube (Figure 2.6) also serves as the shaft and so defines the axis of rotation of the nozzle. Jet fluid is introduced into the jet supply tube after it has been seeded with the marker droplets. Jet fluid exits from the jet supply tube through a stationary diffuser, and is exposed to the inner surface of the rotating external pipe. The inner surface area of the rotating nozzle is minimised by keeping the exposed length to about one diameter. This arrangement is found to impart negligible rotation or swirl to the jet fluid (Schneider, 1996). An external sheath surrounds the rotating pipe to minimise the effects of the external boundary layer on the outer surface of the rotating pipe. Without this sheath a low-pressure region is generated upstream from the jet exit plane within the boundary layer, causing some flow reversal at high rotational speeds.

The contoured internal surface of the nozzle is designed to produce a 'top-hat' velocity profile at the exit of the nozzle and this is achieved with good accuracy when the nozzle is stationary. Phase averaged hot wire data obtained by Schneider (1996) with the 10mm diameter nozzle, while rotating, indicated that the effects of rotation on the exit profile are of second order. The exit diameter of the nozzle used for most the present experiments is 3mm, although the 10mm nozzle is also used.

The deflection angle of the exiting jet can be altered be interchanging the nozzle tips. Nozzles have been manufactured to give deflection angles of 0°, 15°, 30°, 45° and 60°. The 0° nozzle is used for the validation of the system and to provide a datum for a comparison of the effect of precession on the jet.

2.2.5 Data Collection and Reduction.

The collection of data and the experimental procedure are detailed below. The process of reducing the data for statistical analysis is also outlined. All necessary computer code has been purpose written in the computer language PASCAL (BORLAND v7.0 for windows) for the handling and manipulation of data and executed on IBM compatible computers.

2.2.5.1 Experimental Procedure.

Outlined below, in step-wise fashion, is the procedure employed for collecting data. Prior to this, the laser and optics have been assembled in a suitable position under the exhaust hood and a beam dump is suitably positioned to capture the laser sheet. The position of the light sheet and the quality of the light sheet does not vary significantly from experiment to experiment.

Step1. The nozzle to be investigated is positioned under the extraction hood with the light sheet passing through the geometric axis of the nozzle. The geometric axis of the nozzle is also located at the focal length of the focusing lens. The nozzle jet fluid supply is connected to the seeder and the seeder to the nozzle.

Step2. A target is positioned on the axis directly above the nozzle. The target serves several purposes. First, it is used to determine and optimise the field of view of the experiment. Second, it is used to focus the camera. Finally is used as a reference for the spatial resolution of the experiment.

Step3. Once the camera is set, the nozzle and target are removed and replaced with the 'Fish Tank'. This tank, filled with a uniform concentration of Rhodamine B, is used to quantify the spatial variations in the light sheet. Several images of the light sheet, typically 20 off, are collected. An average of these is later used in the data correction process. The camera is not moved until after the end of the experiment. This ensures that the field of view of each pixel remains constant.

Step4. The 'Fish Tank' is replaced with the nozzle and target. The target and the nozzle are aligned to the reference frame / field of view of the camera and an image is collected for scaling of the experiment.

Step5. Images of the background with the **laser off** are collected (typically 20 off).

Step6. Images of the background with the **laser on** are collected (typically 20 off).

Step7. The fluid flow rate through the nozzle is set and seeding adjusted to that required to maximise the dynamic range of the detector and to minimise attenuation noise.

Step8. A series of images is collected. The number of images varies depending on the type and requirements of the experiment.

Step9. Images are down loaded to a bulk storage area. This is necessary because of the large amount of data in each image (0.443 Mb).

Step10. The experiment or nozzle conditions are then changed ready for the next experiment.

If phased average data of the MPJ is being collected, a trigger delay is used to synchronise the rotation of the nozzle with the firing of the laser.

2.2.5.2 Data Reduction

An individual image produced by the detector (CCD camera) is generated from an array of 576 x 384 pixels. Hence each images represents 221,184 individual measurement points of concentration. These are loaded by the program into a two dimensional array, $pix_{(i,j)}$. The use

of arrays allows direct manipulation of images as a whole. An average of nine pixels is used in determining the power of the laser pulse for that image. The nine pixels chosen are centred around a pixel (z,r), which has been predetermined to be located at a position containing 100% nozzle fluid, i.e. in the potential core of the jet. This point is used to correct for the pulse-to-pulse variations in laser power. Below is tabled the procedure for deriving a statistical mean of the data. The calculation of other statistical variables, such as the RMS, is carried out in a similar manner. The algorithm for calculation of the ensemble average is as follows,

(1) FIND THE MAXIMUM PULSE POWER OF ALL THE IMAGES.

for image 1 to n,

LOAD IMAGE	$pix_{(i,j)} = [i\hat{}j]$ ie. in a 2-D array
SUBTRACT BACKGROUND	$pix_{(i,j)} = pix_{(i,j)} - back_{(i,j)}$
FIND MAXIMUM PULSE POWER	$pulse = \frac{1}{9}\sum_{i=z}^{i=z+3}\sum_{j=r}^{j=r+3}[i,j]$
	if pulse > pulse_max then pulse_max = pulse

(2) CORRECT AND AVERAGE THE IMAGES.

for image 1 to n,

LOAD IMAGE	$pix_{(i,j)} = [i\hat{}j]$
SUBTRACT BACKGROUND	$pix_{(i,j)} = pix_{(i,j)} - back_{(i,j)}$
FIND PULSE POWER For this image (this_pulse)	$this\_pluse = \frac{1}{9}\sum_{i=z}^{i=z+3}\sum_{j=r}^{j=r+3}[i,j]$
RELOAD IMAGE	$pix_{(i,j)} = [i\hat{}j]$
SUBTRACT BACKGROUND (with laser on)	$pix_{(i,j)} = pix_{(i,j)} - backlas_{(i,j)}$
CORRECT FOR LIGHT SHEET	$pix_{(i,j)} = pix_{(i,j)} * max(sheet) / sheet_{(i,j)}$
CORRECT FOR PULSE POWER	$pix_{(i,j)} = pix_{(i,j)} * pulse\_max / this\_pulse$
SUM TO AVERAGE ARRAY	$pix\_ave_{(i,j)} = pix\_high\_mem_{(i,j)} * pix_{(i,j)}$
FIND AVERAGE	$average_{(i,j)} = pix\_ave_{(i,j)} / n$

2.2.6 Comments

Care has been take at each step of the experiment work to ensure a consistent experimental methodology and set up of experimental equipment has been carried out. Validation of this methodology, experimental set up, data correction and reduction is presented in the next section.

2.3 THE SCALAR MIXING FIELD OF A SIMPLE JET

2.3.1 Introduction

The present diagnostic technique is validated by comparison of results from a non-precessing jet with those of other researchers who used various single point measurement techniques. The relevant conditions for the experiments and the techniques used are shown in Table 2.2. A wide range of Reynolds numbers and several different working fluids have been used.

Table 2.2 A comparison of the different experimental conditions and techniques used in the present experiment with those used by previous researchers for validation of the experimental method.

Author, date	Jet fluid/ambient fluid	Reynolds number	Method
Becker (1967)	air/air	54,000	Mie scattering
Birch *et al* (1978)	Natural gas/air	33,000	Raman scattering
Lockwood *et al* (1980)	air/air	50,000	Thermometry
Dowling and Dimotakis (1990)	C_2H_4/N_2	5,000	Rayleigh scattering
	C_3H_6/Ar	16,000	
Present Data	air/air	16,400	Mie Scattering

To expedite comparison between the experiments, the data have been normalised by defining dimensionless spatial variables in a cylindrical co-ordinate system. The dimensionless axial coordinate is defined as, $\chi = (z-z_o)/r_o$ where z is measured in the axial direction, z_0 is the location of the virtual origin and r_o is the radius of the nozzle. A dimensionless radial parameter is $\eta = r / (z-z_o)$, where r is the radial distance from the geometric axis of the nozzle is also used to collapse the radial components of different variables in the self similar region of the jet mixing field.

2.3.1.1 Experimental Conditions and Spatial Resolution

The jet issuing from a 3 mm diameter profiled nozzle with a smooth contraction to the inlet is used for the comparison. The diametral contraction ratio is 5.16 and the profile of the contraction is $z = \sin^{1/3} r$. The bulk mean exit velocity of the jet is 98 m/s, as calculated from the volume flow rate, giving an equivalent Reynolds Number of 16,400. Statistical properties of the mixture field are calculated from 1200 full images of a plane of approximate dimensions 300 x 200 mm, giving a spatial resolution of 0.47 x 0.47 x 0.25mm. The latter dimension is an estimate of the light sheet thickness determined for the theoretical minimum spatial length that a laser beam of a set wavelength can be focused with a given lens. The smallest scale in the flow, the Kolmogorov scale, λ_k can be estimated from, $\lambda_k \propto d.Re^{-3/4}$ (Dowling and Dimotakis, 1990). For the present experiment at the jet exit, λ_k is of the order of 2 μm, approximately 200 times smaller than the spatial resolution of the data collector. Thus, the data collected will not resolve the finest scales in the flow.

2.3.2 Interpretation of Concentration Fields

From an individual experiment, a collection of images is used to define and characterize the mixture field. The individual images provide excellent qualitative visualization of the mixing patterns and these can be quantified statistically to reveal the major characteristics of mixture field for a given set of boundary conditions. The statistical methods used, and their implications, are outlined below.

2.3.2.1 Instantaneous Data – Qualitative and Quantitative

Figure 2.7 shows two randomly selected images of a two dimensional slice of the instantaneous concentration in the simple jet. A false colour scale is used to represent the measured

concentration values in the jet, indicated by the colour bar at the bottom of each image. The white background represents "pure" ambient fluid while black represents any nozzle fluid at a concentration above the maximum shown in the colour bar. Radial and axial distances are measured in mm, to give a physical perspective of the flow. *(Note: the planar data presented in this thesis are in absolute units. Where appropriate, constant same colour scales are used in relating images. However a colour bar is provided since a range of false colour scales are used in an attempt to provide good quantitative information.)*

The two images show the qualitative features which have been identified in previous investigations such as large scale structures and random fluctuations (van Cruynigen *et al.* 1990). The instantaneous concentrations depart significantly from the axisymmetry that is assumed in many mathematical models. These matters will be addressed later, but for the moment it should be noted that the experimental technique is able to show the instantaneous structure of the flow (qualitative features) and to provide quantitative information.

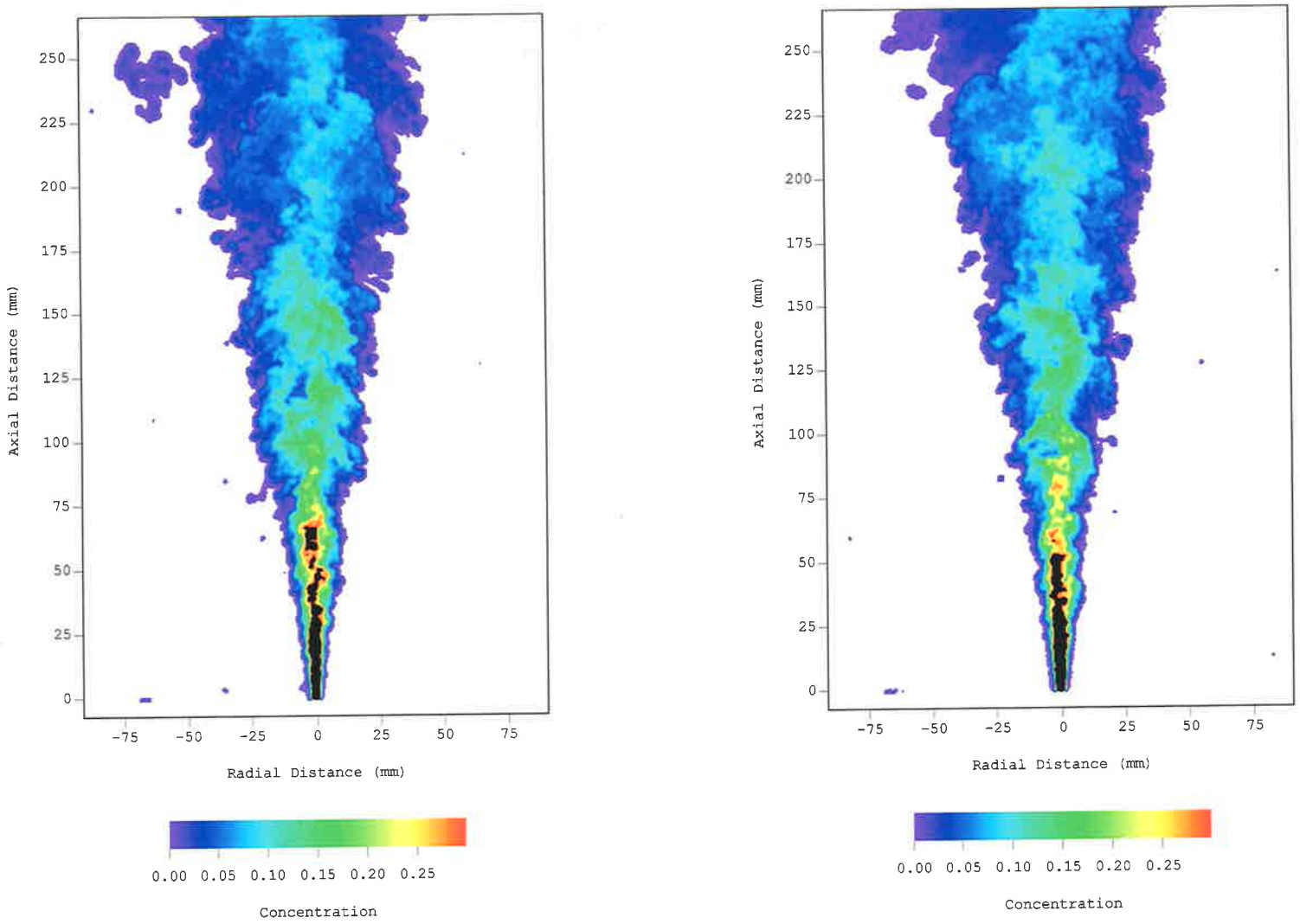

Figure 2.7 Two instantaneous images of concentration of the scalar mixing field of a simple axisymmetric jet obtained with a Mie scattering technique in air : d = 3.0 mm, Re =16,400.

2.3.3 The Average Concentration Field.

The marking of the jet fluid in the present experiments is assumed statistically uniform at the jet exit, spatially across the nozzle and temporally over the experiment. The mass concentration of jet fluid at any point is denoted by $C_i(z, r)$, where z and r represent the cylindrical polar coordinates of the measurement point in the image and i, a particular instantaneous image. If the binary diffusivities of all pairs of molecules in the field are equal, and if the diffusivities of the marker in the field are the same as these molecular diffusivities, then the marker will portray exactly the transport of the marked stream material (Becker,1977).

Average concentration is defined as a function of position downstream, z, and the radial distance from the jet, r, (Hinze, 1959) as

$$\overline{C} = \frac{1}{N}\sum_{i=1}^{N} C_i(z,r)$$

Equation 2.2

Here N is the number of instantaneous images used in the summation and $C_i(z,r)$ is the *i*th instantaneous concentration distribution (corrected for background noise, pulse-to-pulse variation in laser power and variations in the light sheet). An image of the mean concentration field is presented in Figure 2.8. Equation 2.2 defines the average as an ensemble average (Hinze, 1959, pp 4) of the mixture concentration at each pixel in the field. This definition allows the use of statistics to investigate the nature of the mixing field, i.e. the similarity of the average mixture field, gross phenomena (i.e., jet spreading angle, virtual origin etc) and characterize the effects of different experimental conditions.

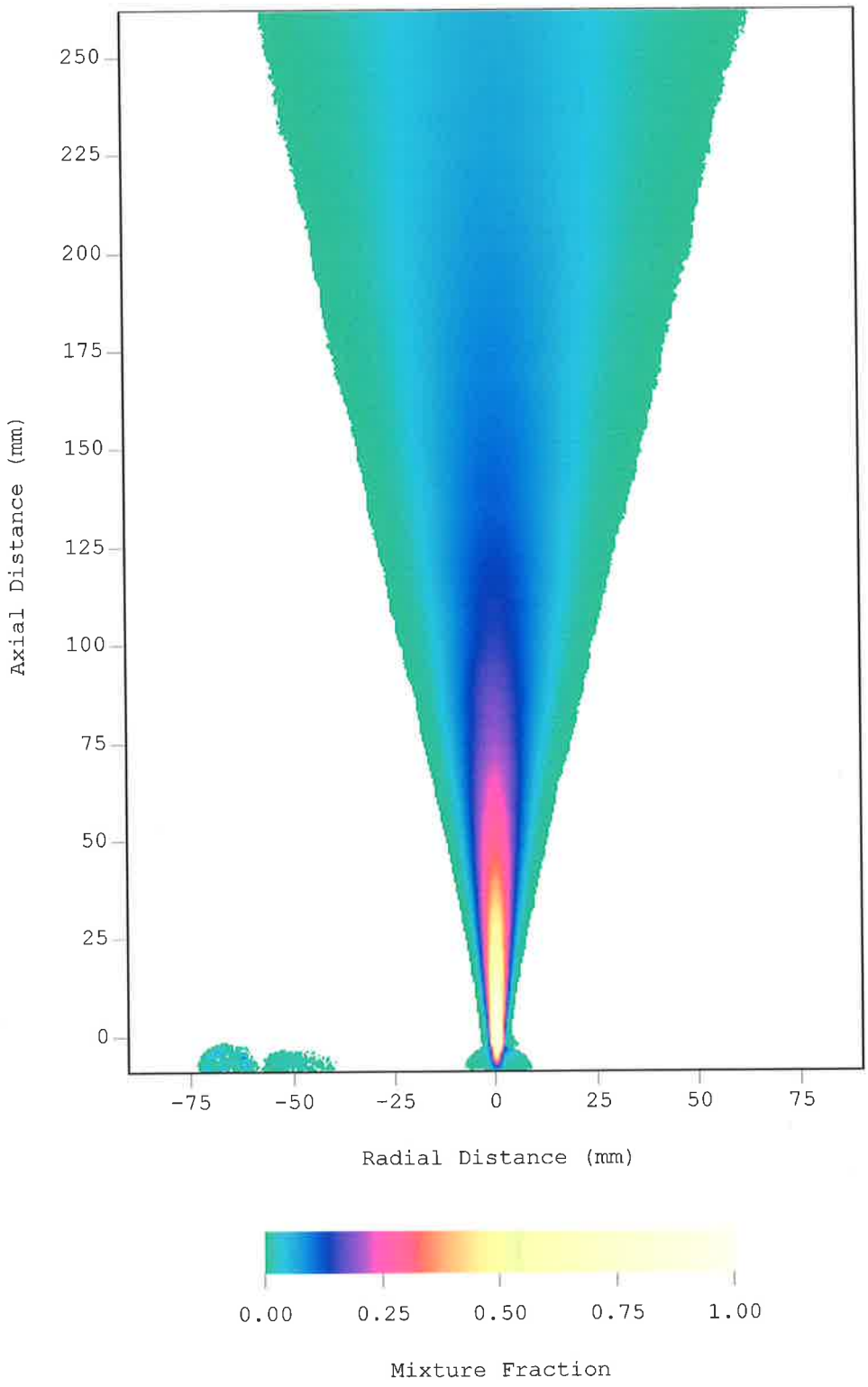

Figure 2.8 The mean mixture field of a simple jet, conditions as in Figure 2.7

2.3.3.1 The virtual origin

Figure 2.9 shows the 1/z axial decay of the mean mixture fraction on the centreline of the mixing field, $\overline{C}(\chi,0)$. The inverse of this plot, 1/ C(z,0) is shown in Figure 2.10 along with the mean decay 'half radius', $C_{½} = C(\chi\ ,\ ½\ )$. Comparison is made with the discrete point measurements of Becker *et al* (1967). A virtual origin, z_o, can be defined for the position at which these curves cross the abscissa. The position of the virtual origin can be determined in two ways. The most common case is to extrapolate from the far field the decay of the concentration along the axis of the jet, scaled with the concentration at the exit of the jet giving the virtual origin for the centre line decay, z_0. An alternative definition is a virtual origin, $z_{1/2}$ is defined by the concentration 'half radius'. Becker *et al* (1967) found the two lines to have a coincident virtual origin and defined separate regression laws for the centreline decay $\left({}^{C_c}/_{C(\chi,0)} = 0.0925[z-4.8r_0]/r_0\right)$ and 'half radius' $\left(C_{r_{1/2}} = 0.106\left[z-4.8r_o\right]\right)$ decay using the single virtual origin. Both are linear. Other investigations have found that the two definitions of the virtual origin are not coincident. Richards and Pitts (1993) have shown the existence of the two virtual origins and also the need to use both in defining the self-similarity relationship of the jet.

The present data for the centre line decay and the 'half radius' decay is plotted in Figure 2.10. As with other investigations the data is linear beyond z/d=20. The two virtual origins, z_o and $z_{1/2}$ are not coincident, consistent with Richards and Pitts (1993). The regression law for the centreline decay is, ${}^{C_c}/_{C(\chi,0)} = 0.0921[z+1.5r_0]/r_0$, and for the half radius decay, $C_{r_{1/2}} = 0.11\left[z-1.7r_o\right]$.

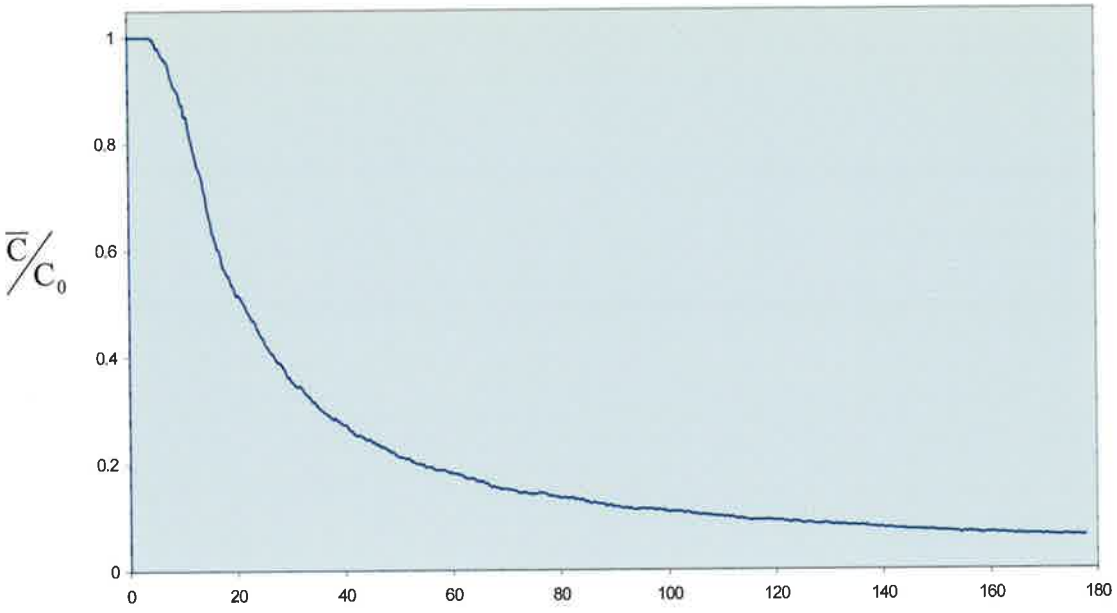

Figure 2.9 The 1/z decay of the mean, centerline, mixture fraction. Conditions as in 2.7

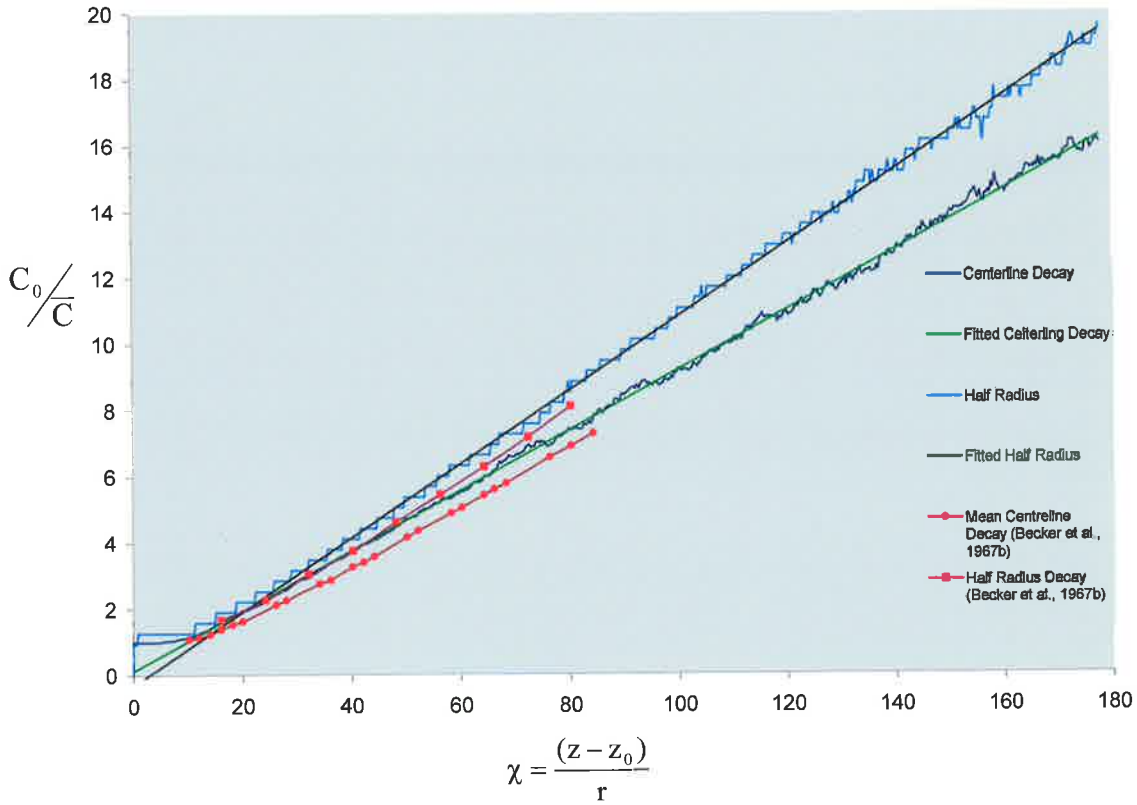

Figure 2.10 The inverse of the normalized decay of centerline concentration and concentration half radius as a function of the normalized axial distance, χ for the nozzle. Conditions as in Figure 2.7

2.3.3.2 Axial Decay

An alternative method for assessing the centreline decay is to plot the scaled mean centreline concentration, $\chi\overline{C}(\chi,0)$ against χ, as shown in Figure 2.11. The scaling of the vertical axis causes the data to fall onto a horizontal line once the far field behaviour of the jet is attained. A scaling parameter for the jet can then be read directly from the vertical axis of the plot. The asymptotic behaviour of the scaled mean centreline mixture fraction in the self-similar region of the mixing field is shown. Two definitions of χ have been used in the literature, one corrects for the position of the virtual origin and the other does not. The present work, scaled with the correction for the virtual origin, compares well with work of Becker *et al* (1967b) who also used the Mie scattering technique but with a significantly higher Reynolds number of 54,000 than the present jet which has a Reynolds number of 16,400.

2.3.3.3 Radial Profiles of Mean Concentration

Dimensionless radial profiles of the scaled mean concentration ($\overline{C}(\chi,\eta)/\overline{C}(\chi,0)$) verses dimensionless radial distance ($\eta = r_o / (z - z_o)$) are shown in Figure 2.12. These profiles have the characteristic "bell" shape as found by others and in general agree well with the data of Becker *et al,* (1967b), Birch *et al,* (1978) and Dowling and Dimotakis (1990). The slight increased spread in the present data in relation to the reported measurements found on the right hand side of the plot is deduced to result from attenuation of the beam as it traverses the flow due to the relatively high concentration of the seeded particles.

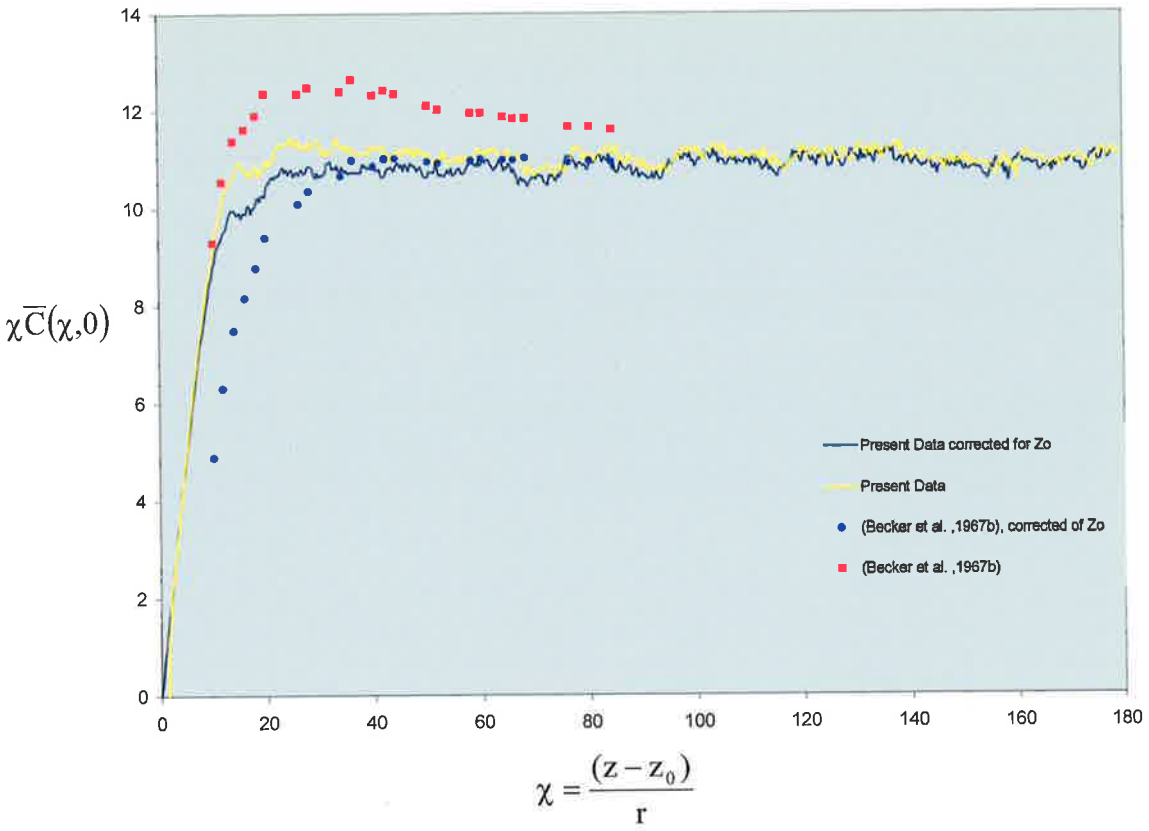

Figure 2.11 Comparison of present result with data from Becker *et al* (1967b) for the scaled mean centreline concentration, $\chi\overline{C}(\chi,0)$, versus scaled downstream location χ, which has and has not been corrected for the virtual origin, z_o. Condition as in Figure 2.7.

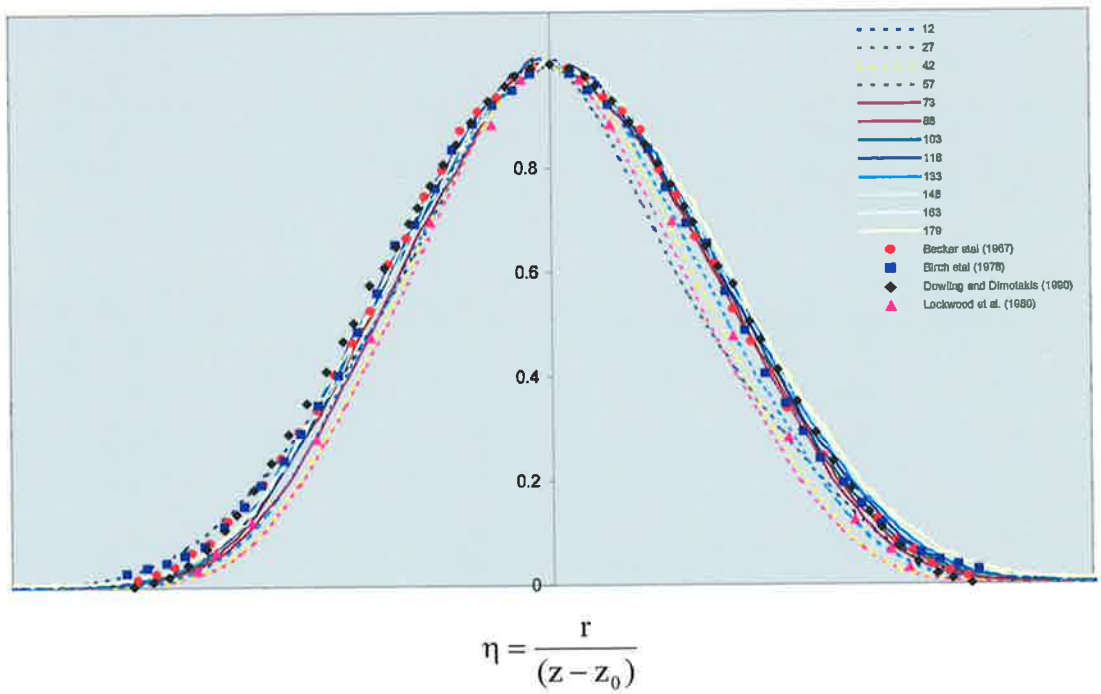

Figure 2.12 A comparison of the mean radial concentration profiles, $\frac{\overline{C}(\chi,\eta)}{\overline{C}(\chi,0)}$, of the present experiment with those cited by others. Condition as in Figure 2.7

2.3.4 The Fluctuating Concentration Field

The instantaneous concentration fluctuation $\tilde{C}(z,r)$ is calculated by subtracting the average concentration from the ith instantaneous realization.

$$\tilde{C}_i(z,r) = C_i(z,r) - \overline{C}(z,r)$$

Equation 2.3

The RMS concentration fluctuation, $C'(z,r)$ is then defined as,

$$C'(z,r) = \left(\frac{1}{N} \sum_{i=1}^{N} \tilde{C}_i(z,r)^2 \right)^{1/2}$$

Equation 2.4

The image of the rms field shown in Figure 2.13 reveals that the regions of highest concentration fluctuation exists along rays emanating from at the nozzle inlet on either side of the axis. This region of high concentration fluctuation correspond to the peaks in the characteristic double hump in the radial profile in Figure 2.14. The rms profile of the concentration field is useful in characterizing the progress toward similarity of the mixture field in the jet. High values of rms are interpreted as indicating the areas of high fluctuation in concentration and hence, the areas of high mixing.

Radial profiles of the rms are shown in Figure 2.14 for χ = 12 to χ = 179 in steps of 15χ . As with the mean radial profiles there is a small asymmetry between the right hand side of the image and the left-hand side due to attenuation of both the light sheet and the scattered signal beam. Some spread is evident in the profile, which suggests that the rms field reaches a self-similar radial profile at an axial station further down stream than the mean.

A comparison of the present results with those available in the literature is shown in Figure 2.14. Beyond χ = 60 there is reasonable agreement for much of the data. In particular the present data agrees well with that in the literature for $-0.15 < \eta < 0$. Toward the outer edge of

the jet ($\eta < -0.15$) the present data is lower than the data of Becker *et al.* (1967b) and Birch *et al.* (1978), but agrees well with Dowling and Dimotakis (1990). Since inadequate spatial resolution will result in an under estimation of rms data (Dowling and Dimotakis, 1990) the good agreement suggests that the present technique has good spatial resolution in the far field, although in the near field it is poorer. The general spread of the data obtained by the different researchers has been attributed to the differences in experimental set-up and conditions (Dowling and Dimotakis 1990, Richards and Pitts 1993).

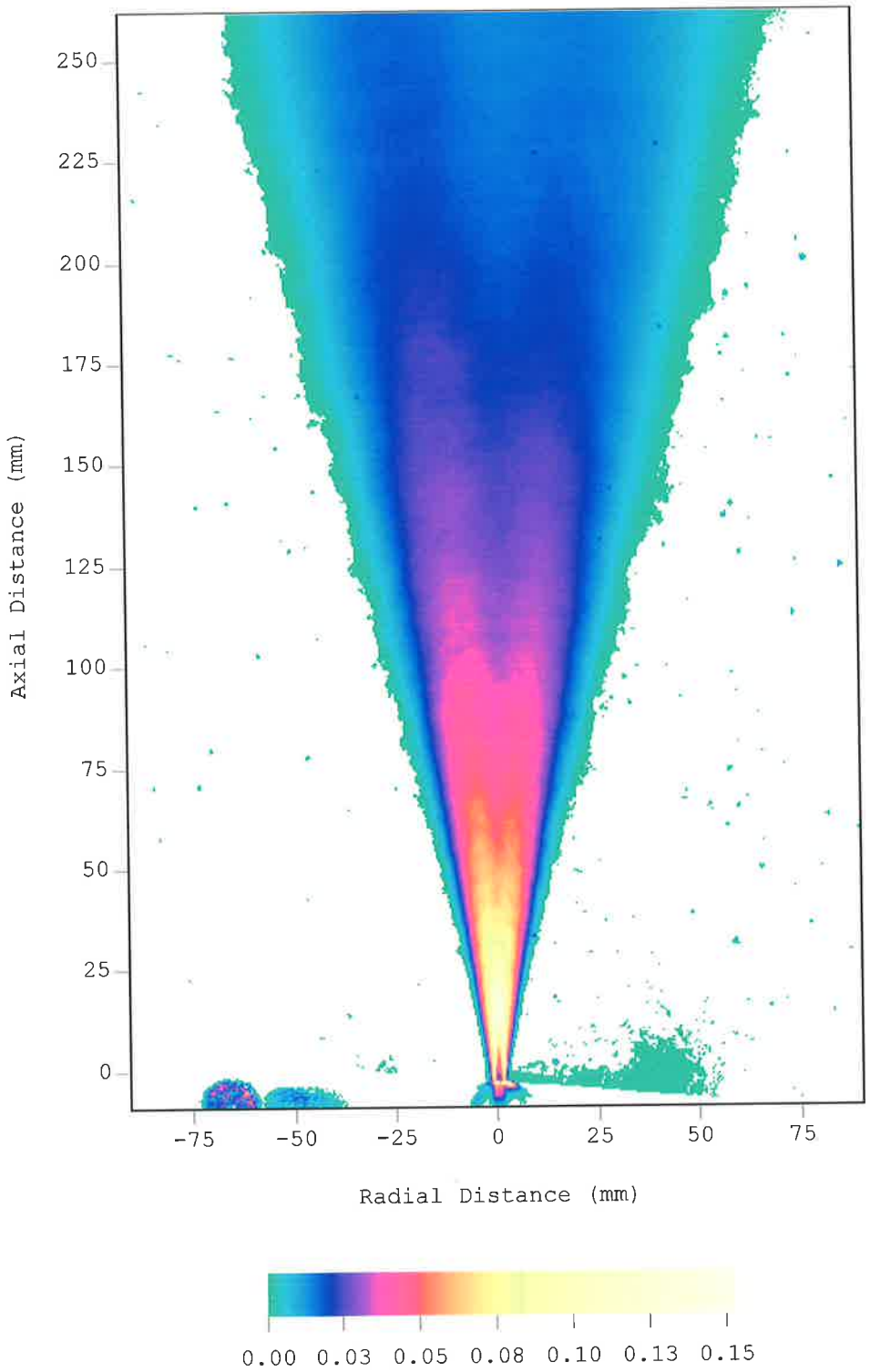

Figure 2.13 A two-dimensional colour map of the RMS field of mixture fraction for the simple jet. Conditions as for Figure 2.7

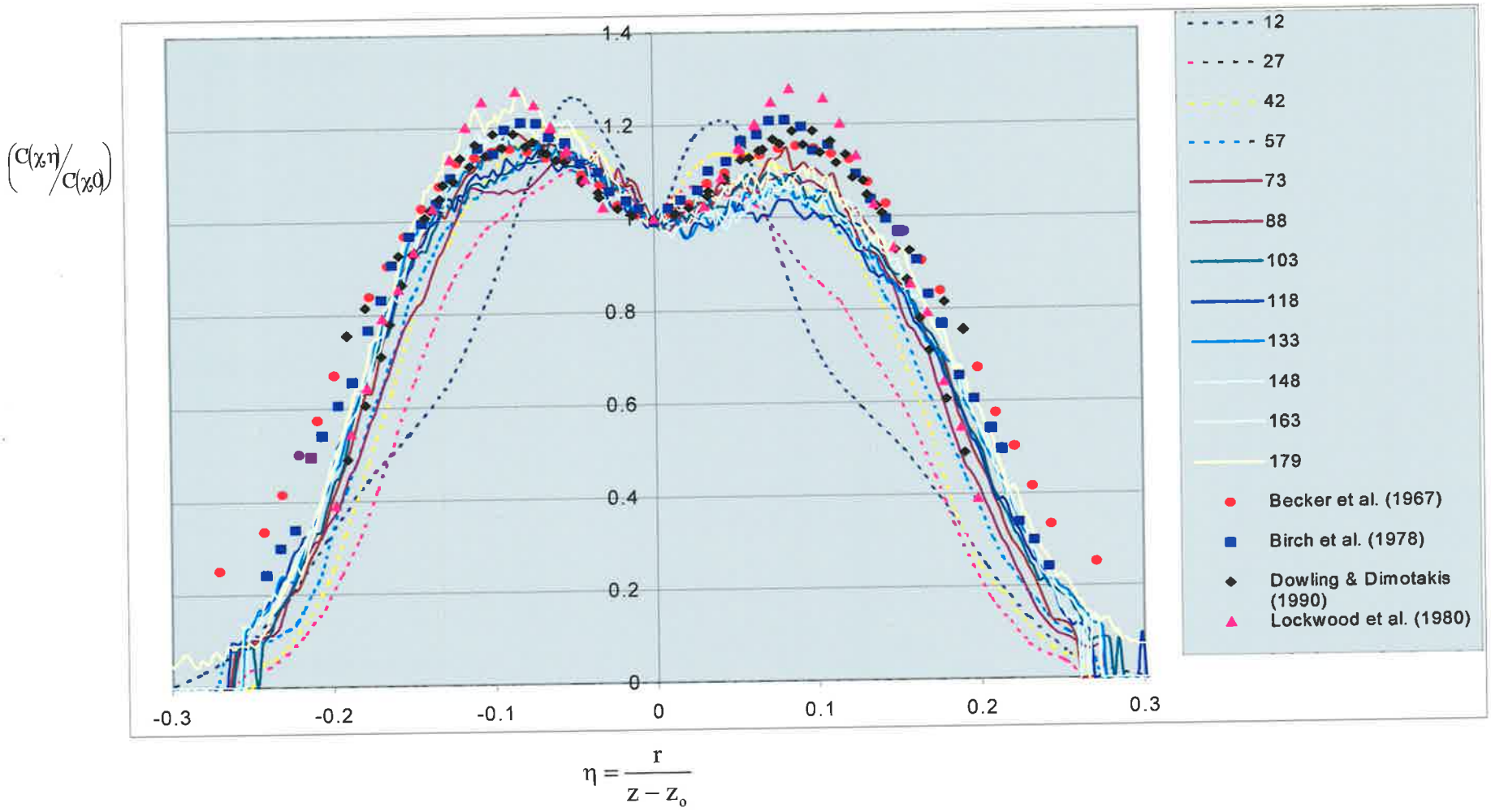

Figure 2.14 Variation in radial profiles of RMS, $\left(C(\chi,\eta)/C(\chi,0)\right)$ versus scaled radial distance, η, compared with the literature. Conditions as in Figure 2.7

2.3.5 Profiles of Centreline Unmixedness

The data shown in Figure 2.15 allows the present data for centreline unmixedness to be compared with results of others. The centreline unmixedness is the ratio of rms to mean concentration along the axis of the flow. The present results compare well, achieving asymptotic behaviour after approximately after $\chi = 80$, suggesting similarity beyond this point.

There are two features of this plot which are of interest. A characteristic 'bump' is found in the present data at $\chi = 15$ and also in the results of Becker *et al* (1967b). Indeed the present results compare well with the results of Becker *et al* (1967b) in general. Both data sets have been derived from the same diagnostic tool (Mie scattering) and at high, though significantly different, Reynolds numbers.

The early investigation of Becker *et al* (1967b) was not extended far enough downstream to determine the value of unmixedness for which the data becomes asymptotic. The presence of a far field asymptotic value has since been well established in the literature (Pitts, 1991a; Dowling and Dimotakis, 1990). Figure 2.15 shows that the present jet not only demonstrates asymptotic behaviour in the far field, but compares well with the generally accepted "far field" value $C' / \overline{C} = 0.233$. A more complete comparison of the asymptotic value found from the present work with the values found by other researchers is given in Table 2.3.

Another form in which this data can be presented is provided in Figure 2.16. The qualitative collapse of the reciprocal of the mixture fraction fluctuation intensity when plotted as a function of the reciprocal of the mean mixture fraction along the jet centre line shows a linear relationship which is characteristic of the self preserving state of the flow. A significant

proportion of this plot follows the linear trend and this can be used to estimate the equilibrium value in the far field, as demonstrated by Becker *et al* (1967b). Becker *et al* (1967b) found a linear relationship which indicated that when the flow reaches self-preservation, $C' = 0.222\overline{C}$. The present data can be fitted by, $C' = 0.25\overline{C}$, compared with the $C' = 0.233\overline{C}$ found in the far field of Figure 2.15. Note too that this plot contains no direct length scale, highlighting the excellent agreement between the present data and data available in the literature.

Table 2.3 Comparison of the asymptotic centreline unmixedness with results reported by others.

Author / Data	Reynolds number	Average Asymptotic Value of Unmixedness
Richards and Pitts (1993)	25,000	0.227
Dowling and Dimotakis (1990)	16,000	0.237
Lockwood and Moneib (1980)	50,000	0.21
Pitts (1991a)	4,000	0.23
Present	16,400	0.233

It should be noted that there is wide variability in the unmixedness data reported in the literature. The present validation is based on selected references which are widely deemed to be representative for that purpose. A notable point unresolved in the literature is that some researchers find the presence of the "hump" (Becker *et al.* 1967b) in the near field and others do not (Lockwood *et al.* 1980). Whether these differences can be attributed to experimental error or to genuine differences in the flows examined by different researches is beyond the scope of this thesis.

2.3.6 Final Comments

The technique presented in this chapter for the planar imaging of concentration has been validated using a well-documented flow field, a simple axisymmetric jet. There is excellent agreement with published results obtained from single point measurements. The good agreement for both the mean and the fluctuating statistics demonstrate that spatial resolution is at least reasonable in the near field and entirely satisfactory in the far field and that the data collection and correction procedures are adequate. This validation process shows that there are no significant errors affecting the results obtained and that the use of this two dimensional imaging technique yields extensive data sets, providing excellent qualitative and quantitative information.

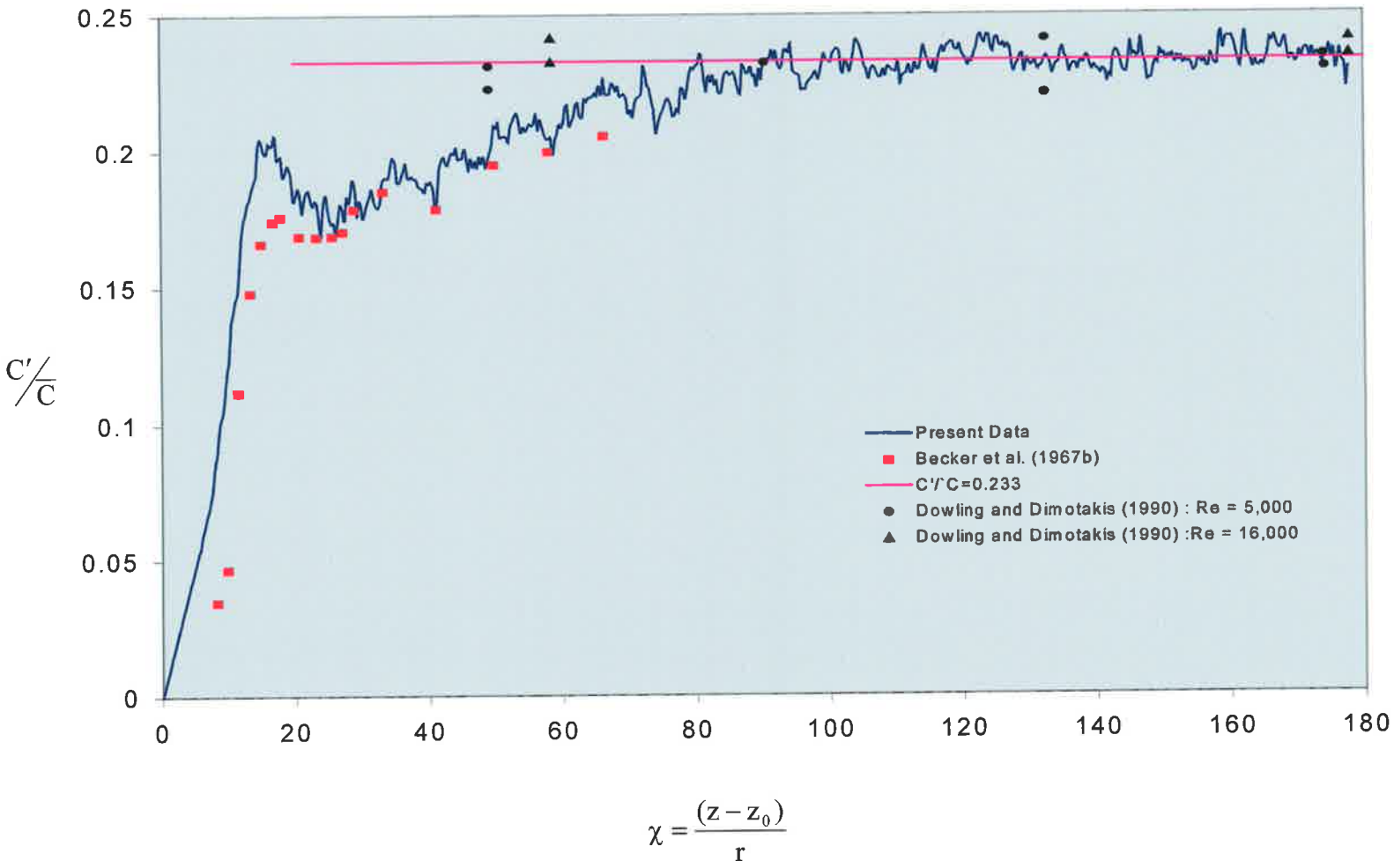

Figure 2.15 A comparison of the centerline ratio of RMS to mean concentration ("unmixedness") versus scaled downstream location will literature data. Conditions as in Figure 2.7

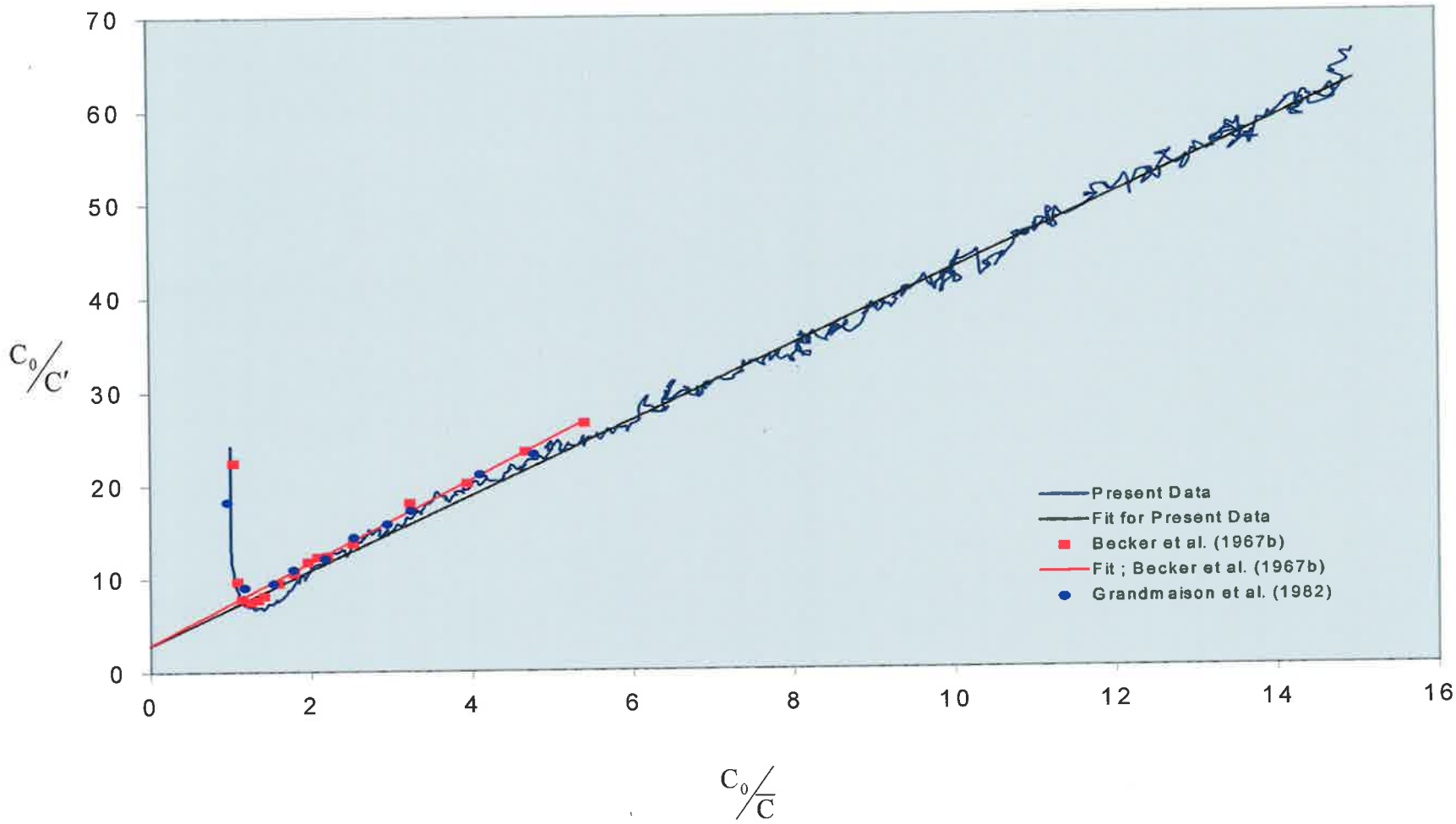

Figure 2.16 The reciprocal of the mixture fraction fluctuation intensity as a function of the reciprocal of the mean mixture fraction along the jet centre line. Conditions as in Figure 2.7

3 DEVELOPING REGION OF MECHANICAL PRECESSING JET (MPJ) FLOWS

3.1 INTRODUCTION

The preliminary study of Schneider (1997) investigated the velocity and pressure field generated by mechanical precession of a jet of fixed exit angle, $\phi = 45°$ for a limited range of both Reynolds number and Strouhal number. Presented here is a broader study of the effects of the major parameters on the mixing field generated by an MPJ nozzle, namely the Reynolds number, the Strouhal number, and the inclination angle (ϕ) and for a limited data set the exit diameter. Phase-averaged data for each of the different conditions have been collected 'on the fly', i.e., collecting only the average and so minimizing the amount of disk storage needed for each experiment. In particular the investigation seeks to identify and characterize the near-field region of the flow in which features that suggest a limit cycle phenomenon are evident.

3.1.1 Definition of the Limit Cycle

Although the term "limit cycle" is used in several fields of engineering and science, in all areas the term has the same basic definition. Two descriptions of the term "limit cycle" are presented here from different areas of science.

"A limit cycle oscillation is a self-sustaining oscillation with limited amplitude that occurs as a result of nonlinear coupling between the dynamic response and unsteady aerodynamic forces.", (Tan and Lan, 1997)

"A closed loop ... is said to be a limit cycle ... if the orbits (of the helix) spiral into it, or away from it. It is stable if all orbits (of the helix) passing sufficiently close to it must ultimately spiral into it, and unstable otherwise.", (Braun 1983, pp 434).

The definition employed in the present investigation is that a variable has characteristics of a "limit cycle" if it approaches a constant value. An example, which will be tested in this chapter, is the character of the radius of the precessing spiral. It has a "limit cycle" character if it approaches a constant value.

3.1.2 Photographs of the MPJ

Whole field images of MPJ flows are shown in Figure 3.1 for four Strouhal numbers to identify microscopic features. The flow visualization technique is achieved using a qualitative, high-resolution Mie scattering technique. Each flow has the same exit Reynolds number of 3,800. The first image, Figure 3.1(a), is for a non-precessing jet ($\phi = 0°$, St = 0). The three images of precessing jet flows, Figures 3.1(b,c,d), all have an exit deflection angle of $\phi = 45°$ and the images are timed to capture the flow at the same phase in the cycle.

The whole-field image of the simple axisymmetric jet (Figure 3.1(a)) displays the features typical of the classical simple jet flow field. The jet spreads at a constant angle. The cross-section of the axisymmetric shear layer is evident on either side of the image. Structures of the order of the jet diameter are apparent over most of the mixing field.

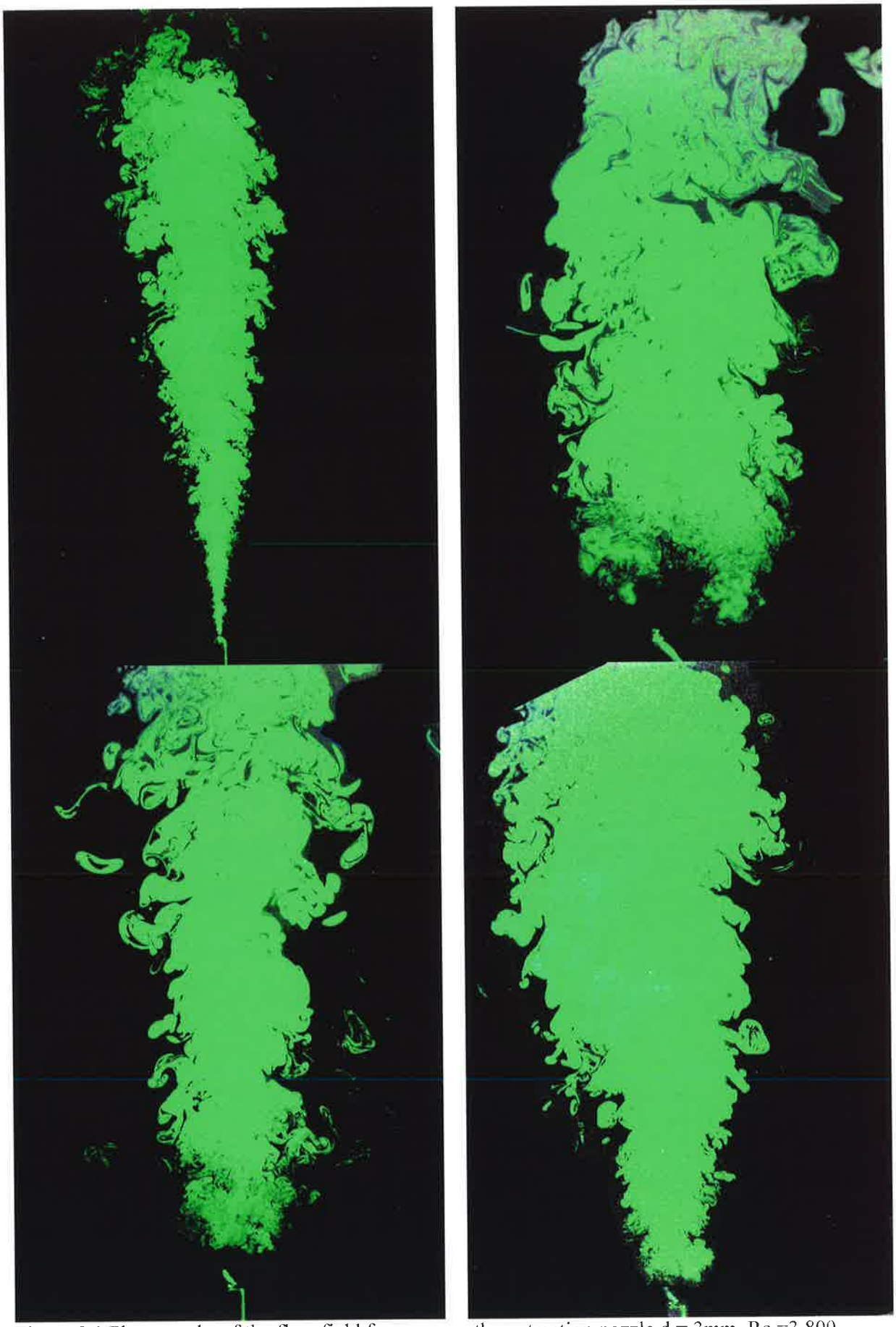

Figure 3.1 Photographs of the flow field from a smooth contraction nozzle d = 3mm, Re =3,800. A simple jet and the flow of an MPJ, $\phi = 45°$ at different Strouhal numbers:

Top left (a) simple axisymmetric jet;
Top right (b) St = 0.0047;
Bottom left (c) St = 0.0078;
Bottom right (d), St = 0.015.

The field of view in Figure 3.1(b-d) is chosen to emphasize how precession influences the far field of the jet. Three regions of flow are evident in each image, the near field region in which only a small slice can be seen corresponding to the jet emerging at 45° to the nozzle axis, the transition region corresponding to a more-or-less parallel flow region, and the far field. While variations in the laser sheet intensity profile do not allow quantitative data to be derived from these photographs, significant qualitative information is evident. In the far field of all three images well-defined vortical motions spanning a range a scales can be observed. In the transition region the largest local length scale, the jet width, decreases with increasing Strouhal number. Likewise, the angle of jet spread in the region adjacent the near field decays much more rapidly, also with increasing Strouhal number. The far field is most evident in the high Strouhal number flow in which the spread angle of the jet is comparable with that of the simple jet, suggesting a return to a related type of asymptotic flow field.

The initial region in the near field also contains the potential core, which can be identified in the region before the core passes out of the light sheet. Following this, a tight, three-dimensional helical foot-print of the jet can be deduced. A transition region follows this, in which there is very little spreading of the jet. After this transition region, the far field develops with characteristics that are more comparable with those of a simple jet in the far field. The axial location of each flow region is also clearly a function of Strouhal number. The present chapter focuses on the region of the flow in which the three-dimensional structure in the flow moves with or contains remnants of the frequency of precession. The effects of precession on the development of the flow are assessed as well as an assessment of the use of dimensionless parameters to characterize the flow.

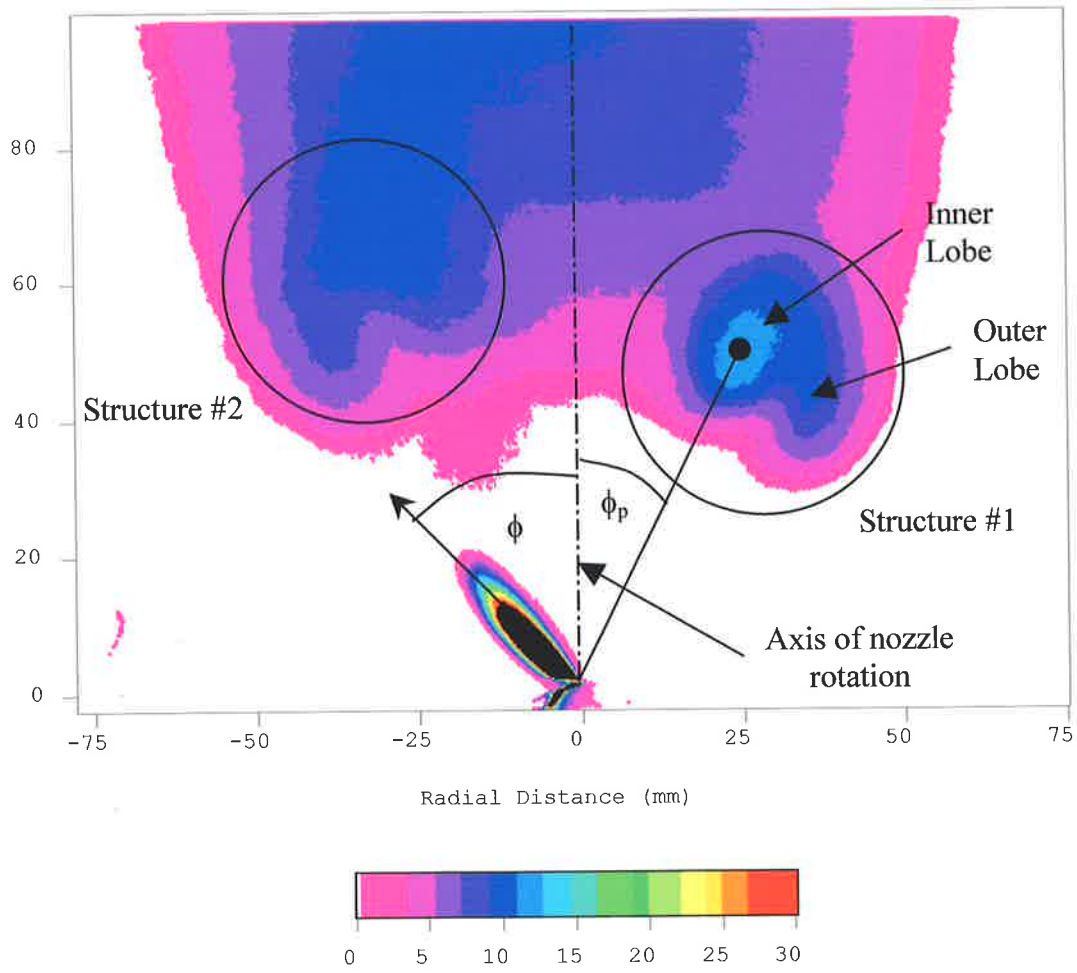

Figure 3.2(a) A typical phase averaged image of the mixture fraction in a precessing jet flow. The figure shows the characteristic features that can be identified and the notation adopted to describe them. The colour bar at the bottom of the image indicates the concentration represented by the false colours. Here the exit angle is $\phi = 45°$, the phase angle is $\theta = 0°$, the Re = 20,000 and St = 0.002.

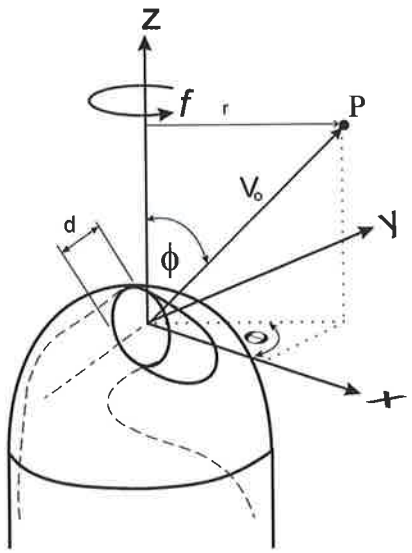

Figure 3.2(b) Notation used to define MPJ conditions and points (P) in the flow from the origin of the jet.

3.2 GENERAL DESCRIPTION OF THE FLOW FIELD

The characteristic features identified from two-dimensional images of the flow are discussed and interpreted qualitatively. The notation and symbols used in the remainder of the thesis are introduced during this discussion.

Phase-averaged data is appropriate for identifying and quantifying characteristic features of the flow. Each phase average is obtained by averaging successive images collected at a specific phase angle in the precessional cycle. A typical, phase averaged image of a flow field is presented in Figure 3.2(a). The qualitative features identified in this image are present in all precessing flows, although quantitative details vary depending upon the phase of the cycle and the nozzle exit parameters. In Figure 3.2(a) the phase angle is $\theta = 0°$, i.e., the plane of the light sheet bisects the emerging jet along the major axis and the image reveals the jet emerging to the left at $\phi = 45°$ to the spin axis. Likewise, all other images presented in Section 3.3 are also collected at $\theta = 0°$ so that the jet entering from the bottom of the picture and is directed toward the left from the vertical axis about which the nozzle rotates. As found by Schneider (1996), precession causes the footprint left by the emerging jet to have strong azimuthal path, so that it passes in and out of the thin light sheet on a helical path. This is confirmed in the present measurements by the sharp cut-off of high concentration fluid and the presence of "pure" ambient across the entire width of the flow in the near-nozzle region.

Further downstream the emerging jet cuts the light sheet in two places, spaced roughly equally on either side of the axis of rotation, and it is clear that there is structure associated with the flow there. Although it is recognized that structure must be present throughout the helical path of the emerging jet flow, for easy reference the structures revealed where the light sheet cuts the helix at $\theta = 180°$ relative to the phase of precession (i.e. on the right side of the

image) is denoted as Structure #1 or the first structure. Similarly the structure revealed where the light sheet cuts the helix at $\theta = 360°$ (on the left side of the inlet) is denoted Structure #2 or the second structure. The notation used is derived from the place on the helix where the structure, illuminated by the light sheet is present. Note the presence of a high concentration of nozzle fluid near the centers of these structures. Downstream from the two structures no distinct features can be identified. This suggests that any other structure, which may be present, is not associated the frequency of precession and hence does not appear in the phase averaged image.

The colours used in the images in this chapter provide quantitative information about the concentration at the particular spatial location. In Figure 3.2(a) the colour scale presents normalized concentration data between 0 and 0.3 of that initially in the jet, so that $\overline{C} > 0.3$ is shown as black. White represents "pure" ambient fluid, i.e. where the concentration is less than the threshold, typically $\overline{C} < 0.002$. Where possible constant scales are used in subsequent images to facilitate direct comparison. However, care should be taken since a number of colour scales have been used to accommodate the widely ranging values of mixture fraction in the different precessing flows.

The spatial position of the data in Section 3.3 is presented in absolute spatial units, i.e. mm, since a number of normalizing length scales are possible. The Strouhal number is used as the dimensionless frequency, following Nathan *et al.* (1996) and Schneider (1996). A comparison of different dimensionless descriptions of the flow is presented in Section 3.4. Note that the orientation of the major axis of the camera image plane relative to the spinning axis of the nozzle has been selected with a view to make the best use of the image array. Thus for some data sets the camera perspective has been rotated by 90°.

3.3 A COMPARISON OF THE PHASE AVERAGED CONCENTRATION FOR A RANGE OF JET EXIT CONDITIONS.

The effect of variations in Strouhal number, Reynolds number and deflection angle (ϕ) on the phase averaged concentration field is shown in the images presented in Figure 3.3 to Figure 3.6. The images are grouped so that each figure contains images of flows with the same deflection angle. Each column corresponds to a constant Reynolds number and each row to a constant Strouhal number. Clear trends are apparent from visual inspection.

3.3.1 Qualitative trends evident from the phase averaged data.

Figure 3.3 shows images of phase averaged concentration for a deflection angle, $\phi = 15°$. The high concentration fluid exiting the nozzle forms a "potential core", which extends to where the footprint passes out of the light sheet. At this deflection angle, for all images the "core" region is significantly longer than occurs with higher angles (presented later), indicating that in the near field the helical footprint has a gentle rate of curvature in the azimuthal direction close to the nozzle.

The maximum phase averaged values of concentration within Structures #1 and #2 is about $\overline{C} = 0.1$ and this occurs for the highest Strouhal number (Figure 3.3(a)). A comparison with other conditions shows this peak value of concentration is relatively low, consistent with Structures #1 and #2 being located relatively far downstream. It is also much lower than the maximum mean concentration in the simple jet at the same axial location (Figure 2.8), where it is about $\overline{C} = 0.25$ on the axis at z = 100mm. This indicates that the mixing is quite intense within the emerging jet region of a precessing jet compared to a simple jet. For most of the conditions shown in Figure 3.3, Structure #1 is clearly evident while Structure #2 is less well defined and is nearly always located close to the spinning axis. Likewise the inner and outer

lobes (see Figure 3.2(a) for definition) within the structures are not as definable as will be seen in other data sets (Figure 3.4 to Figure 3.6). The close proximity of Structures #1 and #2 to the spin axis and the apparent merging of the inner lobes suggests that the helix moves radially inward with distance from the nozzle (i.e. reducing the pitch of the spiral). The effect of the Strouhal number is much greater than that of Reynolds number. It controls both the concentration within the helix and the "tightness" of the helix, i.e. the axial position of Structures #1 and #2.

A comparison of Figure 3.3 and Figure 3.4 shows the effect of increasing the jet exit angle from $\phi = 15°$ to $\phi = 30°$. The radial position of Structures #1 and #2 is significantly further from the spin axis for the deflection angle of $\phi = 30°$ than for $\phi = 15°$. The length of the "potential core" region is shorter and both structures are more distinct as separate entities than at $\phi = 15°$. The two lobes are clearly evident at all conditions except the lowest Strouhal number. The maximum concentration of jet fluid within Structures #1 and #2 at the highest Strouhal number has increased relative to $\phi = 15°$ and is found within the inner lobe. A characteristic feature is seen in all of the $\phi = 30°$ images is that the inner lobe is much larger than the outer lobe and also has a higher concentration of nozzle fluid compared with the outer lobe. The generally higher concentration within the inner lobe relative to the outer is an indication that the inner lobe mixes at a slower rate than the outer lobe. This may be because there is greater shear on the outside of the emerging jet, or because the inner lobe tends to re-entrain nozzle fluid rather than air. Decreasing the Strouhal number decreases the relative size of the outer lobe until it is hardly distinguishable as a distinct feature. Once again the Strouhal number is much more significant than the Reynolds number, which has little effect on the flow.

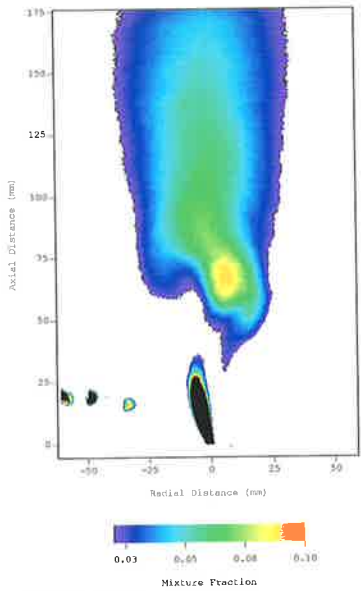

Figure 3.3(a) Re = 10,000;
St = 0.00503; $\phi = 15°$

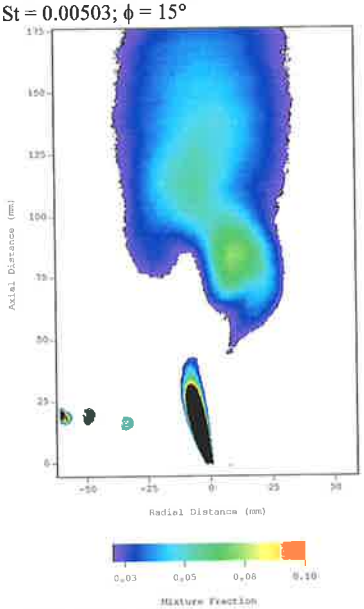

Figure 3.3(b) Re = 10,000;
St = 0.00335; $\phi = 15°$

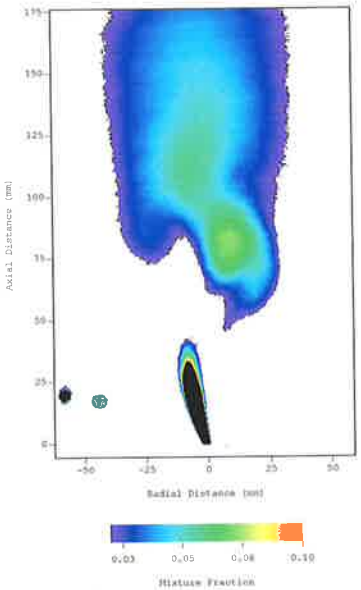

Figure 3.3(c) Re = 15,000;
St = 0.00335; $\phi = 15°$

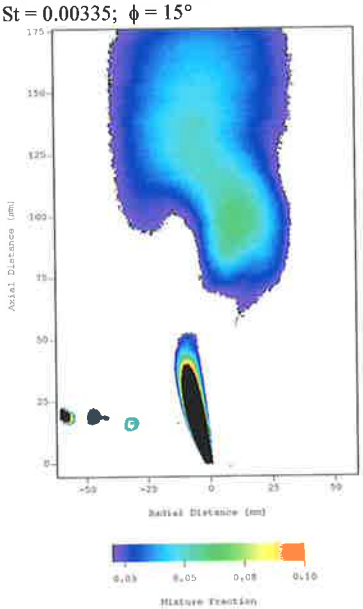

Figure 3.3(d) Re = 10,000;
St = 0.00251; $\phi = 15°$

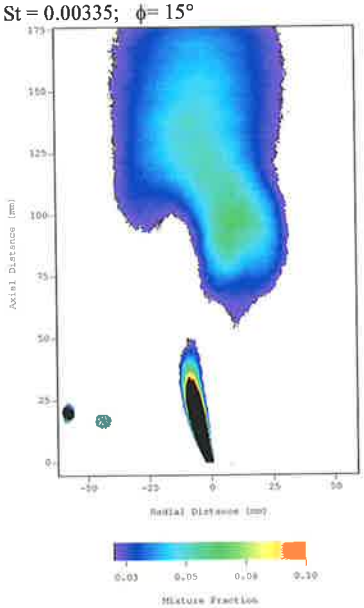

Figure 3.3(e) Re = 15,000;
St = 0.00251; $\phi = 15°$

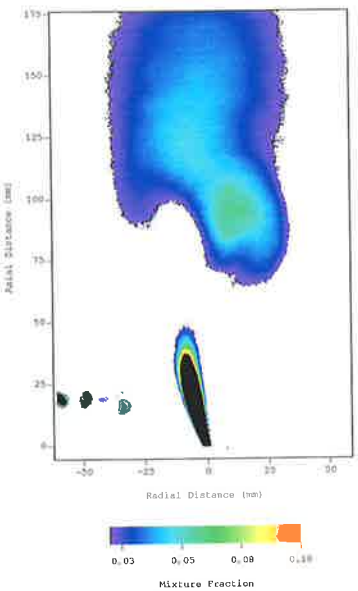

Figure 3.3(f) Re = 20,000;
St = 0.00251; $\phi = 15°$

Figure 3.3 Phase averaged images of the concentration field of the MPJ, $\theta = 15°$

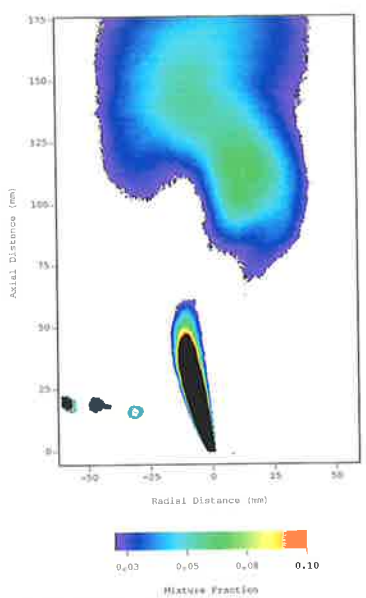

Figure 3.3(g) Re = 10,000; St = 0.00201; $\phi = 15°$

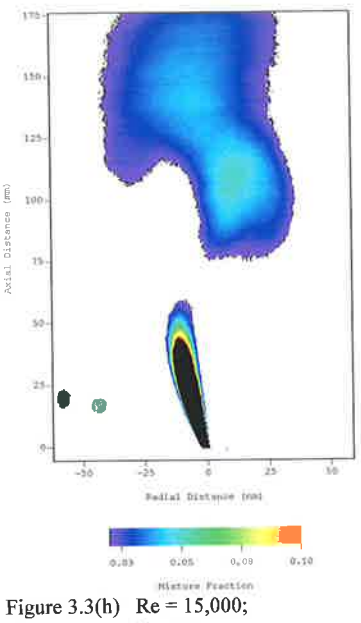

Figure 3.3(h) Re = 15,000; St = 0.00201; $\phi = 15°$

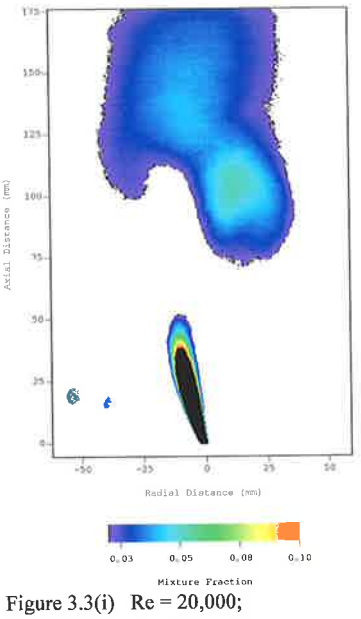

Figure 3.3(i) Re = 20,000; St = 0.00201; $\phi = 15°$

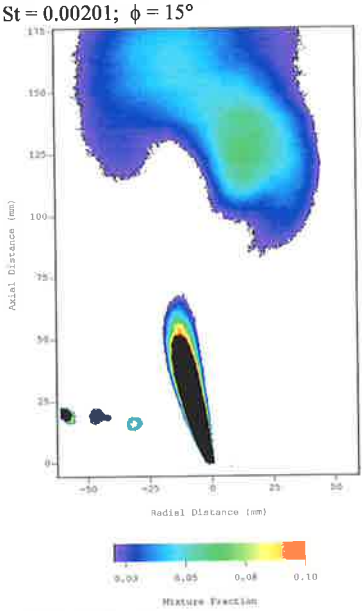

Figure 3.3(j) Re = 10,000; St = 0.00151; $\phi = 15°$

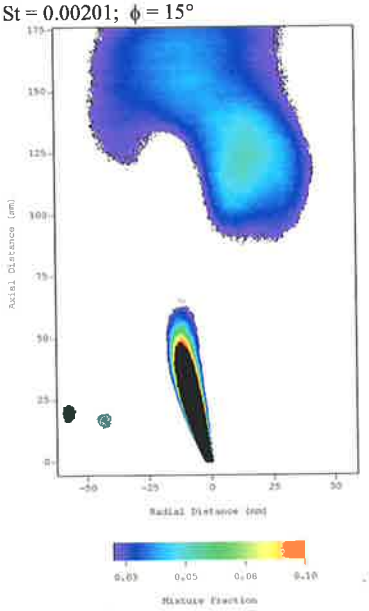

Figure 3.3(k) Re = 15,000; St = 0.00151; $\phi = 15°$

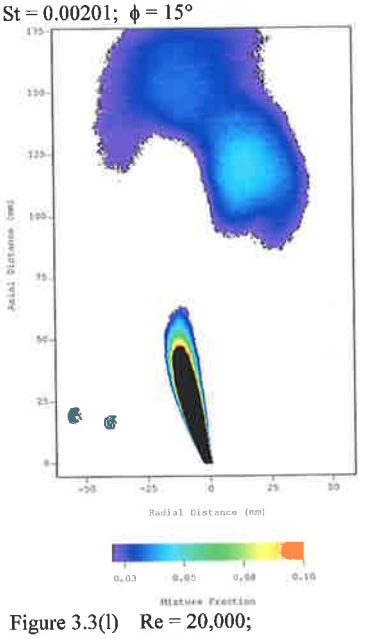

Figure 3.3(l) Re = 20,000; St = 0.00151; $\phi = 15°$

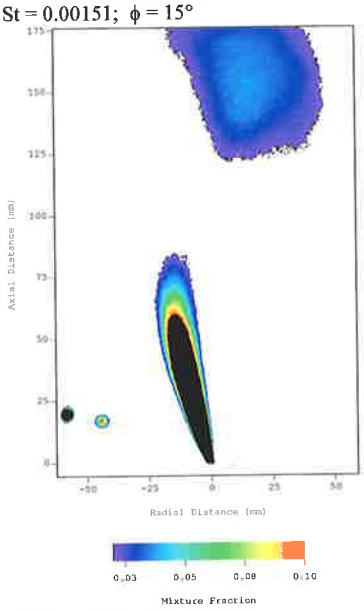

Figure 3.3(m) Re = 10,000; St = 0.00101; $\phi = 15°$

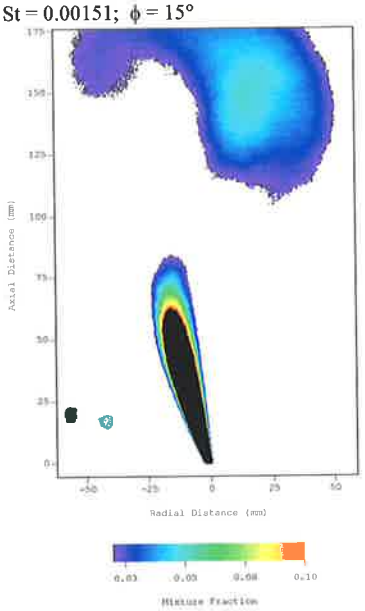

Figure 3.3(n) Re = 15,000; St = 0.00101; $\phi = 15°$

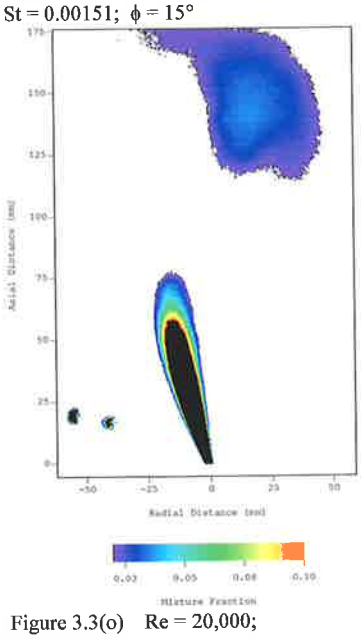

Figure 3.3(o) Re = 20,000; St = 0.00101; $\phi = 15°$

Figure 3.3 Phase averaged images of the concentration field of the MPJ, $\theta = 15°$

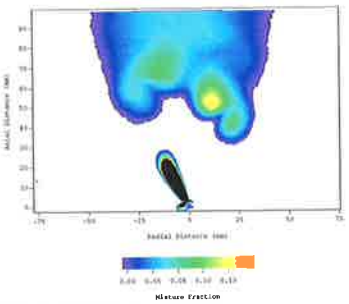

Figure 3.4(a) Re=10,000;
St = 0.00503; $\phi = 30°$

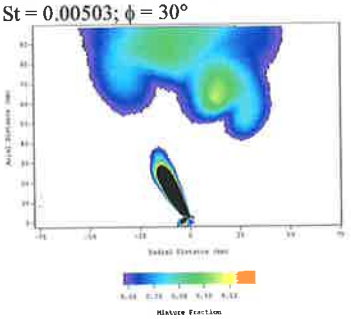

Figure3.4(b) Re = 10,000;
St = 0.00335; $\phi = 30°$

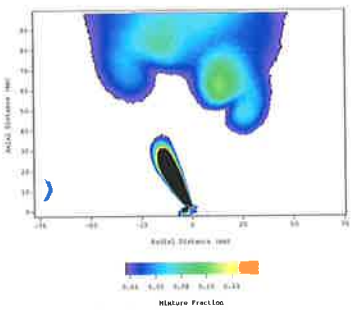

Figure 3.4(c) Re = 15,000;
St = 0.00335; $\phi = 30°$

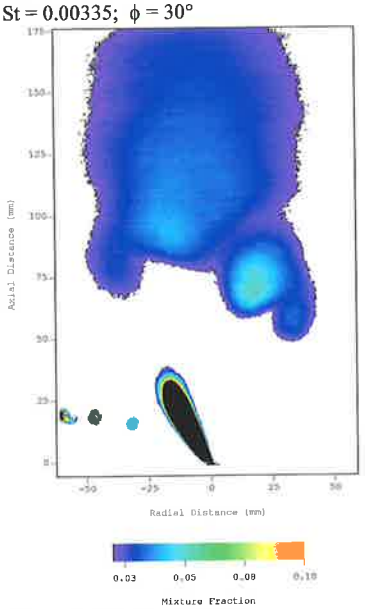

Figure 3.4(d) Re = 10,000;
St = 0.00251; $\phi = 30°$

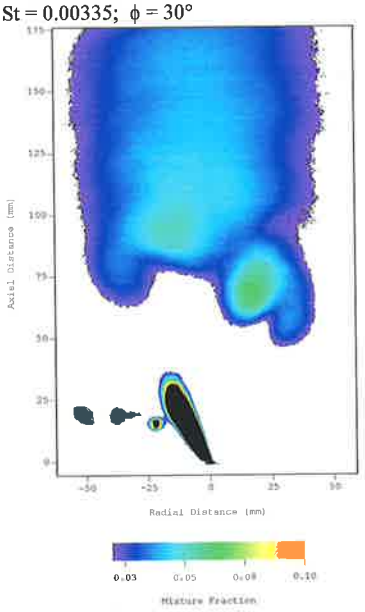

Figure 3.4(e) Re = 15,000;
St = 0.00251; $\phi = 30°$

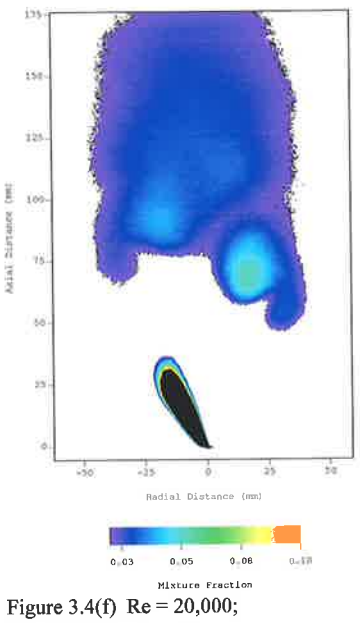

Figure 3.4(f) Re = 20,000;
St = 0.00251; $\phi = 30°$

Figure 3.4 Phase averaged images of the concentration field of the MPJ, $\theta = 30°$

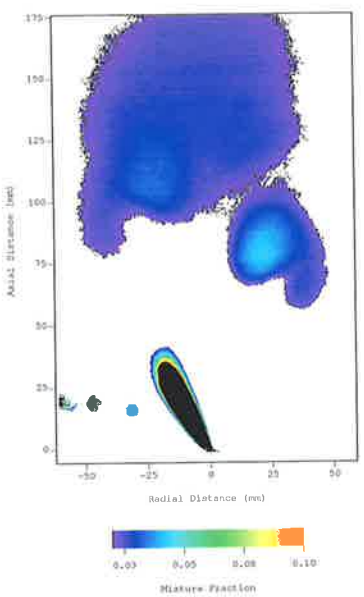

Figure 3.4(g) Re = 10,000;
St = 0.00201; $\phi = 30°$

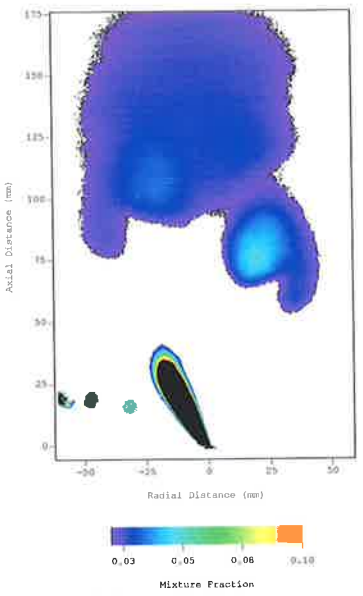

Figure 3.4(h) Re = 15,000;
St = 0.00201; $\phi = 30°$

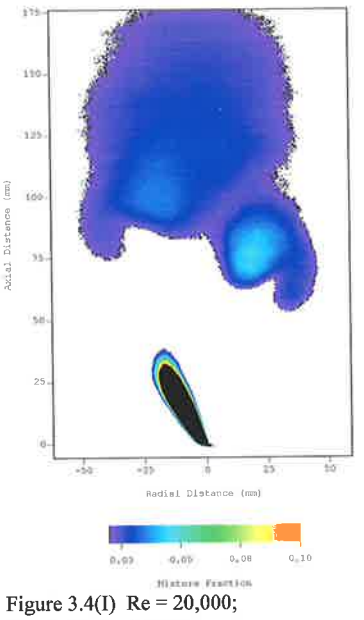

Figure 3.4(I) Re = 20,000;
St = 0.00201; $\phi = 30°$

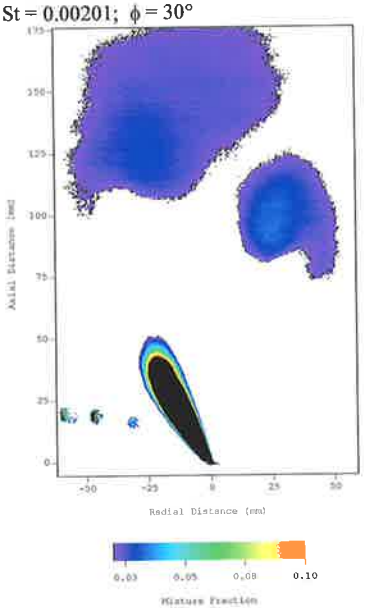

Figure 3.4(j) Re = 10,000;
St = 0.00151; $\phi = 30°$

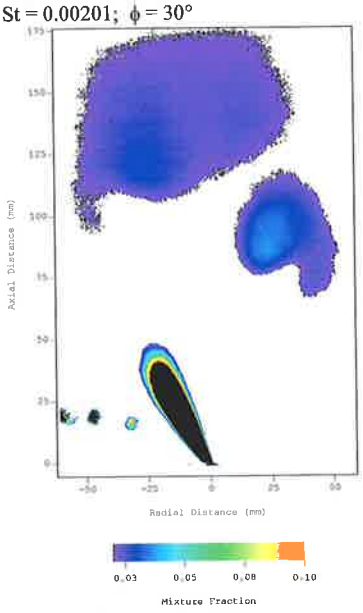

Figure 3.4(k) Re = 15,000;
St = 0.00151; $\phi = 30°$

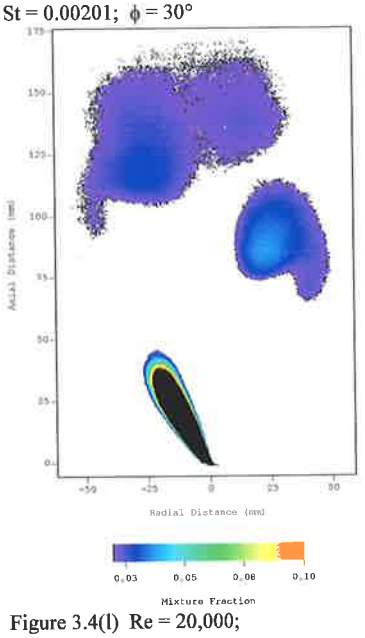

Figure 3.4(l) Re = 20,000;
St = 0.00151; $\phi = 30°$

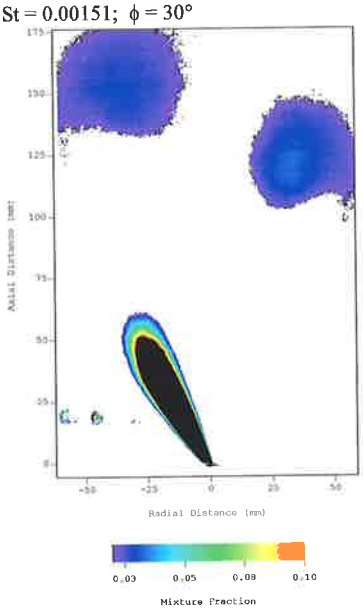

Figure 3.4(m) Re = 10,000;
St = 0.00101; $\phi = 30°$

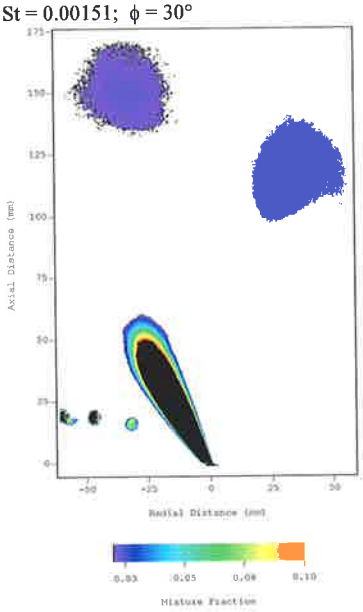

Figure 3.4(n) Re = 15,000;
St = 0.00101; $\phi = 30°$

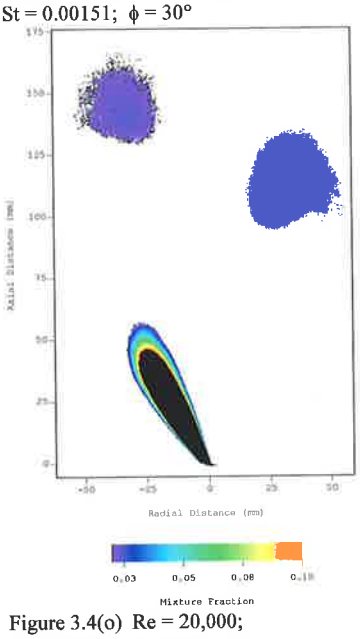

Figure 3.4(o) Re = 20,000;
St = 0.00101; $\phi = 30°$

Figure 3.4 Phase averaged images of the concentration field of the MPJ, $\theta = 30°$

Figure 3.5 shows variations in Strouhal number and Reynolds number for the case $\phi = 45°$. The length of the visible "potential core" noticeably decreases with increasing Strouhal Number. The two structures and corresponding lobes are well defined in all of the images. This and the decreasing axial distance to Structures #1 and #2 at the base of the collapsing spiral region is evidence of a tightening of the spiral for increasing Strouhal Number. Similar trends are seen in the effect of Strouhal number and Reynolds number on the flow as in the lower deflection angle cases. Increasing the Strouhal Number increases the peak concentration value within Structures #1 and #2, and throughout the entire flow field. This is clear when it is noted that the colour map has been changed to read $0.0 < \overline{C} < 0.3$. For all the conditions investigated in Figure 3.5 the radial position of the core of Structures #1 and #2 is well defined and located away from the spinning axis. Again effect of the Reynolds Number is weak.

The conditions investigated for the MPJ flows with a deflection angle of $\phi = 60°$ are shown in Figure 3.6. Variations in the axial and radial positions of Structures #1 and #2, defining the shape of the helix, is apparent. Increasing the Strouhal Number decreases the axial and radial distance from the origin to Structures #1 and #2. The value of concentration within Structures #1 and #2 is, in general higher for this exit angle than for any of the other angles, suggesting that concentration in the helix increases with ϕ. The inner lobe is more dominant than the outer lobe, both in size and in the value of concentration. This trend is consistent with that found with the other cases of deflection angle indicating that mixing is more rapid on the outer edge of the evolving helical flow.

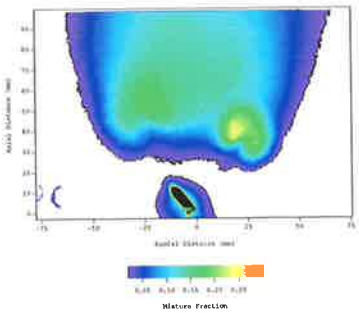

Figure 3.5(a) Re = 10,000;
St = 0.00503; $\phi = 45°$

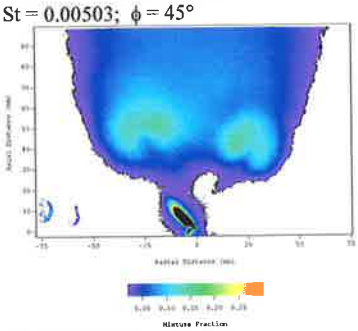

Figure 3.5(b) Re = 10,000;
St = 0.00335; $\phi = 45°$

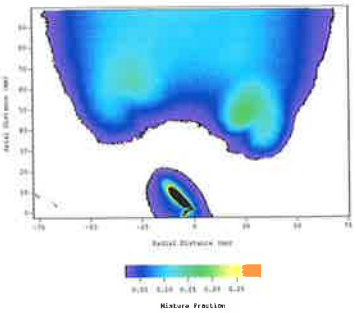

Figure 3.5(c) Re = 15,000;
St = 0.00335; $\phi = 45°$

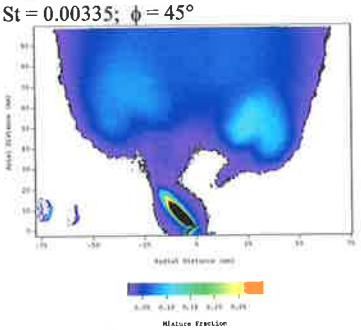

Figure 3.5(d) Re = 10,000;
St = 0.00251; $\phi = 45°$

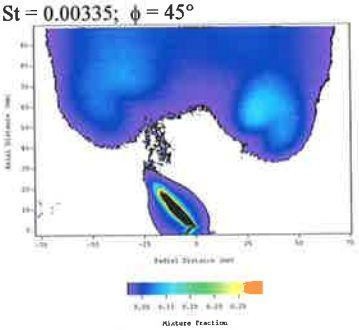

Figure 3.5(e) Re = 15,000;
St = 0.00251; $\phi = 45°$

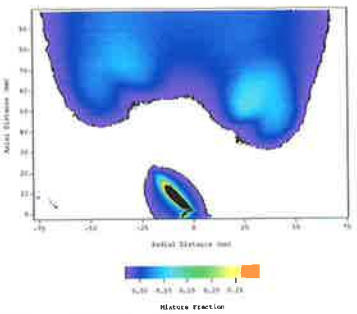

Figure 3.5(f) Re = 20,000;
St = 0.00251; $\phi = 45°$

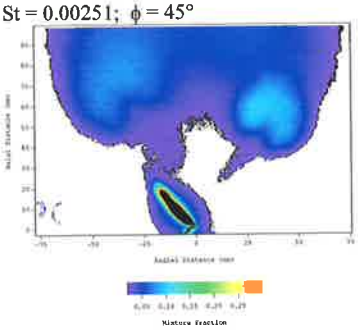

Figure 3.5(g) Re = 10,000;
St = 0.00201; $\phi = 45°$

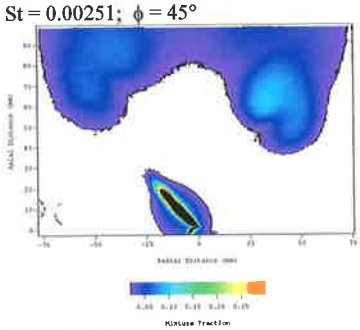

Figure 3.5(h) Re = 15,000;
St = 0.00201; $\phi = 45°$

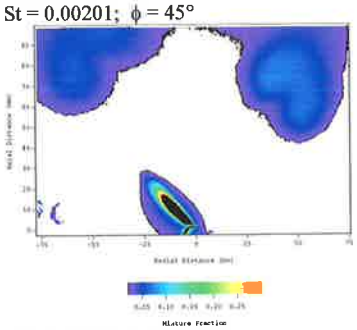

Figure 3.5(I) Re = 20,000;
St = 0.00201; $\phi = 45°$

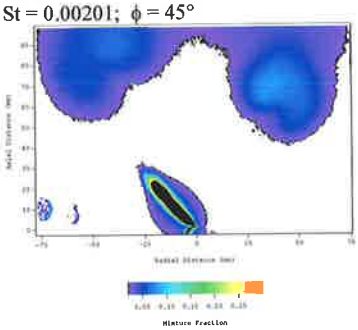

Figure 3.5(j) Re = 10,000;
St = 0.00151; $\phi = 45°$

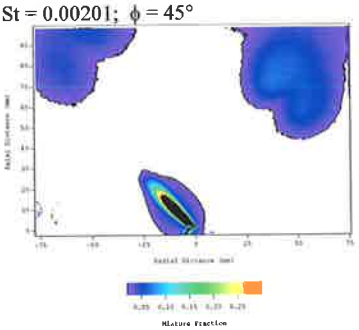

Figure 3.5(k) Re = 15,000;
St = 0.00151; $\phi = 45°$

Figure 3.5(l) Re = 20,000;
St = 0.00151; $\phi = 45°$

Figure 3.5 Phase averaged images of the concentration field of the MPJ, $\theta = 45°$

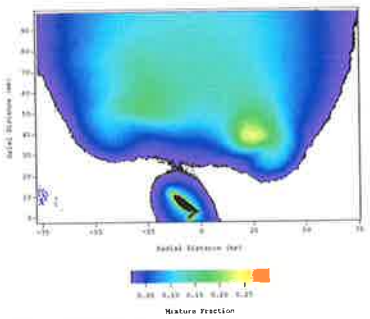

Figure 3.6(a) Re = 10,000;
St = 0.00503; $\phi = 60°$

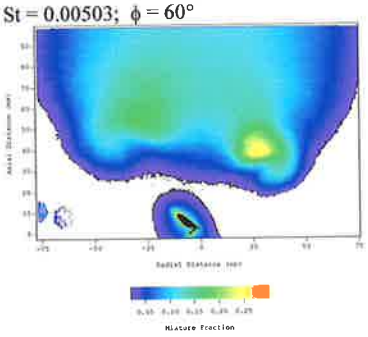

Figure 3.6(b) Re = 10,000;
St = 0.00335; $\phi = 60°$

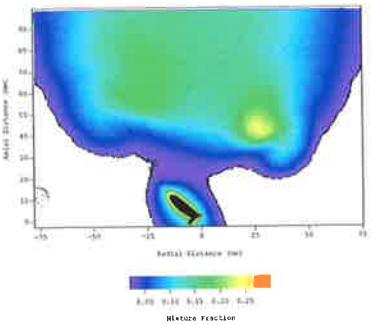

Figure 3.6(c) Re = 15,000;
St = 0.00335; $\phi = 60°$

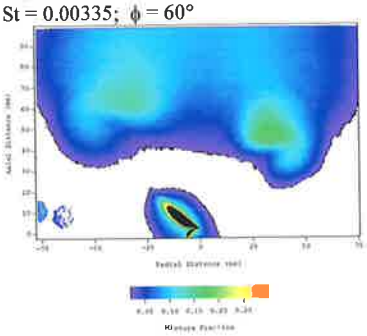

Figure 3.6(d) Re = 10,000;
St = 0.00251; $\phi = 60°$

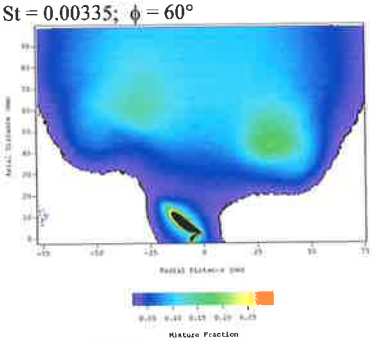

Figure 3.6(e) Re = 15,000;
St = 0.00251; $\phi = 60°$

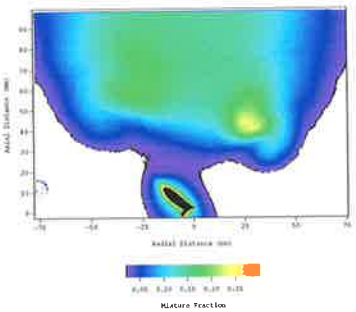

Figure 3.6(f) Re = 20,000;
St = 0.00251; $\phi = 60°$

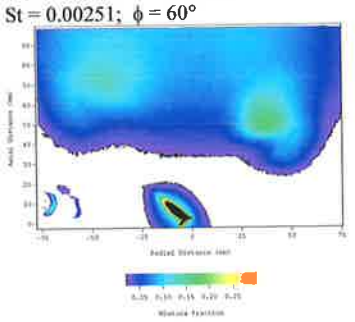

Figure 3.6(g) Re = 10,000;
St = 0.00201; $\phi = 60°$

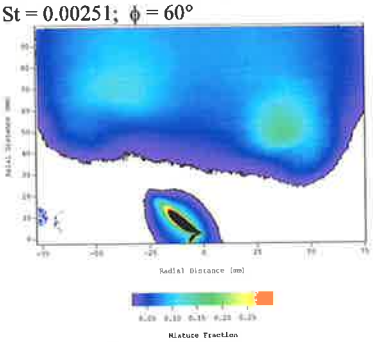

Figure 3.6(h) Re = 15,000;
St = 0.00201; $\phi = 60°$

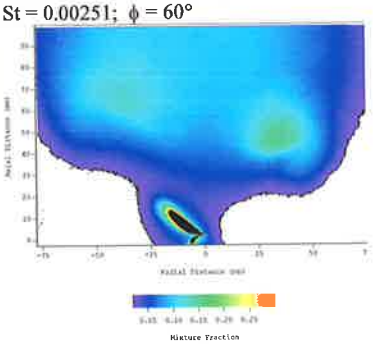

Figure 3.6(I) Re = 20,000;
St = 0.00201; $\phi = 60°$

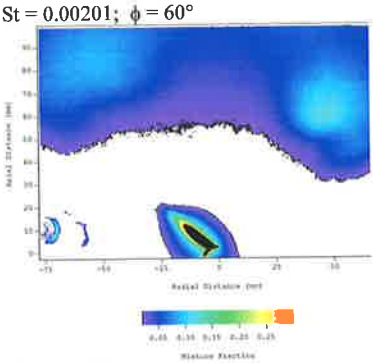

Figure 3.6(j) Re = 10,000;
St = 0.00151; $\phi = 60°$

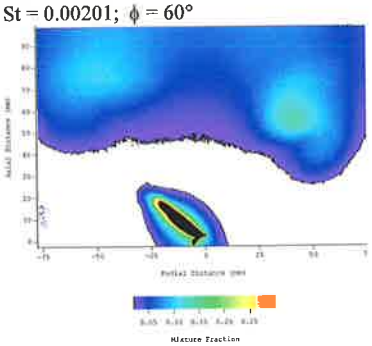

Figure 3.6(k) Re = 20,000;
St = 0.00151; $\phi = 60°$

Figure 3.6 Phase averaged images of the concentration field of the MPJ, $\theta = 60°$

3.3.2 Summary

Clear trends are established by the forgoing analysis. The Reynolds number has minimal effect on the character of the mixing field over the range $10{,}000 < Re < 20{,}000$, while the Strouhal number over the range $0.001<St<0.005$ has a strong influence, consistent with the findings of Schneider (1996). Strouhal number is shown to affect both the shape of the initial three-dimensional spiral and the concentration within it. The deflection angle is also a significant parameter, influencing the spread of the helix as determined by the distance between Structures #1 and #2. A trend of increasing concentration in the helix with increasing deflection angle is also apparent.

Other qualitative features, which can be drawn from the measurements, are as follows. The mushroom shape of the two lobes (Figure 3.2(a)) suggests that they are associated with counter-rotating vortex tubes which draw ambient fluid into the region between the lobes (Nathan *et al.* 1997). The lobes within Structure #2 are not generally as well defined as in Structure #1, although evidence of the vortex tubes is still apparent. The regular location and shape of the lobes (the vortex tubes) can be seen in all of the phase averaged images. The "inner tube" of Structure #1, closest to the spinning axis, always has a higher mean concentration than the outer. The regular appearance of these phase-averaged structures supports the notion that the emerging jet footprint evolves in the form of a continuous 'helix'. Downstream from the location of Structures #1 and #2, the phase-averaged flow becomes symmetrical suggesting that the mixing field develops toward a self-similar condition and that the identity of the emerging "precessing" jet is being lost.

3.4 WHOLE FIELD STRUCTURE

From the previous section, it is evident that there is present within the flow field generated by a MPJ structure of a scale that is not present in a simple jet. This structure is intimately related to the dimensionless precessional frequency and the deflection angle. This section provides more details of these large-scale motions from instantaneous images, and discussion of other research. New data is presented for the flow from a MPJ nozzle with an exit diameter of d = 10mm, at a Reynolds number of 25,600, based on jet exit conditions and various Strouhal numbers. Previous data presented will also be used.

3.4.1 Evidence of Vortex Tubes within the Helix Region

Evidence that vortex tubes are generated within the helix region by the precession of a jet can be seen in Figure 3.7, which presents a random selection of instantaneous images of the MPJ flow field with conditions, Re = 23,800, St = 0.002, $\phi = 45°$ and d = 3mm. The constant false colour scheme across the various images shows the presence of Structures #1 and #2 associated with the helical foot print of the jet. Focusing on Structure #1 to the right of the exiting jet, the majority of the images distinctly show the presence of the two lobes, which are deduced to be associated with a pair of vortex tubes. There are, however, other "modes" present in some images. Sometimes there is only "one lobe" evident and sometimes more complicated patterns exist, such as the presence of three lobes (see the third image from the left on the bottom row of Figure 3.7). That the two-lobe "mode" is dominant is clearly seen in the phase mean images of Figure 3.3-3.6.

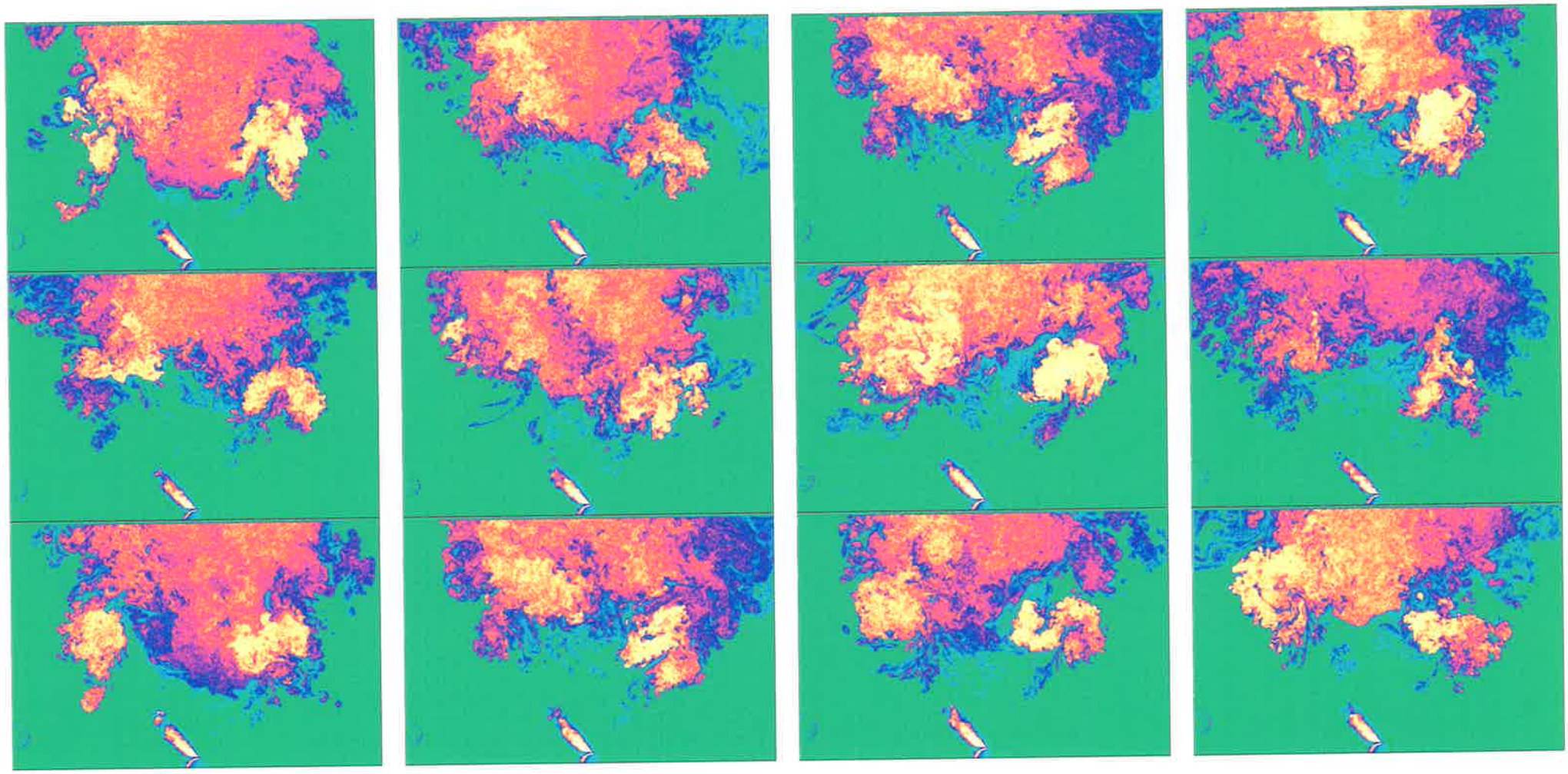

Figure 3.7 A random selection of instantaneous images in the flow from the MPJ nozzle. Conditions: Re = 23,800, St = 0.002, $\phi = 45°$ and d = 3mm.

Phase averaged data collected at a number of different phase angles within the precessional cycle for condition, Re = 24,500, St = 15.3×10^{-3}, $\phi = 45°$ and d = 10mm, are presented in Figure 3.8, for the first 180° of the cycle, and Figure 3.9, for the full 360°of the cycle. These images have been cropped to focus in on the region of interest, and hence only show the helix and collapsing spiral region. The window size is constant for all data presented. The phase angle, θ, is indicated for each image. As θ increases from $\theta = 0°$, the path of the footprint can be observed. Within two nozzle diameters, the two lobes in the concentration field can be distinguished. For $\theta = 67.5°$ and $\theta = 90°$, the developing vortex tubes are approximately symmetrical, but with increasing θ, the structure in the helix deforms so that the inner vortex tube remains at a relatively high level of concentration while the outer tube exhibits rapid decay in concentration. This provides unequivocal evidence that the outer lobe is mixing with the ambient fluid faster than the inner lobe.

It is interesting to examine the position and features of Structure #1 throughout the cycle of precession, shown on the right hand side of the images in Figure 3.8. While its general features are qualitatively similar throughout the cycle, its concentration decreases from $\theta = 0°$ to $\theta = 157.5°$. While the core of the inner vortex tube is generally at a fixed radial distance from the spin axis, the inner edge of the vortex moves toward the axis so that at $\theta = 157.5°$ the vortex can be seen to merge with the remnants of the helix from the previous cycle. This implies that the inner part of the vortex starts to entrain itself, so providing a mechanism for the collapse of the spiral.

The full cycle of precession is shown in Figure 3.9. The second half of the cycle, from $\theta = 180°$ onward shows the same features as discussed above, but mirrored about the spinning axis. This image demonstrates that the features are consistent for different phases in the cycle, separated by 180°.

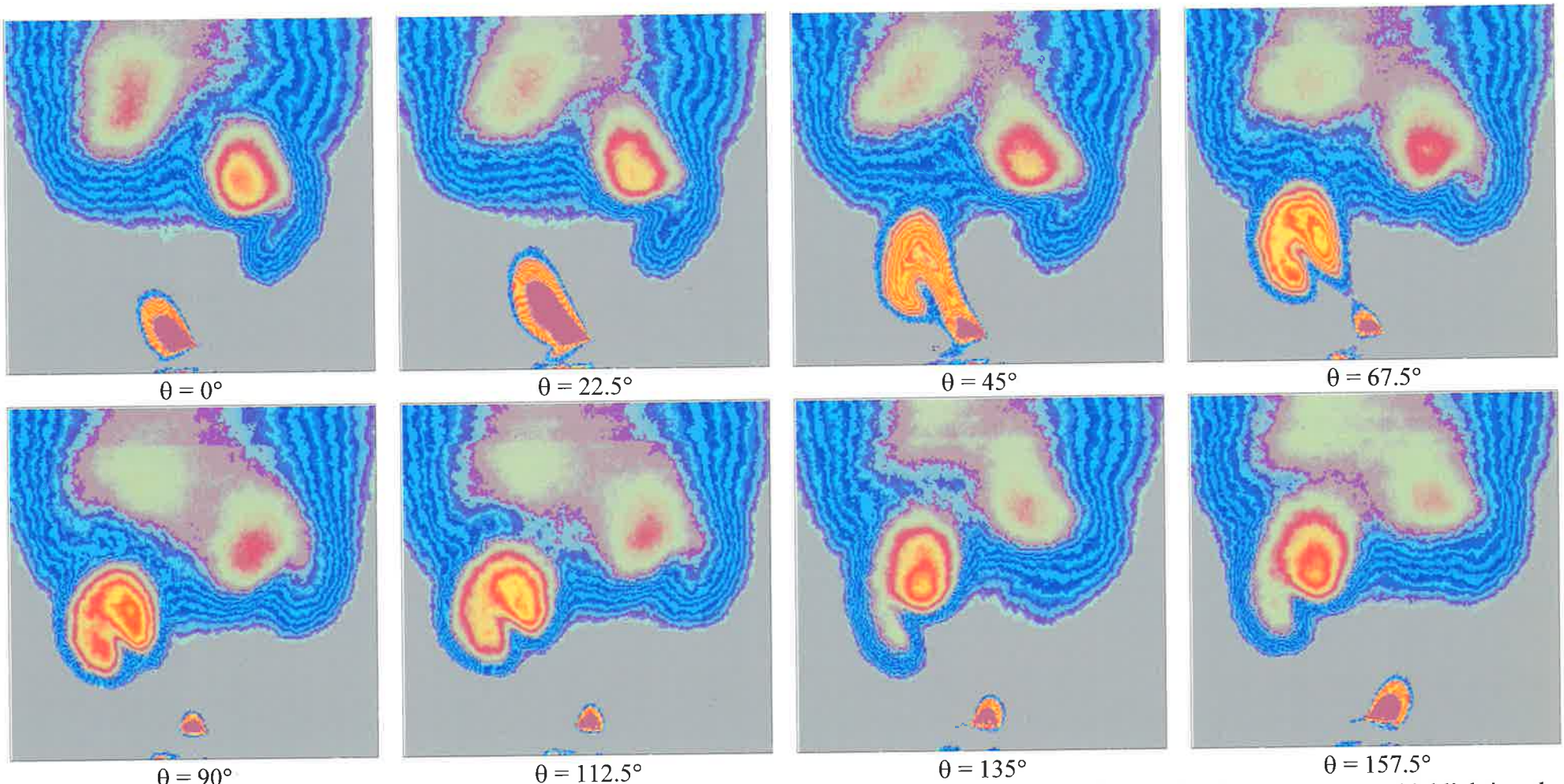

Figure 3.8 Phase averaged images of mean concentration, at phase angles indicated for one-half complete cycle of jet precession, highlighting the development of the jet concentration footprint. Re = 24,500; St = 0.0159 x 10^{-3}; ϕ = 45°; d = 10mm.

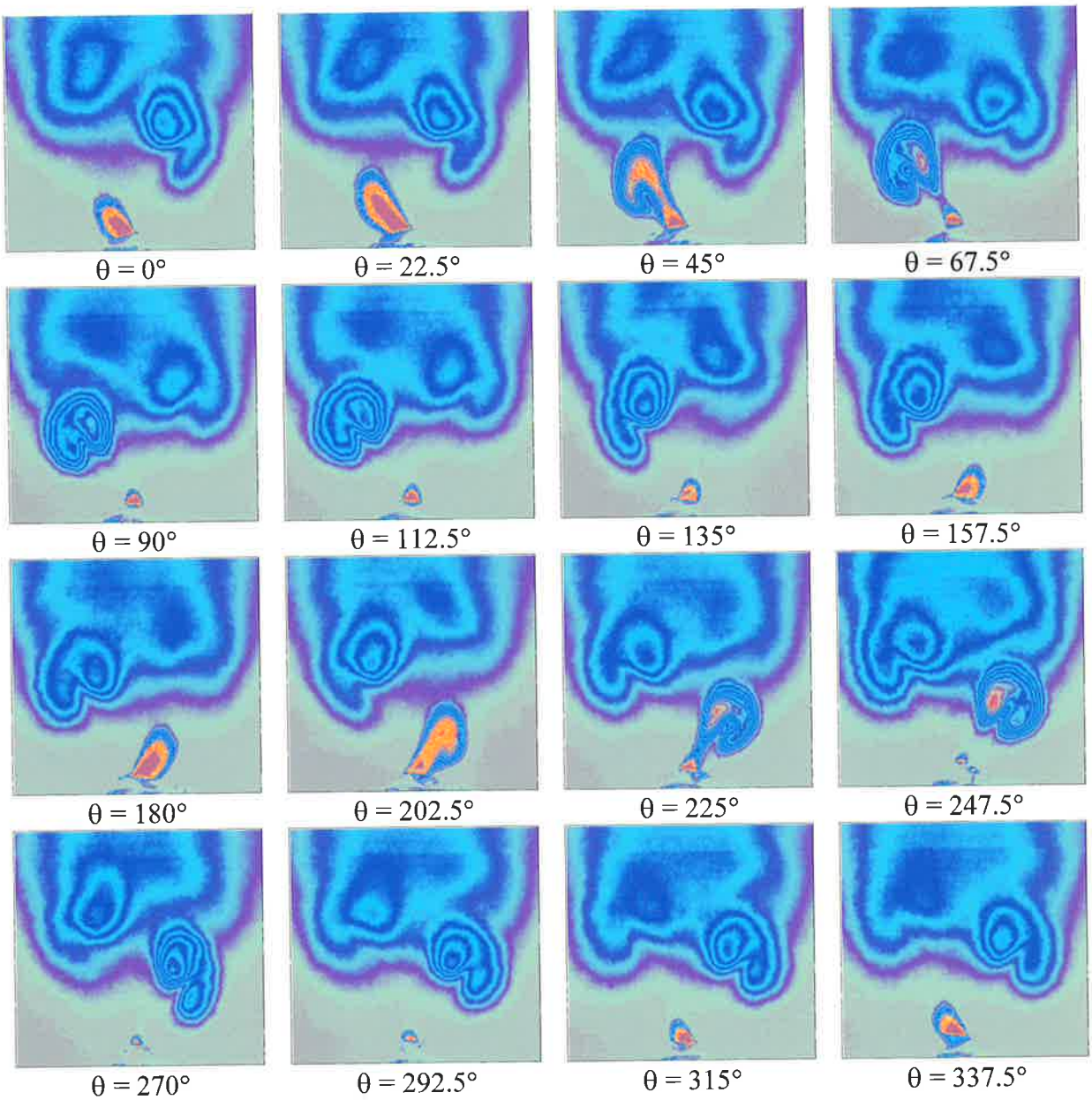

Figure 3.9 Phase averaged images of mean concentration of the flow form an MPJ nozzle, at phase angles indicated for one complete cycle of jet precession. Re = 24,500; St = 0.0159; $\phi = 45°$; d = 10mm.

Further evidence that the helical flow region contains a pair of counter rotating vortex tubes, has been provided by Nathan *et al,* (1997). They superimposed the work of Schneider (1996) on data from the present investigation collected under very similar Strouhal number and Reynolds number conditions, using the same nozzle configuration. That data is reproduced here in Figure 3.10 (note that the velocity vectors in the region of the potential core have been removed to increase the clarity of the image). The plotted velocity vectors in the vicinity of Structure #1 show the counter-rotating flow. There is a strong, axially positive flow drawn between the two vortex tubes, and a reverse flow, on the inner region of the helix, producing a reverse flow along the axis of rotation. Weak, axially negative velocities on the outer edge of the flow are also reported by Schneider (1996). This constitutes conclusive evidence that the lobes are counter rotating vortices, and is totally consistent with the prominent features identified shown in Figure 3.8 and 3.9.

There are several possible mechanisms for the generation of the counter rotating vortices, the detailed resolution of which is beyond the scope of this thesis. It is possible that there is a contribution from Görtler vortices formed by the curvature on the inner surface of the deflected nozzle. However, the size of the Görtler vortices are of the order of the boundary layer thickness and their strength is a function of the radius of curvature of the wall (Ogawa, 1992). That the lobes are present even with low values of ϕ, i.e. $\phi = 15°$, that they are present for low Reynolds numbers and that they are several orders of magnitude larger than the thickness of the boundary layer within only 2 nozzle diameters (yet subsequently grow at a slow rate beyond this position) is sufficient evidence that Görtler vortices are not the primary source of generation of the vortex tubes.

A second possible source of vorticity is the rotation of the jet itself. Schneider (1996) has shown that there is minimal net swirl imparted to the flow by the rotation of the nozzle but, there is a small eccentricity present on the outer edge of the nozzle, since the jet is not a point

source of momentum. Although this will impart some small amount swirl into the jet it is not believed to be the source of the generation of the vortex tubes.

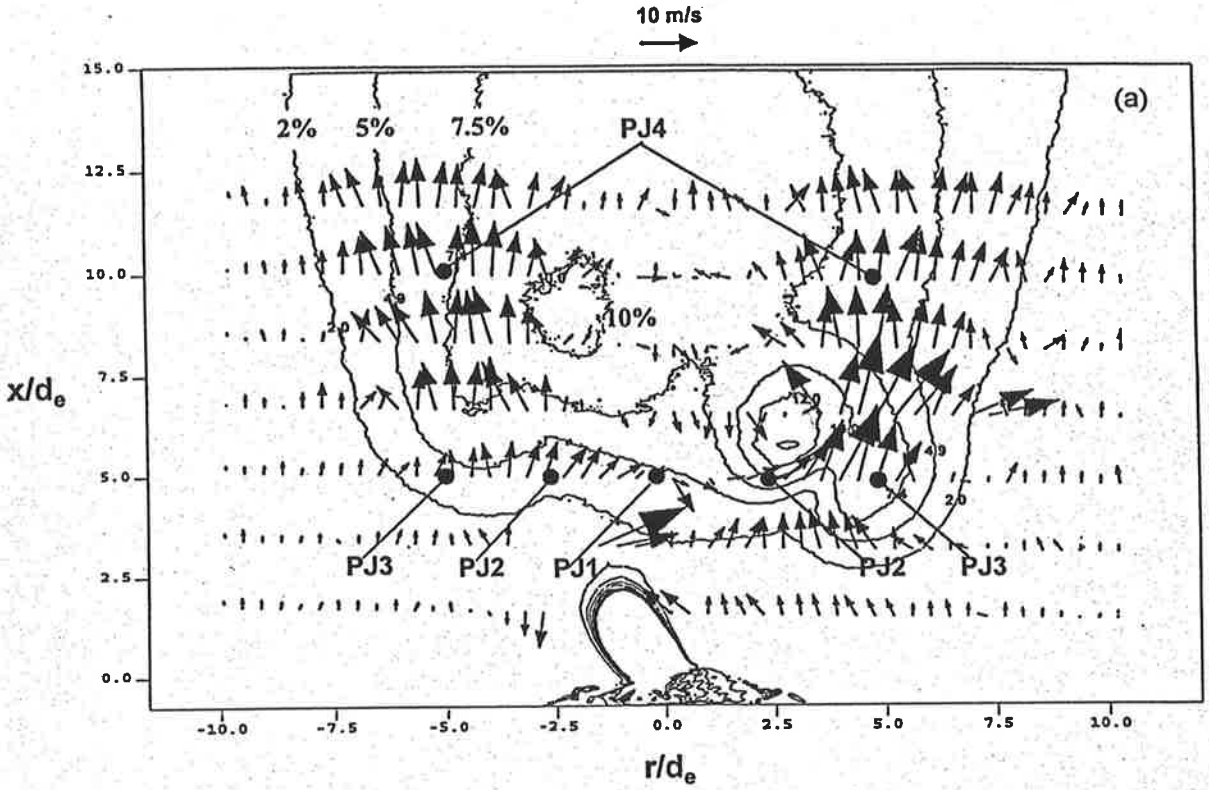

Figure 3.10 A superposition of phase mean velocity vectors on the phase averaged concentration field of an MPJ. Note: Vectors representing the initial exiting jet have been removed. Re = 25,600, St = 0.0159, ϕ = 45°, d = 10mm (Nathan *et al.* 1997)

3.4.2 Evidence for the presence of a Limit Cycle within the flow.

The phase averaged images presented in Figures 3.8 and 3.9 demonstrate that the footprint of the jet emerging from the nozzle follows a spiral path. However the spiral is seen to tend to develop into a helix of approximately constant diameter. This helix then breaks down to a more conventional axisymmetric flow. The generation of a helix of constant diameter bears the dominant features of the definition of a limit cycle given in Section 3.11

Further evidence of the presence of a limit cycle can be seen in Figure 3.11 which provides three-dimensional reconstructions of planar images collected at different phase angles for three different flow fields. Multiple sets of phase averaged data collected in the r-z plane at different phase angles (e.g. the sets in Figures 3.8 and 3.9) have been converted using a space-time approximation into data sets in the r-θ plane. A commercial software package (FORTNER : Transformer, V3.3) was first used to calculate missing data points for a regular grid in the r-θ plane. This was necessary to allow the data to be presented in this 3-D format using a different commercial package (FORTNER : Slicer V1.1). A kernel smoothing algorithm, which generates the additional data points by averaging neighboring matrix elements, introduces significant smoothing of the data at the expense of the loss of the original hard data values. Thus the images are only qualitative in nature, but provide an interpretation of the field through the use of iso-contours representing scaled values of the locus of the maximum in that particular r-θ plane. The data used to generate these images was collected from experiments with the 10mm diameter MPJ nozzle under the following conditions : Re = 25,600, $\phi = 45°$ and (a) St = 0.0159, (b) St = 0.0098 and (c) St = 0.0027.

The three dimensional images of the MPJ flow in Figure 3.11 show the jet entering the view from the bottom centre of each image. In each case the foot-print of the jet follows a helical trajectory that lags behind the nozzle rotation. The three-dimensional spiraling region can

clearly be seen, followed by an almost axisymmetric region. For increasing values of Strouhal Number the helix or spiral can be seen to tighten in the azimuthal direction and the diameter of the helix reduces. At the same time the flow field is compressed in the axial direction. At all but the lowest Strouhal Number (where the flow field is restricted) the parallel core region can be seen clearly. It is argued here that the trend in which the foot print of the helix forms a constant diameter constitutes a limit cycle and this controls the character of the transition region between the near, precessing helix region and the far field fully developed region. The sudden reduction in the spreading of the flow field is in all images and implies a dramatic reduction in entertainment of surrounding ambient fluid. A possible mechanism for this is the merging of the vortex tubes so that the helix principally entrains "itself", that is, jet fluid. This transition is so dramatic that the growth of the total jet in this region can almost totally cease, as evident by the region of near parallel flow in the photographs of Figure 3.1.

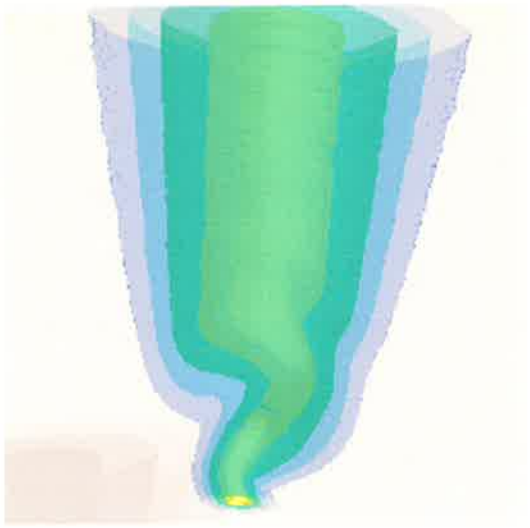

(a) Re = 25,600, St = 0.0159, $\phi = 45°$

(b) Re = 25,600, St = 0.0098, $\phi = 45°$

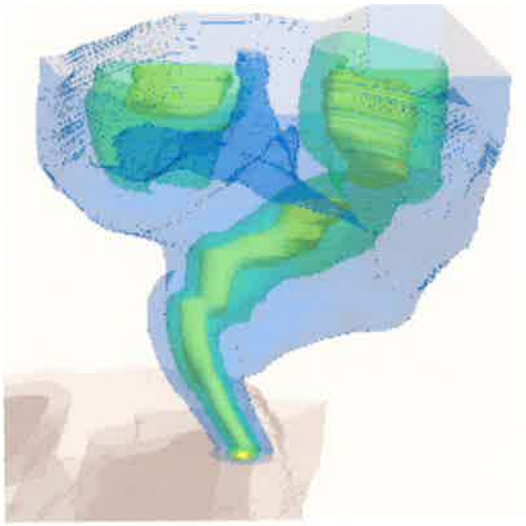

(c) Re = 25,600, St = 0.0027 , $\phi = 45°$

Figure 3.11 (a-c) 3-D images of concentration field of the precessing jet flow for different values of Strouhal number. (Note: iso-contours are not true iso-values of concentration)

3.5 DIMENSIONLESS PARAMETERS FOR NORMALIZATION OF DATA

The previous sections have shown that precession superimposes additional length and time scales on the flow of a jet. It has been shown that the initial trajectory of the flow is that of an expanding helix, which has a characteristic angle. Further downstream the helix collapses onto another characteristic diameter. These phenomena are related to the exit angle of precession and the frequency of precession. This section will compare the ability of different dimensionless parameters to characterize the dominant features of the MPJ flow. The following describes the principle three parameters which are investigated.

3.5.1 The Strouhal Number.

The Strouhal Number of precession has been found to be a useful dimensionless parameter to characterize the flow for a fixed exit angle. It has been used previously by Schneider (1996), Schneider *et al.*(1997a, 1997b) and Nathan *et al.* (1997) to characterize the flow from the MPJ and by Nathan (1988), Nathan, Luxton and Hill (1997) to characterize the flow from the FPJ.

With reference to Figure 3.12, the Strouhal number is a dimensionless frequency defined as,

$$St = \frac{fd}{V_o}, \qquad \text{Equation 3.1}$$

where f, is the frequency of precession of the nozzle, d is the exit diameter and V_o the velocity at the nozzle exit and is a dimensionless frequency of the flow. There have been other forays into the equations of motion by Luxton (1993, 1994) and these have shown that the Strouhal number is a relevant parameter.

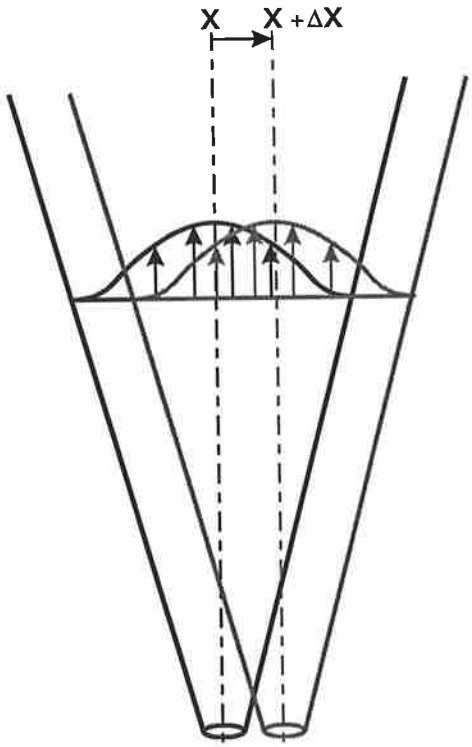

Figure 3.12 A schematic representing the addition of strain to a jet by the translation of the momentum source from, x to x+Δx during the time Δt

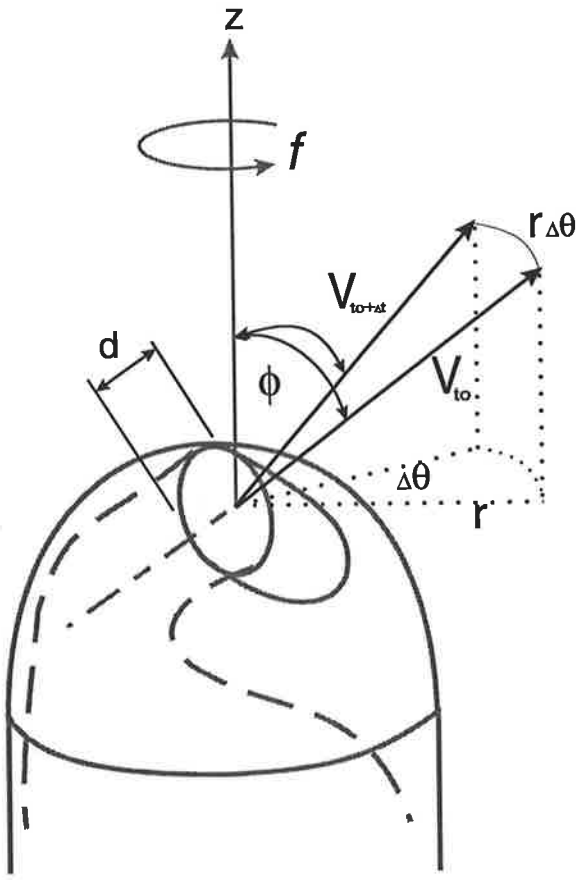

Figure 3.13 Definition of variables used to generate dimensionless terms.

3.5.2 The Dimensionless Strain Rate.

The Strouhal Number only takes into account the effects of precession for a fixed deflection angle. The present work has demonstrated however that the deflection angle has a significant effect on the flow field. It is argued here that the mixing rate is altered through the addition of strain by the act of precessing the jet. The strain rate in a jet is usually characterized by the parameter V/d, which has the units of s^{-1}. This characterizes the transverse velocity gradient in a jet and has been used to characterize the mixing in jet and flames for many years. For example, Kent and Bastin (1984) used it to characterize soot formation and Røkke *et al.* (1994) used it to characterize NO_x emissions. The additional strain introduced by precession is illustrated in the following way.

Consider a free jet which is translated by a length of Δx during the time Δt. The additional strain imparted by the translation of the jet is illustrated in Figure 3.12. The additional strain is introduced by the translation is clear from the high velocity gradient indicated by the overlapping mean velocity profiles. The translation of the jet through a distant Δx during time Δt introduces an additional strain relative to the characteristic axial translation of the jet $V\Delta t$ during the same time. Hence the additional strain rate due to translation is characterized by the parameter $\frac{\Delta x/\Delta t}{(V\Delta t)}$.

However in a precessing jet flow the "translation" of the momentum vector is more complicated and is a function of both the defection angle and the frequency of precession, as illustrated in Figure 3.13. If the defection angle is $\phi = 0°$ and the nozzle tip rotates at a set frequency f, then the amount of additional strain added to the flow field will be zero.

However, if the deflection angle is $\phi = 90°$, then the addition of strain from precession will be at a maximum.

Referring to Figure 3.13, the vector V_{to} moves during time Δt through an angle $\Delta\theta$ to position $V_{to+\Delta t}$ as a result of precession. If the fact that V_{to} and $V_{to+\Delta t}$ are not parallel is ignored, ie $r\Delta\theta$ is assumed to be very small, then the momentum vector moves by a distance $r\Delta\theta$ in a time Δt. The relative distance moved by the jet during the same interval is $V\Delta t$. Hence we can write:

$$\text{Strain rate due to precession} \sim \frac{r\Delta\theta/\Delta t}{V\Delta t} \qquad \text{Equation 3.2}$$

$$\sim \frac{r.f}{V.\Delta t} \qquad \text{Equation 3.3}$$

$$\sim \frac{(V.\sin\phi.\Delta t)f}{V.\Delta t} \qquad \text{Equation 3.4}$$

$$\sim f.\sin\phi \qquad \text{Equation 3.5}$$

Thus the ratio of strain rate of precession to that of the original jet scales with the parameter,

$$\frac{f.\sin\phi}{V/d} \equiv \frac{fd}{V_o}.\sin\phi = St.\sin\phi \qquad \text{Equation 3.6}$$

This modification which accounts for the strain addition from precession will be referred to below as the dimensionless strain rate.

3.5.3 A modified Strouhal Number- a *Rossby number.*

It has been shown in previous sections that it is possible to distinguish several different regions within the flow field, each with characteristic length scales. The length scale used in the Strouhal number is that of the exit diameter. However, further downstream, in the

transition region in which the helix collapses and the flow field is characterized by a constant characteristic width, the dominant length scale is the radius of the helix rather than the inlet diameter. Introducing this length scale generates a modified Strouhal number, St_m, and is defined as,

$$St_m = \frac{f\,r}{V_o}, \qquad \text{Equation 3.7}$$

where r is the radius of the helix. The reciprocal of this modified Strouhal number has the appearance of a Rossby number. The Rossby number is a cross product of two velocities, an axial velocity and an azimuthal velocity, while the Strouhal number is a ratio of two frequencies. The modified Strouhal number uses the exit velocity and the frequency of precession. For this number to be equivalent to a Rossby number would require that there are azimuthal velocities within the flow field. Schneider *et al.* (1996) resolved that if azimuthal velocities were present they are of very low magnitude. In the following section data for the modified Strouhal number will be presented in a form similar to the Rossby number, i.e. as the reciprocal of this modified Strouhal number, $1/St_m$ and will be denoted as the modified Strouhal number.

3.6 NORMALIZATION OF THE FLOW FIELD.

3.6.1 Introduction

A quantitative assessment of the effectiveness of the various dimensionless parameters discussed in the previous section in characterization of the flow can be obtained by quantifying specific features in the phase averaged flow field. Figure 3.2(a) identifies four features in the phase-averaged flow that can be quantified. Two large structures, 180° out of phase, are imaged as the light sheet slices through the helix. These structures have been characterized further into two lobes, which represent the cross-sectional view of two counter rotating vortex tubes. The location of the locus of these tubes relates to the shape of the helix and can be defined with respect to an origin. The mixing of the jet is described by the value of concentration at this point. The origin is chosen to be at the centre of the nozzle exit on the spinning axis. In a Cartesian coordinate system (x,y,z), the spatial location at which the helical path of each of the vortex tubes cuts the light sheet at a phase angle of 180° and 360° relative to the exit can be defined by a distance parallel to the spinning axis and a distance perpendicular to the same axis. Alternatively, a spherical coordinate system (z,ϕ,θ) would define the location of the point by a distance from the origin to the location of the vortex tube and an angle from the spinning axis. The data is presented here for both coordinate systems. (Note that distances defined by a cylindrical coordinate system (z,r,θ) are equivalent to those defined by the Cartesian coordinate system.)

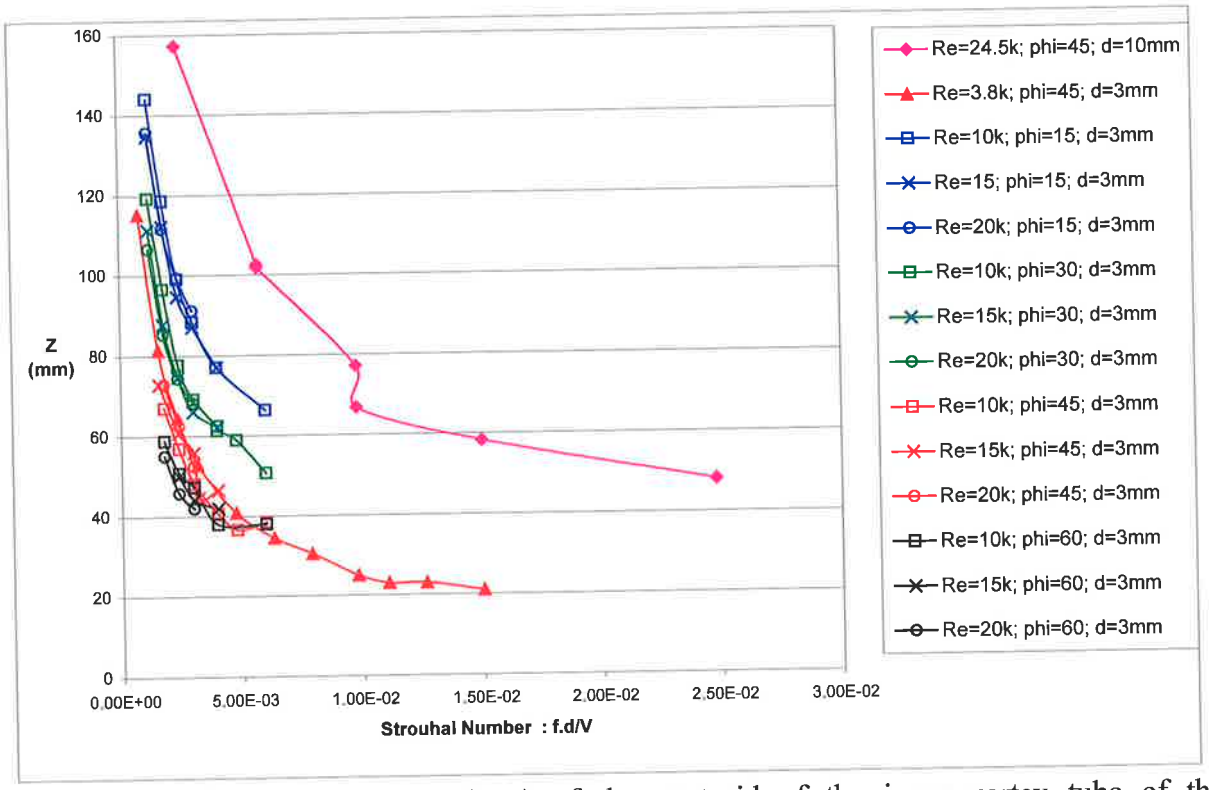

Figure 3.14 The axial distance (mm) of the centroid of the inner vortex tube of the Structure #1 as a function of Strouhal number.

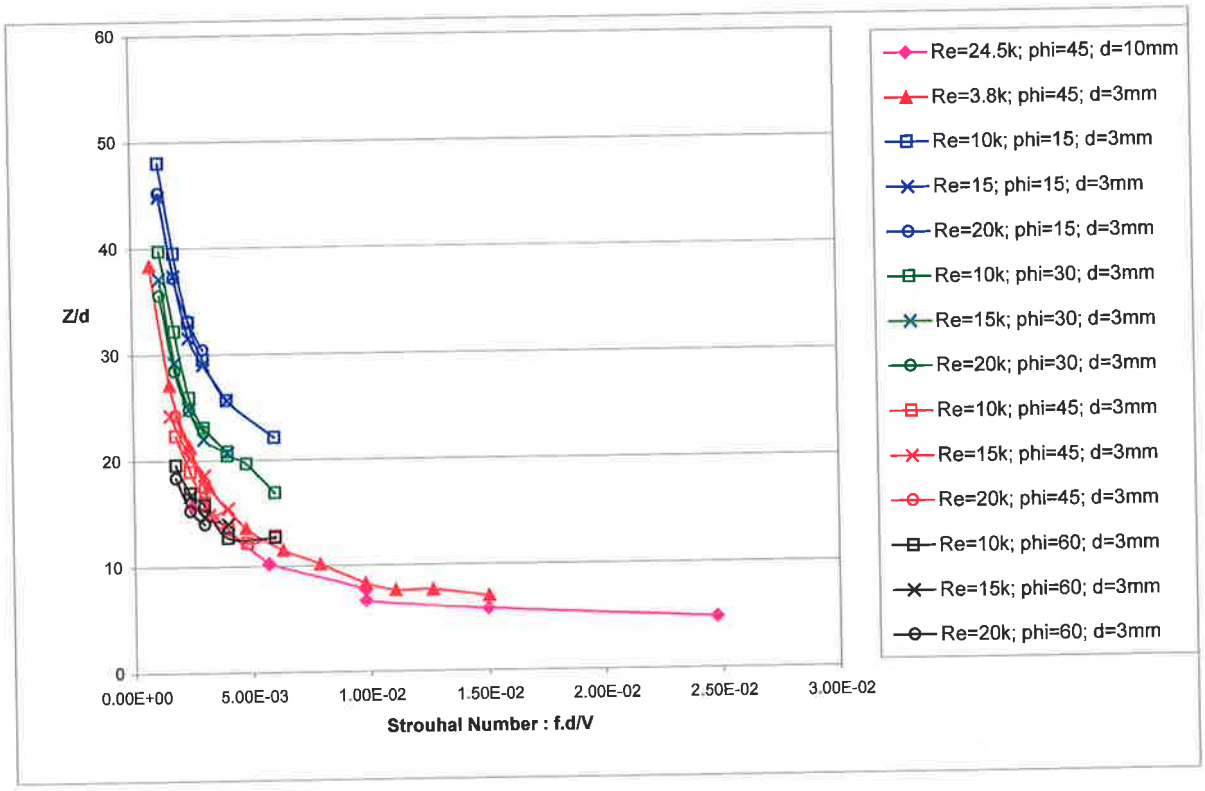

Figure 3.15 Normalized axial position (z/d) of the inner vortex tube of the Structure #1 as a function of Strouhal Number.

Figure 3.14 compares the axial location of the inner vortex tube of Structure #1 for different experimental conditions. The axial distance is plotted in absolute units (mm) against the dimensionless frequency (Strouhal number) based on the exit conditions. The characteristics of the helix formed under each of the set of conditions investigated in the phase averaged data in Figures 2.3 - 2.7 are contained in Figure 3.14. Included in this figure are data for the 3 mm diameter nozzle at a low Reynolds number of 3,800 and for a 10 mm diameter MPJ at a Reynolds number of 24,500. Each colour in Figure 3.14 corresponds to conditions of constant nozzle deflection angle. The shape of the symbols used are constant for constant values of Reynolds number.

Some trends can be seen in Figure 3.14. For each data set, reducing the Strouhal number causes the axial distance to the inner vortex tube to tend asymptotically toward infinity. Conversely, increasing the Strouhal Number causes the axial distance to tend toward a constant value. Close examination shows that variations in Reynolds number have little effect on the axial location of the vortex tube.

Normalization by the Strouhal number but using absolute axial units does not collapse different sets of data for different exit angle or exit diameter. By contrast, normalizing the axial distance by the nozzle exit diameter, alters the relative position of the data for d = ϕ10mm, aligning it with the other set of $\theta = 45°$ data obtained for d = 3mm. This is shown in Figure 3.15. Investigation of other variable, such as the radial distance from the spin axis to the vortex tube shows the same trend, that normalizing with respect to the nozzle diameter collapses groups of data with different exit diameters. Hence this form of normalization has been used in subsequent figures.

The remainder of the present section will discuss and present data defining the shape and concentration of the helix, using the dimensionless parameters discussed in Section 3.5. The

data is organized into subsections, each of which address one parameter. Each of the three dimensionless parameters are presented together for a single parameter/location in the flow. Conditions for each of the data sets are the same as for Figure 3.14 and Figure 3.15. A legend *is not* included in each graph for clarity.

3.6.2 A Spatial Description of the Helical region

3.6.2.1 The characteristic "pitch" of the helix.

The pitch of the helix is characterized by the axial distance, z, to the features associated with Structures #1 and #2. Figures 3.16(a) to 3.16(d) shows the data for these parameters.

Collapse of the data with the Strouhal number is consistent with the data presented in Figure 3.15. The Strouhal number does not collapse the effect of exit angle, so that the data is bunched into groups of constant ϕ. With the dimensionless strain rate, the collapse of data is excellent for all values of ϕ. Significantly, for the outer vortex tube of Structure #2 (Figure 3.16(d)) the data is spread more than for the other locations. This is an indication that an additional or alternative scaling parameter becomes significant in this region. Collapse of data for the modified Strouhal number is varied. The data is bunched into groups of constant ϕ. There is a near linear behavior for $1/St_m > 5{,}000$ and for values of $1/St_m < 5{,}000$ the axial distance tends towards zero.

The ability of the Strouhal number and the dimensionless strain rate to characterize the pitch is consistent for all features in the helix. For increasing values of Strouhal number, the axial distance tends towards a constant value. For decreasing values of Strouhal number and dimensionless strain rate the normalized axial distance tends towards infinity. This indicates that for low values of the dimensionless parameter, the helix pitch tends towards infinity. For high values of Strouhal number the helix pitch tends towards a constant value. For Structure #1 the asymptotic distance is $z/d \approx 5$ and for Structure #2, $z/d \approx 7$. This close proximity of values for the helix pitch, only 180° apart, shows that the pitch of the helix decays between $\theta = 180°$ and $\theta = 360°$. This is an indication that the helix is beginning to collapse on itself

after only one cycle and that the normalized axial distance, z/d is an indication of where this collapse occurs.

3.6.2.2 The characteristic "diameter" of the helix

The radial distance from the spin axis to Structure #1 and Structure #2 characterizes the diameter of the helix. Data for the normalized radial distance to the vortex tubes is presented in Figure 3.17(a) to 3.17(b). None of the parameters provide good collapse for the helix diameter although, collapse is best at high ϕ. There is a clear trend of decreased helix diameter with decreased deflection angle suggesting that a radial pressure gradient is established. None of the dimensionless parameters take this radial pressure field into account, consistent with the poor collapse. Although the trends are similar for the different values of ϕ across the three dimensionless parameters and the four spatial locations, the collapse of data is not consistent. The data in all cases is noticeably bunched into groups of constant deflection angle, ϕ.

The trends with the Strouhal number and dimensionless strain rate are consistent. For increasing values of Strouhal number the normalized radial distance tends towards a constant value. For decreasing values of Strouhal number, the normalized radial distance tends towards infinity. This indicates that the helix asymptotes towards a diameter of constant value.

The modified Strouhal number arguably provides the best collapse for different values of ϕ. This is evident for the high deflection angle cases of $\phi = 45°$and $\phi = 60°$, where the data has reasonable collapse. These plots show that for low values of the modified Strouhal number the normalized radial distance tends towards zero, rather than a constant value as shown for the Strouhal number and the dimensionless strain rate.

That none of the three dimensionless parameters characterless the diameter of the helix implies that the radial pressure gradient in the core of the helix, as measured by Schneider (1996) is not adequately accounted for. In particular it implies that the radial pressure gradients are relatively stronger at smaller exit angles, causing greater relative decay in helix diameter then occurs for the larger deflection angles.

3.6.2.3 Normalized total linear "growth" of the helix.

The normalized total (axial and radial) distance from the origin to the vortex tubes, (R), is a measure of the "growth" of the helix and can be defined using Pythagoras's theorem, $R = \sqrt{(z^2 + y^2)}$. The data calculated in this manner is presented in Figures 3.18(a) to 3.18(d).

The general trends are similar to those found in the axial characterization, i.e., the dimensionless strain rate characterizes the total (vector) velocity of the helix very well, and much better than the other two normalizing parameters. The collapse is better for the beginning of the helix (Structure #1) than in the beginning of the collapsing region (Structure #2). A noticeable feature of the data collapse for the modified Strouhal number is that the data collapses better for the outer vortex tube then for the inner vortex tube for both of Structure #1 and #2. This is an indication that the modified Strouhal number becomes important in the transition region.

Trends for the Strouhal number and the dimensionless strain rate are similar for the normalized radius, as found for the normalized axial distance and the normalized radial distance. An interesting feature of the inner vortex is the clustering of data at very low values of the modified Strouhal number, about a constant value of the normalized radius. This is an indication that for decreasing values of the modified Strouhal number the location of the inner

vortex footprint does not vary. However the data for the same jet conditions for the outer vortex does vary. This would indicate a "twisting" of the footprint of the jet. Supporting evidence of this can be seen in the images presented in section 3.2.

3.6.2.4 The rate of change of the "spreading" angle of the helix

The "spreading" angle, ϕ_p, can by calculated from the axial and radial positions using, $\phi_p = \arctan(r / z)$. Data for the calculated angle (ϕ_p) from the spinning axis to the point of interest is presented in Figures 3.19(a) to 3.19(d). For all of the data presented in that section there is no significant collapse for the different values of deflection angle (ϕ) for the dimensionless parameters used. All plots show that the data is bunched into groups of constant deflection angle (ϕ), and that the measured angle (ϕ_p) remains nearly constant over the range of the dimensionless parameters used. This trend is consistent for all locations investigated except for the inner vortex tube of Structure #2, where the measured angle (ϕ_p) is seen to vary in magnitude.

The uncorrelated collapse of data in Figure 3.19 has prompted the normalization of the measured angle (ϕ_p) by the deflection angle of the nozzle exit nozzle tip (ϕ), i.e. ϕ_p/ϕ. Data presented in this fashion is shown in Figures 3.20(a) to 3.20(d). Using this method of normalizing the measured angle for a helix defined by an Archimedean spiral would have values of $\phi_p/\phi = 1$, i.e., the spatial location where fluid exiting the nozzle has not deviated from its original trajectory. For $\phi_p/\phi < 1$, the location is closer to the spin axis then would be predicted by the Archimedean spiral, and likewise the results for $\phi_p/\phi > 1$ indicates that the location is further from the spin axis.

There is better collapse of the data when it is presented in this manner. Figure 3.20(a), of the inner vortex of Structure #1 has values of $\phi_p/\phi = 0.4$ to 0.7, indicating that this vortex has been deflected towards the spin axis. The corresponding outer vortex tube of Structure #1 (Figure 3.20(b)) has values of the normalized angle of 1. Thus the outer vortex tube is. at this point in the phase of precession, following the exit trajectory from the nozzle. A discernible difference is observed in the location of the outer vortex tube half a cycle on. Figure 3.20(d) shows values of $\phi_p/\phi < 1$, indicating that by end of one phase cycle, the outer vortex tube has been deflected toward the spin axis.

The measured normalized angle to the inner vortex tube of Structure #2 (Figure 3.20(c)) shows significant variations in magnitude. This would tend to indicate that the jet footprint, while having a uniform spiral growth, is being "twisted" resulting in the variation of the location of the inner vortex tube. Also, all high values of Strouhal number or dimensionless strain rate and low values of the modified Strouhal number the inner vortex of Structure #2 has been shown to merge with the inner vortex of Structure #1. The dynamics of this interaction have yet to be well defined and is a potential source of the variation in the position of the inner vortex tube.

3.6.2.5 Summary on the spatial description of the helix.

The shape of the helical footprint of the emerging jet has been quantified by identifying the features of the helix. The applicability of various scaling parameters in characterizing these features has been assessed. In general the results demonstrate that the initial growth of the helix is well described by the dimensionless strain rate parameter, supporting the simple analytical model presented in section 3.5.2. However this parameter does not take into account the radial pressure field generated by precession and does not characterize the diameter of the helix well.

The analysis also shows that additional parameters become significant after the first 180° of the helix, as the spiral begins to collapse and the transition region emerges. This is to be expected, since the analytical strain rate does not account for these effects. The improved ability of the modified Strouhal number, that based on the helix diameter, in the latter part of the spiral (Structure #2) suggests that this length dimension may characterize the transition region, supporting the concept of a limit cycle.

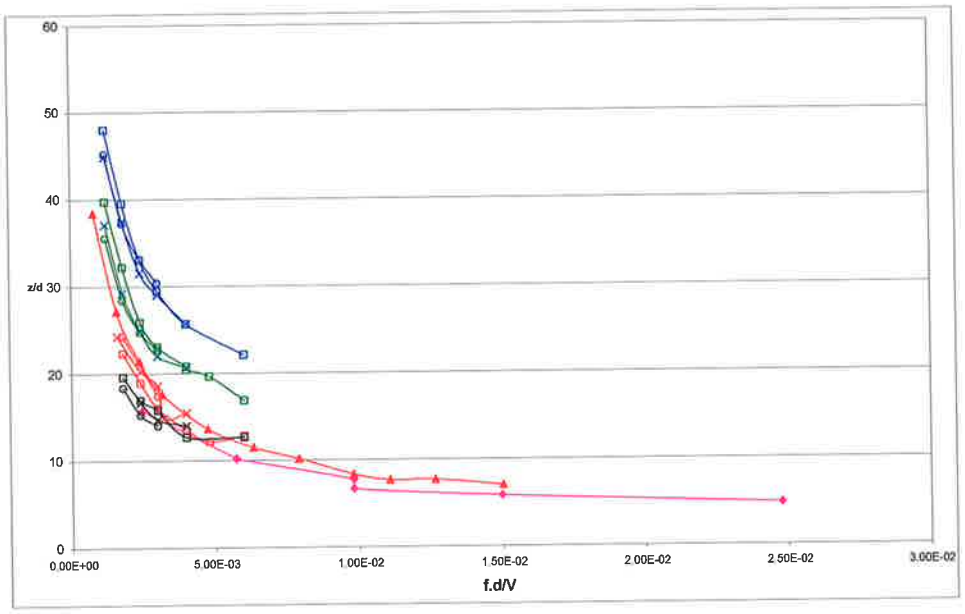

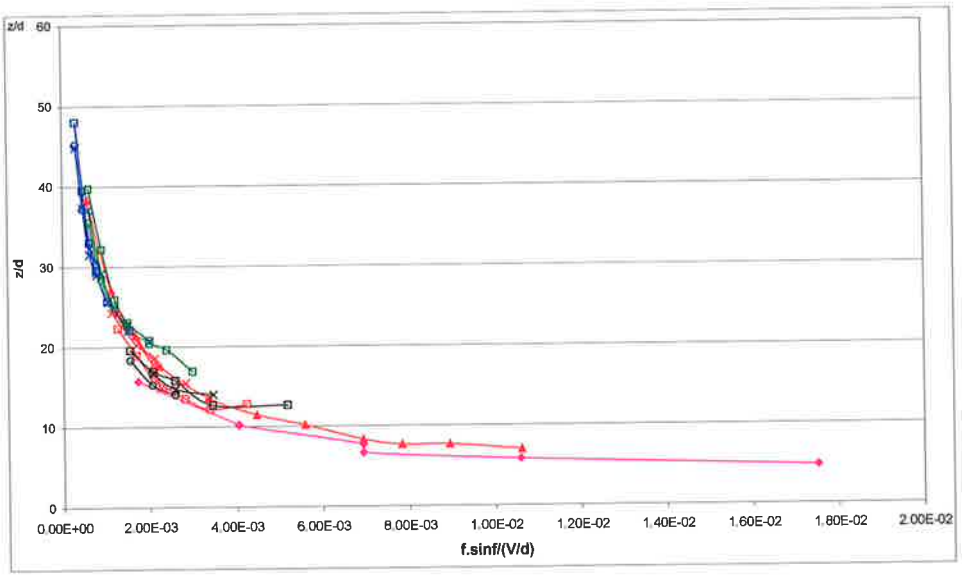

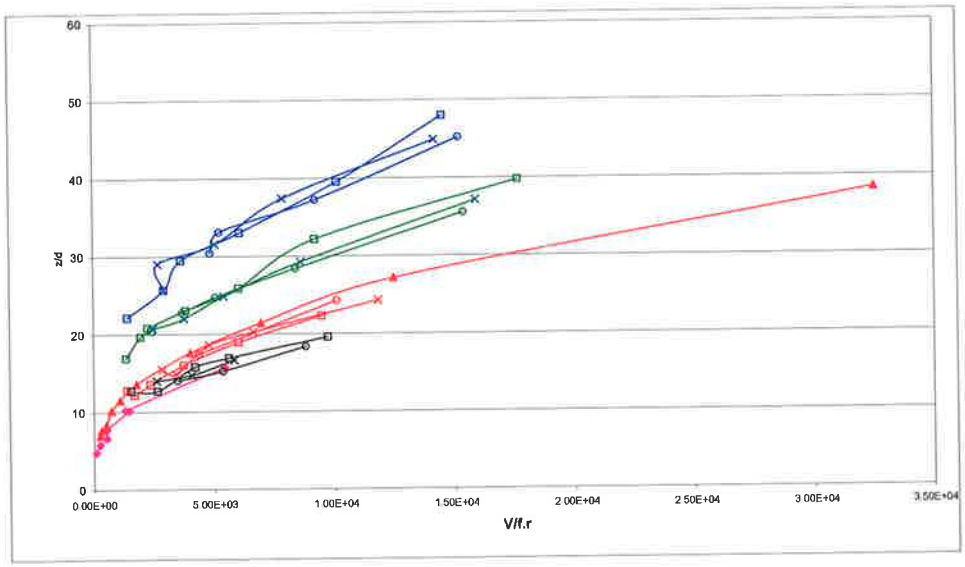

Figure 3.16(a) The axial position of the **Inner** vortex tube, **First** structure

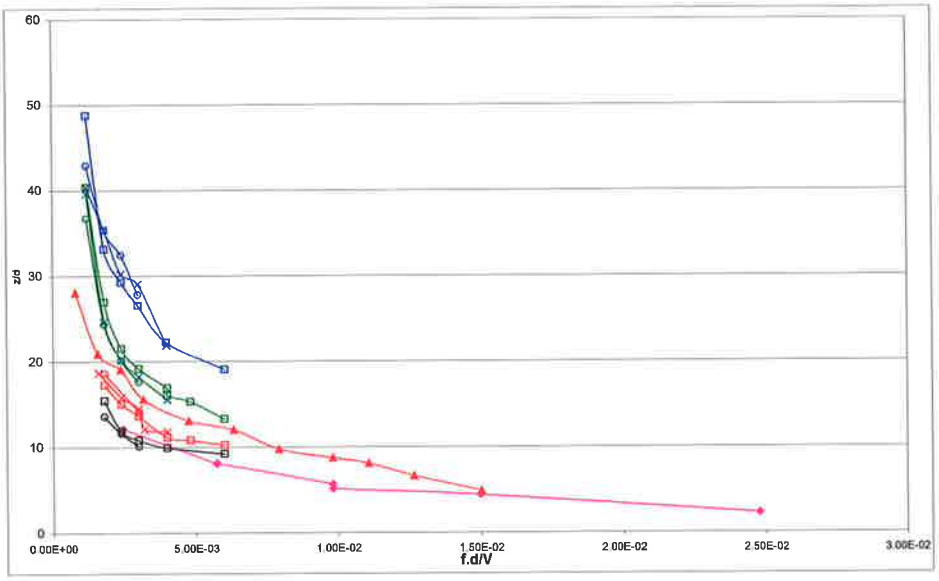

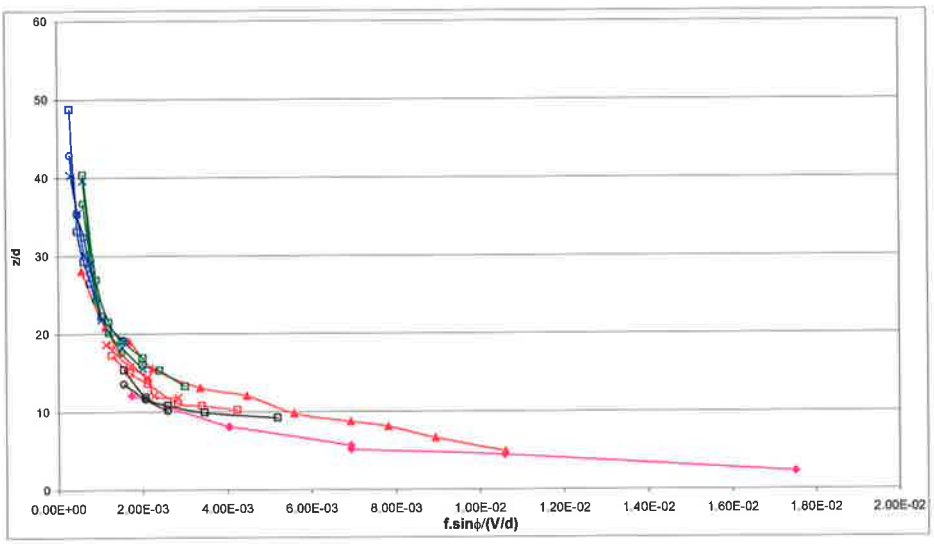

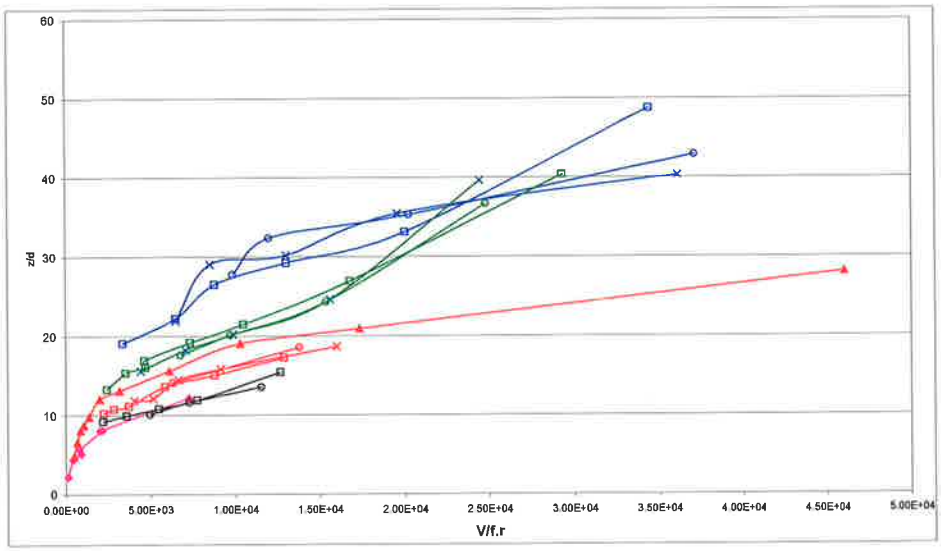

Figure 3.16(b) The axial position of the **Outer** vortex tube, **First** structure

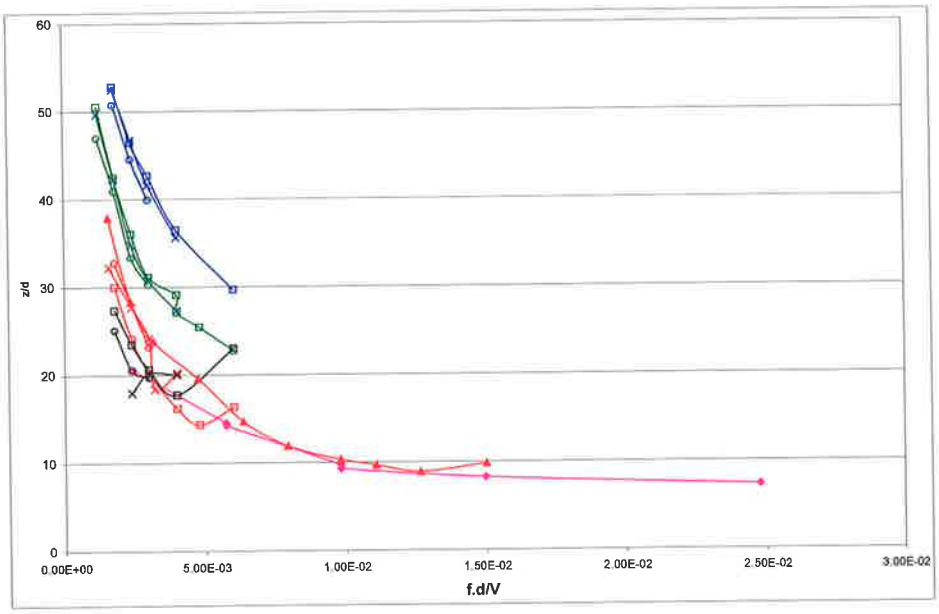

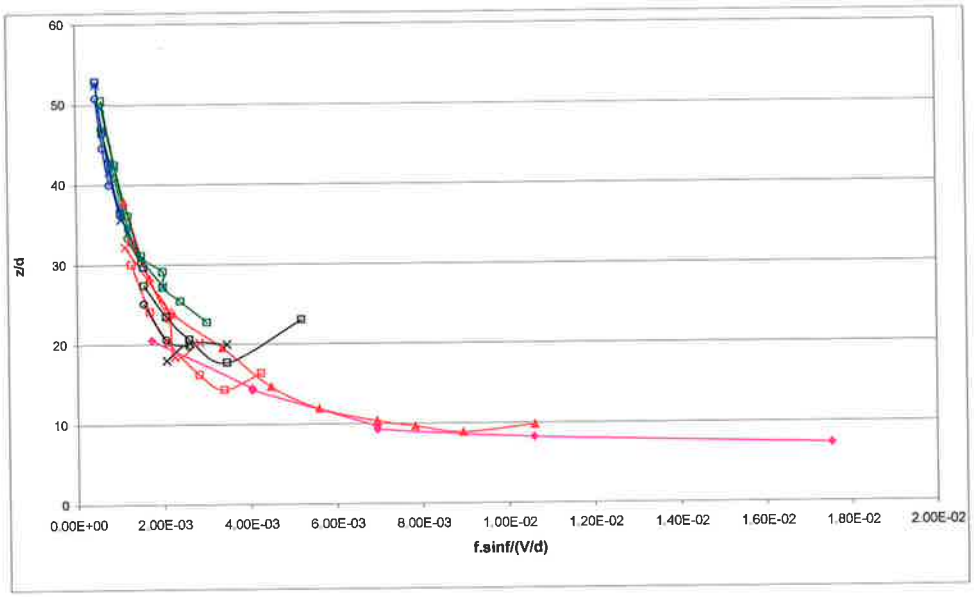

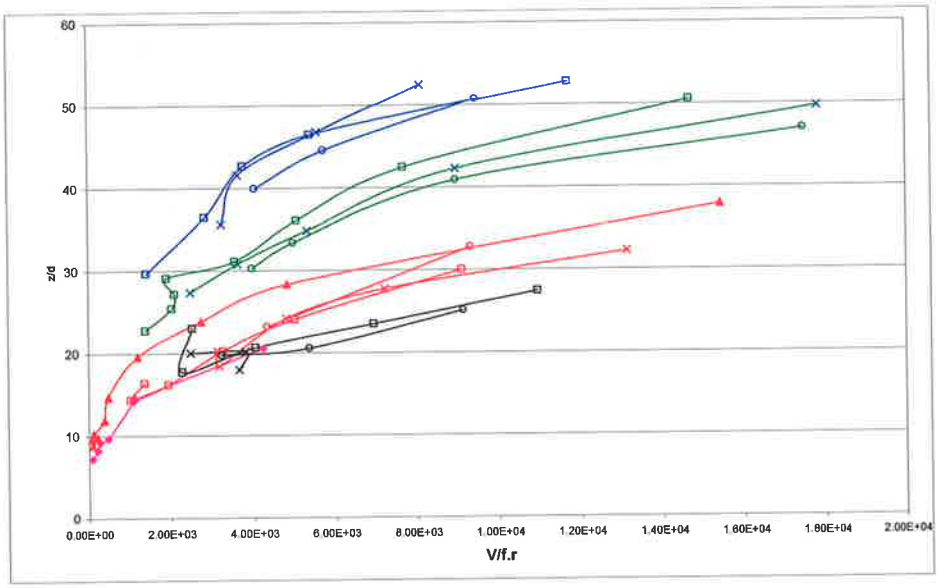

Figure 3.16(c) The axial position of the **Inner** vortex tube, **Second** structure

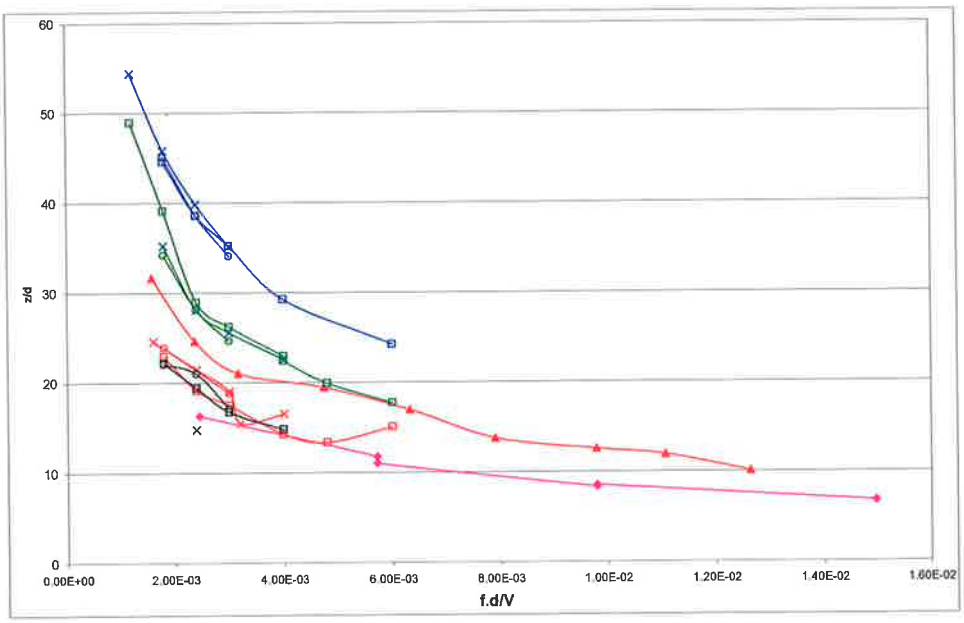

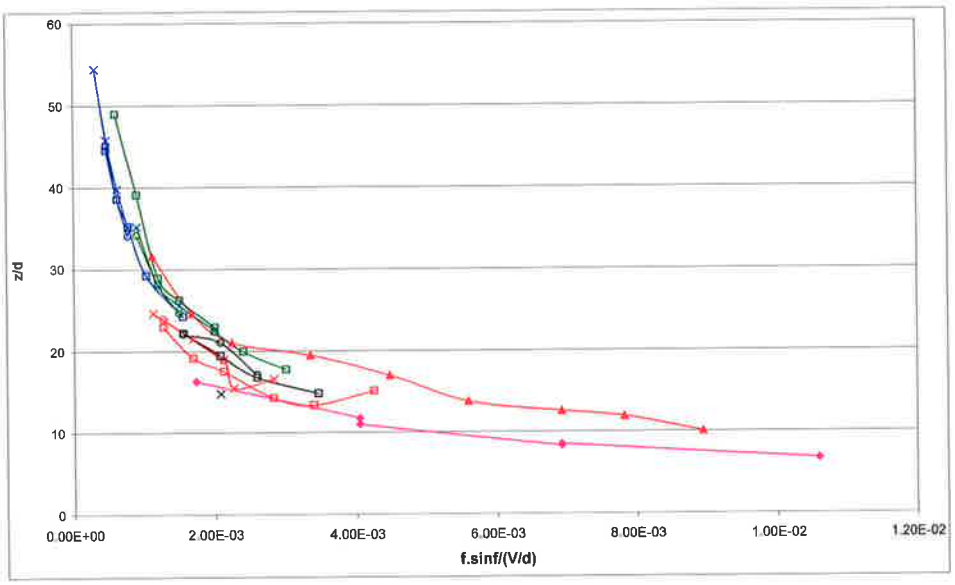

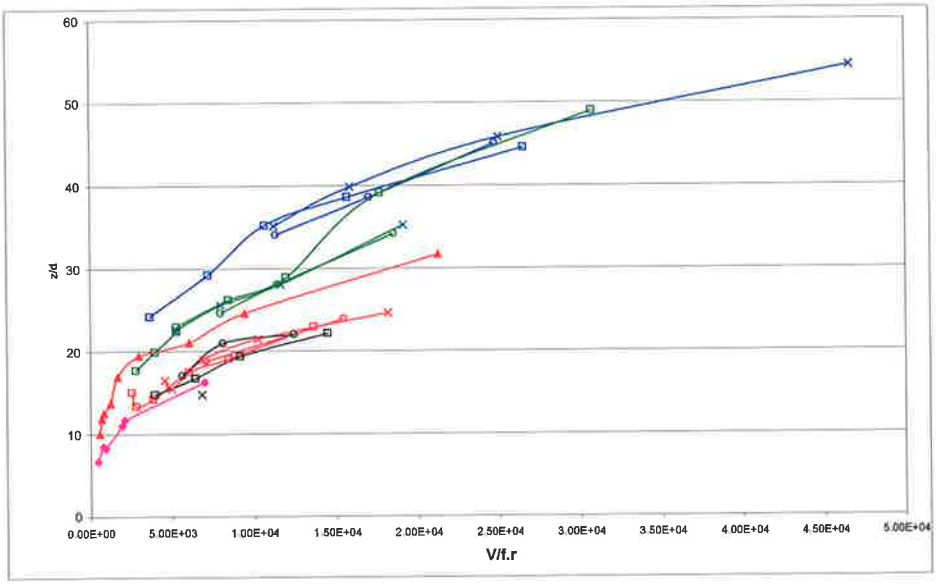

Figure 3.16(d) The axial position of the **Outer** vortex tube, **Second** structure

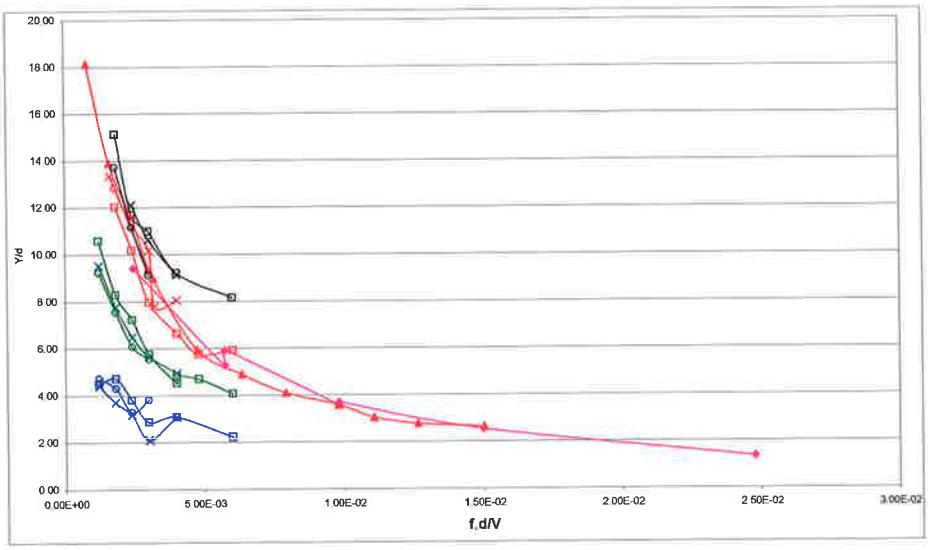

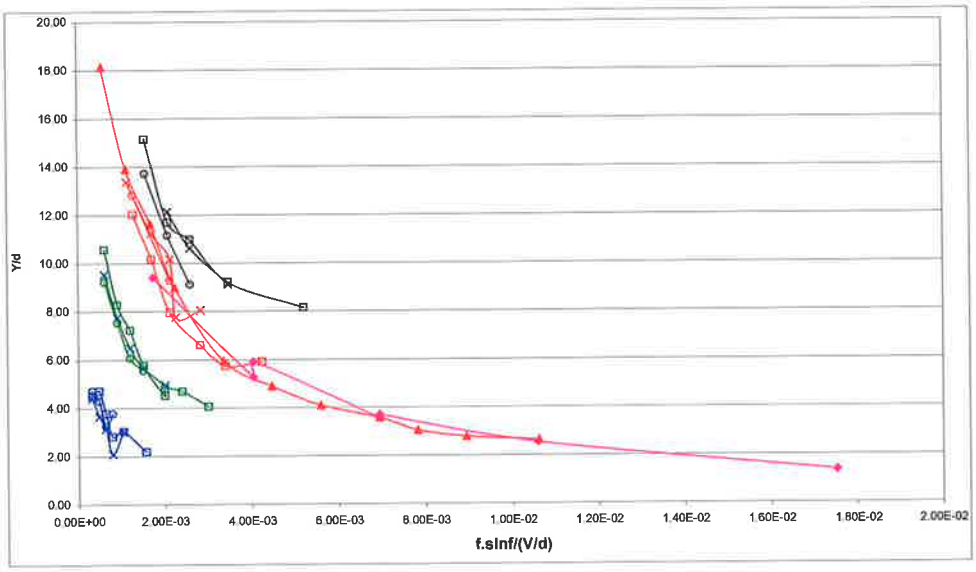

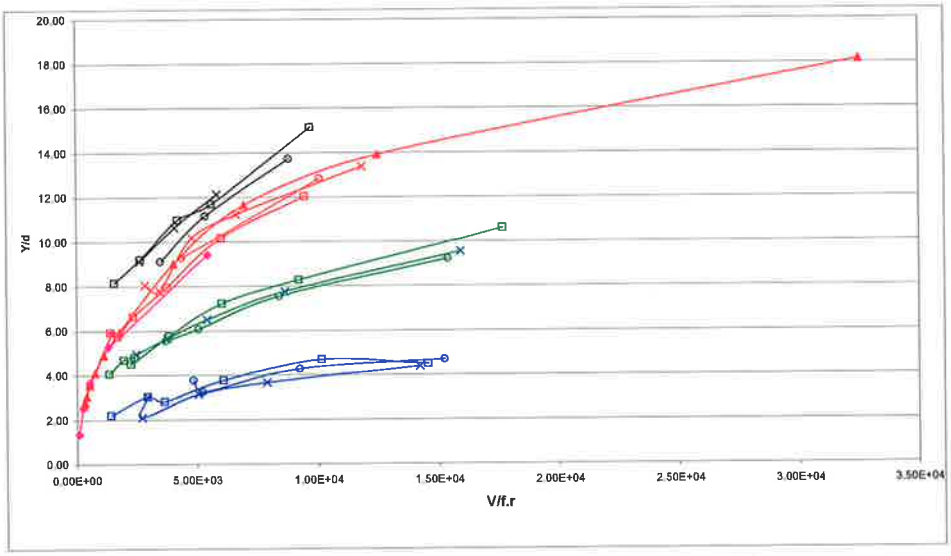

Figure 3.17(a) The radial position of the **Inner** vortex tube, **Structure #1**

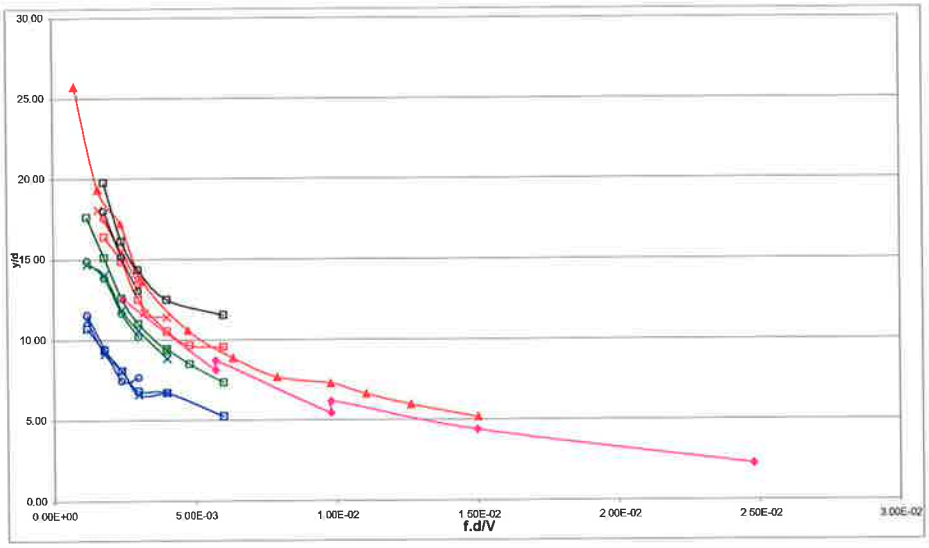

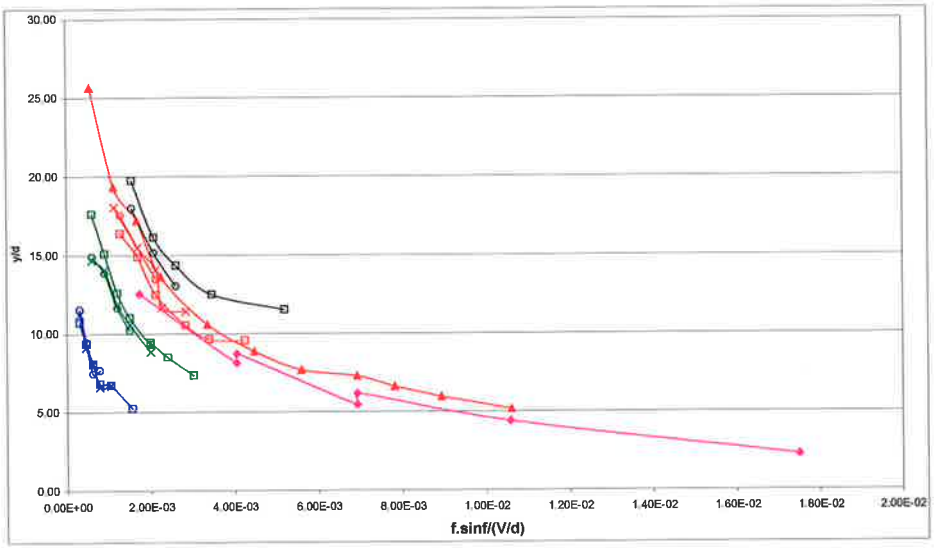

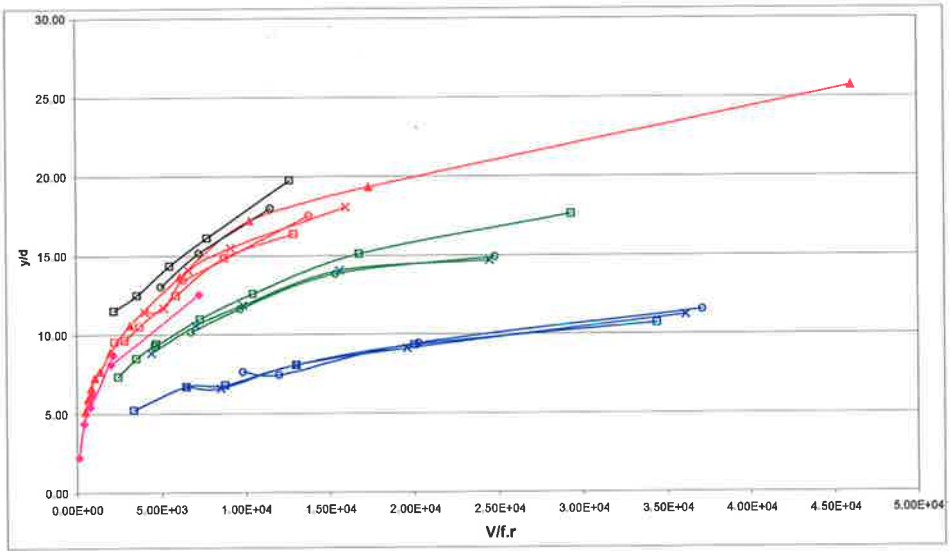

Figure 3.17(b) The radial position of the **Outer** vortex tube, **Structure #1**

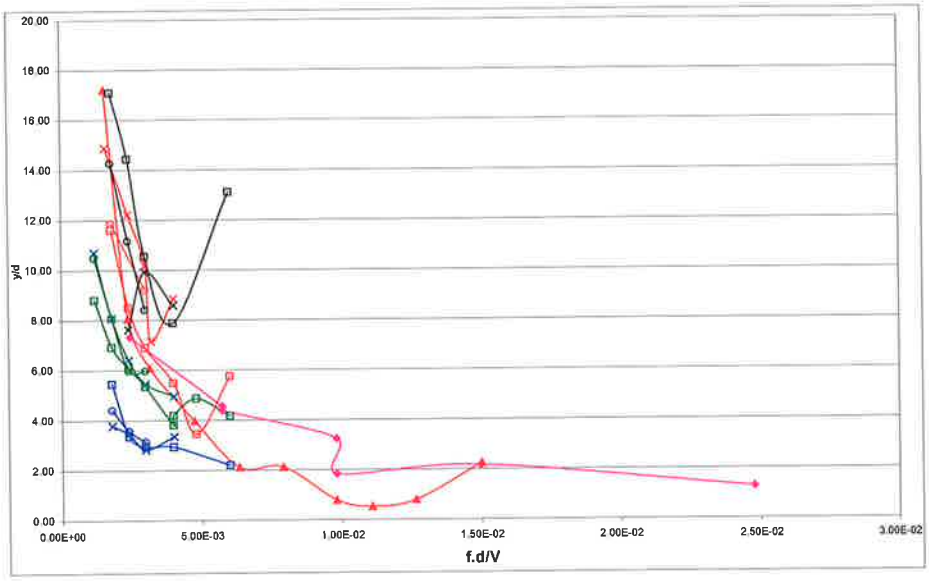

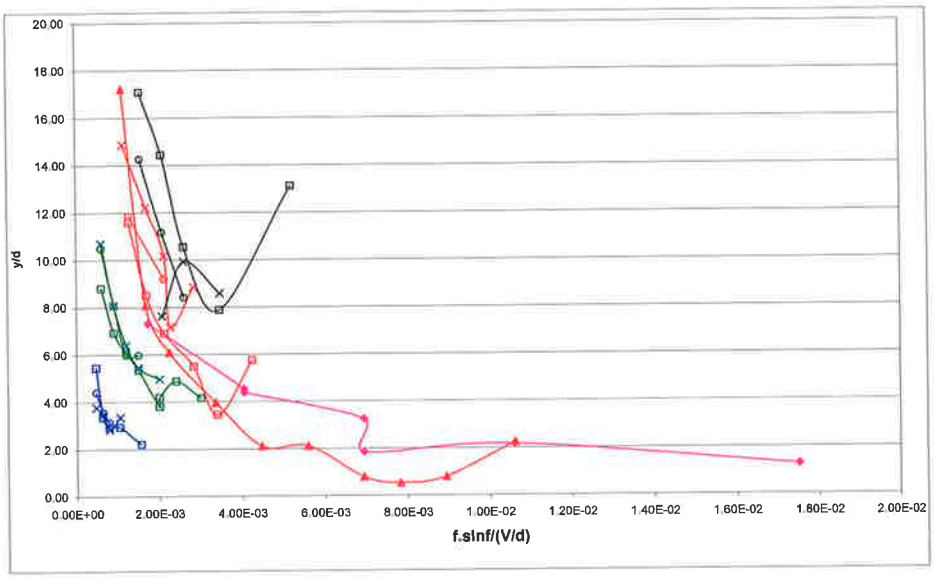

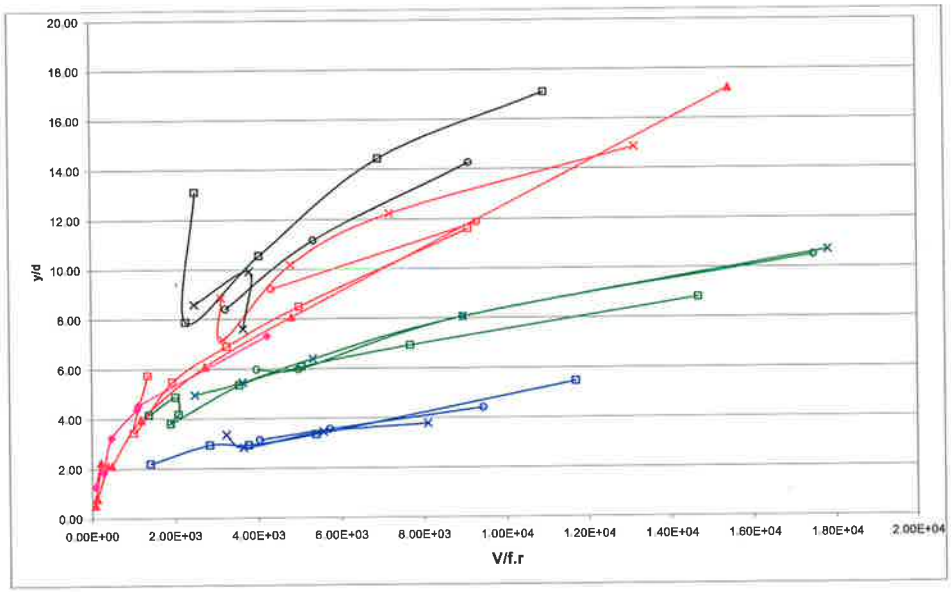

Figure 3.17(c) The radial position of the **Inner** vortex tube, **Structure #2**

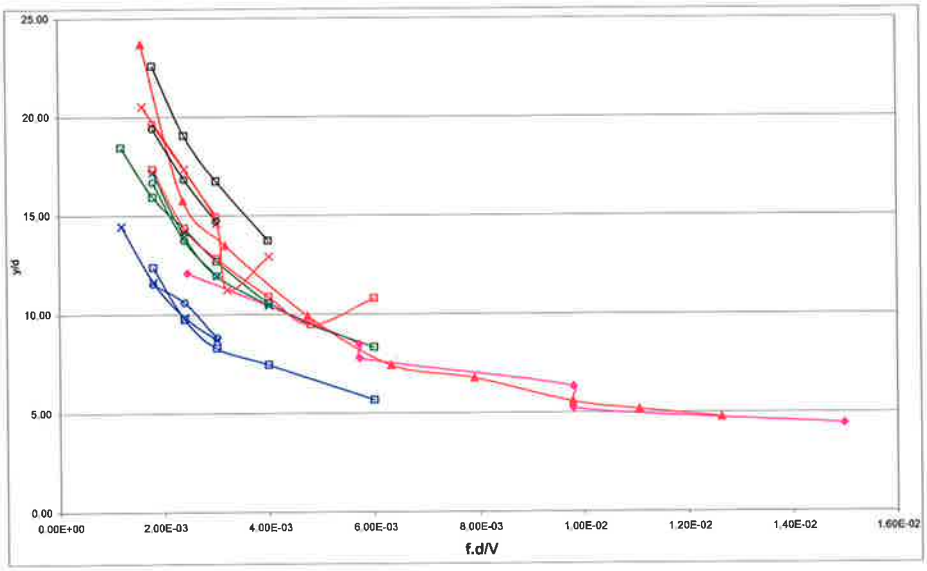

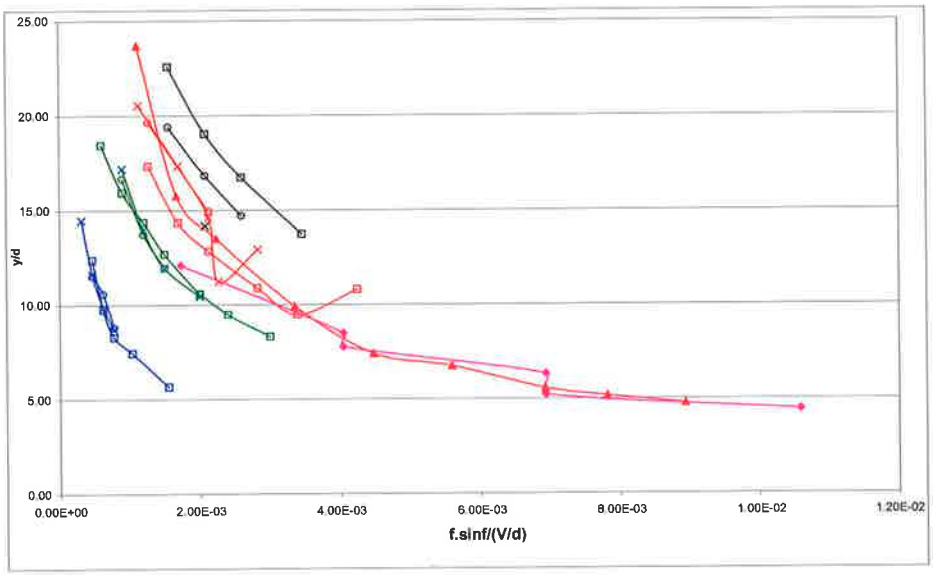

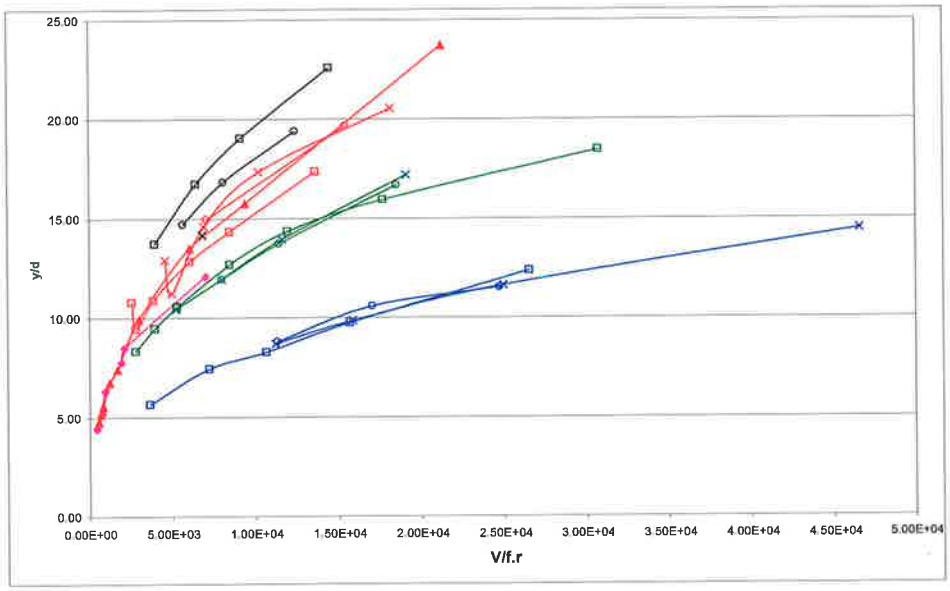

Figure 3.17(d) The radial position of the **Outer** vortex tube, **Structure #2**

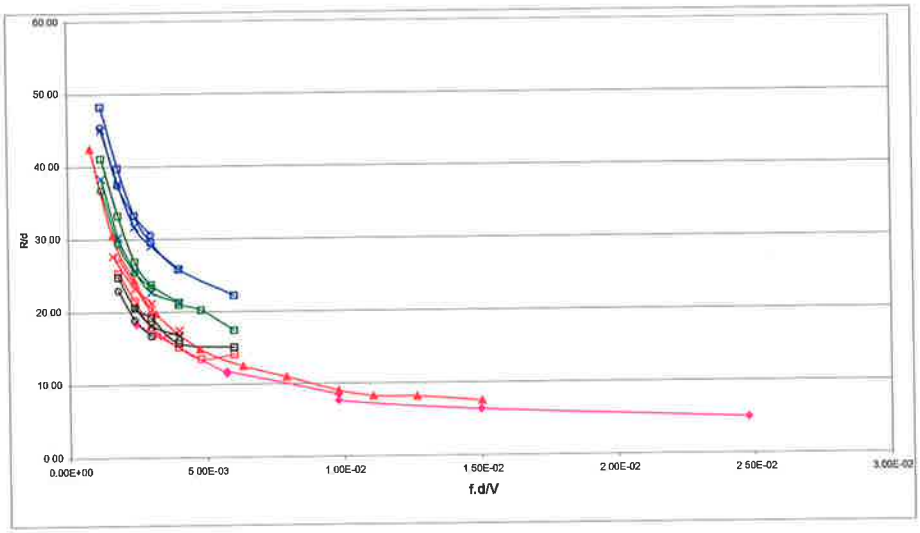

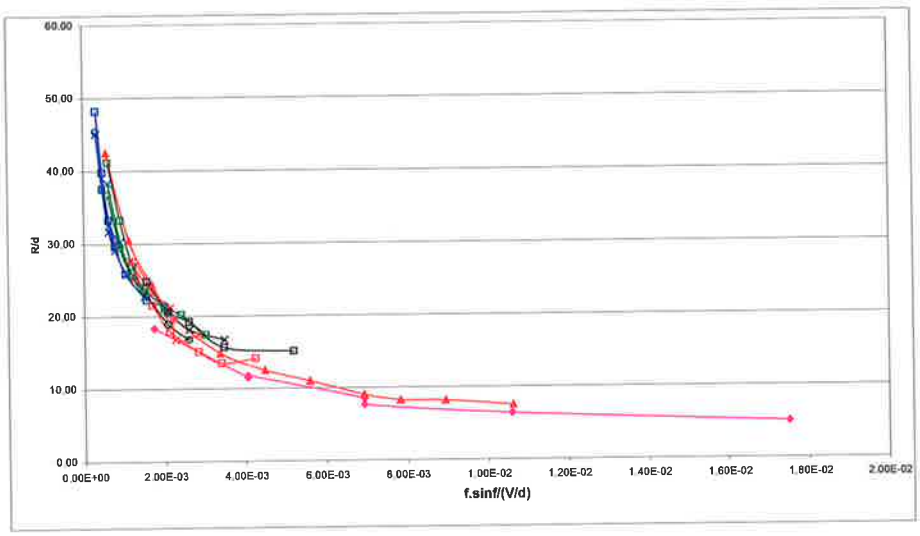

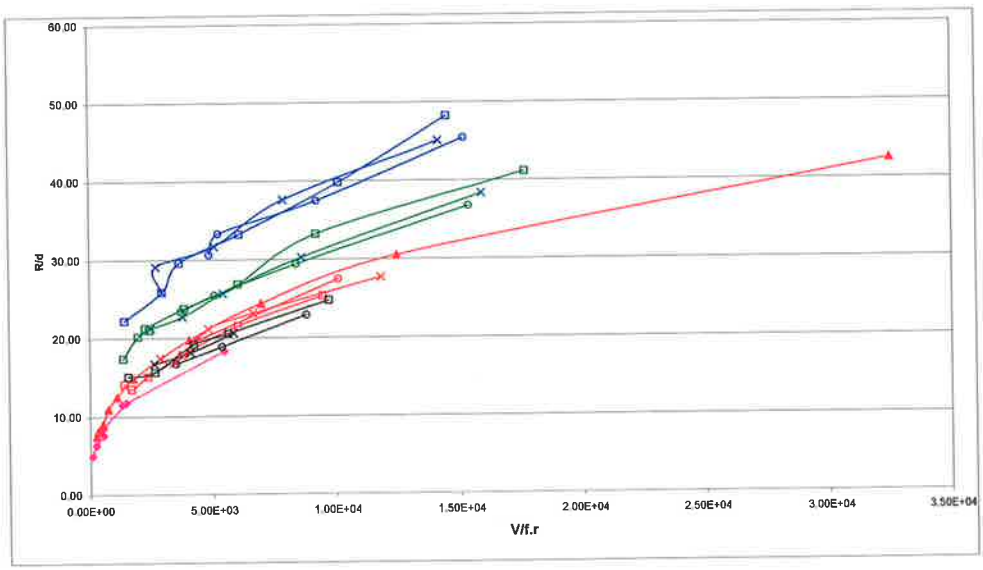

Figure 3.18(a) The radius (R) to the **Inner** vortex tube, **Structure #1**

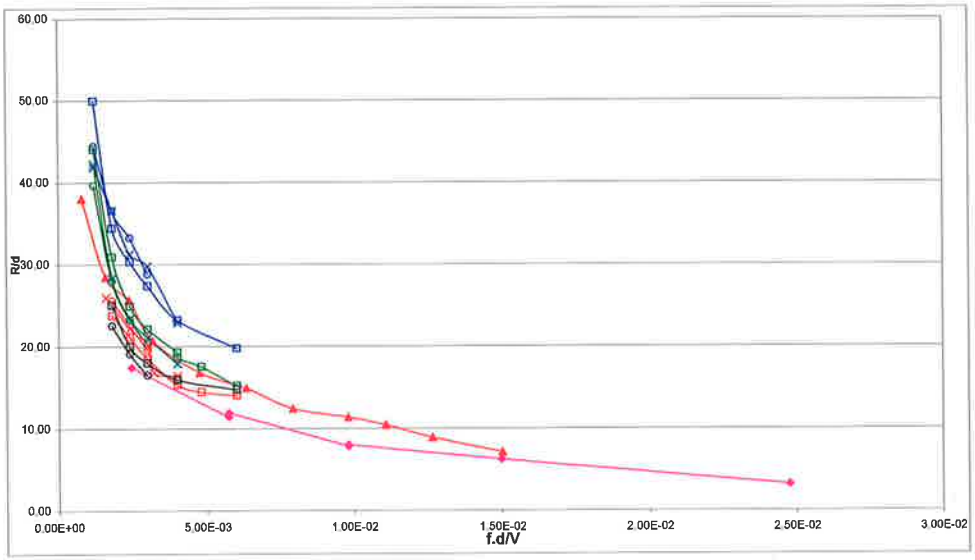

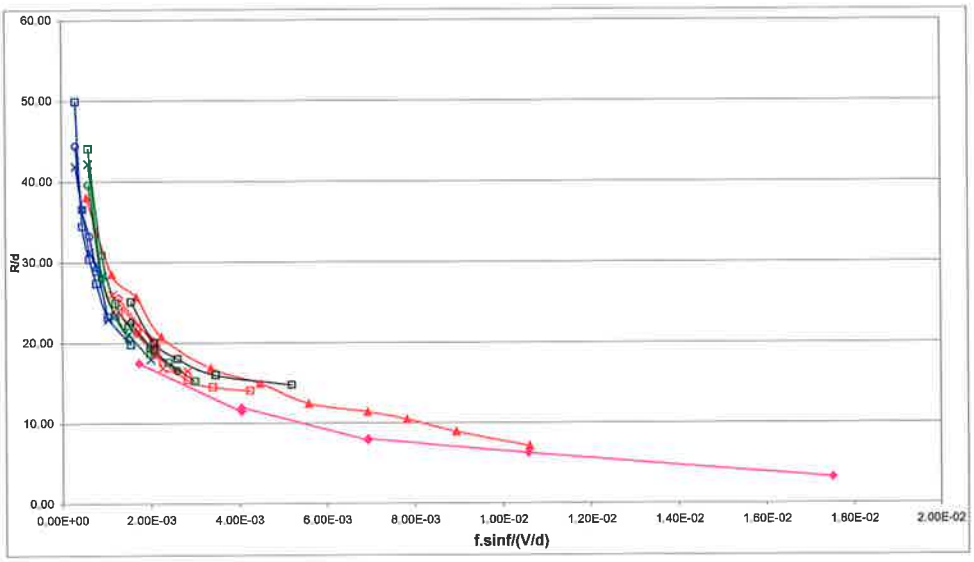

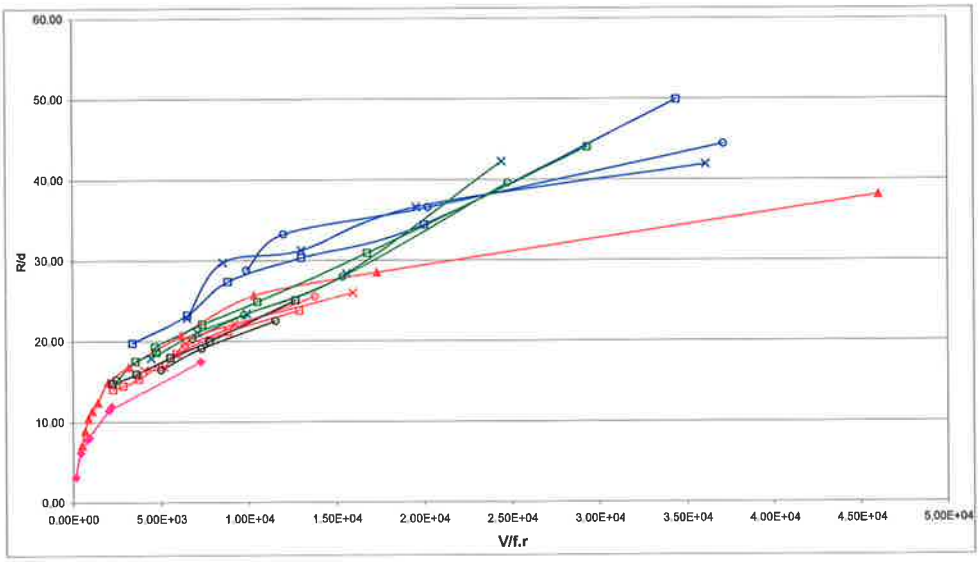

Figure 3.18(b) The radius (R) to the **Outer** vortex tube, **Structure #1**

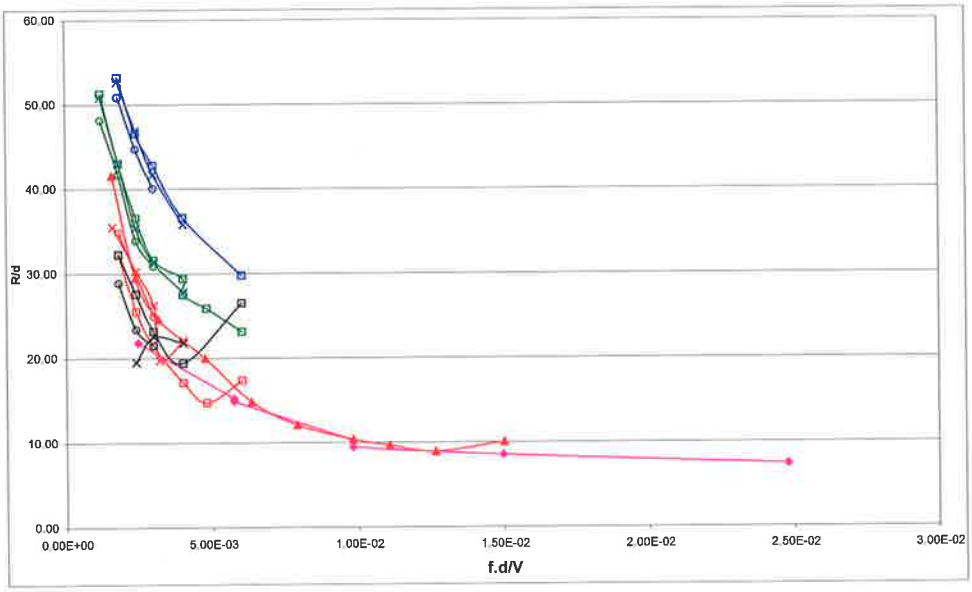

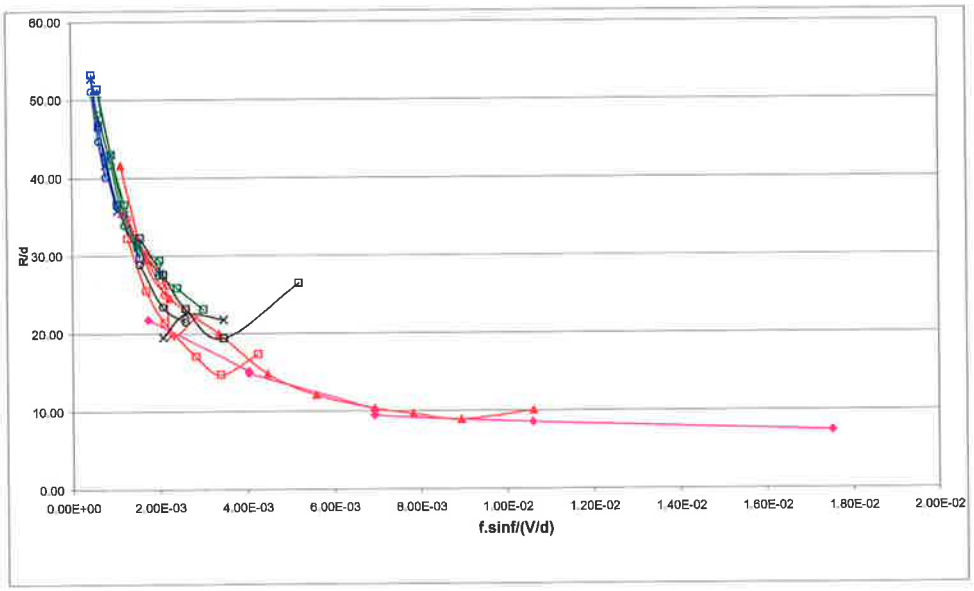

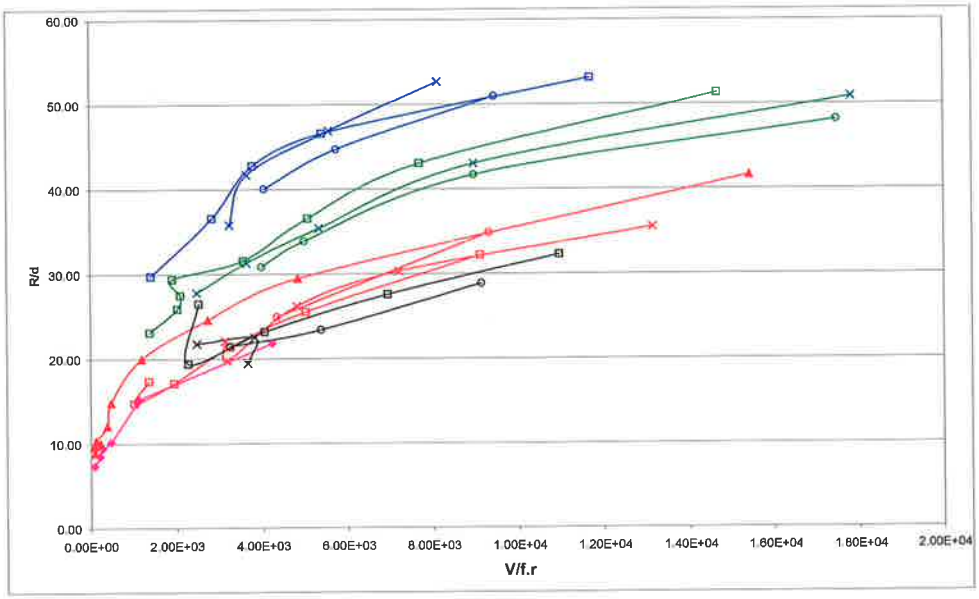

Figure 3.18(c) The radius (R) to the **Inner** vortex tube, **Structure #2**

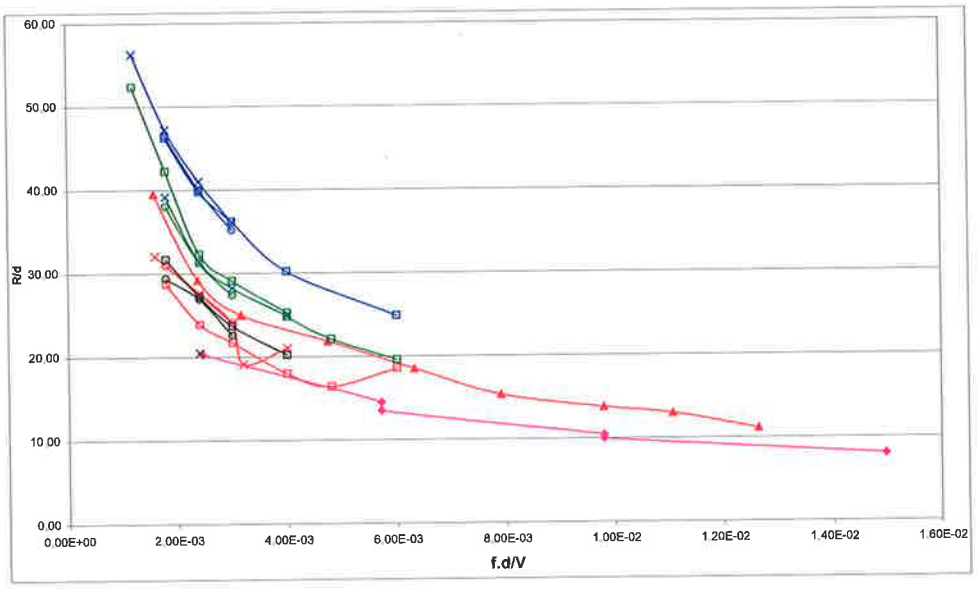

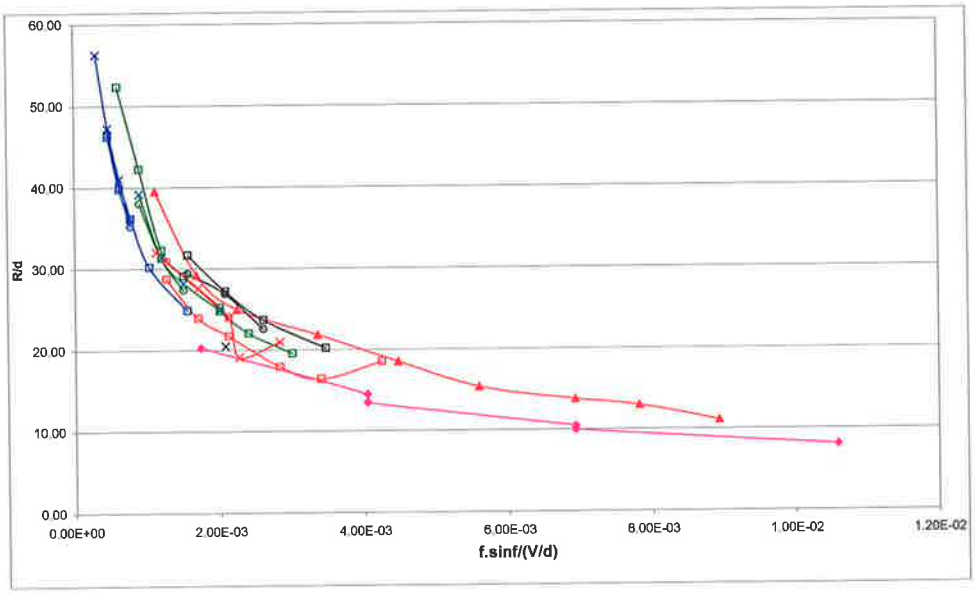

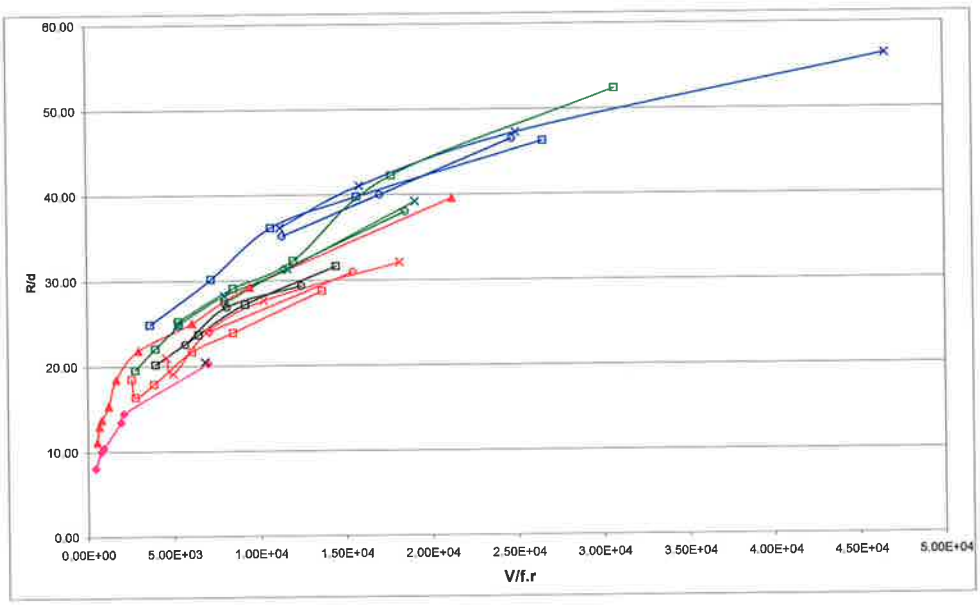

Figure 3.18(d) The radius (R) to the **Outer** vortex tube, **Structure #2**

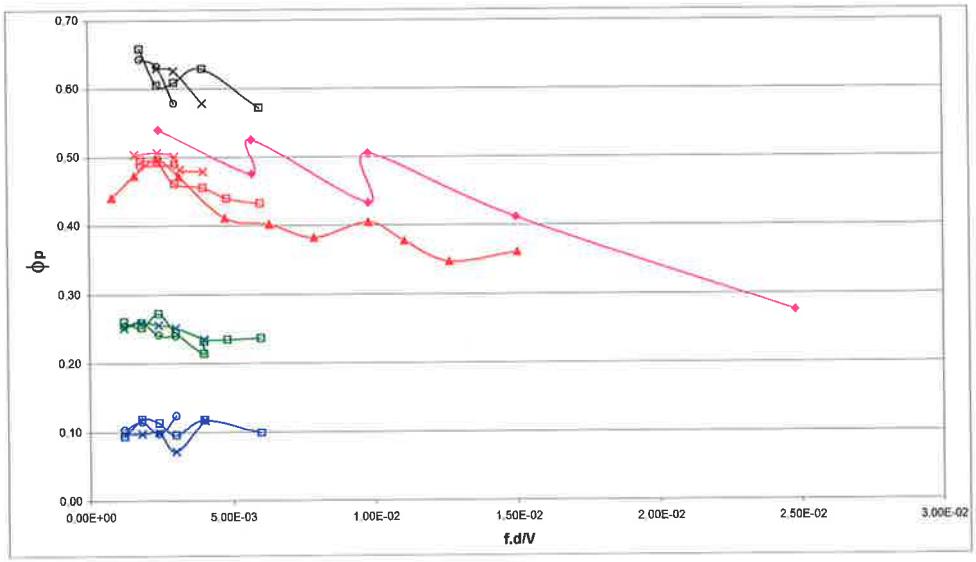

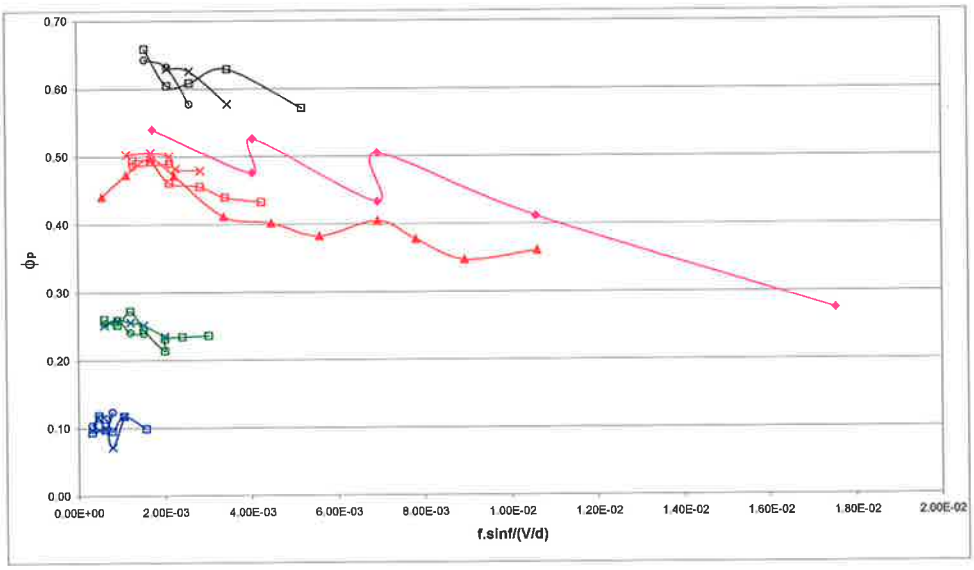

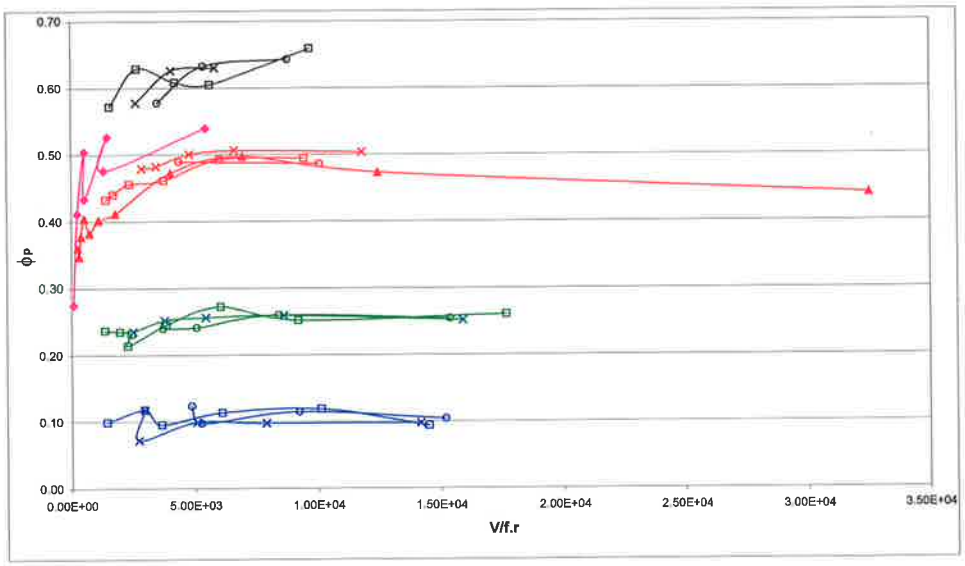

Figure 3.19(a) Measured angle (ϕ_p) to the **Inner** vortex tube, **Structure #1**

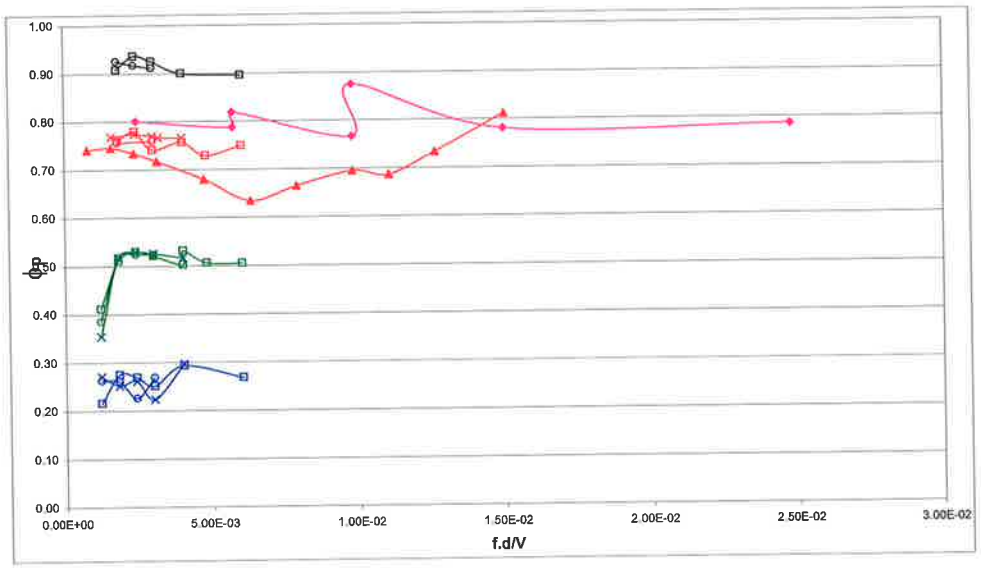

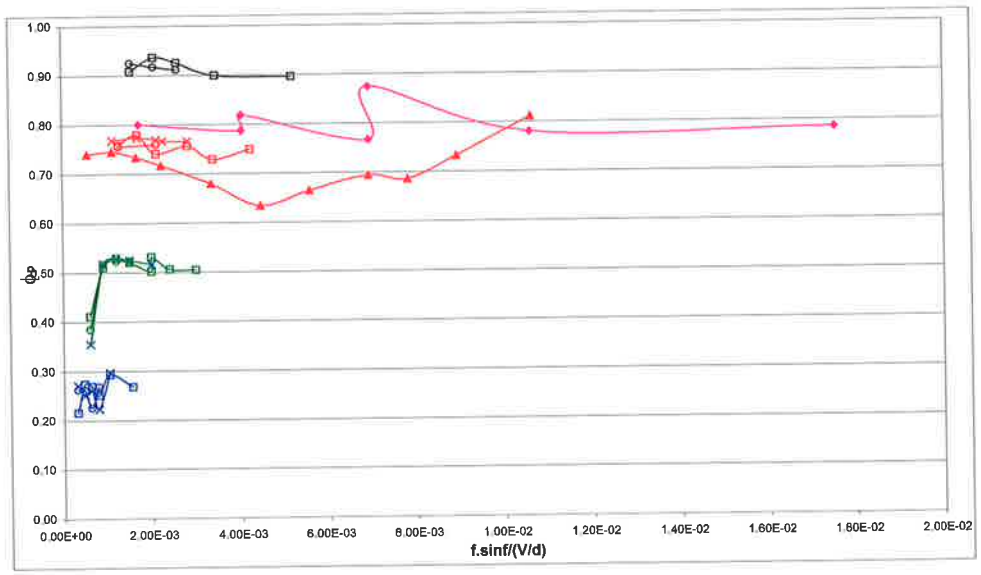

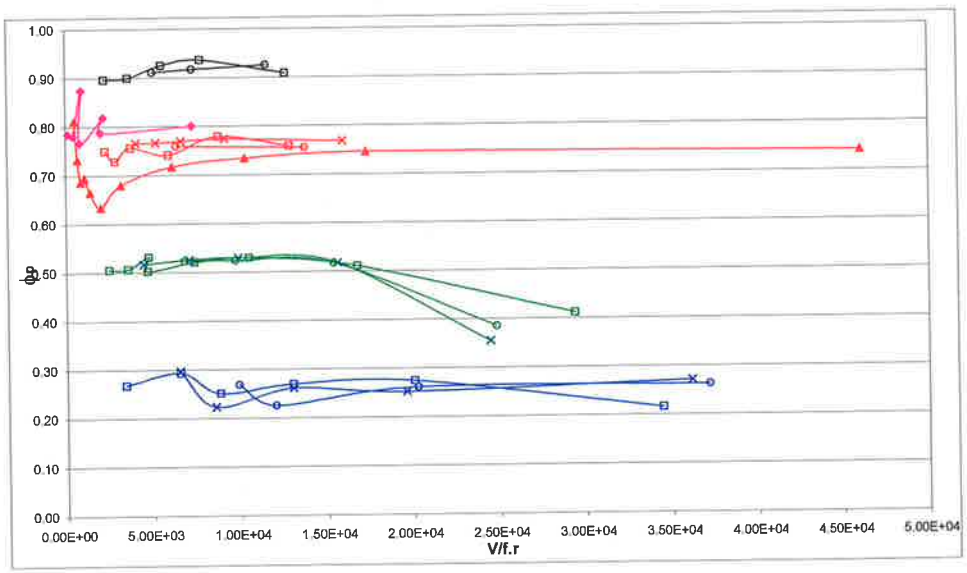

Figure 3.19(b) Measured angle (ϕ_p) to the **Outer** vortex tube, **Structure #1**

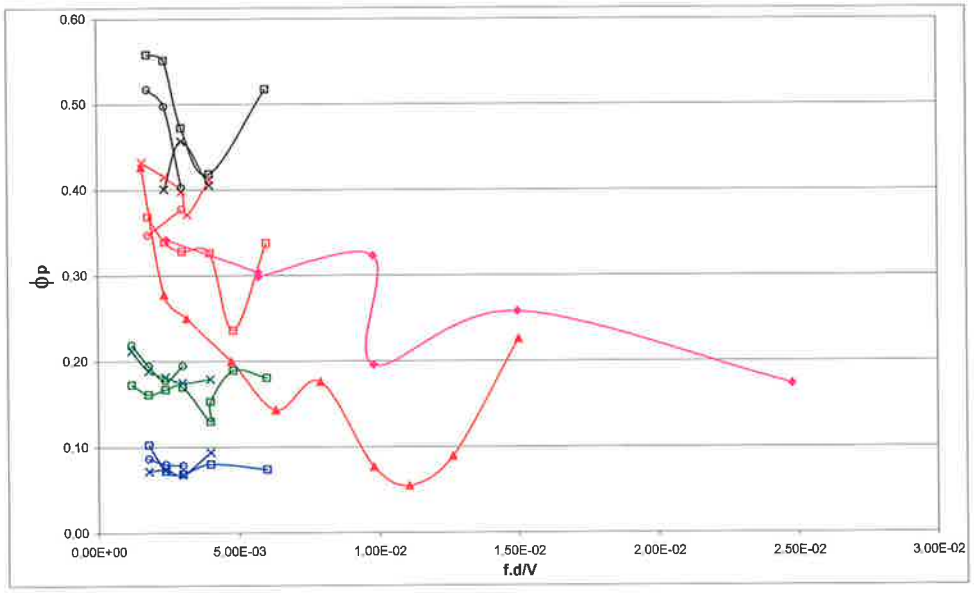

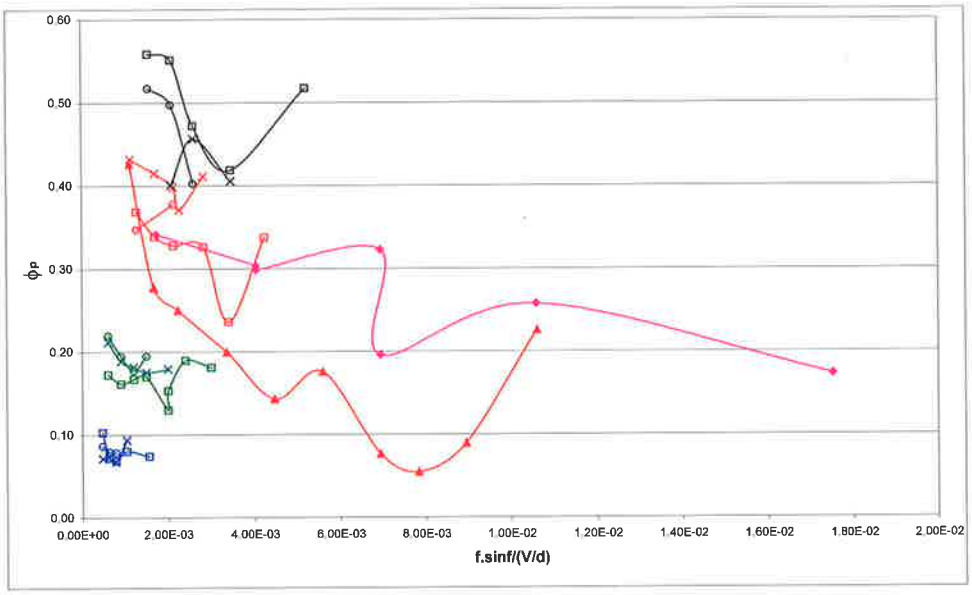

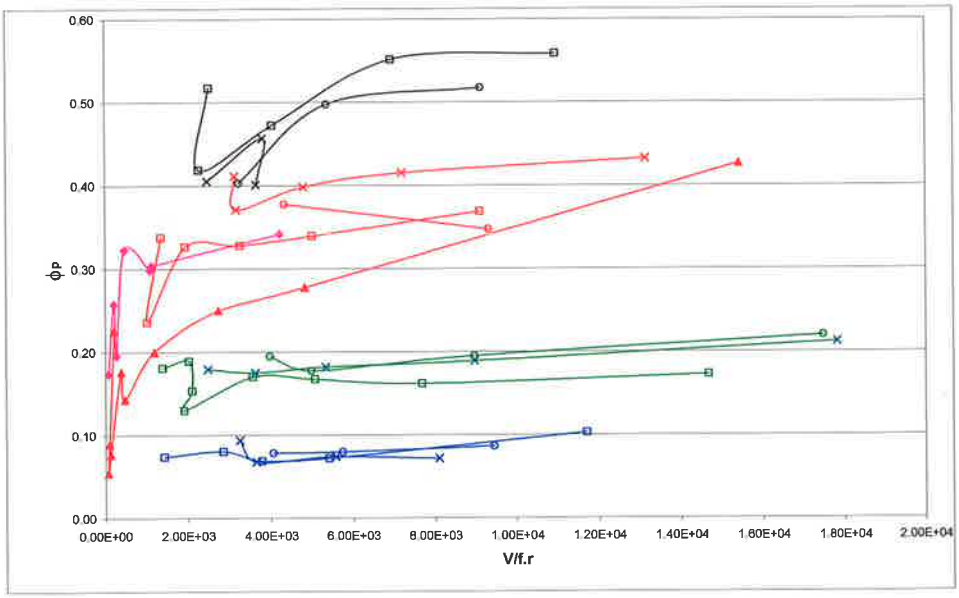

Figure 3.19(c) Measured angle (ϕ_p) to the **Inner** vortex tube, **Structure #2**

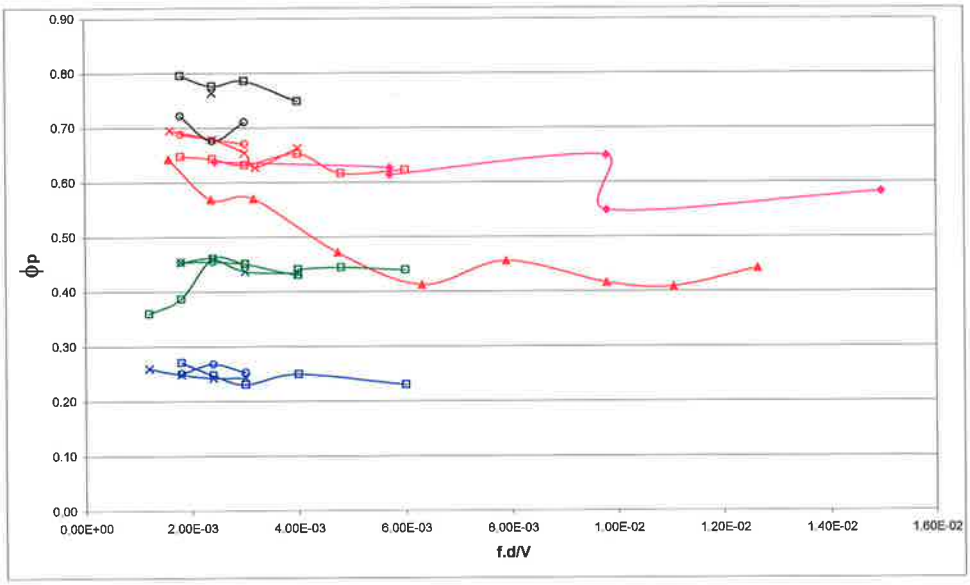

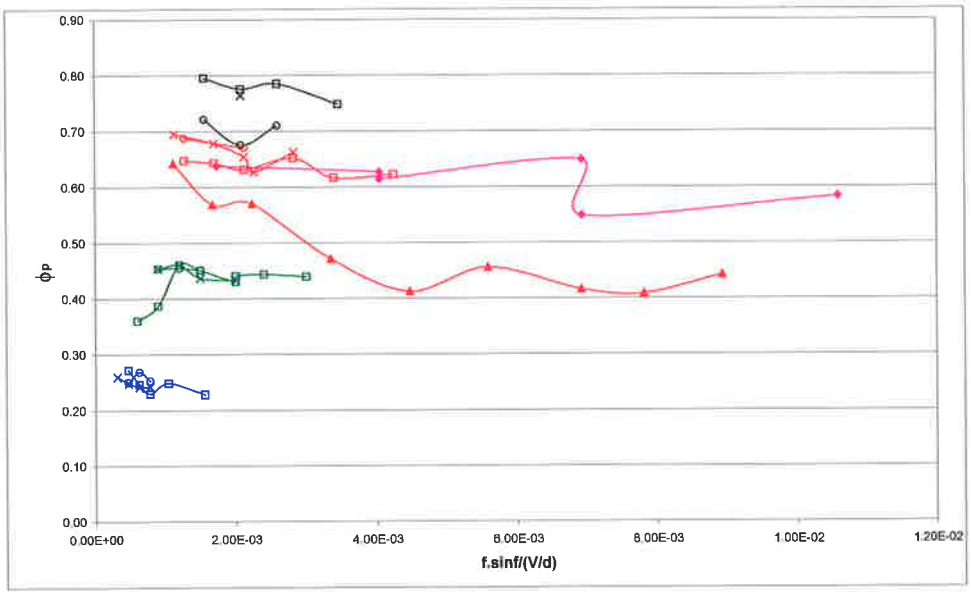

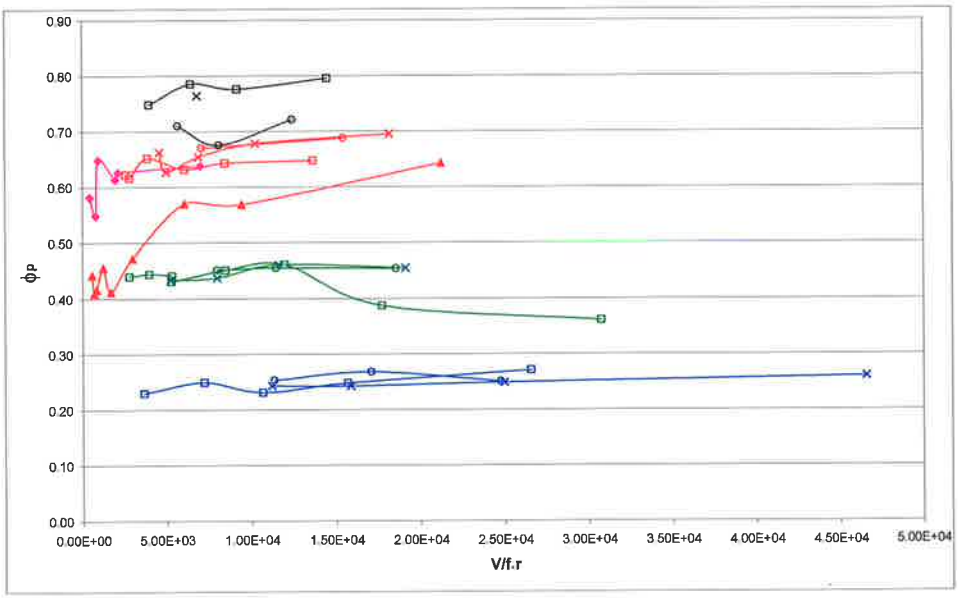

Figure 3.19(d) Measured angle (ϕ_p) to the **Outer** vortex tube, **Structure #2**

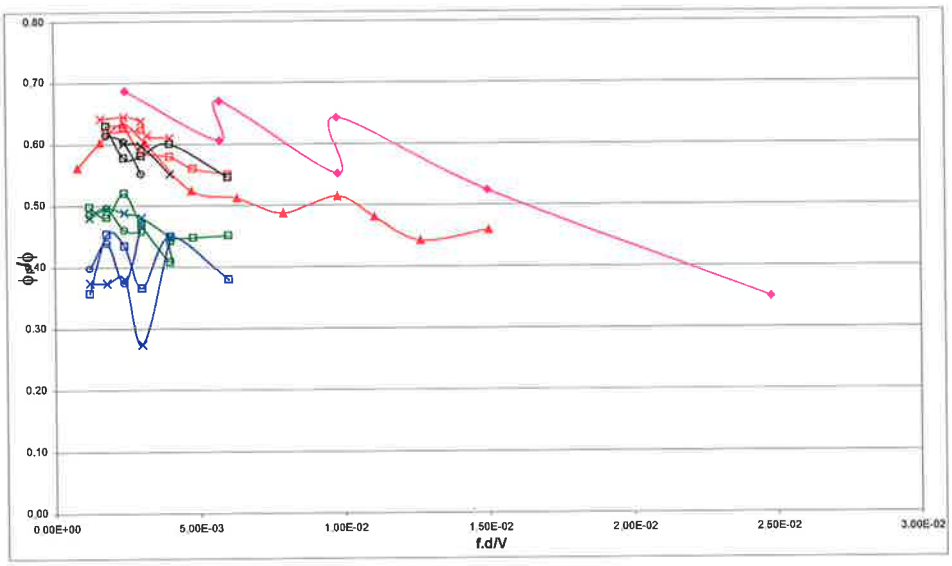

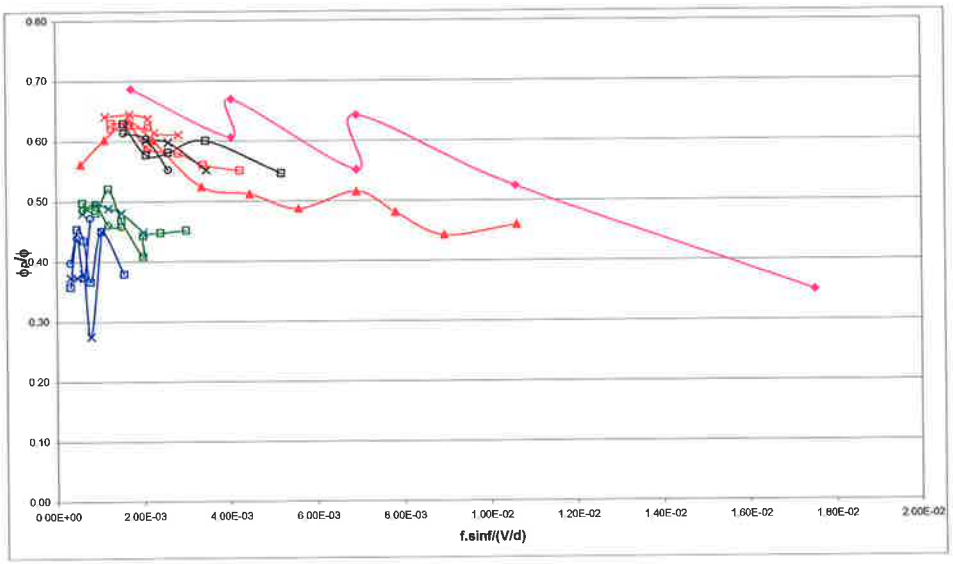

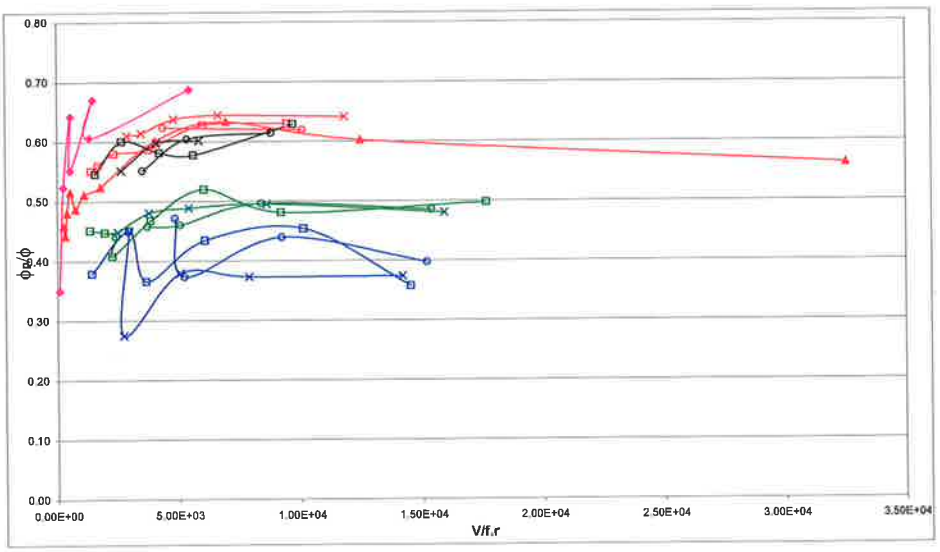

Figure 3.20(a) Normalized angle (ϕ_p/ϕ) to the **Inner** vortex tube, **Structure #1**

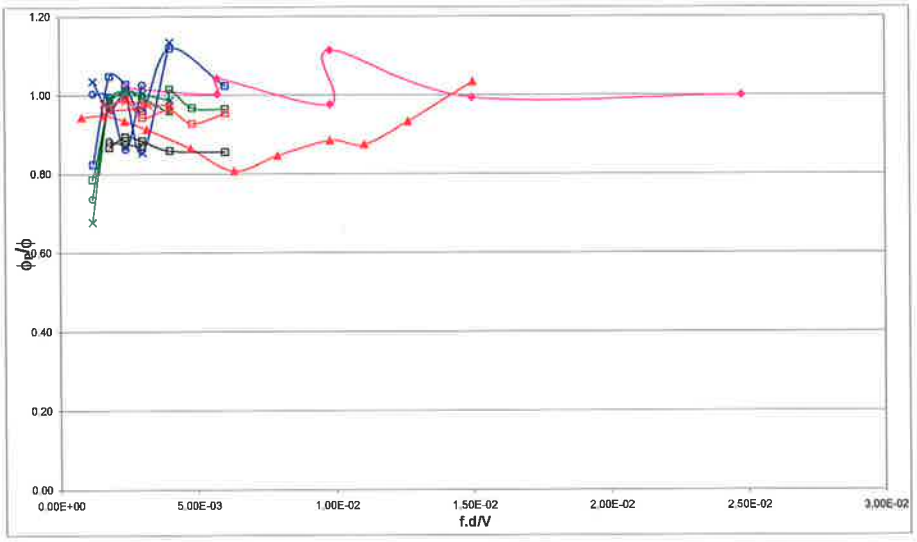

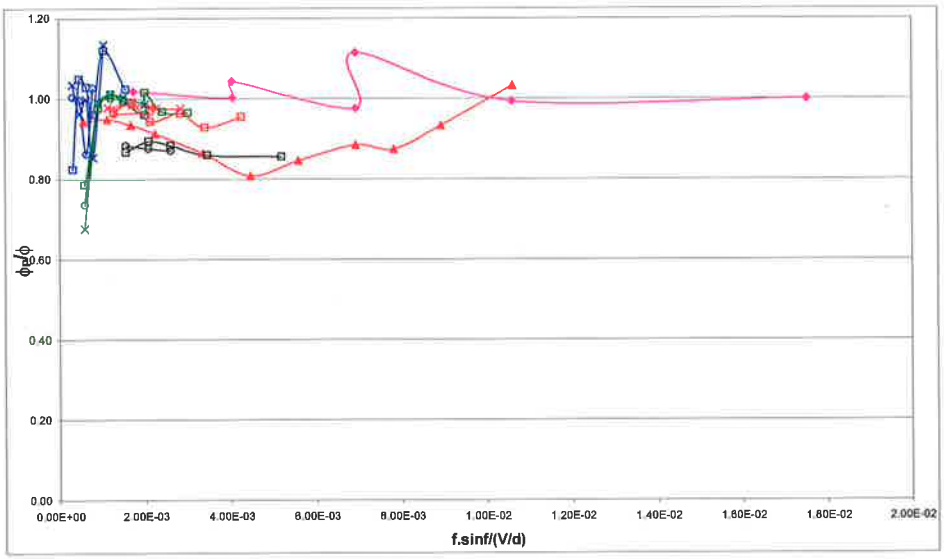

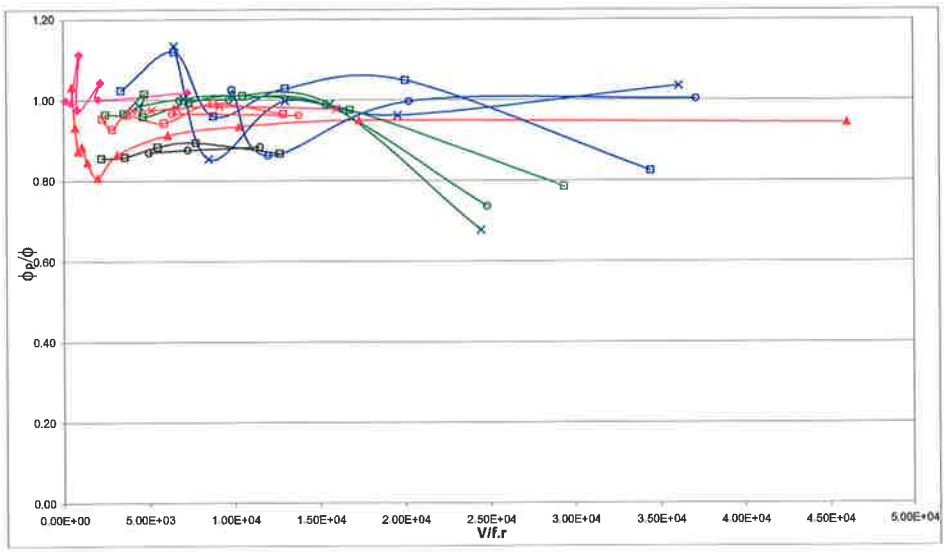

Figure 3.20(b) Measured angle (ϕ_p/ϕ) to the **Outer** vortex tube, **Structure #1**

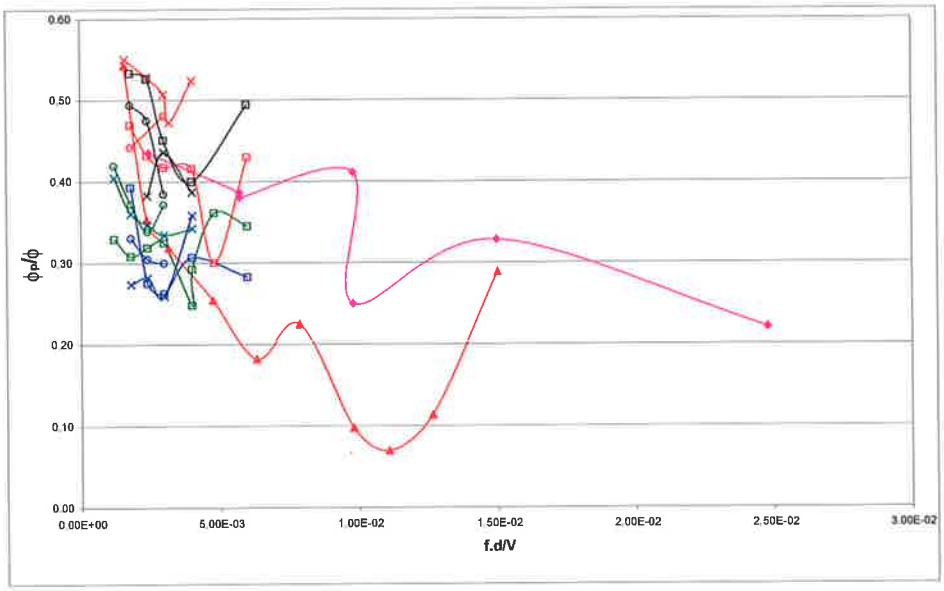

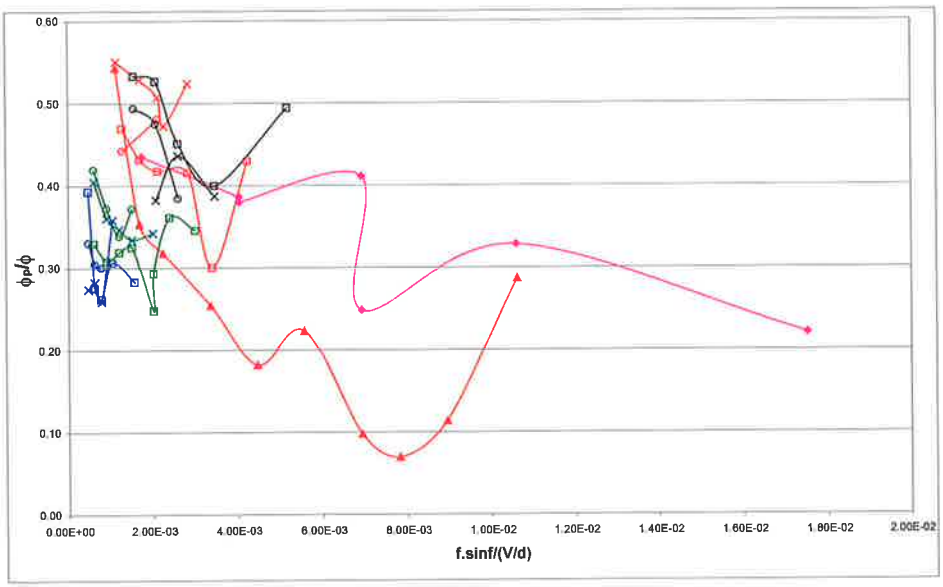

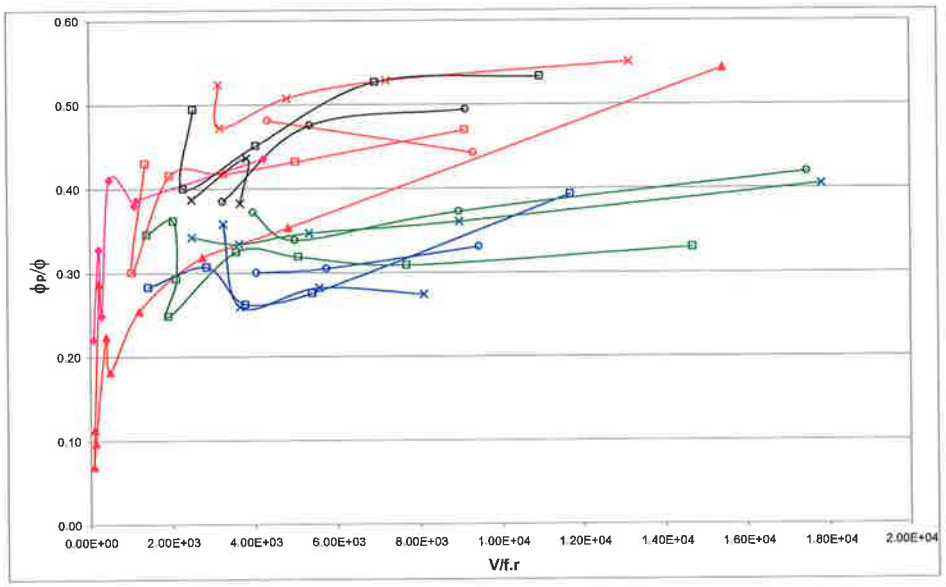

Figure 3.20(c) Measured angle (ϕ_p/ϕ) to the **Inner** vortex tube, **Structure #2**

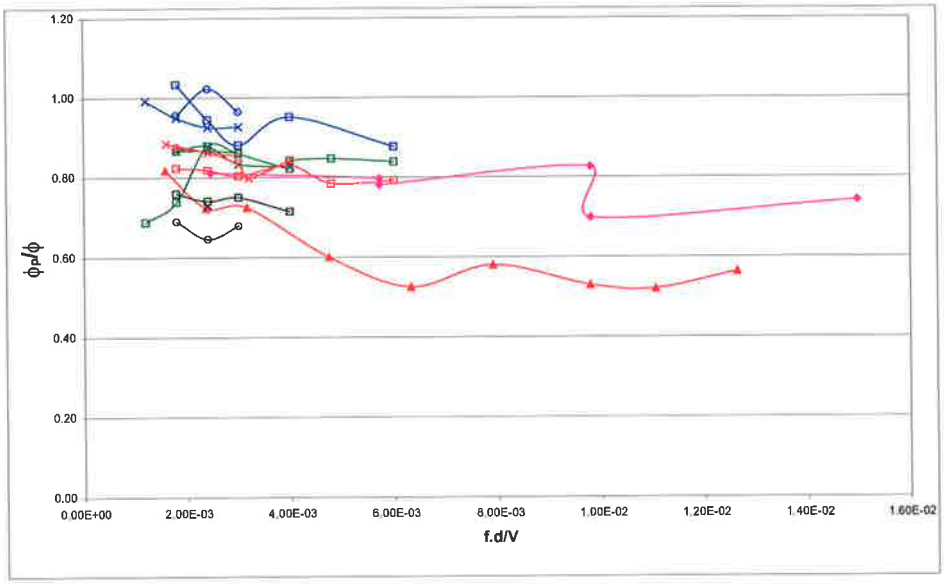

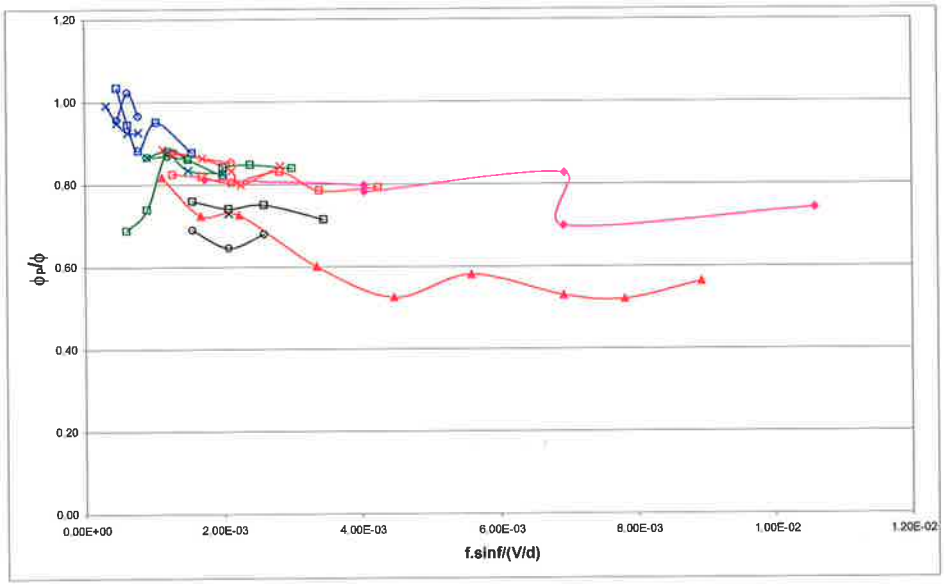

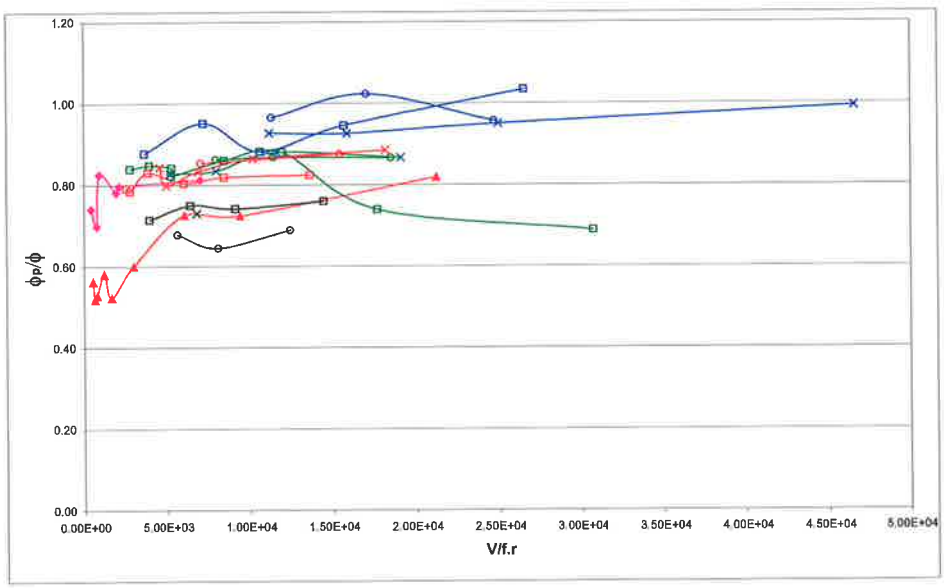

Figure 3.20(d) Measured angle (ϕ_p/ϕ) to the **Outer** vortex tube, **Structure #2**

3.6.3 Effect of precession on concentration within the helix

Quantitative measurement of the mean concentration at the core of the vortex tubes has been made and results are presented in Figures 3.21(a) to 3.21(d). The layout and the dimensionless variables are in the same format as for the previous section. In general it can be seen that the dimensionless strain rate parameter provides the best collapse of the data. However, in all of the normalizations there are two lines onto which the data collapses. The data for the conditions, Re = 3,800, d = 3 mm, $\phi = 45°$ and Re = 24,500, d = 10 mm, $\phi = 45°$ collapse on a line of different gradient to all other sets of data. The reason for this is, as yet, unknown, but suggests that there may be different "modes" in the helix possibly due to interactions between the vortex tubes.

A basic trend is clearly evident for all of the plots presented. For increasing values of precessional frequency the concentration within Structures #1 and #2 of the helix increases. While it is apparent that increased strain will result in increased entrainment, and hence dilution, it also results in a much tighter helix so that the position of the transition region moves upstream and the helix starts entraining itself closer to the nozzle exit. For low values of precessional frequency the mean concentration within the vortex tubes approaches a constant value, as seen in the plot of the modified Strouhal number.

A trend which has also been noted in section 3.2 is clearly evident here, that is the concentration within the inner vortex tube is measurably higher than for the outer vortex tube, consistent with the greater observed size of the outer vortex tube. This indicates that mixing is slower for the fluid within the inner vortex tube. For increasing values of deflection angle, the concentration within the vortex tubes at the same phase in the helix also increases. A length scale based on the exit diameter, collapses the data for the inner vortex tube, while a

length scale based on the width of the mixing region collapses well the data for the outer vortex tube.

3.6.4 Summary

Increasing the precessional frequency tightens the helix, reducing its maximum diameter toward a constant value and reducing the axial position at which this diameter is established (the pitch of the helix). The concentration within the vortex tubes increases, suggesting that mixing is slower, suppressed by the precession within the helix.

The dimensionless Strouhal number as defined and used by previous investigators is useful in collapsing data. However, the dimensionless strain rate, which accounts for the increased strain added to the jet by different values of the deflection angle is seen to give significantly better collapse. The length scale used in both of these dimensionless numbers, the exit diameter of the jet is observed to be the appropriate length scale of this initial near field region of the flow.

The length scale used in the modified Strouhal number is seen to have little influence on collapsing the data. The only notable exception to this is for the collapse of the mean concentration within the vortex tubes.

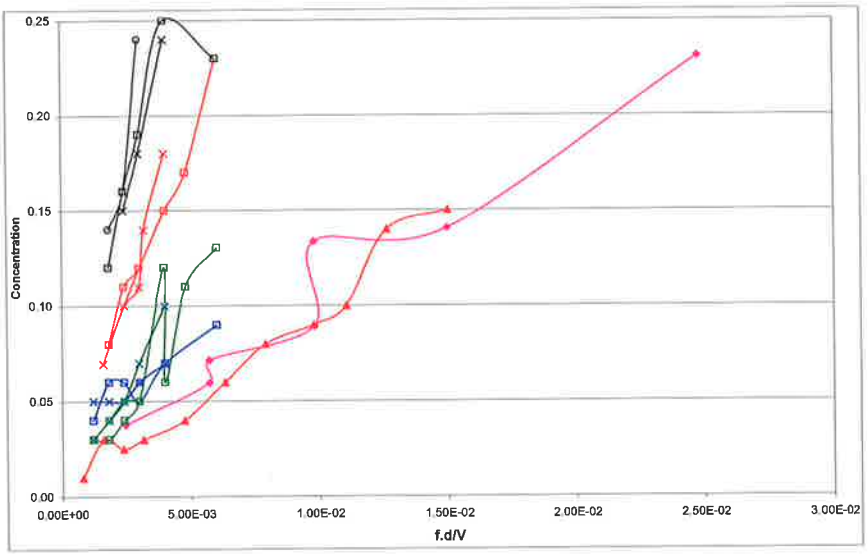

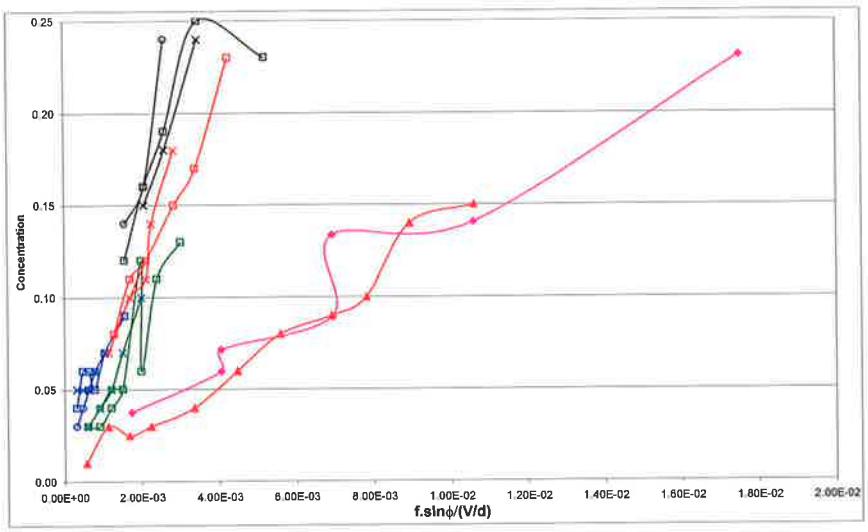

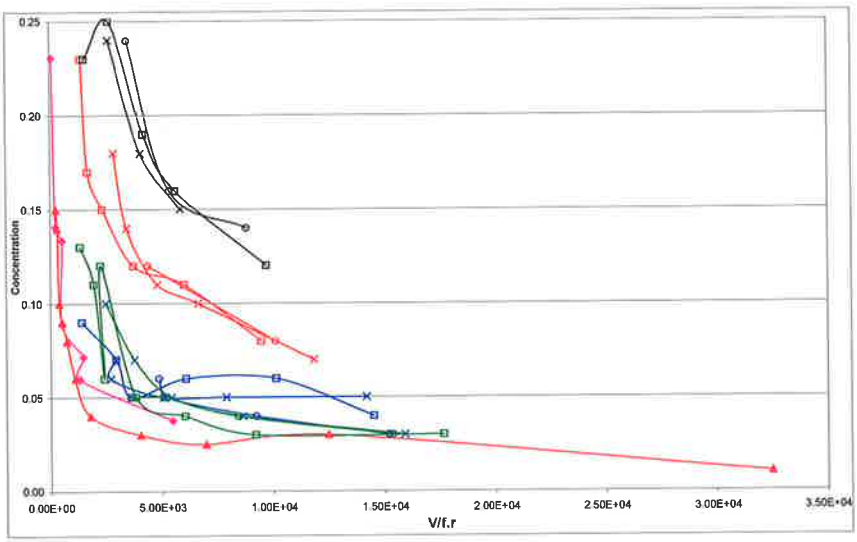

Figure 3.21(a) Concentration $\overline{C}/C_0$ of the selected point in the **Inner** vortex tube, **Structure #1**

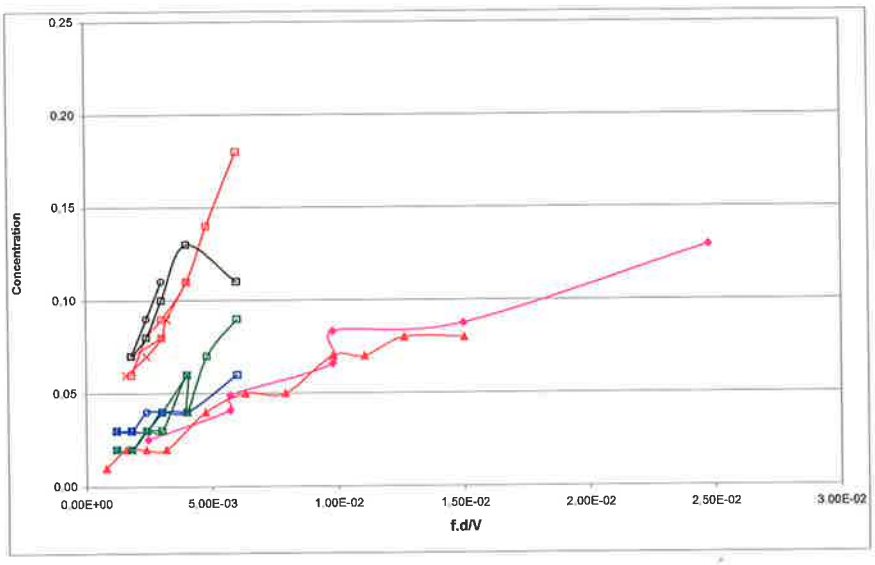

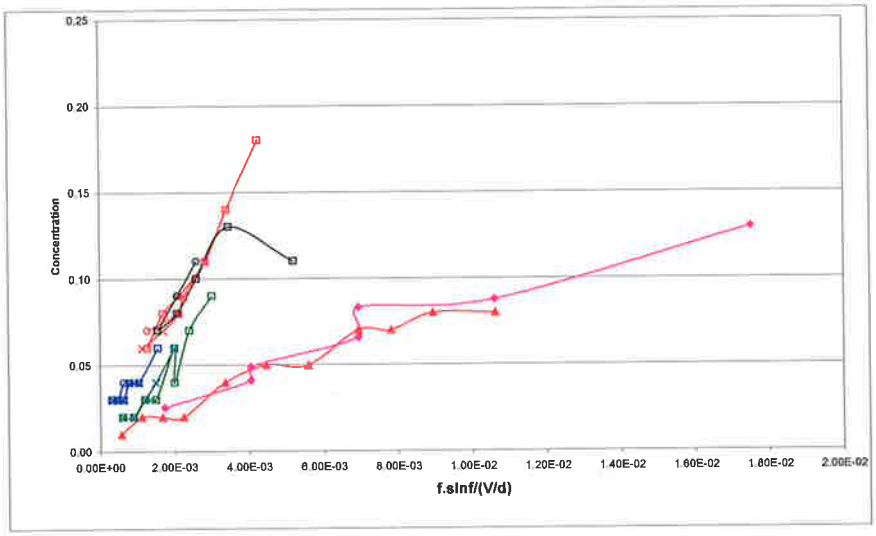

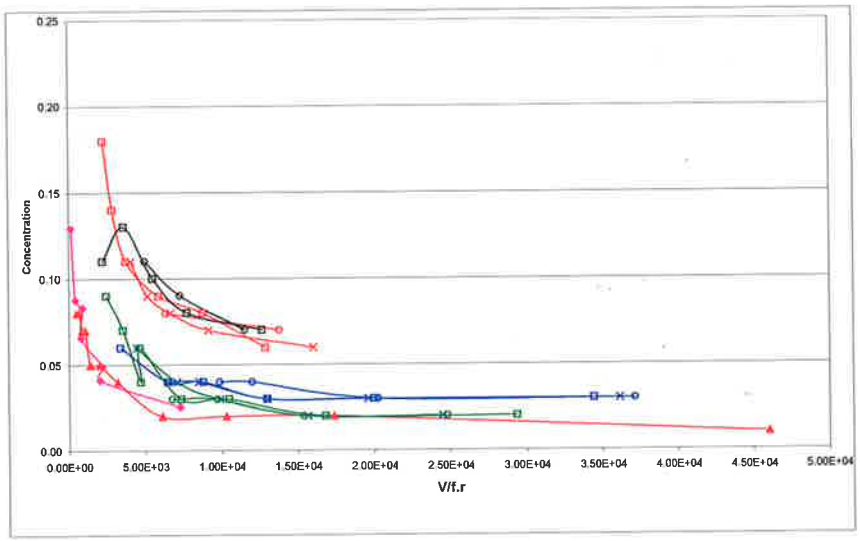

Figure 3.21(b) Concentration $\bar{C}/C_0$ of the selected point in the **Outer** vortex tube, **Structure #1**

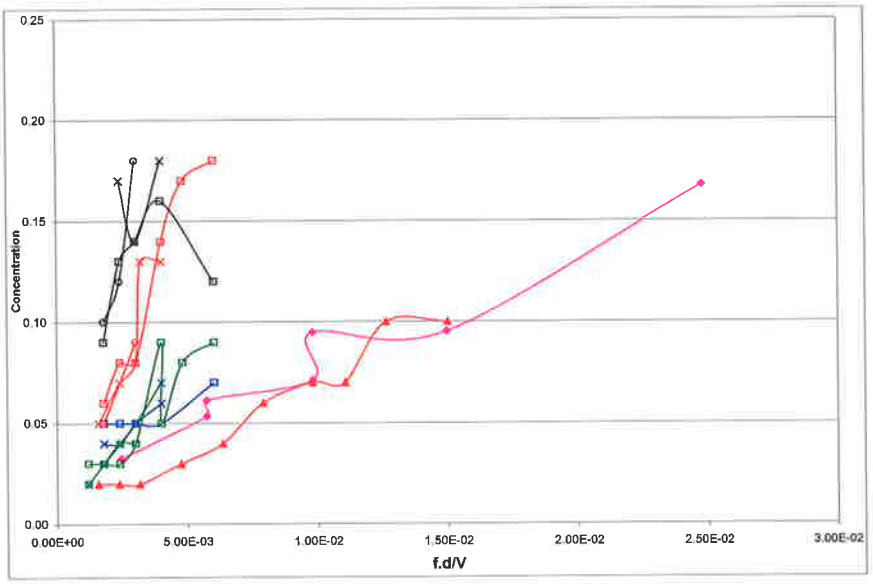

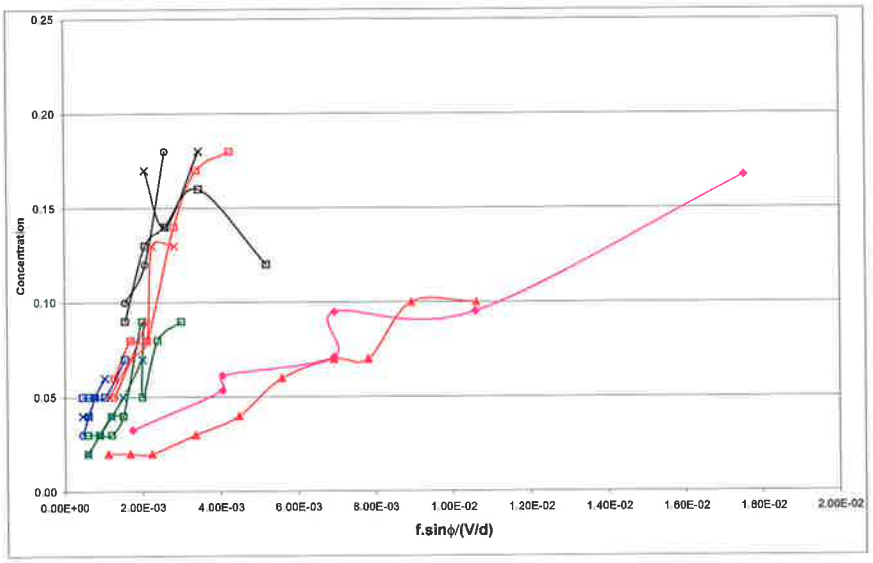

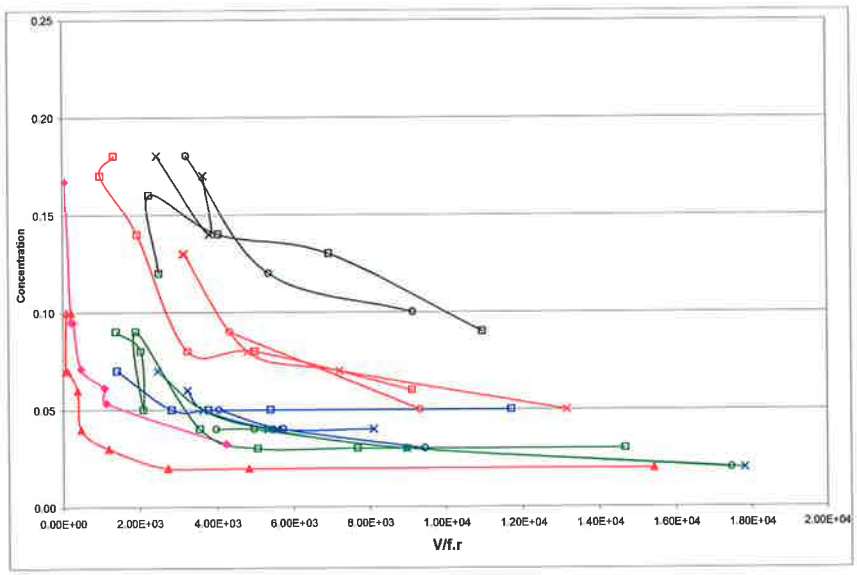

Figure 3.21(c) Concentration $\overline{C}/C_0$ of the selected point in the **Inner** vortex tube, **Structure #2**

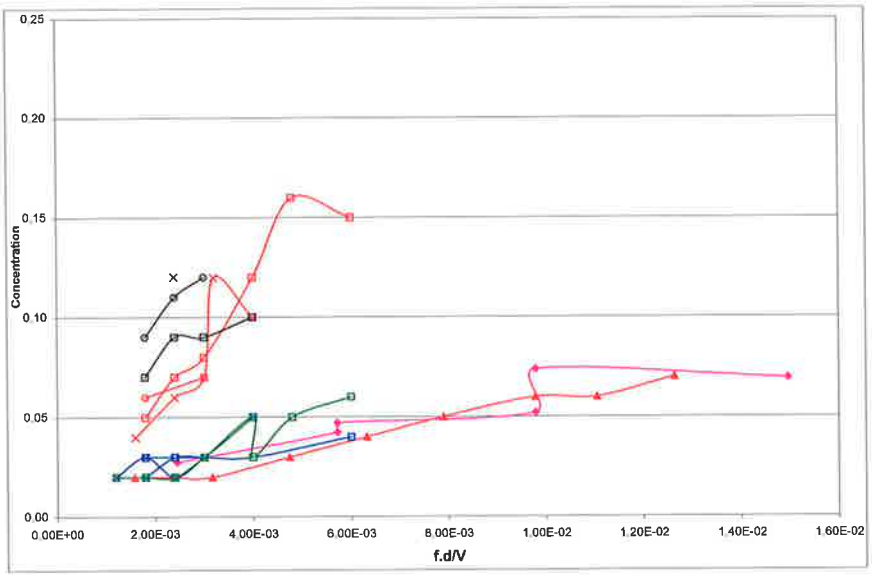

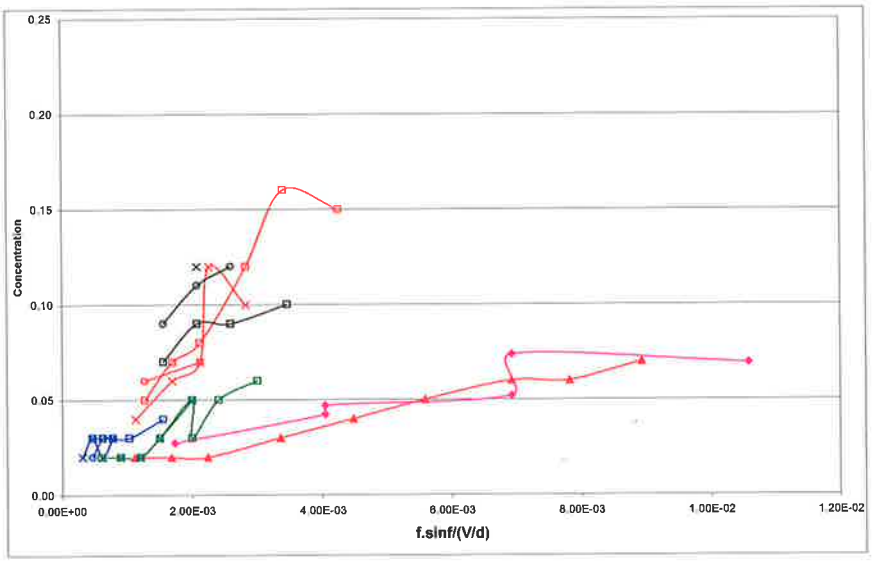

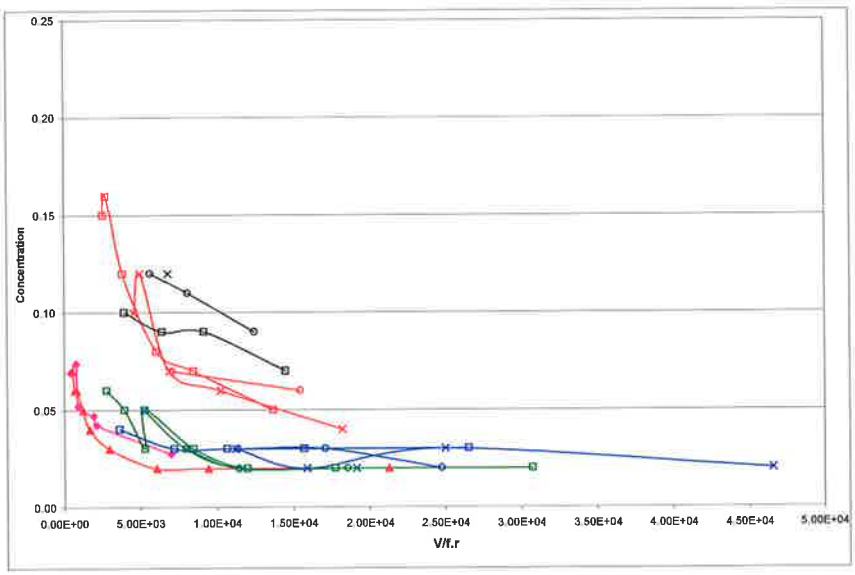

Figure 3.21(d) Concentration $\overline{C}/C_0$ of the selected point in the **Outer** vortex tube, **Structure #2**

3.7 CONCLUSIONS

The work presented in this chapter demonstrates that the footprint of the flow emerging from an MPJ nozzle has the shape of a helix and that this helix collapses upon itself in a manner that can be described by a limit cycle. Critical features of the initial helix region are:

1. That it can be characterized by the rate of additional strain introduced by precession related to the strain rate of a non- precessing jet, $f.\sin\phi / (V_o/d)$
2. That precession acts to generate a pair of counter rotating vortex tubes within the emerging jet.
3. The outer vortex in the pair has much lower concentration than the inner, consistent with increased surface area on the outer of the jet.
4. The vortex tubes merge at about $\pi < \theta < 2\pi$ radians, suggesting that the collapse of the helix is associated with the vortex tubes entraining themselves.

In the region immediately beyond the collapsing helix region the flow can be described by a limit cycle with the following key features:

1. The characteristic diameter of the limit cycle region appears to be the ("fixed") diameter of the helix
2. The total jet has very low growth rate in this region, as evident by "parallel" edges in some cases.

An increase in the dimensionless strain rate, (corresponding to an increase in Strouhal number for fixed angle ϕ) results in:

1. A tightening of the helix so that the "collapsed helix" region moves upstream towards the nozzle.
2. An increase in the concentration within the collapsed spiral and transition region.

Note that while all the evidence supports the hypothesis that precession acts to increase the strain rate in the emerging jet, the present dimensionless parameters do not account for radial pressure gradients and do not characterize the diameter of the helix in the limit cycle region.

4 MEAN AND FLUCTUATING CONCENTRATION IN THE MPJ FLOW FIELD.

4.1 INTRODUCTION

The effects of precession on the mixing characteristics of flows generated by an MPJ nozzle are investigated in this Chapter using a statistical approach as used in the validation of the experimental techniques in Chapter 2.3. One configuration of MPJ nozzle is used and this is compared with the simple jet for similar exit conditions. The experimental configuration examined has a constant deflection angle of $\phi = 45°$, a constant Reynolds number of 3,800 and an exit diameter of d = 3mm. The Strouhal number is varied over the maximum possible operating range of the experimental equipment. The mixing field of a simple jet at $\phi = 0°$, Re = 3,800 and St = 0 is shown for comparison. The field of view is chosen to allow the far field to be well characterized in both the axial and radial directions, whilst obtaining reasonable resolution of the near field. The aim is to provide a quantitative statistical description of the effect of precession on the concentration field of each jet. As with the validation section of Chapter 2, both linear plots and two-dimensional images of the data are presented.

4.2 MEAN FLOW FIELD

4.2.1 Two Dimensional Images of the Phase Averaged Mixing Field

Two dimensional images of the phase averaged mixing fields for each of the conditions examined are shown in Figure 4.1(a-h). A banded colour scale has been chosen to present iso-contours and highlight the phase mean structure within the mean mixing field whilst relating information about the absolute values of concentration.

Figure 4.1(a) shows that the mixing field of the simple axisymmetric jet is typical of the classical flow. A constant spreading angle is apparent with rays of concentration emanating from the nozzle exit being clearly evident. There is no apparent structure within this averaged flow field other than the constant spreading of the mixing field itself.

Figure 4.1 (b-h) are of the mixing field generated by the MPJ. The nozzle exit conditions are indicated. Figure 4.1(b) shows the mixing field at a low Strouhal number. Features of this field are consistent with those described in Chapter 3.2. Structure associated with the limit cycle are apparent in the transition region and a significant region of pure ambient fluid appears close to the nozzle exit across the entire region normal to the spinning axis. An evolution toward a mixing field which, on average, is symmetrical about the spin axis, can be seen in the far field.

The general trends with increasing Strouhal number described in Chapter 3 are also evident in the images shown in Figure 4.1(b-h). The features in the transition region associated with the limit cycle field are a strong function of Strouhal number, as demonstrated by the position at which the light sheet cuts through the helix. Both the axial and radial position of the flow features in the slice associated with the helix move closer to the nozzle exit. Also with increasing Strouhal number there is a general trend for the average concentration within these

structures to increase. The largest length scale of the far field, the local jet width, decreases with increasing Strouhal number. Broad regions of constant concentration are apparent on the centerline (spin axis) at low values of Strouhal number, e.g. Figures 4.1 (b) and (c). At higher values of Strouhal number a negative axial gradient in the centerline mean concentration is apparent. For all Strouhal numbers shown in Figure 4.1(b-h), the inner vortical tube of the jet helix interact with each other and appear to eventually merge, as discussed in Chapter 3. As the helix tightens with increasing Strouhal number, the interaction becomes stronger.

For the highest values of Strouhal number examined (Figure 4.1(g-h)) it is apparent that the helix interacts strongly with itself, forming a region of high concentration on the axis of the flow. Concentration gradients are also much larger both axially upstream and downstream from this merging structure. For the higher Strouhal number flows the region where "pure" ambient fluid cuts through the helix for the phase averaged data is very small, in contrast to the low Strouhal number case. The apparent deflection of the flow to the right in the far field, observed in Figure 4.1 (h) is deduced to be a consequence of a weak cross draft. The very low convection velocity of nozzle fluid in the far field locations allows the flow trajectory to be susceptible to such weak cross flows. Subsequent analysis has shown that only the radial statistics are affected to any significant degree by the cross flow in this set of data. Other data sets are virtually unaffected.

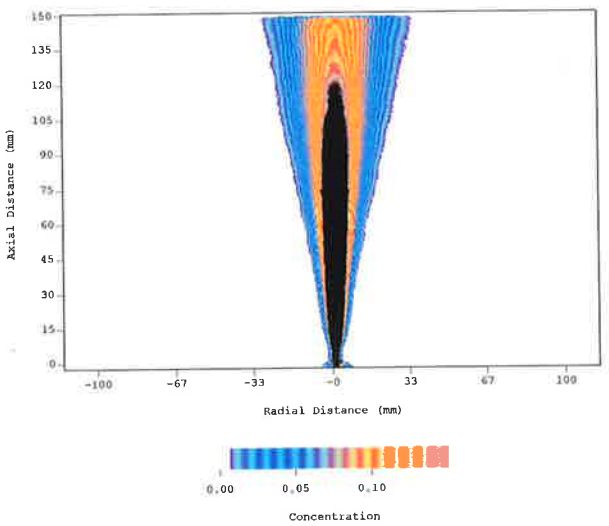

Figure 4.1 (a) Re = 3,800; St = 0; $\phi = 0°$

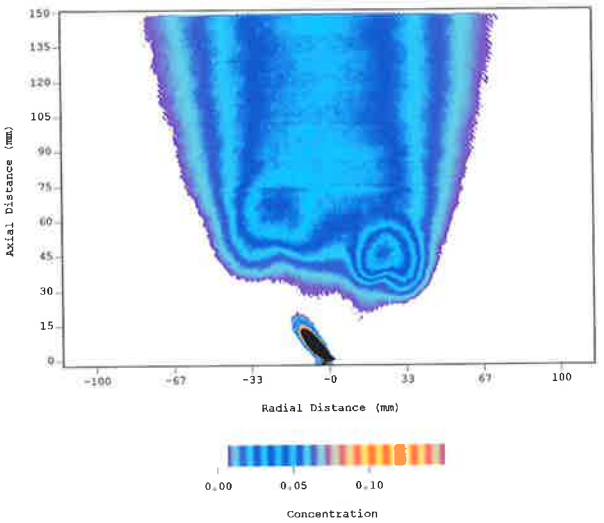

Figure 4.1 (b) Re = 3,800; St = 0.0047; $\phi = 45°$

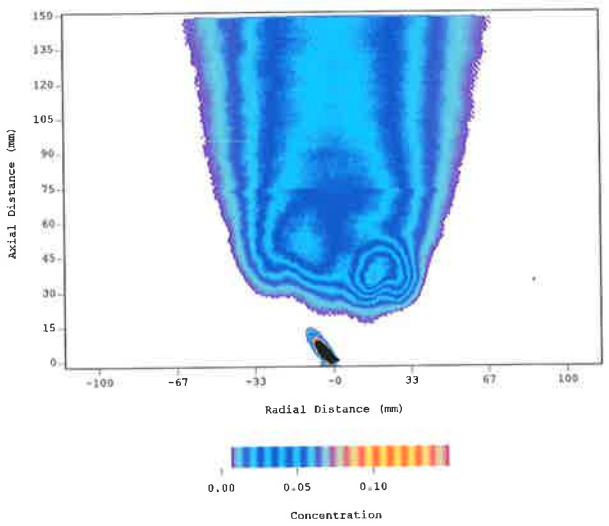

Figure 4.1 (c) Re = 3,800; St = 0.0063; $\phi = 45°$

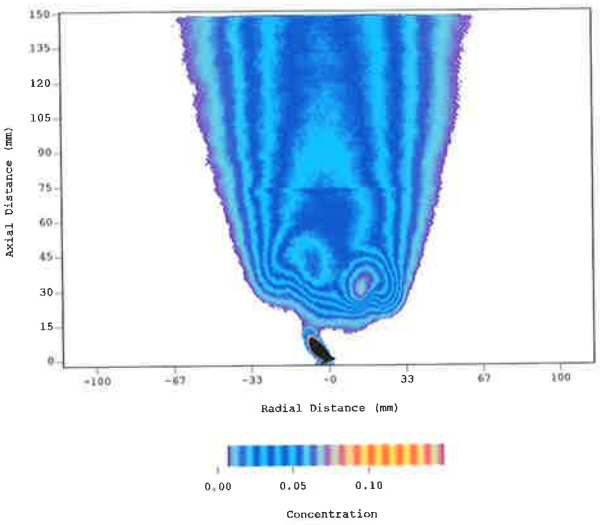

Figure 4.1 (d) Re = 3,800; St = 0.0079; $\phi = 45°$

Figure 4.1 Two-dimensional images of the phase averaged concentration field of an MPJ flow.

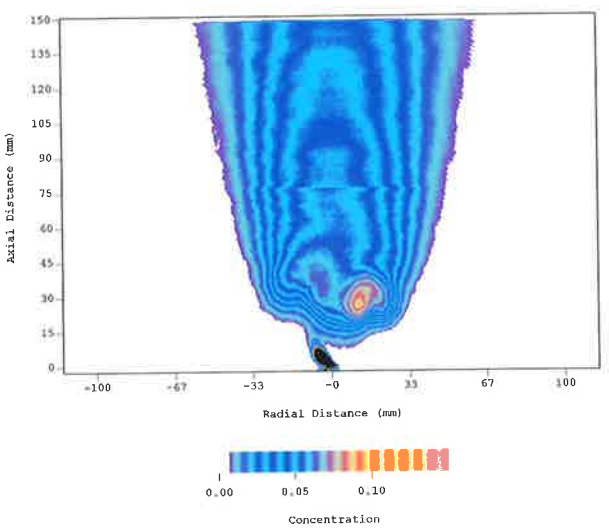

Figure 4.1 (e) Re = 3,800; St = 0.0098; $\phi = 45°$

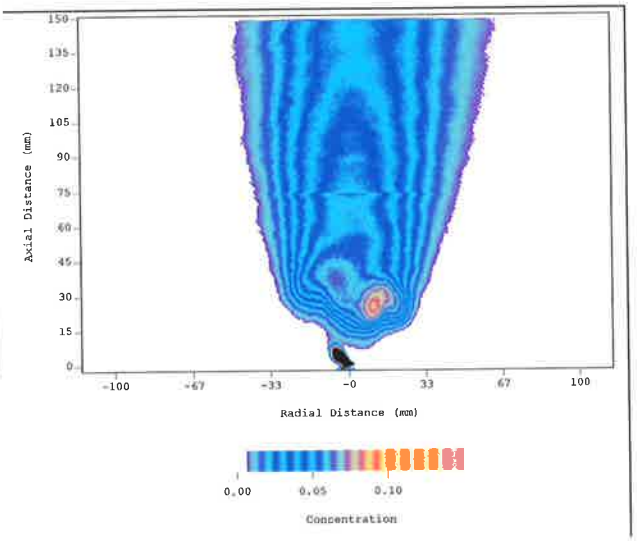

Figure 4.1 (f) Re = 3,800; St = 0.011; $\phi = 45°$

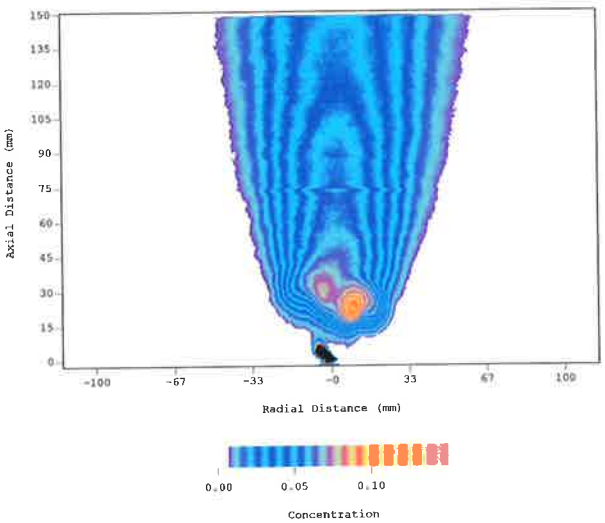

Figure 4.1 (g) Re = 3,800; St = 0.0126; $\phi = 45°$

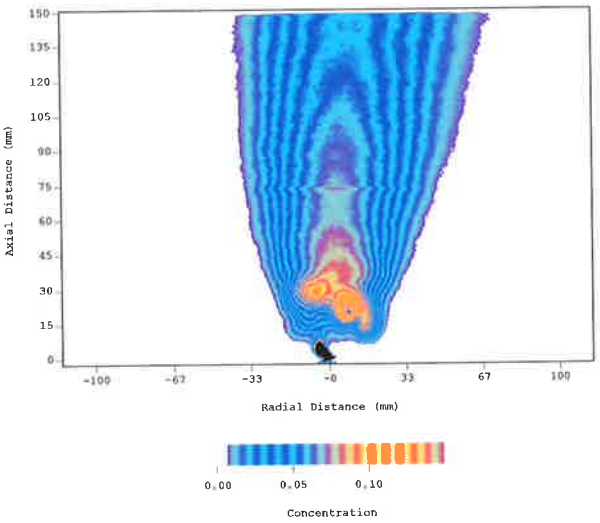

Figure 4.1 (h) Re = 3,800; St = 0.015; $\phi = 45°$

Figure 4.1 Two-dimensional images of the phase averaged concentration field of an MPJ flow.

4.2.2 Centerline Decay of Concentration.

A plot showing the decay of mean concentration along the centerline of the mixing field is presented in Figure 4.2. For the simple jet, a potential core region of pure jet fluid is observed in the near field followed by the typical $1/\chi$ fall-off in concentration. The plot also clearly demonstrates that the centerline mean concentration in all of the precessing jet flows is very much lower than that of the simple jet, and has a totally different character, consistent with the helical nature of the jet fluid in the near field.

The mean centre line concentration of jet fluid tends to zero in the near field of all of the MPJ cases i.e. there is negligible detection of jet fluid. "Pure" or near pure ambient fluid dominates in this region. The same data is re-plotted in Figure 4.3 with a different scale for the concentration axis to provide more detailed resolution. A distinct dependence on the Strouhal number is evident with a monotonic decay beyond an initial peak being apparent in all cases. With increasing Strouhal number there is an increase in the magnitude of concentration of jet fluid. The presence of ambient fluid in the near field is again highlighted. The axial location of the peak in concentration is also a function of Strouhal number and occurs between z/ r= 15 and z/r = 30. The rate of decay beyond the peak concentration increases with increasing Strouhal number and is nearly linear.

The rate of decay can be determined from Figure 4.4 in which the reciprocal of the mean centerline concentration is plotted as a function of normalized axial distance. From this plot the rate of decay (the gradient of a fitted straight line, using a linear regression) and the virtual origin of the field for each Strouhal number has been determined. The results appear in Table 4.1. While the asymptotic decay rates of different jet flows are in the same range, the effect of Strouhal number is significant. A clear increase in decay rate with increasing Strouhal number is evident both from Table 4.1 and Figure 4.4, highlighting that higher initial mixing occurs with the lower Strouhal number cases resulting in lower concentration values in the far

field. It is also interesting that the asymptotic mixing rate of the simple jet lies in the middle of the spread of decay rates, suggesting that the far field flow, as measured along the spinning axis, does not converge to that of a simple jet for either St = 0 or St $\rightarrow \infty$. The virtual origins for all of the MPJ cases are far upstream from the nozzle inlet plane, a result of the rapid initial spread of the time averaged jet generated in the near field.

From these results some observations can be made:

- The asymptotic rate of decay of concentration in the MPJ flows is the same order as that of the simple jet. However this decay is unmistakably a function of Strouhal number.
- The magnitude of the *mean* concentration on the centerline is an order of magnitude lower for the MPJ than for the simple jet at similar axial positions in the range investigated consistent with the greatly augmented initial bulk entrainment.
- The virtual origin of all of the MPJ flows is the order of 100 diameters upstream from the inlet plane, consistent with the greatly augmented initial spread.

These points indicate that the far field mean mixing characteristics of the MPJ are comparable with, but distinctly different from, the *far field* characteristics of the simple jet. Precession alsodramatically alters the near-field mean mixing characteristics with the magnitude of concentration on the centerline being greatly reduced. A clear trend of increasing axial concentration with increasing Strouhal number is apparent.

Table 4.1 Rate of decay and the position of the virtual origin for the different cases.

Hz	Inlet diameter (mm)	St	Re	Deflection Angle ϕ	Decay Rate	Virtual Origin (z_o/r)	Half Radius Decay Rate	Half Radius Virtual origin
0	3	0	3850	0	0.075	-11.9	0.103	-2
95	3	0.015	3850	45	0.165	-52.8	0.04	-270
80	3	0.0126	3850	45	0.134	-87	0.1	-116
70	3	0.011	3850	45	0.125	-110	0.06	-267
62	3	0.0098	3850	45	0.123	-114	0.09	-167
50	3	0.0079	3850	45	0.097	-192	0.12	-150
40	3	0.0063	3850	45	0.078	-332	0.9	-260

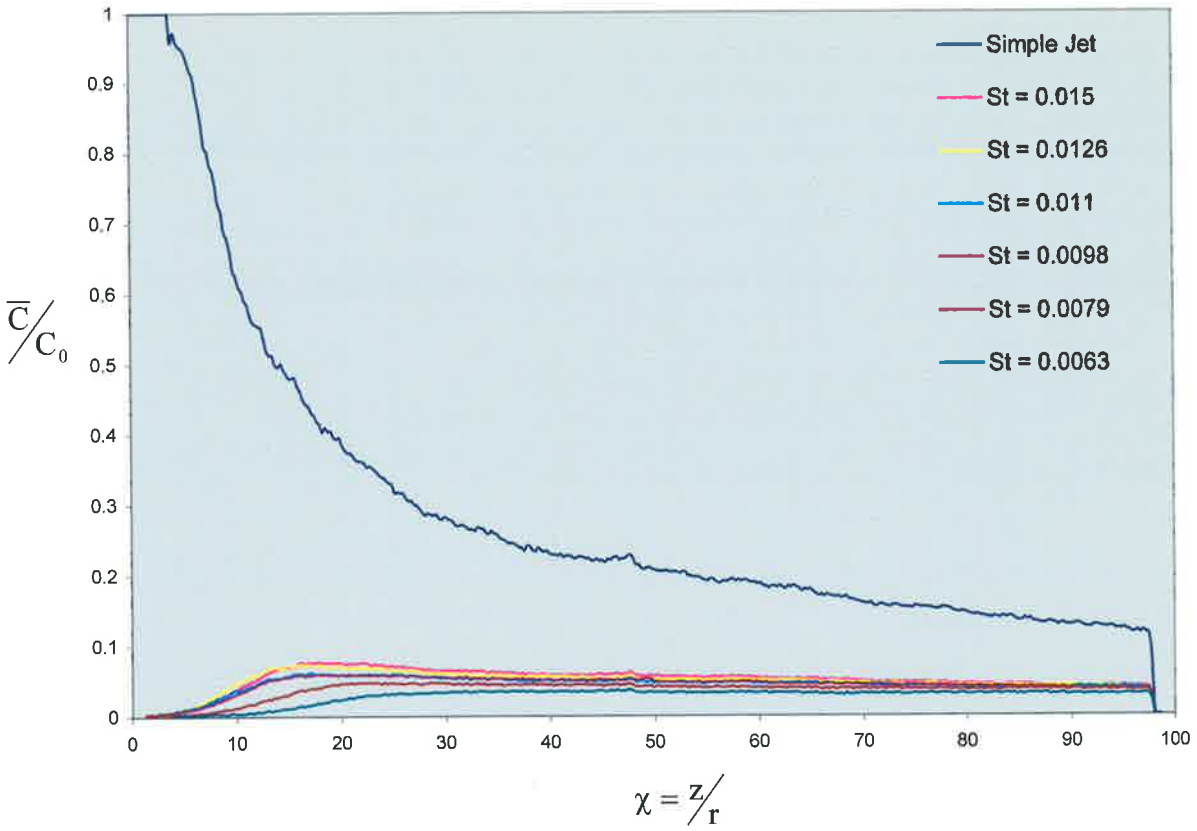

Figure 4.2 Decay of mean concentration along the centerline for the different jets.

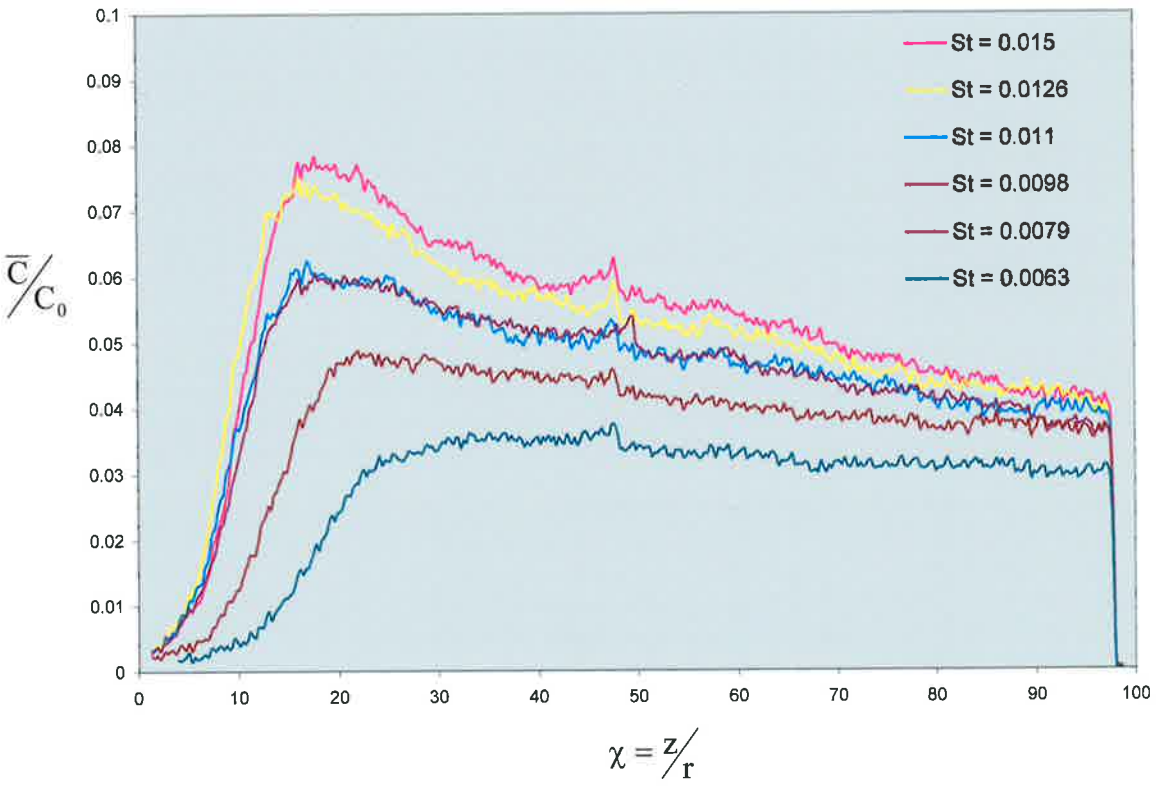

Figure 4.3 Mean centre line decay for the MPJ jets only.

4.2.3 Centerline Half Width

The radial position at which the mean concentration has fallen to half its centerline value ($C(\chi,½)$) is a measure of the spread, or growth of a free shear flow field. Figure 4.5 shows the reciprocal of the half width ($1/C(\chi,½)$) plotted against normalized axial location (χ). A half width decay rate and a virtual origin can be defined for each of the conditions of the MPJ and for the simple jet case. The initial region, $z/d < 25$ is the region in which the flow field of the MPJ nozzle is still developing. The phase collection technique emphasizes the three-dimensional helical nature of the near field. Beyond this, a steady slope is obtained suggesting similarity in the mean has been attained. Values for the decay rate and virtual origin from this definition are also shown in Table 4.1.

The simple axisymmetric jet has the classical half width growth rate. The virtual origin based on the half radius is then very close to the exit of the nozzle.

For the low Strouhal number precessing jet flow, the asymptotic growth rate is comparable to that of the simple jet. However the actual width of the field at a given location is significantly greater due to the "step" function introduced by the initial deflection angle and the precession. A virtual origin based on the half width falls well upstream of the exit plane of the nozzle.

As Strouhal number is increased the local width of the field decreases, indicating that the initial spread, for a given mass flow is decreased. The growth angle also decreases and, for two of the high values of Strouhal number (St = 0.011 and St = 0.015), approaches zero. However for the third highest Strouhal number case (St = 0.0126) the growth rate is more comparable with that determined by the mean decay rate of axial concentration. Examination of Figure 4.5 shows that the low spreading rates are associated with the flows influenced by a cross draft discussed earlier. The higher value is thus deduced to be more representative of the half width decay rate of a precessing flow. It indicates a slightly higher decay rate than the simple jet in the far field.

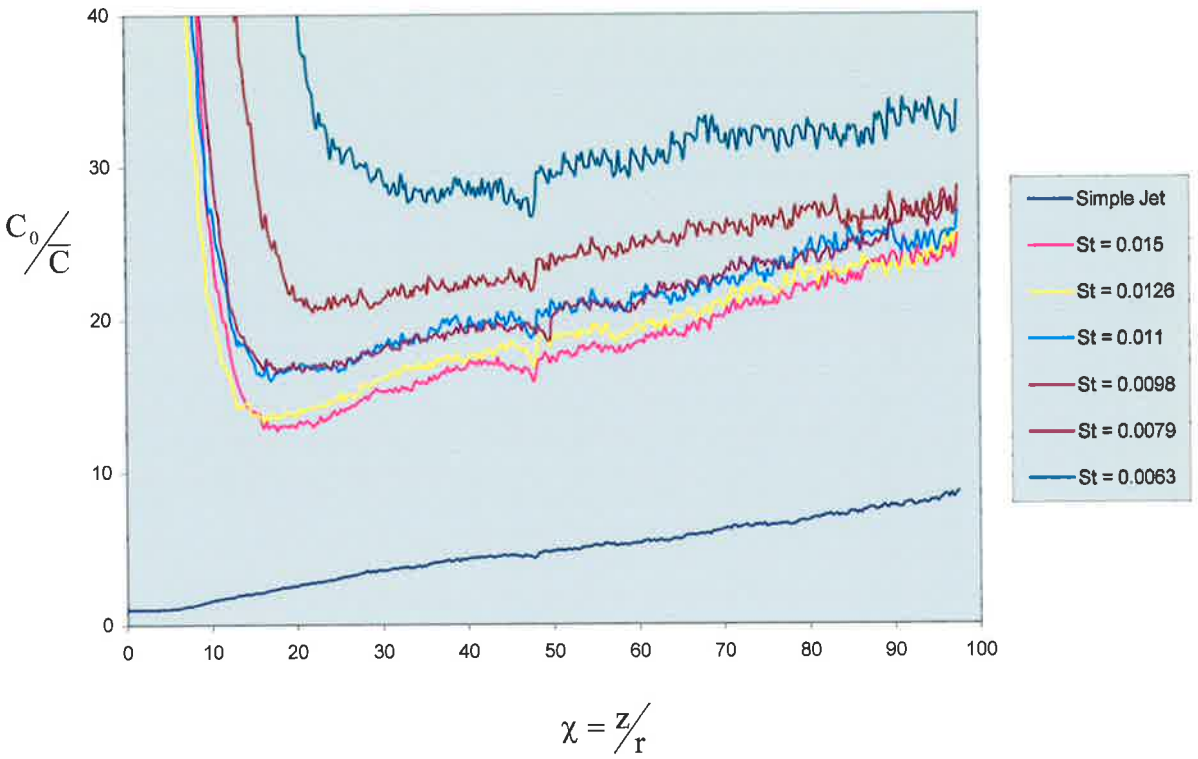

Figure 4.4 The reciprocal of the centerline mean concentration.

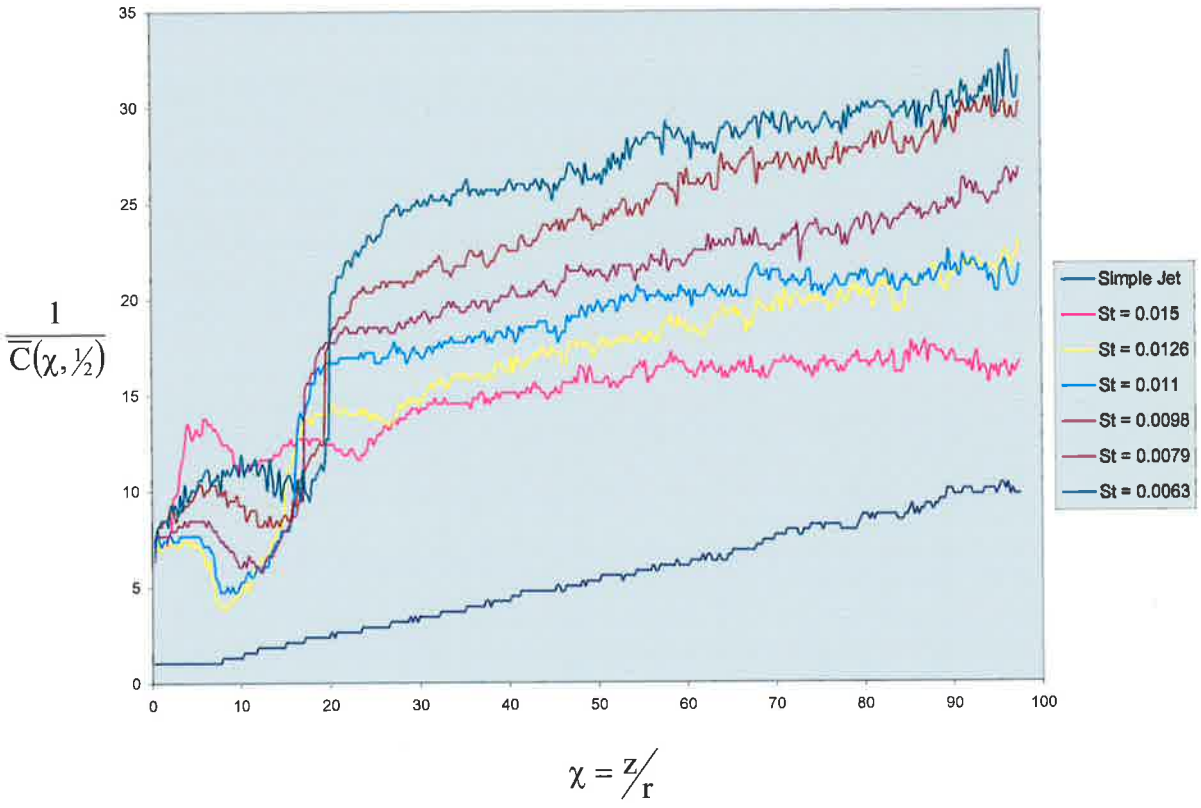

Figure 4.5 Plot of axial half width of the mean concentration field.

4.2.4 Radial Decay of mean concentration

The radial decay of the mean concentration $\left(\frac{\overline{c}(\chi,\eta)}{\overline{c}(\chi,0)}\right)$ is shown in Figure 4.6(a) for the simple jet and in Figure 4.6(b-g) for the various MPJ flows. The key shows the axial position, normalized by the exit diameter, at which the radial profiles have been collected for inclusion in the plot. The radial profiles presented here are all physically taken at the same axial location downstream from the nozzle. The data represented by any given colour is shown as the distance downstream from the virtual origin appropriate to that case condition. Hence the axial positions indicated in each of the plots are recorded to be at different normalized locations, which are significantly different given the high values of the axial location of the virtual origin based on the half width of the concentration field.

Radial profiles of the mean concentration for the simple jet (Figure 4.6(a)) shows that the mean mixing field becomes self similar by $(z - z_o) / r = 65$. Profiles closer to the nozzle than this do not display self-similarity in the mean, consistent with the findings of others (see Chapter 2.3). This is the transition region in which the flow develops toward self-similarity.

Normalized radial profiles of mean concentration for the different ranges of the MPJ flows (Figure 4.6(b-g)) also show good collapse at positions sufficiently far downstream, demonstrating that similarity is achieved in the mean (far field). Again in the near field, where turbulence and the mixing field are developing, the profiles are not self-similar. The asymmetry in the near field profiles is, again a consequence of the phase referenced collection technique. Although good collapse of radial profiles is achieved for each data set, it is clear that the shape of the self-similar profiles for MPJ flows are not the same as those of the simple jet; indeed they are different for each value of Strouhal number. A general trend of increased spread in the normalized profiles with increased Strouhal number is apparent. The shape of the normalized radial profile is a strong function of the virtual origin. There are

significant differences in the position of the virtual origin for the different MPJ flows and the magnitude of which is much larger than the simple jet (see Table 4.1). Thus any small error in the calculation of the position of the virtual origin will alter the shape of the normalized radial profile. There is however, a discernable trend in the change of spreading of the profiles, indicating that the normalization of the radial profile is not wholly dependent on the position of the virtual origin.

The asymmetry in the radial plot for the highest Strouhal number case, Figure 4.6(g), highlights the effect of the cross flow mentioned earlier. It is only for this, the highest Strouhal number case, that the peak for the radial profiles is off axis. This indicates that the draft only has a slight effect on the similarity of local radial statistics.

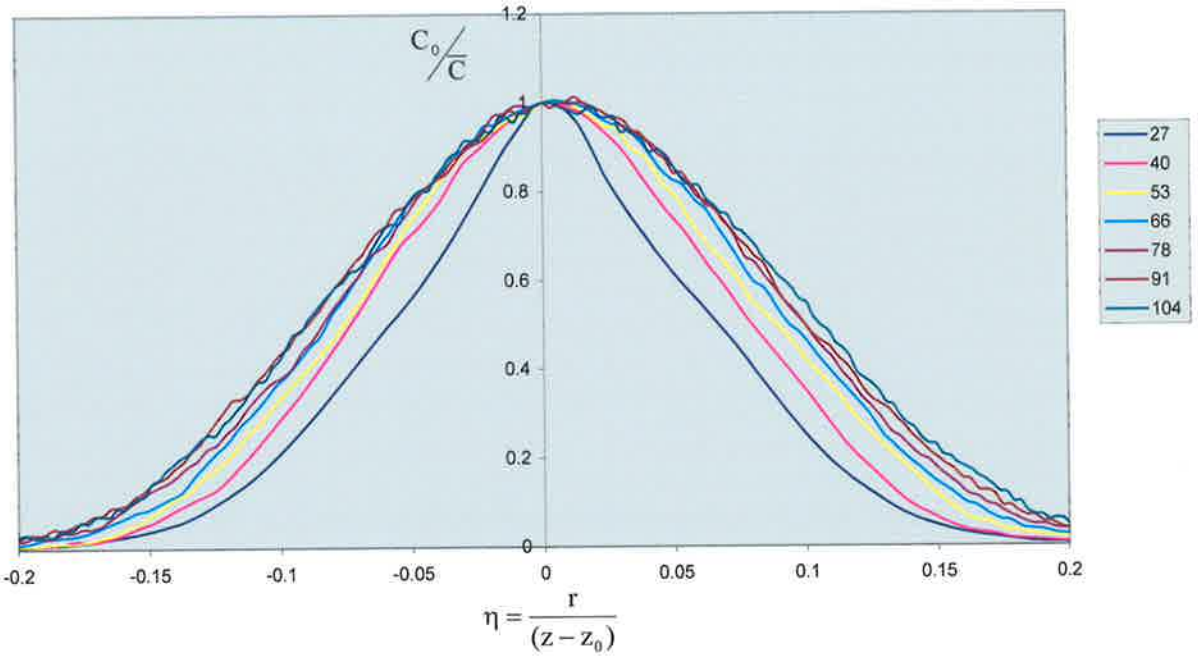

Figure 4.6 (a) Radial profiles of mean concentration for the simple jet: Re = 3,800; St = 0; $\phi = 0°$. The axial position, χ, corrected for the virtual origin for each profile is show in the legend.

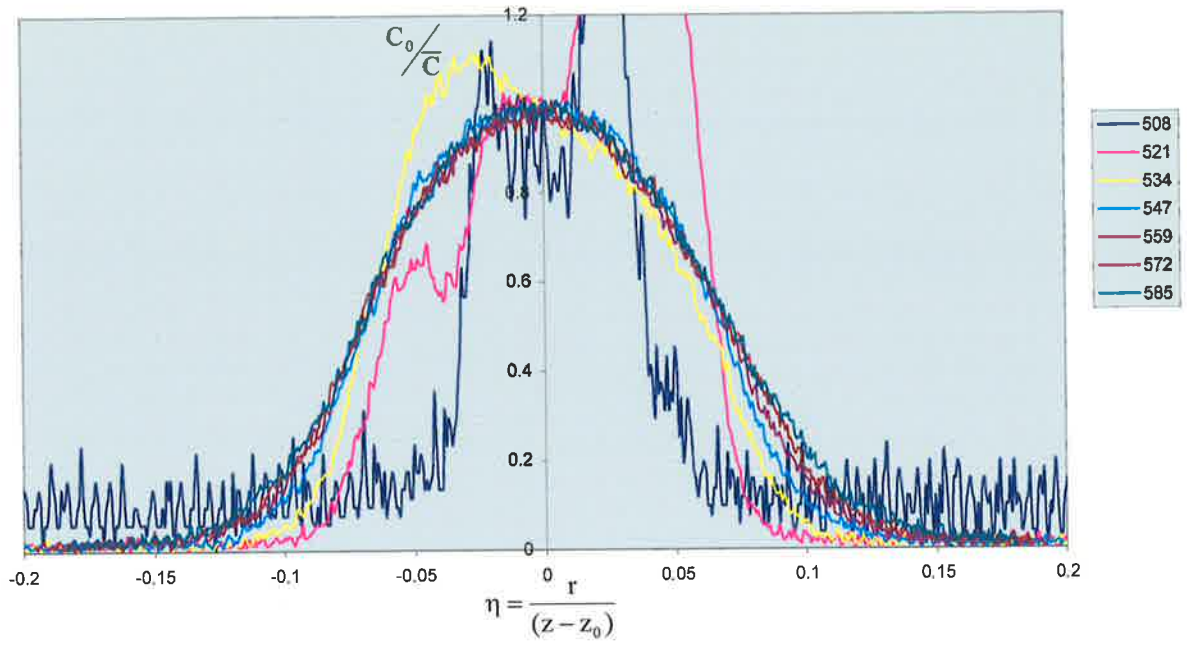

Figure 4.6 (b) Radial profile of mean concentration: Re = 3,800; St = 0.0063; $\phi = 45°$. The axial position, χ, corrected for the virtual origin for each profile is show in the legend.

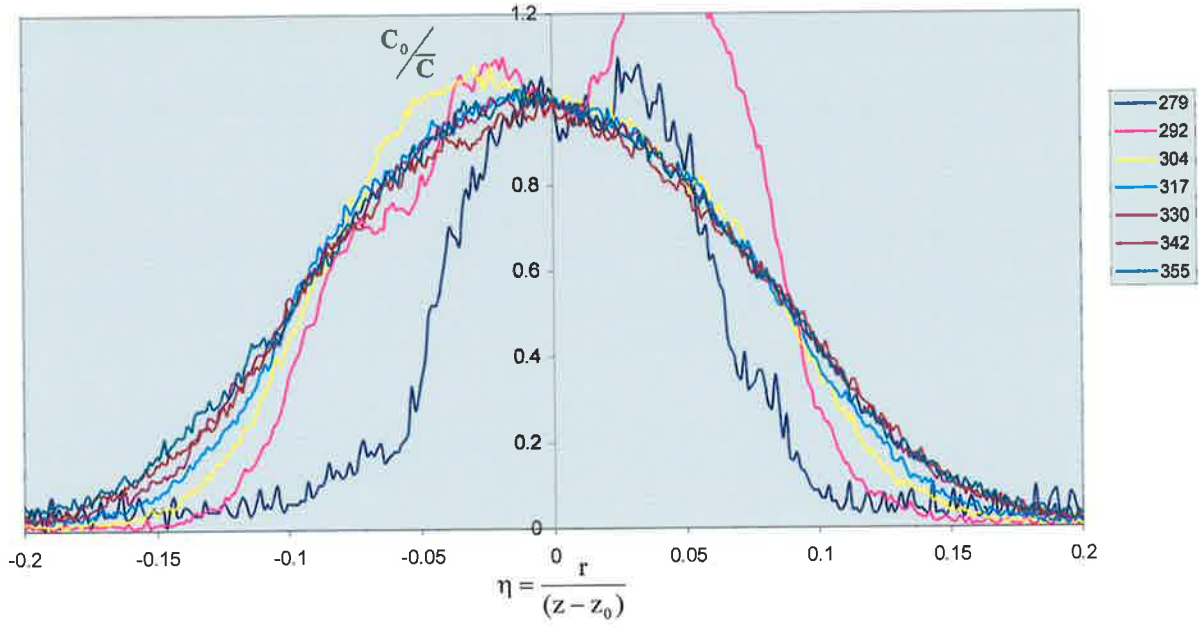

Figure 4.6 (c) Radial profile of mean concentration: Re = 3,800; St = 0.0079; $\phi = 45°$. The axial position, χ, corrected for the virtual origin for each profile is show in the legend.

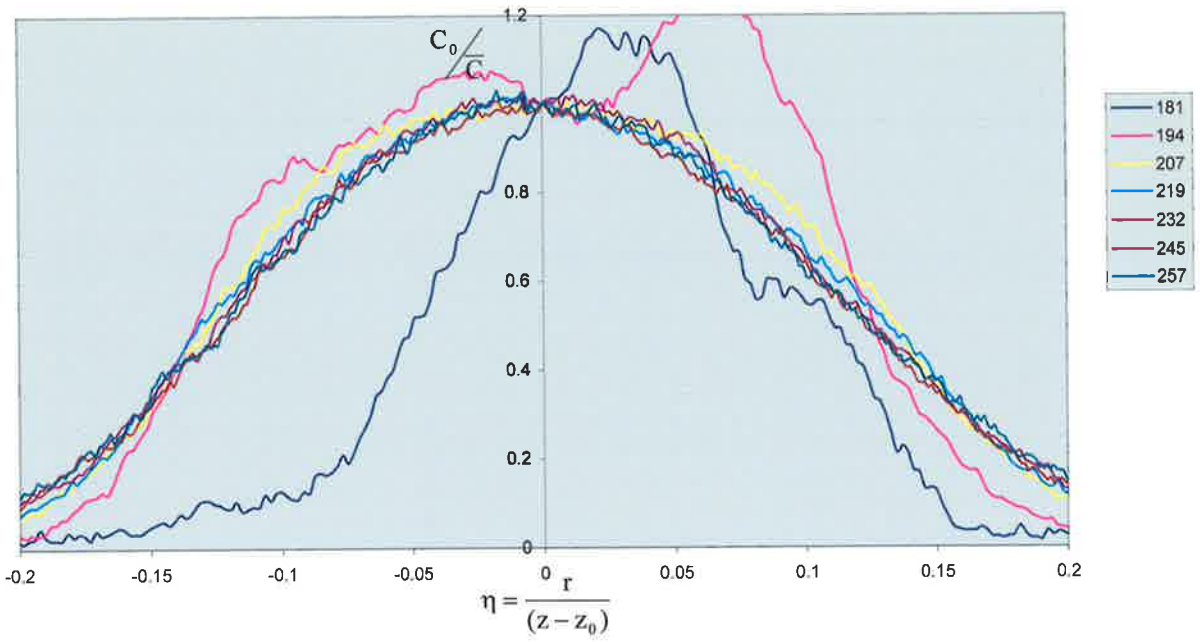

Figure 4.6 (d) Radial profile of mean concentration: Re = 3,800; St = 0.0098; $\phi = 45°$. The axial position, χ, corrected for the virtual origin for each profile is show in the legend.

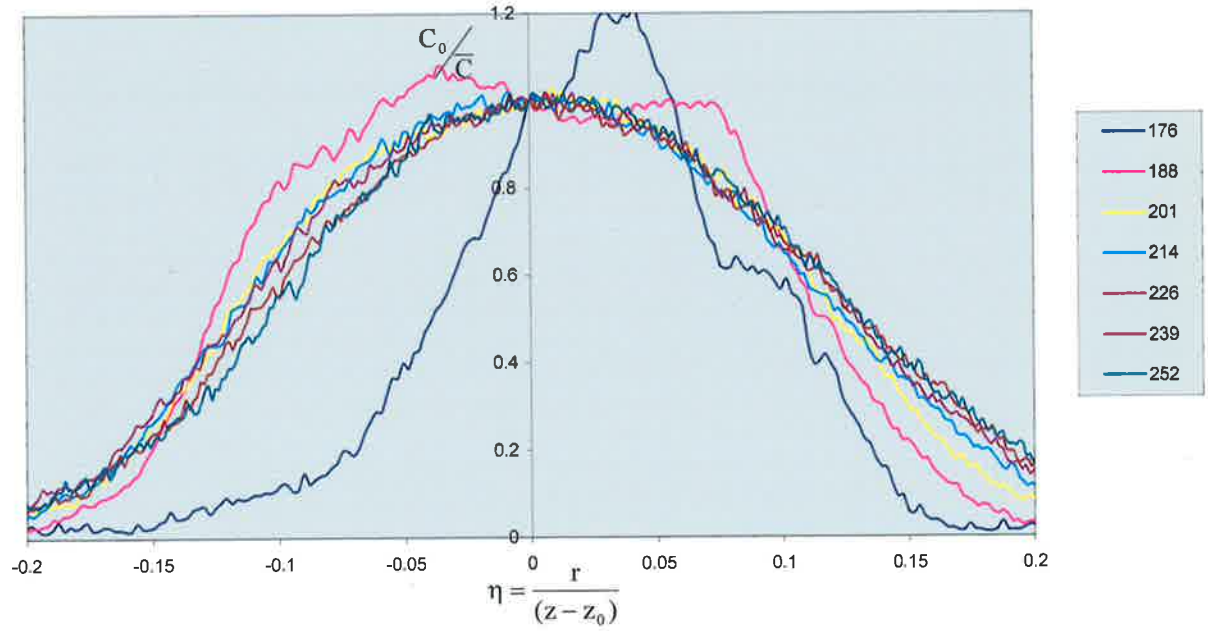

Figure 4.6 (e) Radial profile of mean concentration: Re = 3,800; St = 0.011; $\phi = 45°$. The axial position, χ, corrected for the virtual origin for each profile is show in the legend.

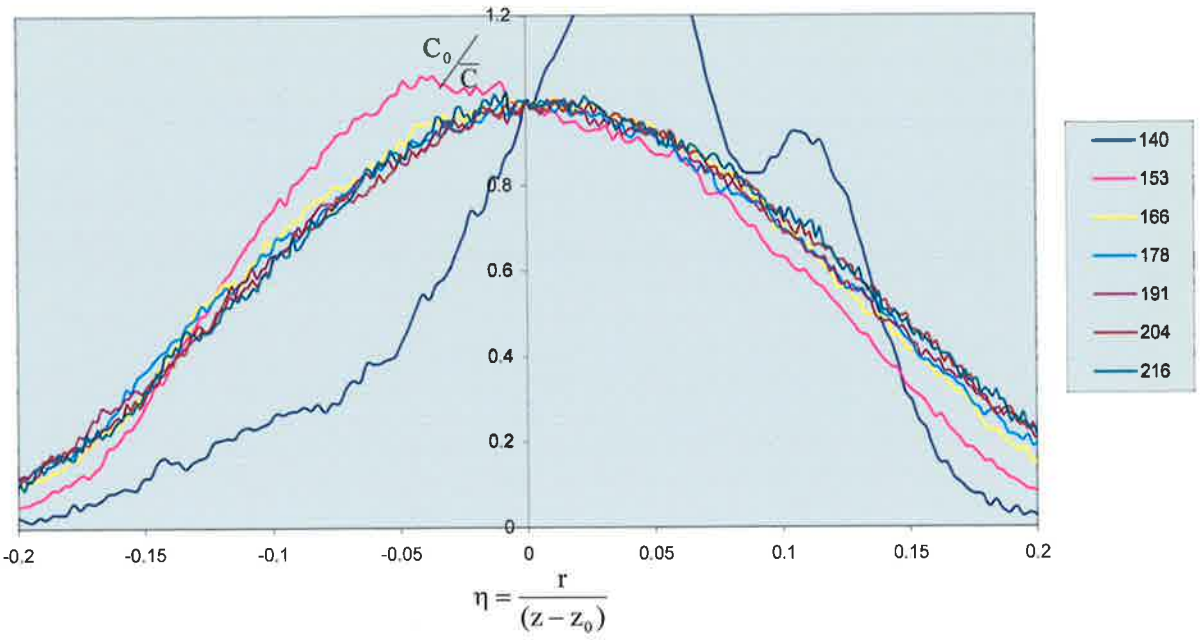

Figure 4.6 (f) Radial profile of mean concentration: Re = 3,800; St = 0.0126; $\phi = 45°$. The axial position, χ, corrected for the virtual origin for each profile is show in the legend.

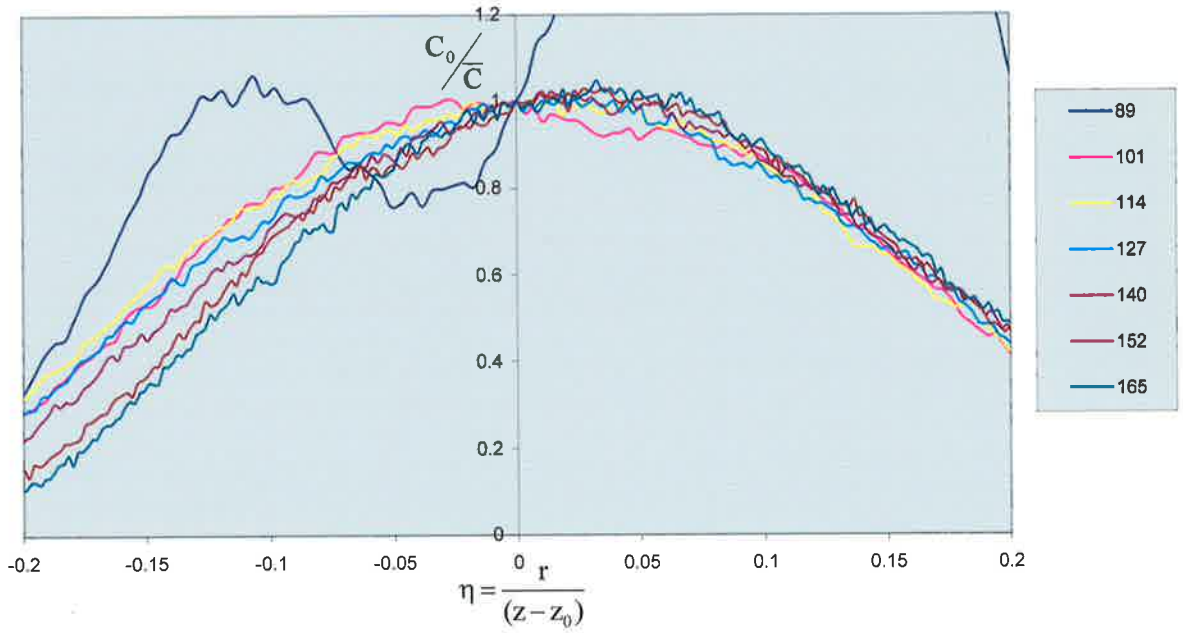

Figure 4.6(g) Radial profile of mean concentration: Re = 3,800; St = 0.015; $\phi = 45°$. The axial position, χ, corrected for the virtual origin for each profile is show in the legend.

4.3 SIMILARITY OF THE FIELD

Examining the behavior of parameters, which from similarity theory should show asymptotic behavior on the centerline of the flow, can be used to test the self-similar nature of the MPJ mixing field. Three such parameters are considered here: the scaled mean centerline concentration, the unmixedness and the reciprocal of the mean field versus the reciprocal of the fluctuating fluid. The procedure follows the methods described in the validation section of Chapter 2.3.

4.3.1 Scaled Centerline Concentration

Scaling the mean concentration by the normalized axial position, *without correcting for the virtual origin,* is a method of showing the normalized axial position at which the mean flow field becomes asymptotic. Plots for the different MPJ conditions and the simple jet appear in Figure 4.7.

The present low Reynolds number simple jet reaches an asymptotic value of the scaled centerline decay of concentration at approximately $z/r = 70$. This is further down stream than is found for the jet used for validation in Chapter 2.3. A possible reason for the difference is the lower value of Reynolds number of the present jet (3,800) compared with Re=16,400 for the jet in Chapter 2.3.

Precession alters the scaled mean centerline concentration significantly. Maximum values are approximately one third of those of the simple jet (Figure 4.7). The slopes in the data for all of the MPJ cases are in the same range and display consistent general trends. No asymptotic value is reached in the region investigated. Low values of Strouhal number give the lowest values of scaled mean concentration, and a trend of increasing magnitude in scaled mean concentration with increasing Strouhal number is apparent.

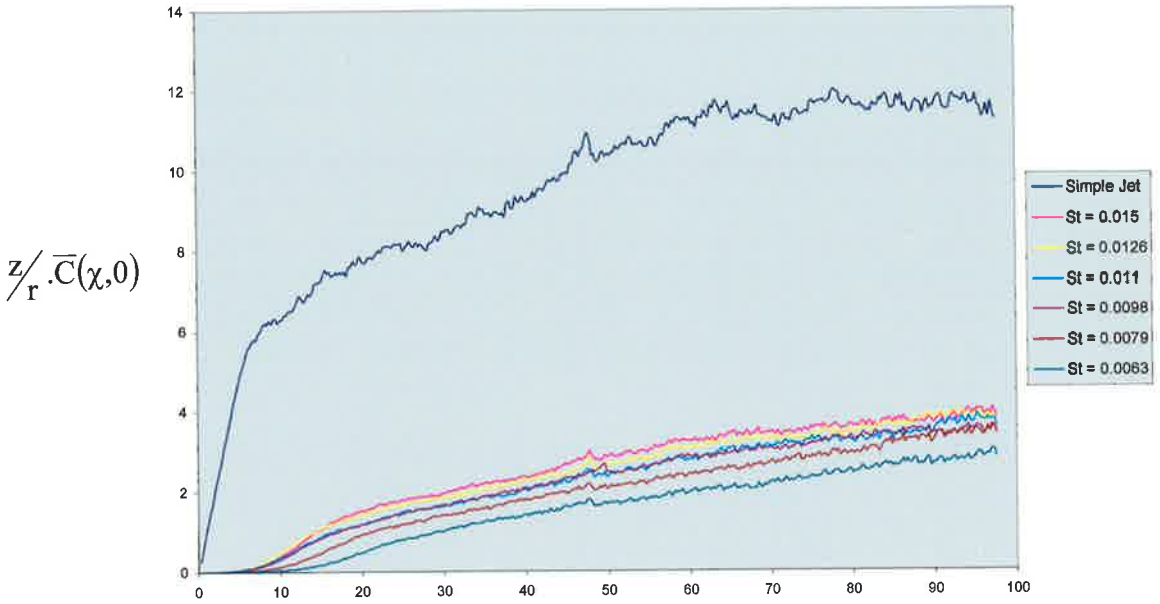

Figure 4.7 Scaled mean concentration on the centerline of the flow.

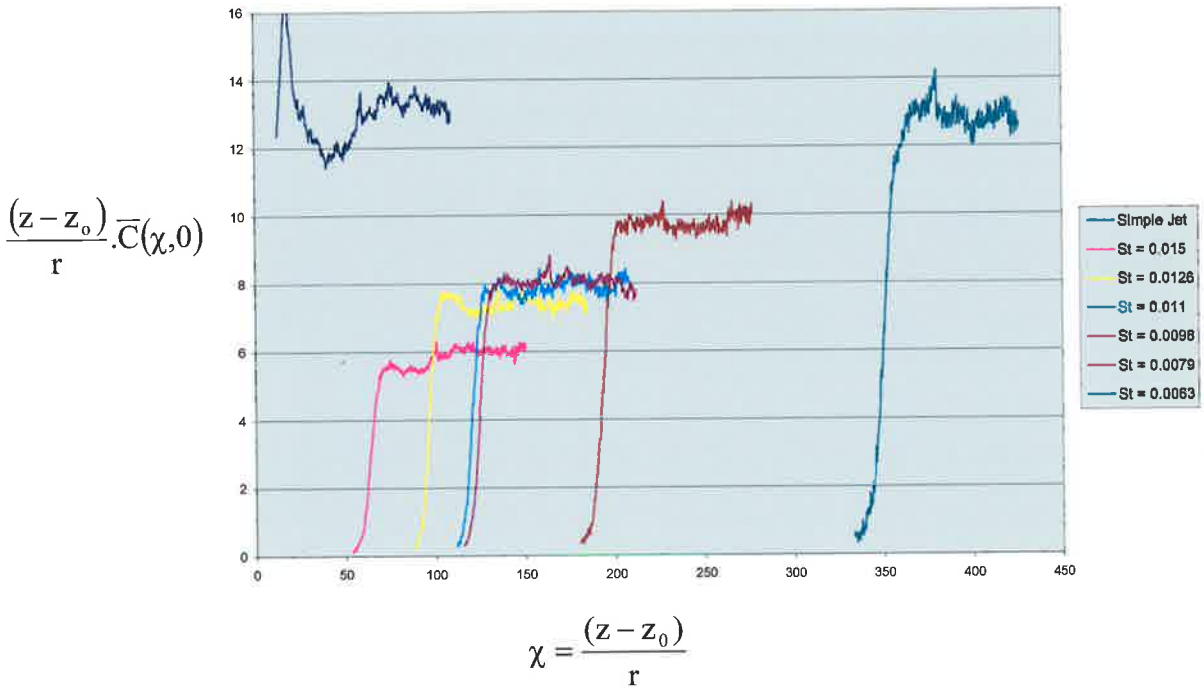

Figure 4.8 The scaled mean concentration on the centerline, corrected for the virtual origin.

The normalized axial position can be corrected for differences in the growths in the mean field by correcting for the position of the virtual origin. The scaled concentration data is re-plotted using this correction in Figure 4.8. The behavior of the simple jet is consistent with the data found in the literature (Dowling and Dimotakis, 1990) becoming asymptotic in the far field. A maximum is observed in the near field for the present data, not seen for the jet of Chapter 2.

An asymptotic value is reached for all of the MPJ data when it is scaled in this manner. The actual magnitude of the scaled asymptotic concentration depends on the scaling parameter, which in turn is dependent on the position of the virtual origin. Table 4.1 shows that the distance to the virtual origin for all of the MPJ results is very large so that the scaling parameter is sensitive to the estimate of the virtual origin, which is calculated from linear regression of the available data. The field of view for the MPJ flows does not extend far enough to resolve the position of the virtual origin accurately. Thus the absolute magnitude of the present estimates of the scaled concentration are open to question. Never-the-less a consistent trend is apparent and the influence of precession on the character of the mixing process is profound.

For increasing values of Strouhal number the calculated value of the scaled mean centerline concentration decreases. Each set of data asymptotes to a constant value as predicted by fields having similarity characteristics, which suggests that the position of the virtual origin is reasonably well defined. Furthermore, the trend of decreasing values of the scaled centerline concentration with increasing Strouhal number, is consistent with the tend in mean concentration decay rate shown in Table 4.1. Note that the mean concentration decay rate for the St = 0.0063 MPJ flow is almost identical to that of the simple jet (Table 4.1), and also, the scalar centerline concentration also agrees well (Figure 4.8), suggesting that the far field turbulence in the two flows is similar. However the corrected position at which asymptotic

behavior is reached is much further downstream at $(z-z_o)/r = 375$, compared to$(z-z_o)/r = 75$ for the simple jet. Mixing in this low Strouhal number jet appears to be largely shear driven, as in the simple jet, suggesting that the mixing field of the low Strouhal number case is similar to the simple jet *in it's far field.*

As Strouhal number increases, the asymptotic value of centerline concentration decreases along with the position at which the asymptotic value is reached. This leads to the tentative conclusion that the form of the mixing processes is dependent on the Strouhal number. Further, it can be postulated that as the Strouhal number is increased progressively from zero, the character of the mixing alters progressively from being shear driven, as in the simple jet, to become a folding process in which shear plays a less dominant part. For a given Strouhal number above some lower limit, this folding processes nevertheless achieves an asymptotic scaled mean concentration of jet fluid on the centerline which is lower than that for the simple jet. The question remains as to whether this scaled mean concentration is an adequate measure of the "style" of mixing process. Unmixedness is an appropriate measure to determine this and unmixedness is discussed below.

4.3.2 Two Dimensional Images of Unmixedness

Two-dimensional images of the unmixedness parameter are shown in Figure 4.9 (a-h). The low value points that appear as black dots in the body of the ambient can be attributed to noise. The banded colour scale used is limited to values of unmixedness between 0 and 1. Hence values of unmixedness greater than 1 are shown as solid black.

Figure 4.9(a) is the unmixedness image for the simple jet. The consistent spreading angle of the jet is clearly apparent. The edge of the jet is characterized by a region of high unmixedness associated with the passage of individual high concentration structures

intersected with regions of ambient fluid. A constant value of unmixedness on the centerline of the flow in the far field can be observed. Note that this is the minimum value of unmixedness found in the flow field captured in the image.

The distinct presence of the limit cycle in the near field at the low Strouhal number case can be observed in Figure 4.9(b) where there are parallel contours in the region downstream from the helix. It is also evident from the position of the region of unmixedness in the helical, spiral structure, which is comparable with that found in the far field. The far field shows a substantial region of unmixedness, which can be linked to that in the case of the simple jet. Around the edge of the flow field is a broad rim of high unmixedness values. This is associated with the motion of large intermittent regions of high and low concentration at the edge of the mixing field. In the near field close to the region of ambient fluid on the centerline there is higher unmixedness surrounding the helical structure.

For increasing values of Strouhal number there are some distinct changes in the flow field. This is especially noted in the near field where the structures associated with the limit cycle can be observed to merge together. High values of unmixedness occur only at the rim of the mixing field for the higher Strouhal numbers. The local width of the jet, i.e. the local length scale, is again seen to decreases with increasing values of Strouhal number as observed in Chapter 3.3.

Distinct flow structures associated with the limit cycle helix, can still be detected for the high Strouhal number cases, e.g. Figure 4.9 (g-h). In these images the outer vortex tube can still be observed while the inner vortex tube has merged and the unmixedness is indistinguishable from the values of unmixedness in the far field.

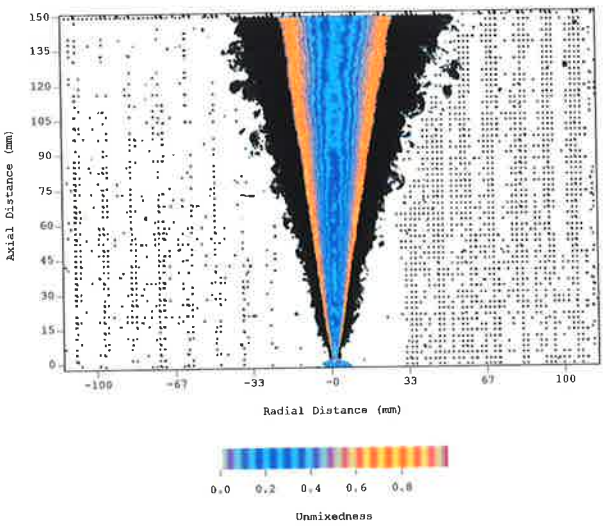

Figure 4.9 (a) Re = 3,800; St = 0; $\phi = 0°$.

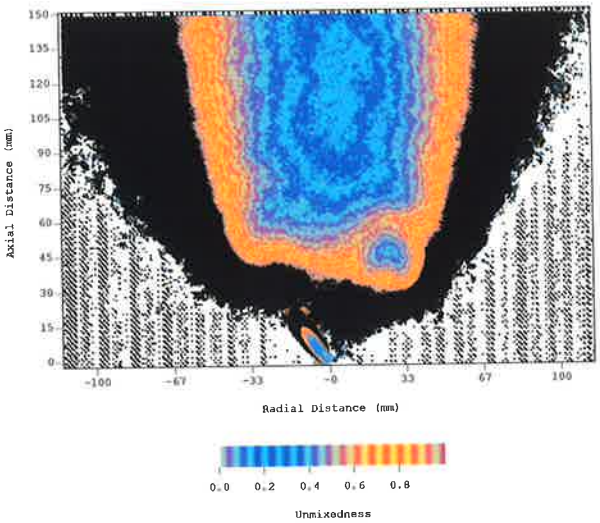

Figure 4.9 (b) Re = 3,800; St = 0.0047; $\phi = 45°$.

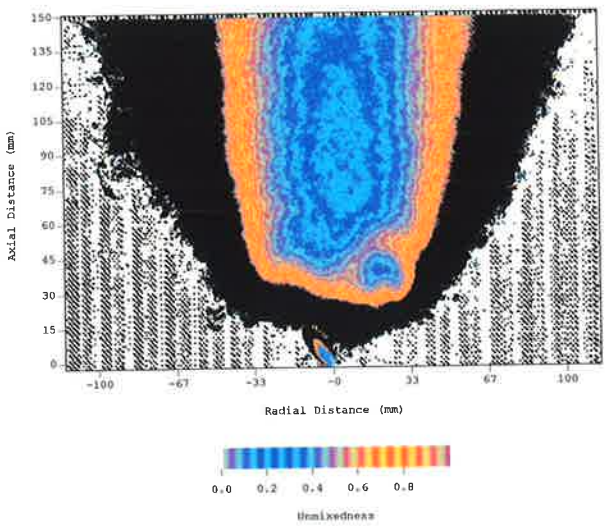

Figure 4.9 (c) Re = 3,800; St = 0.0063; $\phi = 45°$.

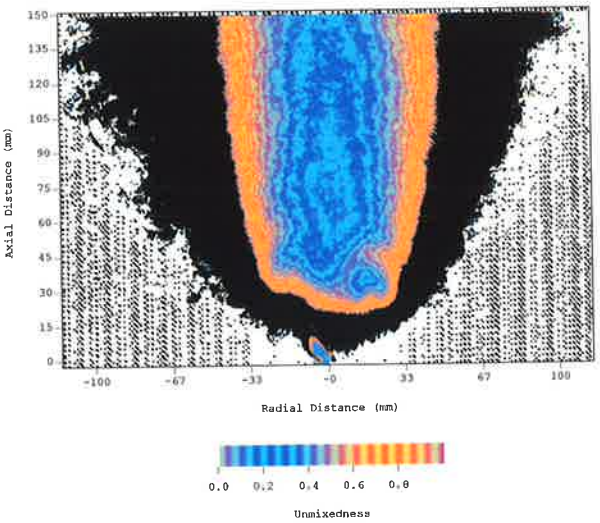

Figure 4.9 (d) Re = 3,800; St = 0.0079; $\phi = 45°$.

Figure 4.9. Two-dimensional plots of the unmixedness, C'/C, field.

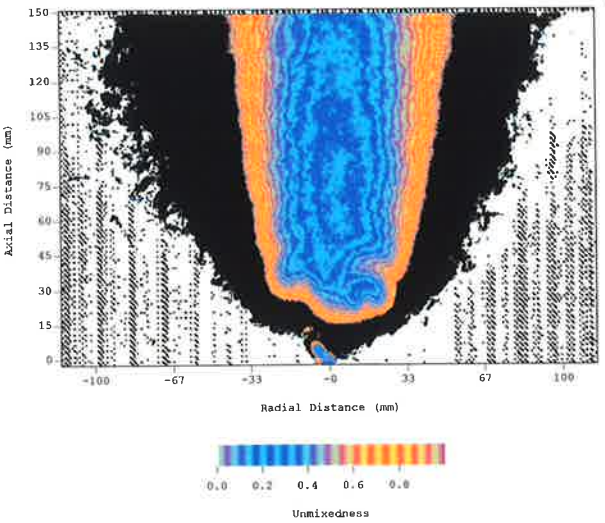

Figure 4.9 (e) Re = 3,800; St = 0.0098; $\phi = 45°$.

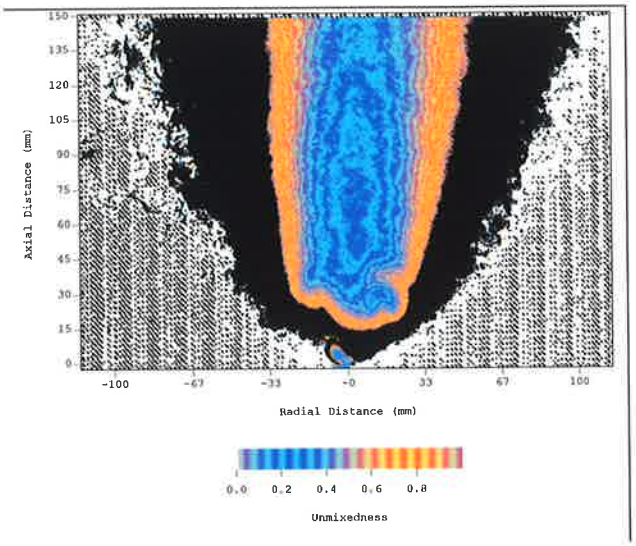

Figure 4.9 (f) Re = 3,800; St = 0.011; $\phi = 45°$.

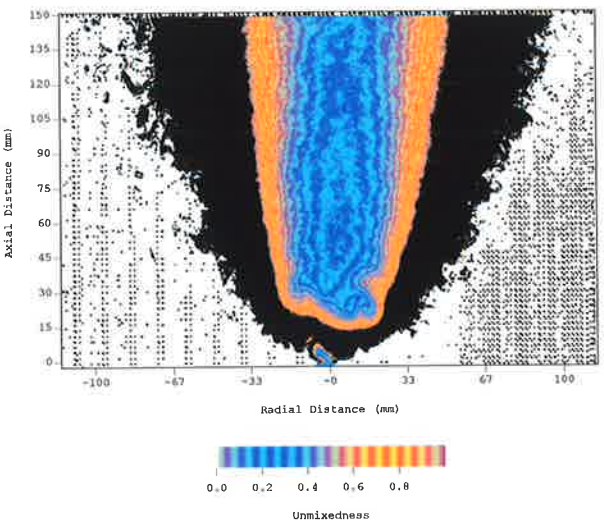

Figure 4.9 (g) Re = 3,800; St = 0.0126; $\phi = 45°$.

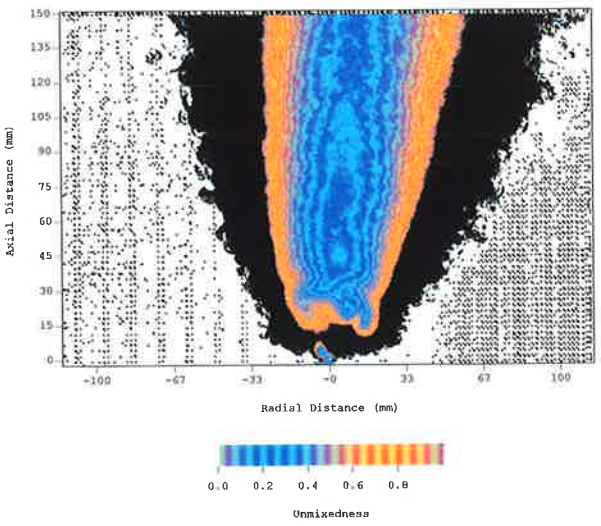

Figure 4.9 (h) Re = 3,800; St = 0.015; $\phi = 45°$.

Figure 4.9. Two-dimensional plots of the unmixedness, C'/C, field.

4.3.3 Axial Plots of Centerline Unmixedness

A measure of the point at which the flow field becomes self-similar, for both the mean and fluctuating fields can be assessed by comparison of the performance of unmixedness on the centerline of the flow. Figure 4.10 shows the centerline data including the near field dynamics for all for the flows investigated in this section. It shows that in the near field, high unmixedness values are produced by the MPJ flows. By z/d = 40, these unmixedness values have fallen to be comparable to those found in the simple jet. A more detailed view of the far field behavior is seen in Figure 4.11.

The low Reynolds number simple jet does not reach an asymptotic value in the field of the region investigated, even though the mean field has become asymptotic, as seen in the results of the scaled mean concentration of the previous section. The rms field is therefore still developing, and this results in the increasing values of unmixedness toward the limit of the imaged field. The maximum value in the far field is $C'/\overline{C} = 0.275$, which is higher than the asymptotic result of $C'/\overline{C} = 0.223$ found in Chapter 2.3. Again, this is believed to be a consequence of the low Reynolds number of these experiments.

Figure 4.11 shows that precession introduces a change of up to 25% in the far field centerline unmixedness, for the high Strouhal number flows. By contrast the low Strouhal number flows have similar asymptotic values to those of a simple jet. Measurements of the centerline value of unmixedness found in the literature show that a wide range of asymptotic values are measured, using a wide range of different techniques to investigate different jet exit conditions (Pitts, 1991a, 1991b). That the present results, which use the same diagnostic tool, show a trend that is a function of precessional frequency is significant. In the near field, the very high value of unmixedness is a result of the deflection of the jet, where in the three dimensional helical region the jet concentration falls to zero on the centerline. This region therefore returns spurious results of unmixedness and is not comparable with the simple jet measurement within the potential core region.

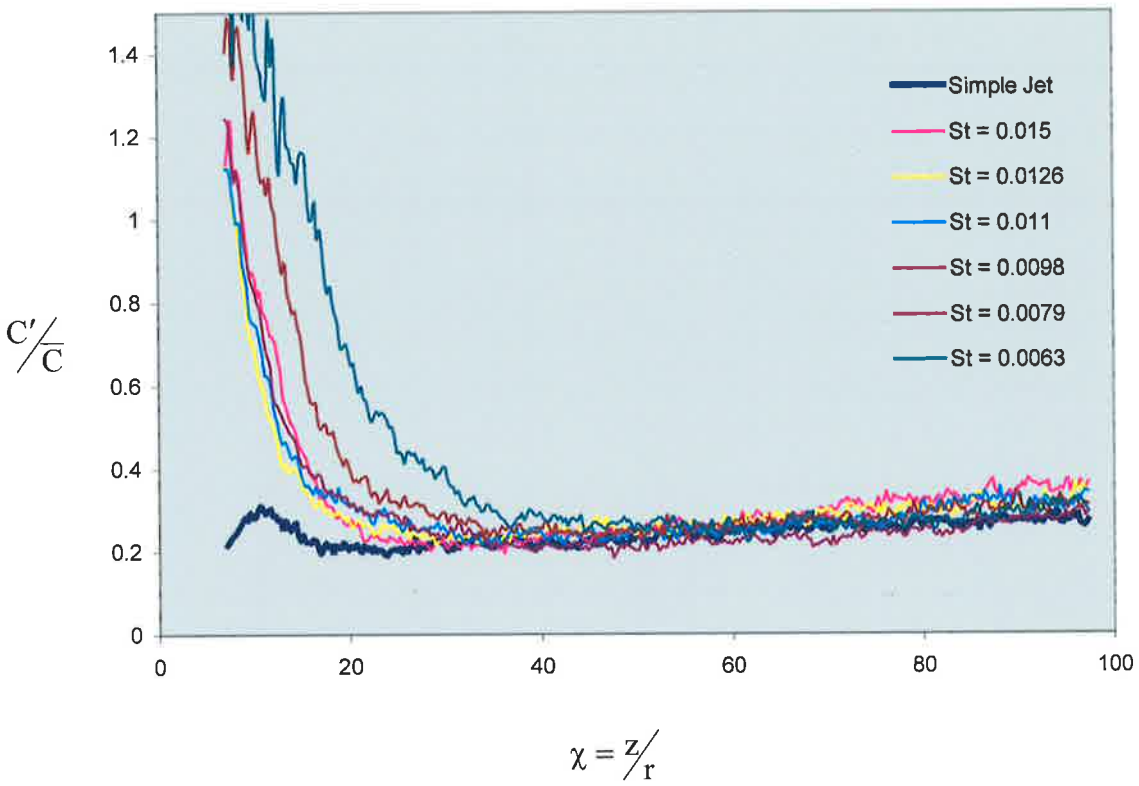

Figure 4.10 A comparison of the centerline unmixedness for the different flows.

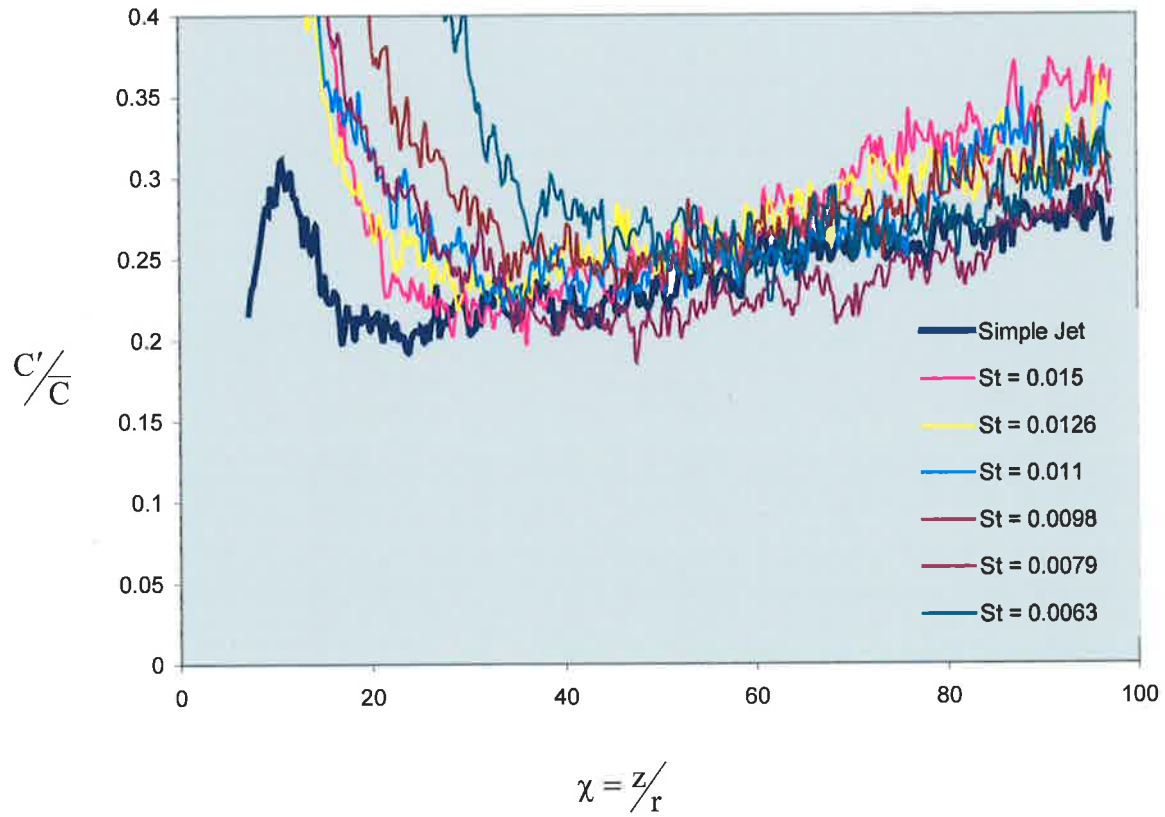

Figure 4.11 A closer view of the data presented in the previous plot

4.3.4 Reciprocal of Local Fluctuation Vs Reciprocal of Local Mean

Becker *et al* (1967b) plotted the reciprocal of the local mean concentration against the reciprocal of the local mean concentration fluctuation (see their Figure 7). Although their results for the unmixedness parameter did not extend into the asymptotic region, plotting the reciprocal of the concentration fluctuation intensity as a function of the reciprocal of the mean concentration along the centerline of the mixing field of the jet showed linear behavior. This can also be seen in the present validation results shown in Figure 2.16 of Chapter 2.

There are some interesting points to be noted about the manner in which the data is presented in this plot. At no point in the flow can the mean fluctuation be larger than the maximum mean concentration in the flow, i.e. at the exiting jet. Hence the ratio of the mean fluctuation to the maximum concentration will not be greater than 1. There are therefore two limits within this plot. Values of the reciprocal of the fluctuation and the reciprocal on the mean concentration will not fall below 1.

The results are presented in this manner in Figure 4.12. The simple jet data because of it's character is compressed into the bottom left corner of the figure. To show more clearly the results near the origin, a closer view of this region has been re-plotted in Figure 4.13. The data plotted in this manner is not a direct function of location in the jet; hence no length scale is involved. These plots are purely a comparison of the mean concentration fluctuation to the mean concentration at any point.

Precession has a dramatic effect on the mixing field when the data is plotted in this manner. Several features emerge which are different from the simple jet results. Figure 4.12 shows that a significant proportion of the data in the MPJ flows and all of the simple jet data, falls near to a ray emanating from the origin, which is the self-similar limit. This correlates with the finding in Figure 4.11, that the ratio of the fluctuating to mean concentration for MPJ flows tends to self-similar behavior. A closer view of this region (Figure 4.13) shows that there is a trend toward asymptotic behavior evident, especially for the high Strouhal number cases. The implication is that for a range of values of mean concentration, the fluctuation is independent of the mean concentration for a given Strouhal number.

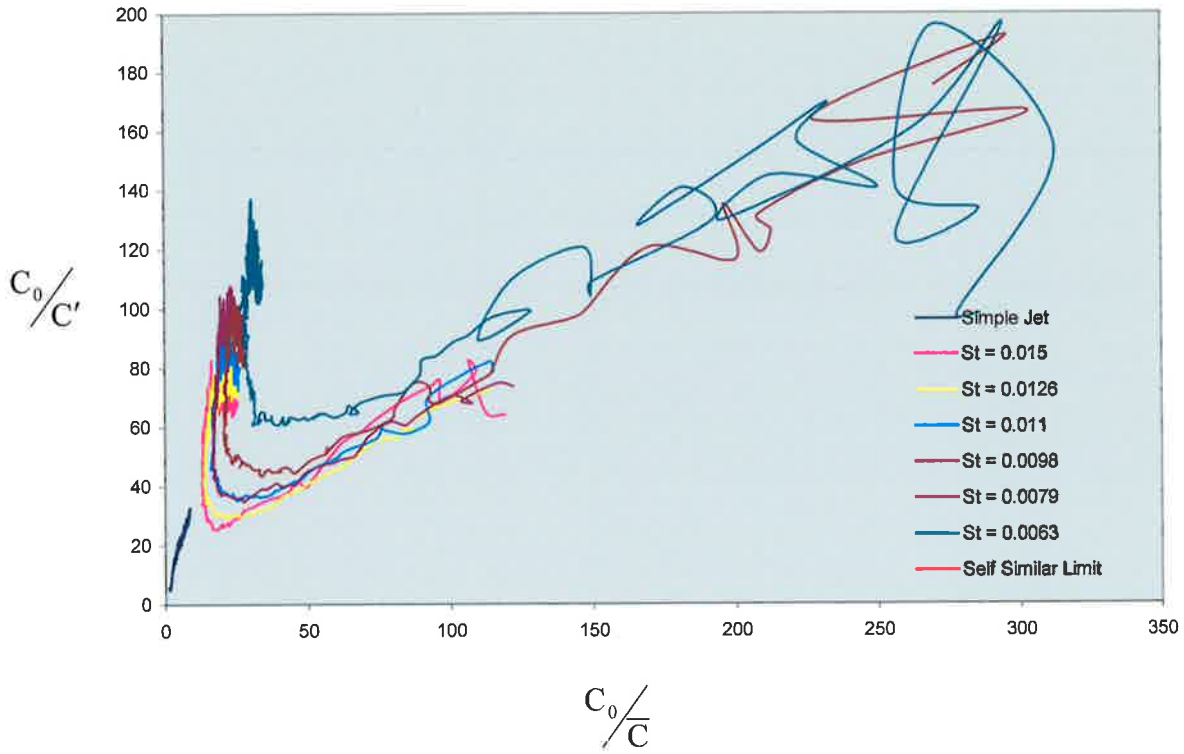

Figure 4.12 The reciprocal of the concentration fluctuation intensity as a function of the reciprocal of the mean concentration along the centerline of the mixing fields

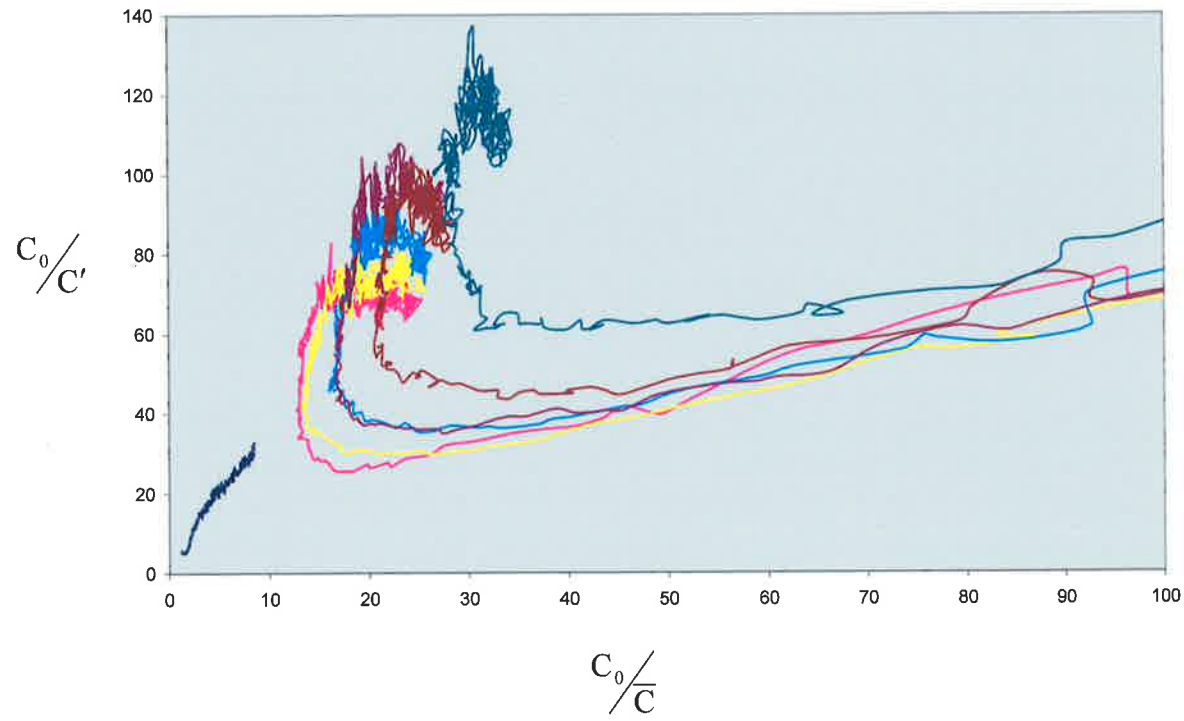

Figure 4.13 A closer view of the reciprocal of the concentration fluctuation intensity as a function of the reciprocal of the mean concentration along the centerline of the jet

4.4 COMMENTS / CONCLUSIONS

Statistics of variables of the concentration field of a simple jet and an MPJ jet at different values of Strouhal number have been presented. The results show that the mean and fluctuating field is significantly effected by precession. Precession has the of reducing the magnitude of the mean concentration significantly from that of a simple jet. With increasing Strouhal number the mean concentration increases throughout the field. The ratio of the fluctuation to mean concentration is seen along the centerline to be approximately the same as that of the simple jet although it is 25% higher for the high Strouhal number case. This indicates that while the far field asymptotic behavior of the MPJ flow resembles that of a simple jet, precession can fundamentally change the fully developed turbulence. Evidence presented in this data suggest that with increasing Strouhal number there is a change in the mixing characteristics of the flow field, from one which is shear dominated to one where large scale folding of the flow becomes more significant.

5 THE EFFECT OF PRECESSION ON A MACRO MIXING LENGTH SCALE

5.1 INTRODUCTION

This chapter presents results of the effects of precession on the integral length scale at different points in the flow field. The length scale of the flow is calculated from a two-point spatial correlation technique. The definition of the length scale and a comparison of the results of the calculation procedure with data from the literature are presented in the next section. This is based on the simple jet flow described in Chapter 2.3, which gives validation of the experimental technique. The length scales are then calculated for the MPJ presented in Chapter 4 to assess the effect of precession on the mixing lengths. The present experiments are all performed with constant exit angle, so the results only investigate the effects of precession. The dimensionless parameter used in this discussion is the Strouhal number.

5.2 DEFINITION OF THE LENGTH SCALE

Four length scales of turbulence are frequently cited in the literature. In increasing order of size these scales are (Turns, 1996);

λ_K - Kolmogorov micro-scale

λ_T - Taylor micro-scale

Λ - Integral length scale or Taylor macro-scale

L - Characteristic width of flow or macro-scale

The technique used in this investigation has insufficient spatial resolution to resolve the two smaller scales, the Kolmogorov scale and Taylor micro-scale except in the far field. A measure of the characteristic width of the flow, or macro-scale is presented in Chapter 4 using the half width of the mean flow field. Here a method of measuring the Integral Length Scale

in two-dimensions at many points in the flow field is presented based on calculation of a two point spatial correlation.

5.2.1 Two Point Spatial Correlation

The Two Point Spatial Correlation can be calculated from a collection of instantaneous images at selected points in the flow to quantify the length scales across the mixture field. The spatial correlation is defined by Hinze, J.O. (1975) to be,

$$R_{\Lambda}(z,\Delta z,r,\Delta r)=\frac{\overline{(C'(z,r).C'(z+\Delta z,r+\Delta r))}}{\left(\overline{C'(z,r)^2}\right)^{1/2}.\left(\overline{C'(z+\Delta z,r+r\Delta)^2}\right)^{1/2}} \qquad \text{Equation 5.1}$$

where C'(z,r) is the instantaneous fluctuation from the mean concentration at a fixed point (z,r), $\left(\overline{C'(z,r)^2}\right)^{1/2}$ is the time-averaged value of the concentration fluctuations at (z,r), and Δz, Δr represent the spatial distance from the fixed location. The Integral Length Scale, Λ, is then defined as

$$\Lambda=\int_0^{\infty}R_{\Lambda}\partial\varsigma, \qquad \text{Equation 5.2}$$

where ς is the distance between the points. This integral represents the area under the correlation curve, defined by Equation 5.1 and can be resolved in any plane about the point at which the correlation has been calculated.

In the literature, measurements of Λ have been based on various approximations and assumptions. Becker *et al* (1967b) measured Λ approximately from single point measurements by using Talyor's hypothesis to relate spatial and temporal data. This assumes that the turbulence passing the point is "frozen" and is moving at a local mean velocity, U. Namazian *et al* (1992) calculated Λ from planar data using the two point spatial correlation above and took the distance across an iso-contour, R = 0.5 of the correlation peak, to be a representative measure of Λ.

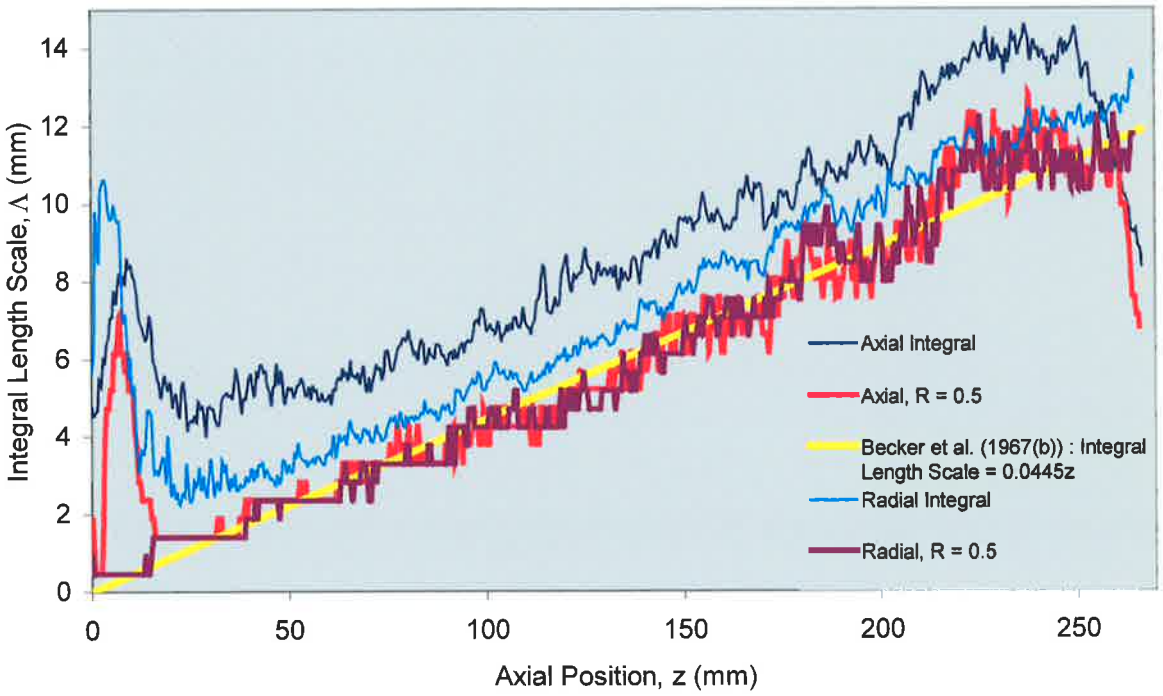

Figure 5.1 A comparison of various measures of the integral length scale, Λ using the present data (Re = 16,800). The integral $\Lambda = \int_0^\infty R_\Lambda \partial\varsigma$ is measured in two directions and is compared with the R_Λ=0.5 correlation contour method of Namazian *et al.* (1992), in both the axial and radial directions on the centerline of the jet, and with the results of Becker *et al.* (1967b) obtained using the Taylor hypothesis (Re = 54,000)

5.2.2 Measurement of the Integral Length Scale

Figure 5.1 shows a comparison of various measures of Λ in the simple jet flow at Re = 16,400 used for the validation of the experimental method (see Chapter 2.3). Measurements have been made using the integral of Equation 5.2 in both the axial and radial directions and the representative method of Namazian *et al* (1992), also in both directions. The single point results of Becker *et al.* (1967b) (a fitted curve, $\Lambda = 0.0445z$) is also shown for comparison.

The length scale measured in both the axial and radial directions defined by the $R_\Lambda = 0.5$ contour compares well with the results of Becker *et al.* (1967b). The length scale grows linearly with increasing axial location. The length scale in both the axial and radial directions calculated using Equation 5.2 is larger in magnitude but has approximately the same linear growth rate with distance. There is significant difference in the measured value of Λ based on Equation 5.2 in the axial and radial directions.

The definition of the two point spatial correlation given by Equation 5.1 is based on the assumption that the flow becomes uncorrelated so that the correlation approaches zero at a finite distance. The present calculations show that this is indeed the case for measurements in the radial direction, where the concentration of jet fluid does go to zero at the finite edge of the mixing field. However, in the axial plane the correlation does not approach zero, but instead converges to a "noise" floor or a "correlation" floor. Thus, if the integral is to be calculated meaningfully an arbitrary value for the "noise" floor must be chosen, and is taken to be, R_Λ = 0.05. Whether this "noise" floor is actually a "correlation" floor, implying that the flow is partially correlated in the far field due (say) to the existence of large-scale structure in the flow, or whether it is true noise, i.e. experimental error, is a question worthy of further investigation. Hence, due to the ambiguities associated with this method the $R_\Lambda = 0.5$ contour has been chosen as the measure of Λ, as used by Namazian *et al* (1992).

The representative method of Namazian *et al* (1992) allows contours of the two point spatial correlation to be plotted at a given point within the flow. The use of a contour provides information both about the magnitude of the local length scale and about any anisotropy in the length scale. Figure 5.2 is a two-dimensional plot of iso-contours of $R_\Lambda = 0.5$ and 0.8 for numerous selected points over the mixture field, including along the centre line of the flow. Superimposed on the plot are contours of the mean mixture field, which indicate the position of the jet.

There is linear, isotropic growth in the correlation length scale on the centerline of the jet as show in Figure 5.1. However, in the shear layer of the jet the correlation contours show that the length scales are anisotropic, with the major axis of the elliptical contour aligned at 45° in the direction of principle shear. The alignment of the length scales to the line of principal shear was also found by Namazian *et al* (1992). It is apparent that the macro scale is larger in the region of highest shear, radially away from the jet axis, than in the regions of reduced shear, along the nozzle axis or at the edge of the jet.

5.2.3 Summary

Two-dimensional plots of R are useful in identifying both the magnitude of the macro length scales at different locations in the mixture field and the isotropic nature of the scales. This can be interpreted to identify regions of shear. Comparisons carried out in the remainder of the Chapter will use the representative method of Namazian *et al* (1992) as a measure of the length scale, Λ.

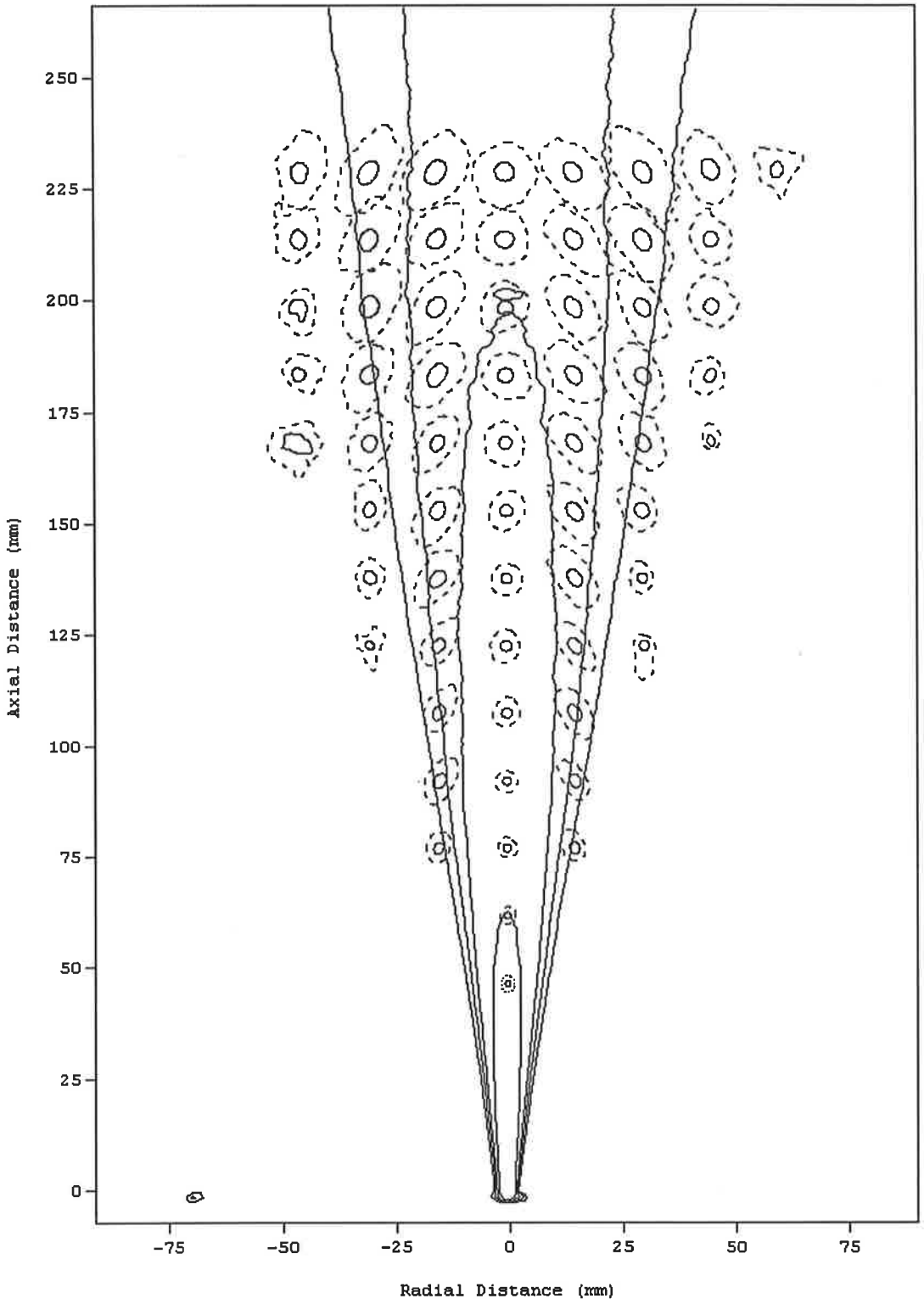

Figure 5.2 Contour plot of the two point spatial correlation at many selected points in the flow. Contours are for $R_\Lambda = 0.5$(dashed) and 0.8 (solid). Included also are contours of the mean concentration field, indicating the position of the jet.

5.3 THE EFFECT OF STROUHAL NUMBER ON THE INTEGRAL LENGTH SCALE, Λ

Presented in this section is the effect of variations in the Strouhal number of precession on the integral length scale. Plots of Λ along the centerline are presented first, followed by two-dimensional field measurements of Λ obtained in the fashion presented in Section 5.2. The data is collected for the 3mm diameter jet at a Reynolds number of 3,800 and a deflection angle of ϕ = 45 °. This Reynolds number allows a wide range of Strouhal number to be generated with the experimental equipment available.

5.3.1 The Integral Length Scale, Λ on the Centerline

A measure of Λ on the centerline of the simple jet and the MPJ at six different conditions of Strouhal number is presented in Figure 5.3 (a-g). The left ordinate shows the value of Λ in millimetres (plotted in blue). The result of Becker *et al.* (1967b) is shown as a reference of the length scale of a jet (plotted in yellow). Also included is the centerline behavior of the mean concentration scaled against the exit mean concentration (plotted in purple), to indicate the general character of the mixing field. Values of $\overline{C}/C_o$ are shown on the right ordinate.

A linear increase in Λ for the simple jet case is shown in Figure 5.3(a). The result of Becker *et al.* (1967(b)) highlights that the present simple jet flow follows a similar trend to that of jets at much higher Reynolds number (Figure 5.1). The value of Λ in the present data is slightly higher for all axial positions, possibly an effect of Reynolds number. The mean concentration field shows the typical 1/z decay of a simple jet and there is no apparent correlation between the mean field and the measured length scale.

Centerline plots of the normalized mean concentraion for all of the phase averaged MPJ data show broadly similar trends although the effect of Strouhal number is clearly significant. There is a region in the near field about which the emerging jet precesses, in which no jet fluid is measured, consistent with Chapter 4. Data associated with the very near field of the exit jet has been removed to improve the clarity of the plots. The jet fluid concentration rises from zero to a maximum with axial distance, followed by a near linear decay. The magnitude of the maximum concentration and the decay rate are observed to be a function of the Strouhal number, as discussed in Chapter 4.

For all Strouhal numbers a near field peak is found in the measured length scale, Λ, coinciding closely with the position of maximum centerline mean concentration, indicating the presence of a large jet fluid structure in the near field. For high values of Strouhal number, i.e. Figure 5.3 (b & c) the magnitude of Λ appears to become approximately constant at about 4mm (i.e. $\Lambda/d \approx 1.3$) within the field of measurement, although values fluctuate between 2.5 and 6 mm. For lower values of Strouhal number, i.e. Figure 5.3 (d-g) a trend of increasing growth in the length scale with increasing axial position is observed for distances beyond the local minimum. The rate of growth in Λ is a maximum for St = 0.0098, seen in Figure 5.3 (e). For lower values of Strouhal number the growth rate of Λ is observed to decrease, although there are fluctuations in the data, particularly at the end of the imaged region of the lowest Strouhal number case presented, Figure 5.3 (g). The rapid early growth rate of the integral length scale relative to the simple jet is deduced to be closely related to the character of the helical region (Chapter 4). It can also be seen that the centreline measure of integral length scale, Λ, is lower than that of the simple jet at the end of the imaged region for all values of Strouhal number. However, as the next section will show, the $R_\Lambda = 0.5$ contours indicate that the macro length scales away from the nozzle axis are increased relative to the simple jet by precession.

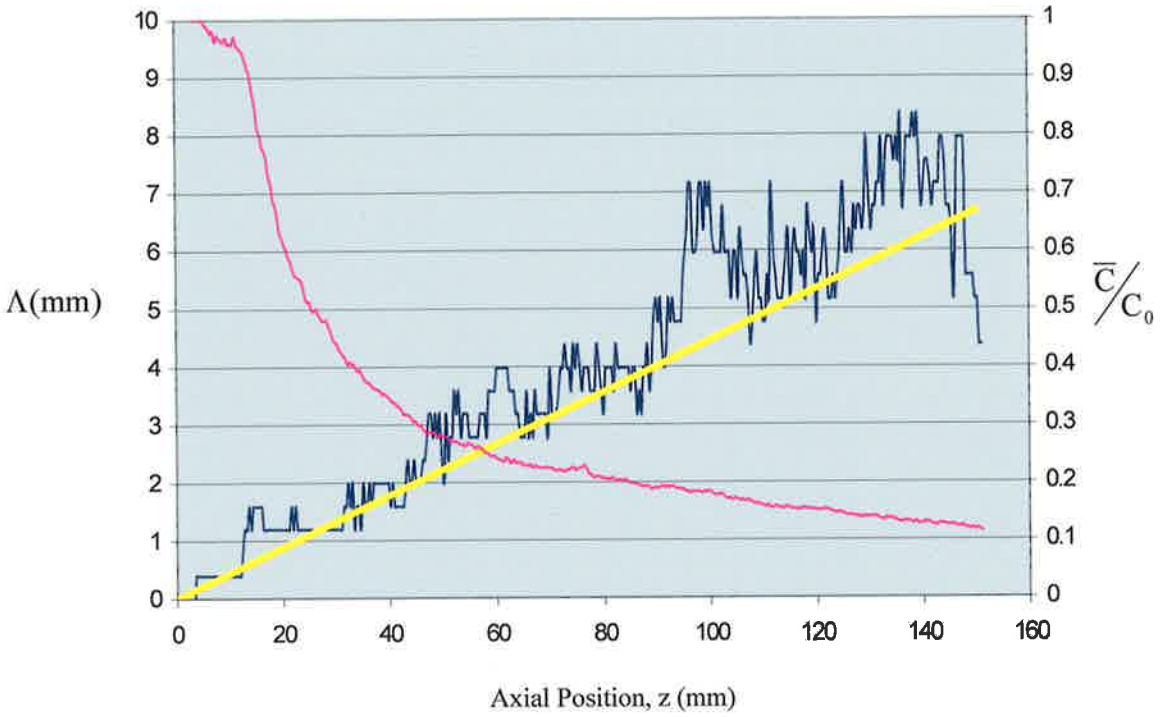

Figure 5.3(a) Re = 3,800; St = 0; $\phi = 0°$; d = 3mm

Figure 5.3(a-g) A measure of the integral length scale along the centerline of the various jet mixing fields, using the $R_\Lambda = 0.5$ contour of the two point spatial correlation. The local mean concentration relative to the exit value is also plotted to highlight the character of the mean mixing field. Exit conditions are as indicated on each graph.

Mean centre line concentration —— ;

$R_\Lambda = 0.5$ contour of the two point spatial correlation —— .

Result of Becker *et al.* (1967(b)) ——

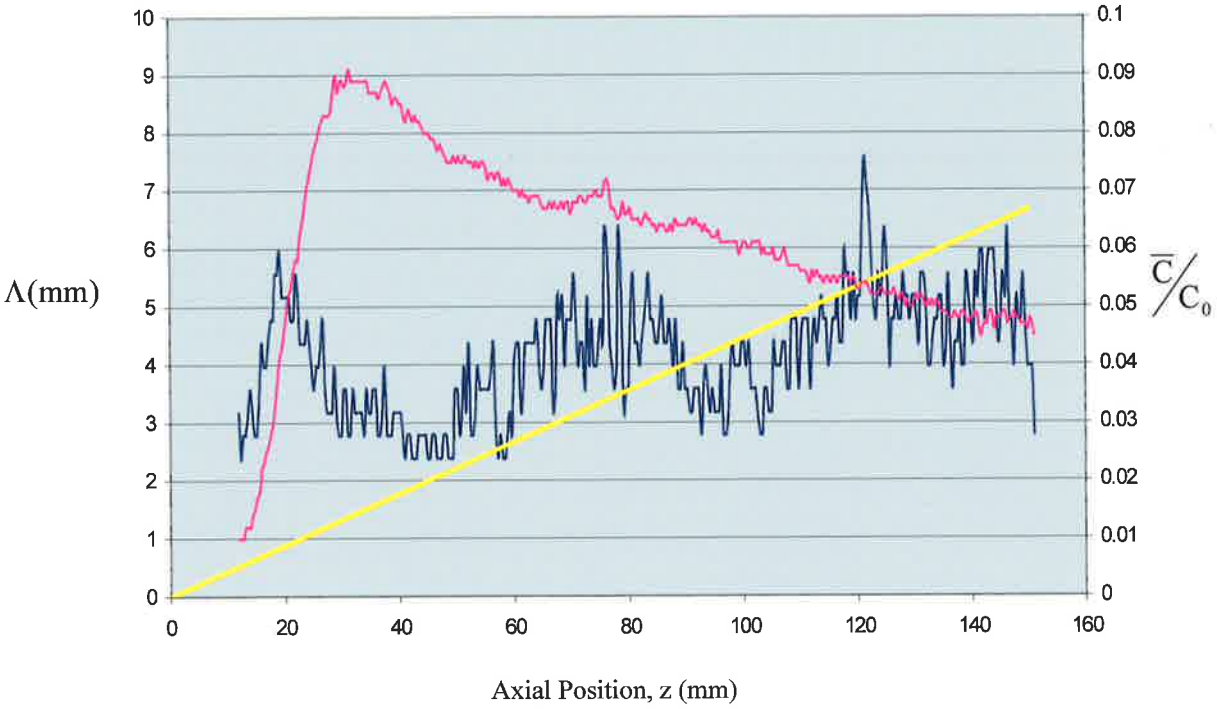

Figure 5.3(b) Re = 3,800; St = 0.015; $\phi = 45°$; d = 3mm

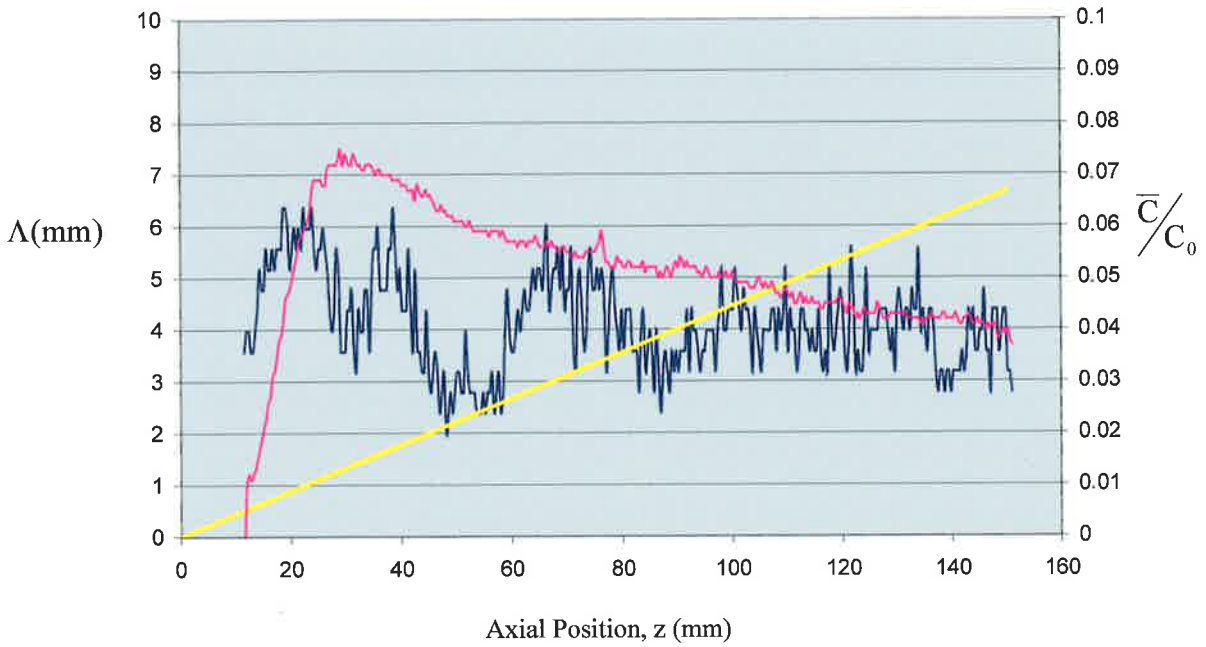

Figure 5.3(c) Re = 3,800; St = 0.0126; $\phi = 45°$; d = 3mm

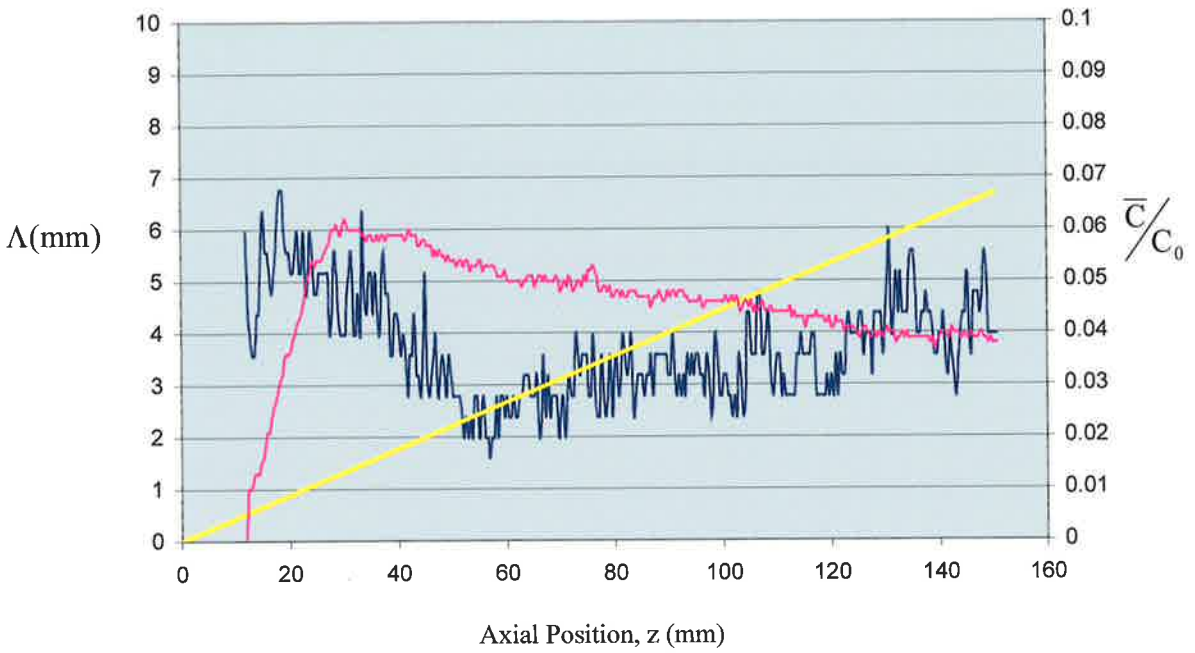

Figure 5.3(d) Re = 3,800; St = 0.011; ϕ = 45°; d = 3mm

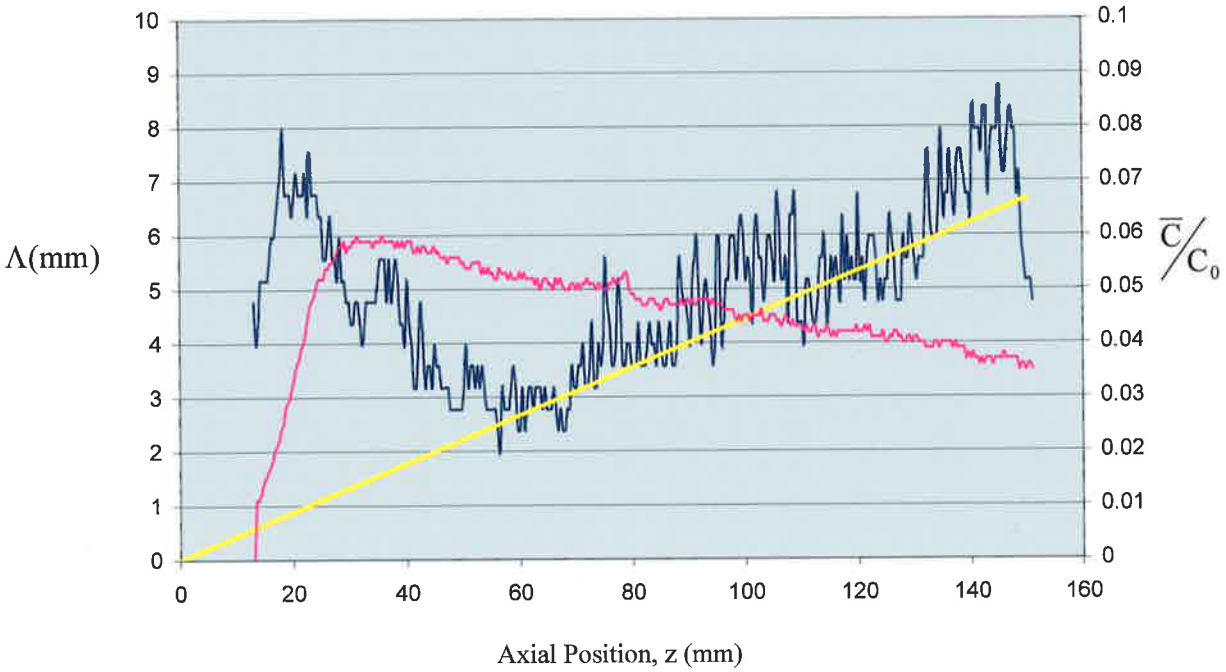

Figure 5.3(e) Re = 3,800; St = 0.0098; ϕ = 45; d = 3mm

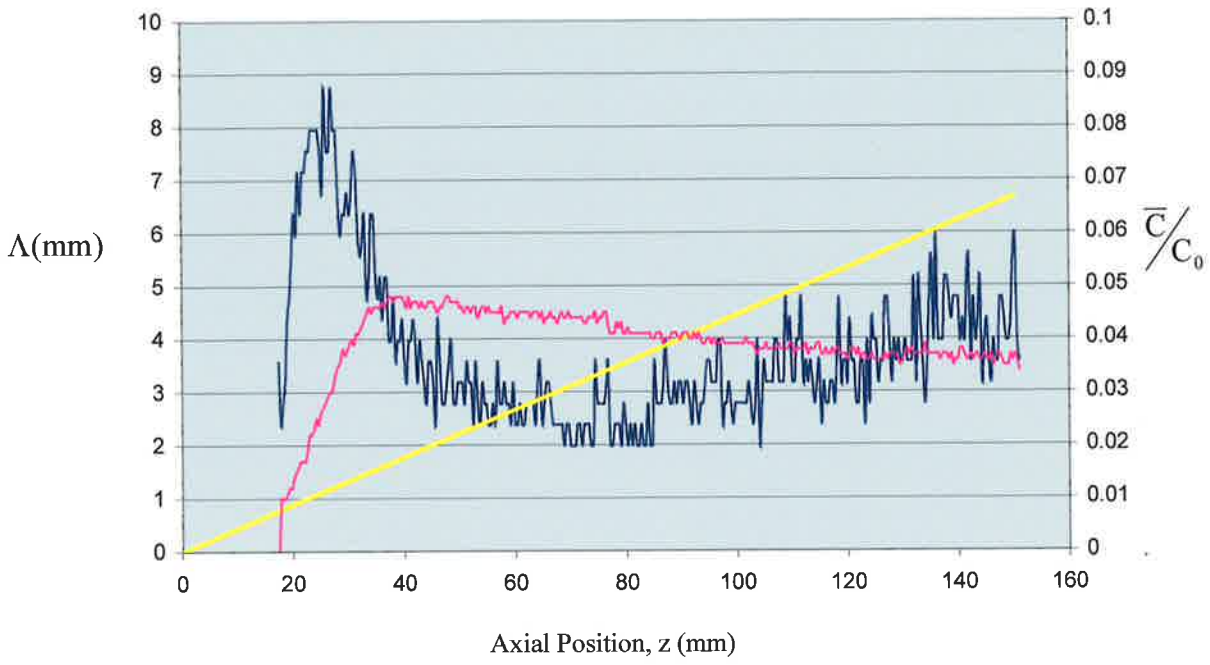

Figure 5.3(f) Re = 3,800; St = 0.0079; $\phi = 45°$; d = 3mm

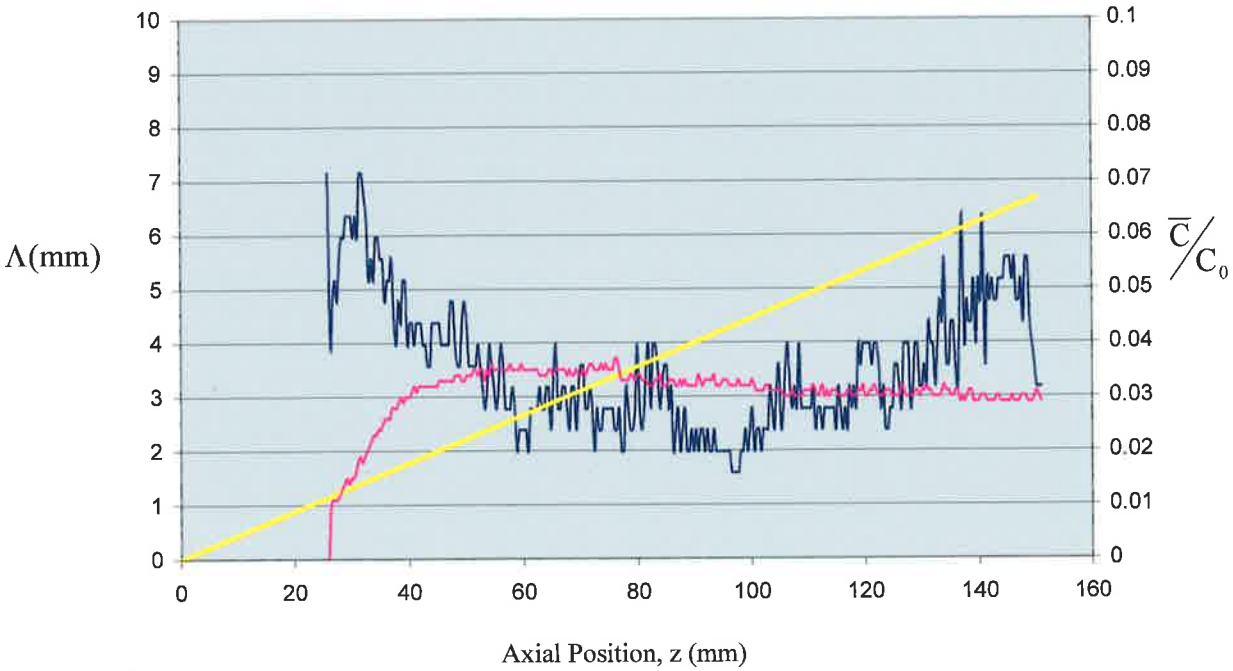

Figure 5.3(g) Re = 3,800; St = 0.0063; $\phi = 45°$; d = 3mm

5.3.2 Integral Length Scales in the Two - Dimensional Field

Two-dimensional plots of iso-contours of the R_Λ correlation for the simple jet and for the MPJ at Strouhal number values of St = 0.0126 and 0.0063 are presented in Figures 5.4 - 5.6 respectively.

Iso-contours for R_Λ = 0.5 and 0.8 for the simple jet case are presented in Figure 5.4. The flow field has similar characteristics to those of the simple jet used for validation, presented in Chapter 5.2. There is a linear increase in the magnitude of the length scale for increasing axial distance on the centreline. Both the R_Λ = 0.5 and 0.8 length scales are roughly symmetrical, implying the turbulence at these scales has a measure of isotropy along the centerline. However the R contours in the shear region are distorted at 45° toward the edge of the jet, as discussed earlier. Overall the simple jet has a narrow mean mixture field and shows the characteristic constant spreading angle.

The field of view in the data presented for the MPJ flows is the same as that for the simple jet to facilitate comparison. Thus it is not optimised for the display of the set of data. An interesting feature of this data set is the increase in magnitude of the length scales away from the centre line representative of large motions within the shear region.

To avoid the possible contamination by the cross flow observed in the highest Strouhal number data set presented in Chapter 4, a lower value of Strouhal number is used here. Thus, data for which St = 0.0126 will be presented for the "high" Strouhal number case.

In Figure 5.5(a), the contours of concentration have been superimposed on the R contours to characterise the physical extent of the mean mixing field. In the near field the helical, limit

cycle region can be distinguished from the far field, which in the mean, is axisymmetric about the spin axis. The length scale along the centreline is isotropic and the scale does not grow significantly in the axial direction, as shown in the centreline plot of Λ in Figure 5.3(c). Toward the outer edge of the mixing field the $R_\Lambda = 0.5$ iso-contour indicates that the length scale is distorted (anisotropic) and grows in size with increasing axial position. The distortion is evidence of a shear region away from the axis of the mixing field. The increased size of the $R_\Lambda = 0.5$ and 0.8 contours compared to Figure 5.4 would infer that the scale of structures within the shear region are larger. An instantaneous image of concentration under the conditions for this high Strouhal number case is presented in Figure 5.5(b). The presence of large structures spanning the entire width of the flow can be seen in this image. These structures are significantly larger than can be detected by the $R_\Lambda = 0.5$ contour in the imaged region. There are large regions of generally uniform concentration along the central region of the flow, consistent with the small value of calculated integral length scale, Λ. Large structures are also present at the very edge of the mixing field. The large, distorted R contours are probably a consequence of these structures and their motion within the shear layer.

The superimposed contours of the mean concentration field and the R contours for the low Strouhal number case in Figure 5.6(a) show the field to be physically wider than in the high Strouhal number case. A more detailed view of the phase-mean concentration fields can be seen in Chapter 4 for the two Strouhal number cases presented here. Generally, the concentration at the low Strouhal number is lower than for the high Strouhal number. This tend is also observed in the two instantaneous images of Figure 5.5(b) and 5.6(b). The helical foot print of the jet also extends further from the exit plane of the nozzle with lower Strouhal number.

The iso-contours of $R_\Lambda = 0.8$ within the low Strouhal number mixing field is presented in Figure 5.6(a). A clear difference between this and the high Strouhal number flow is the presence of a very broad central region of nearly isotropic length scales. The $R_\Lambda = 0.5$ iso-contour within the mixing field marked by the mean concentration contours are nearly circular and do not vary significantly in magnitude across this region of the field. As with Figure 5.5(b), large regions of relatively uniform concentration can be seen near the nozzle axis in the instantaneous image of Figure 5.6(b). At the outer edge of the mean field the contours grow in size and become elliptical, indicating again the presence of a shear region. However the aspect ratio of the elliptical contours appear less than in the simple jet case. The edge of the far concentration field dominated by large length scales, which are not particularly distorted. Evidence that the shear is not as strong as that seen by the highly distorted contours of the simple jet in Figure 5.4 and Figure 5.2.

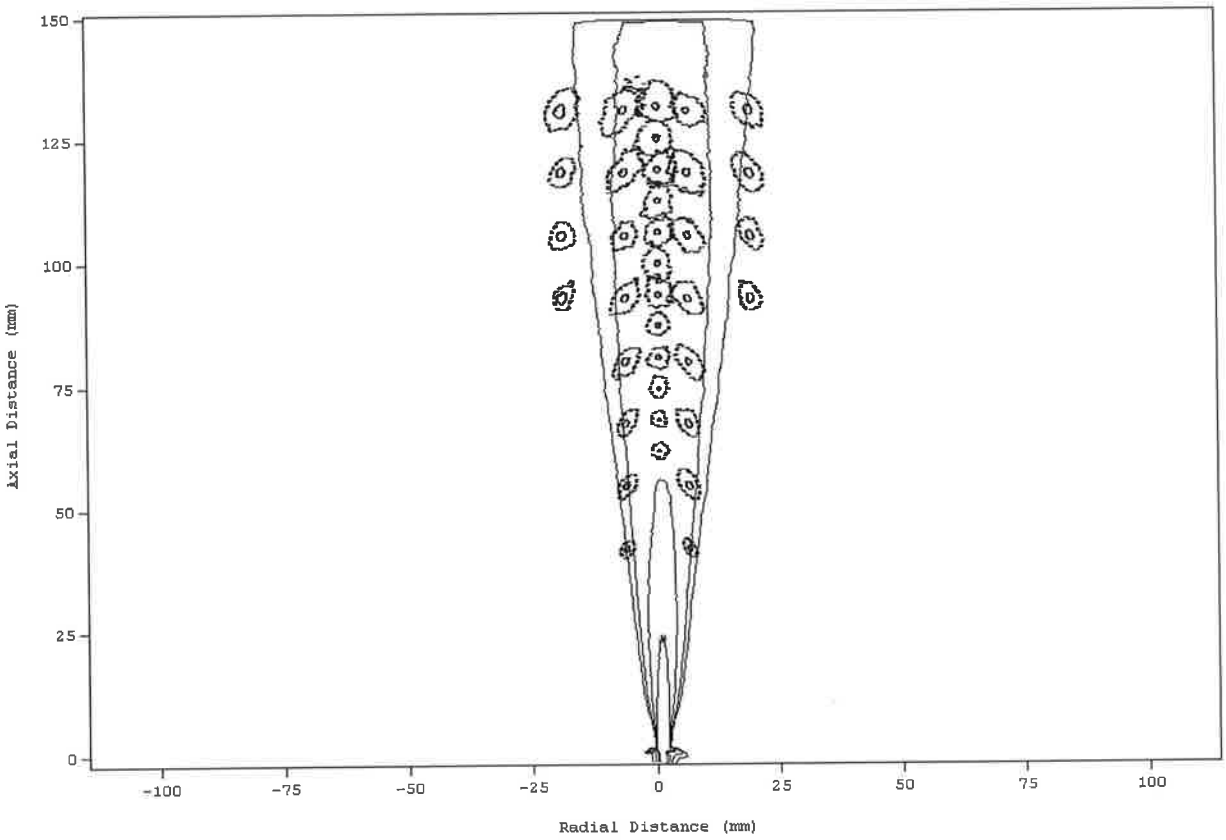

Figure 5.4 Iso-contours of the two-point spatial correlation for the Simple Jet. Re = 3,800; St = 0; $\phi = 0$; d = 3mm
$R_\Lambda = 0.8$: —
$R_\Lambda = 0.5$: .....
Mean concentration contours :—

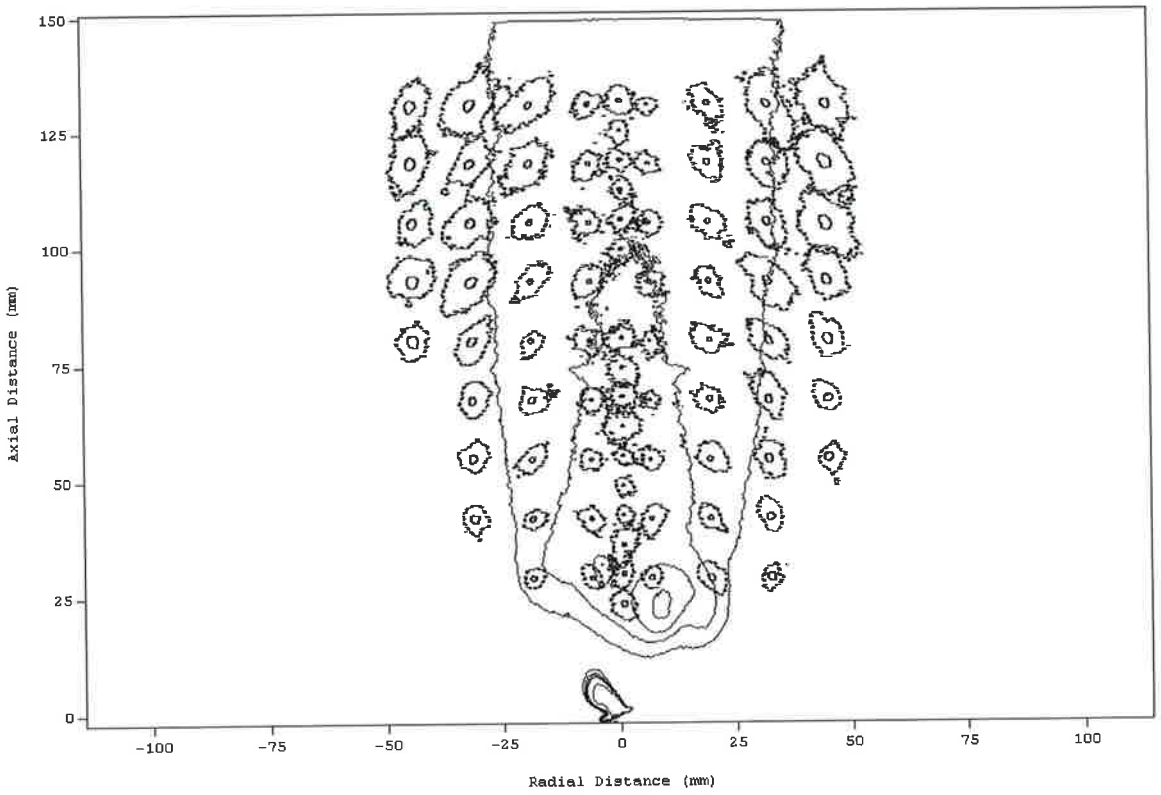

Figure 5.5(a) Iso-contours of the two-point spatial correlation coefficient, R_A, for the MPJ. Re = 3,800; St = 0.0126; $\phi = 45°$; d = 3mm (contours as per Figure 5.4).

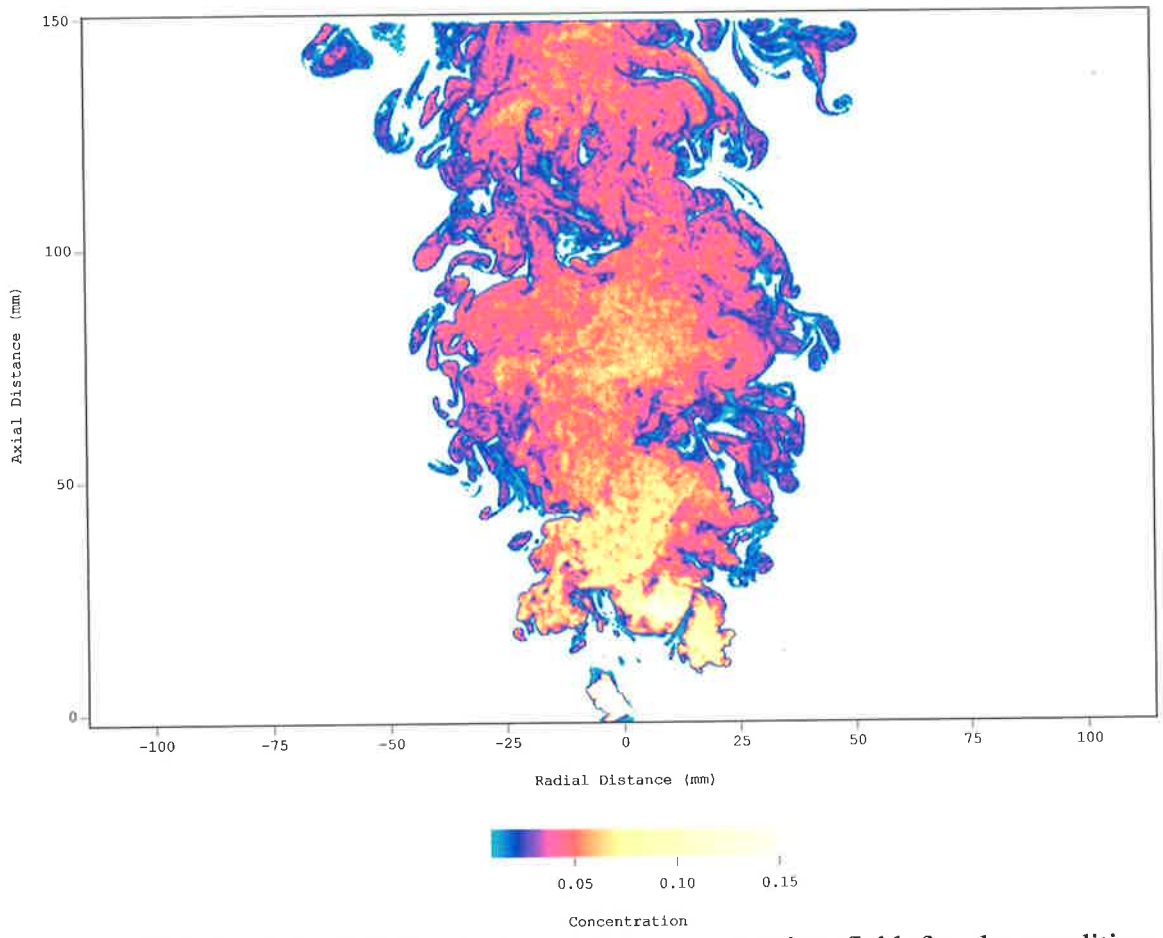

Figure 5.5(b) An instantaneous image of the concentration field for the conditions above.

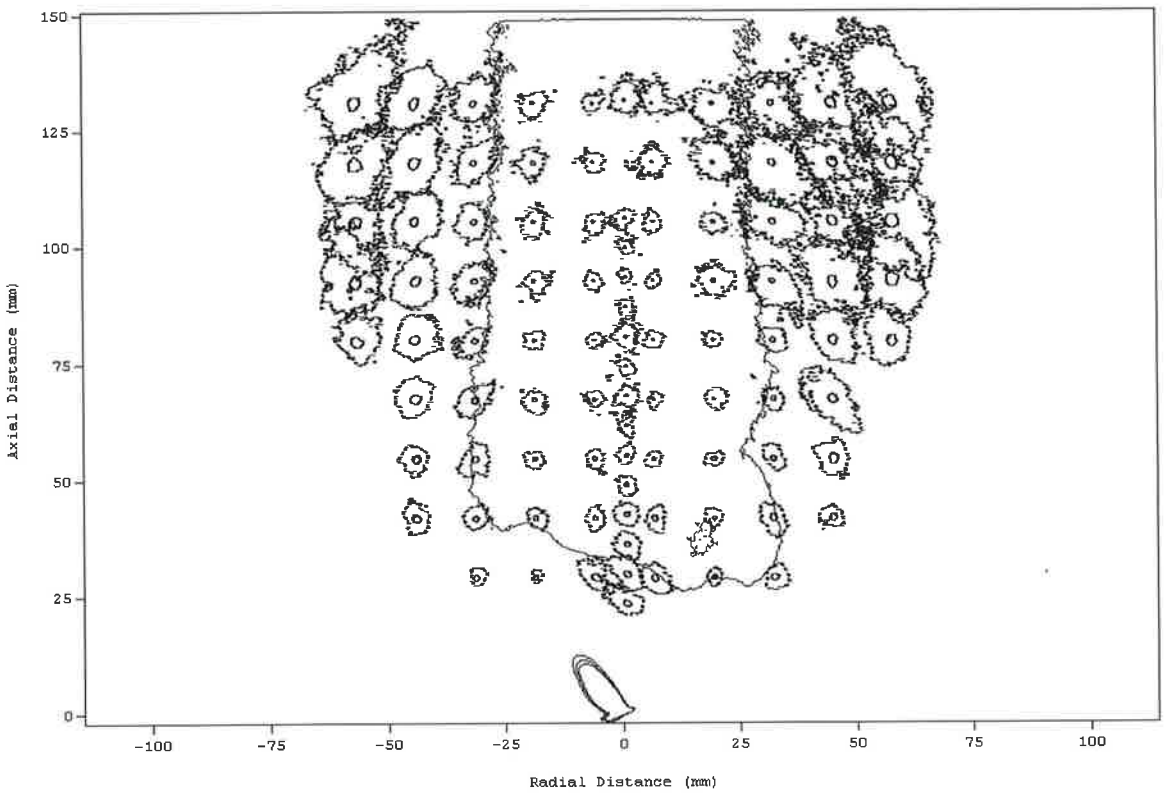

Figure 5.6(a) Iso-contours of the two-point spatial correlation coefficient, R_Λ, for the MPJ. Re = 3,800; St = 0.0063; ϕ = 45°; d = 3mm (contours as per Figure 5.4)

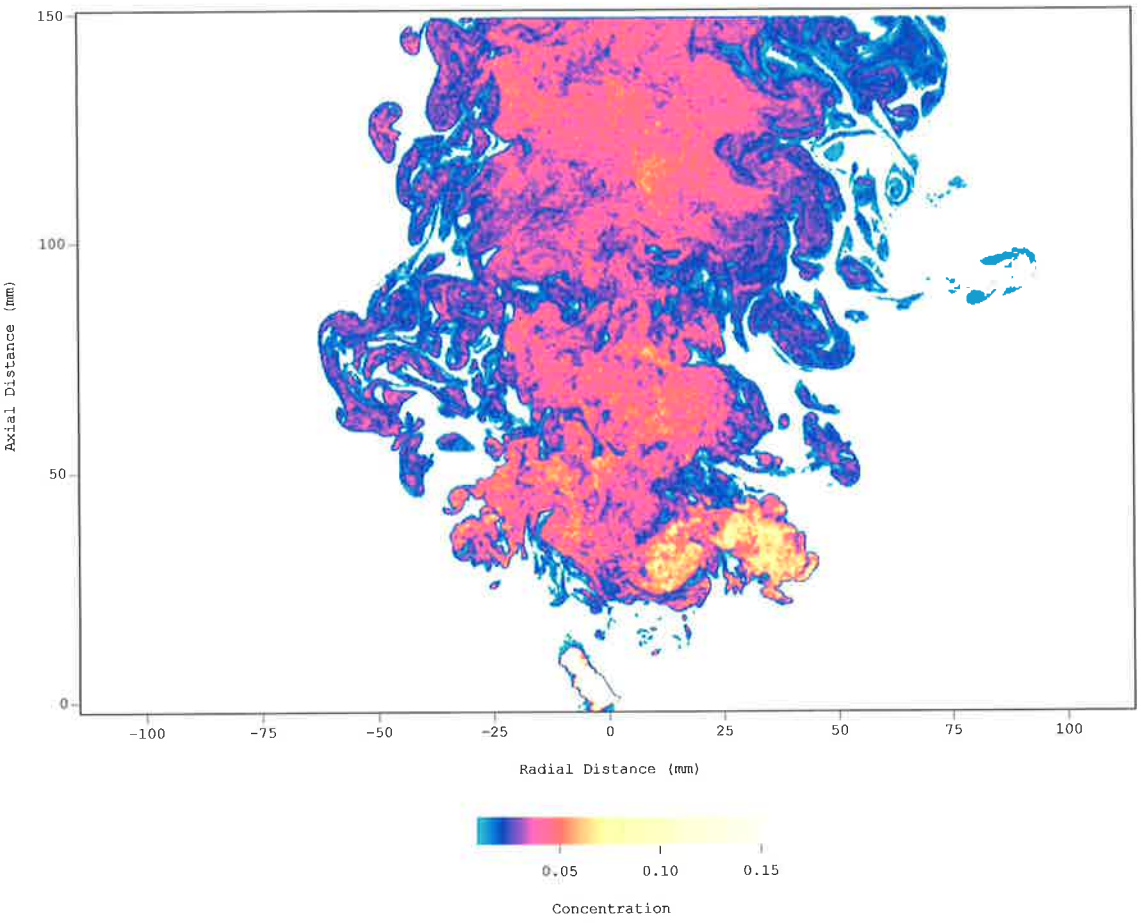

Figure 5.6(b) An instantaneous image of the concentration field for the conditions above

5.4 COMMENTS.

Precession of a jet is found to increase the magnitude of the integral length scale throughout the mixing field. Large scales are found at the edge of the MPJ mixing field, as found in the simple jet, however precession increases the size of these scales. If the distortion in the iso-contours of the two-point spatial correlation can be taken as a measure of the intensity of shear, then precession, in the near field reduces the intensity of shear. While in the far field the shear is indicative of a plume or the far field of a simple jet. The shape and magnitude of the iso-correlation contours can be directly related to instantaneous images.

If the mixing fields presented in this section were of a combustion system (i.e. natural gas fuel into air) some comments on the effect of change in length scales can be made. The concentration region corresponding to a flammable mixture, coloured yellow in Figure 5.5 (b) is predominantly located near to the base of the helical region and, above it, in the regions of low shear. In the region at the base of the helix, Λ is very much larger than occurs for the simple jet. That most of the flammable mixture is contained within regions of relatively isotropic length scales suggest that, if the flow were reacting, the reaction would occur under relatively low shear. This is consistent with the observed yellow (sooting) flames described by Nathan *et al.* (1996) and the measurements of Newbold *et al.* (1997) who show that strain in precessing jet flames is reduced relative to a momentum dominated jet flame.

6 EFFECT OF PRECESSION ON SCALAR MIXING

6.1 INTRODUCTION

Mixing comprises a combination of the velocity controlled process of turbulent diffusion the much slower, viscous limited molecular diffusion process. Reaction chemistry is related to which of these two mechanisms is dominant (Namazian *et al.* 1988). Scalar dissipation can be used as a measure of the rate at which two fluids mix. Schefer *et al.* (1994) considered scalar dissipation to be the rate at which concentration non-uniformities relax towards zero due to molecular diffusion. Thus scalar dissipation can be used as measure of the local rate of mixing at the molecular scale. The combustion community has recognized the influence of scalar dissipation on local mixing of two fluids as important in the prediction and understanding of turbulent combustion (Dibble *et al.* 1984). There are limited measurements of scalar dissipation in the literature even though it has been used as basis for combustion models (Namazian *et al.* 1988). The Probability Density Function (PDF) of the scalar can also be used in combustion models and provides a means for characterizing the scalar mixing field.

6.2 DEFINITION OF SCALAR DISSIPATION

There are several definitions for the formulation of scalar dissipation that can be found in the literature. The fundamental definition is based on the spatial gradient of scalar concentration (Schefer *et al*, 1994). Variations on this theme have included accounting for the effects of strain (Feikema *et al.* 1996) and a definition based on a temporal scalar gradient (Dowling, 1991). The fundamental definition based on the spatial scalar gradient is used here.

Instantaneous scalar dissipation, Φ, (in cylindrical coordinates) is defined as,

$$\Phi = \Phi_z + \Phi_r + \Phi_\theta, \qquad \text{Equation 6.1}$$

a sum of the axial, radial and azimuthal components of the scalar gradient. In general form the scalar dissipation in a given direction is defined following Schefer *et al*, (1994) as,

$$\Phi_i = 2D\left(\frac{\partial C}{\partial x_i}\right)^2, \; i = z, r, \theta \qquad \text{Equation 6.2}$$

where C is the conserved scalar jet fluid concentration, and D is the scalar molecular diffusion coefficient, which for air in air is, D = $1.5 \times 10^{-6} m^2/s$ and x_i is the direction in which the gradient is being calculated.

6.3 A MEASURE OF SCALAR DISSIPATION - THE SCALAR GRADIENT

Table 6.1 A comparison of the Kolmogorov (λ_k) and Batchalor (λ_b) scales flow the jet fluid and the marker particle at the nozzle exit.

	Reynolds number of the flow	Schmidt number	Nozzle Diameter d (mm)	λko (mm)	λbo (mm)	λkc at x/d = 100 (mm)	λbc at x/d = 100 (mm)
Air	16,400	0.7	3	0.0259	0.030928	1.1385	1.360824
Particle	16,400	38,000	3	0.0259	0.000133	1.1385	0.005841

A measure of scalar dissipation is assessed and presented here using the data set with the highest number of images used in the validation section, Section 2.3. The spatial resolution of the imaging devise of this set of data is 0.4 x 0.4 x 0.25 mm, several orders of magnitude larger than both the Kolmogorov and Batchalor scales at the nozzle exit (λ_{ko}, λ_{bo}), as shown in Table 6.1. However both λ_k and λ_b scale with distance from the nozzle. Scalar Dissipation is a measure of the molecular diffusion and definitive measurement will require resolution of the Batchalor scalar. Clearly the present experiment does not measure to that scale at the nozzle exit although the scale is resolved by the end of the imaging region. (see Table 6.1).

Furthermore, the marker particles have a significantly different Schmidt number to that of air resulting in Batchalor scales which are two orders of magnitude smaller. The results presented here cannot therefore be taken as definitive quantitative measurement of the scalar dissipation although, as is shown later, they do nevertheless agree well with other published measurements of scalar dissipation.

Presented here are measurements of the scalar gradients, which are used to investigate the effect of precession of the scalar gradient field, and to allow some insight to be drawn on the effect precession will have on the scalar dissipation. The instantaneous scalar gradient in an image is determined here using a 3x3 pixel central difference algorithm, based on a Roberts filter. Thus, the scalar gradient in the axial direction (z direction) at a point in an image is calculated using;

$$\frac{\partial C}{\partial z} = \tfrac{1}{8}\left[C_{(z+1,r+1)} - C_{(z-1,r+1)}\right] + \tfrac{1}{4}\left[C_{(z+1,r)} - C_{(z-1,r)}\right] + \tfrac{1}{8}\left[C_{(z+1,r-1)} - C_{(z-1,r-1)}\right]$$

Equation 6.3

The mean value of the scalar dissipation in a particular direction is calculated using a conventional averaging scheme. A total mean scalar gradient is calculated at each point using

$$\nabla C = \left(\frac{\partial C}{\partial z}\right)^2 + \left(\frac{\partial C}{\partial r}\right)^2 + \left(\frac{\partial C}{\partial \theta}\right)^2$$

Equation 6.4

which is proportional to Equations 6.2, by assuming partial isotropy, i.e. that azimuthal component is equivalent to the radial component, following the practice adopted by Namazian *et al.* (1988) and van Cruyningen *et al* (1990). It is clear from previous discussion that this is a crude assumption, especially away from the centerline of the flow. Nevertheless the results are sufficient to allow qualitative results to be drawn from the data on the effects of precession.

Further verification of how well the experimental technique resolves the scalar gradient can be made through a comparison of data collected and reported in the literature. Namazian *et*

al.(1988) resolved the scalar dissipation field of a 5.1 mm diameter jet of methane issuing from a pipe nozzle at a Reynolds number of 7,000 using a Raman scattering technique. A comparison of the data is shown in Figure 6.1, radial plots of scalar dissipation, as defined by Equation 6.1 against the normalized half radius of the jet, following Namazian *et al.* (1988). In this plot the data of Namazian *et al.* (1988) is obtained at x/d = 9, while data from the present measurements is plotted at x/d = 9 and 10. The plot shows that there is reasonable agreement between the measured scalar dissipation obtained from both techniques. There are differences in the shape of the profiles and an offset in the virtual origin by one diameter. The differences, though significant, are of the same order as can be expected from differences between pipe flow (Namazian *et al*, 1988) and a smooth contraction (present) and the fact that Namazian's data was of a system with different density fluids. Figure 6.1 shows that present planar measurement of the scalar field using Mie scattering does provide a reasonable measure of the scalar dissipation. The point of interest in the following sections is the effect of precession on the scalar gradients, and hence the term scalar gradient will be used for the variable defined by Equation 6.1.

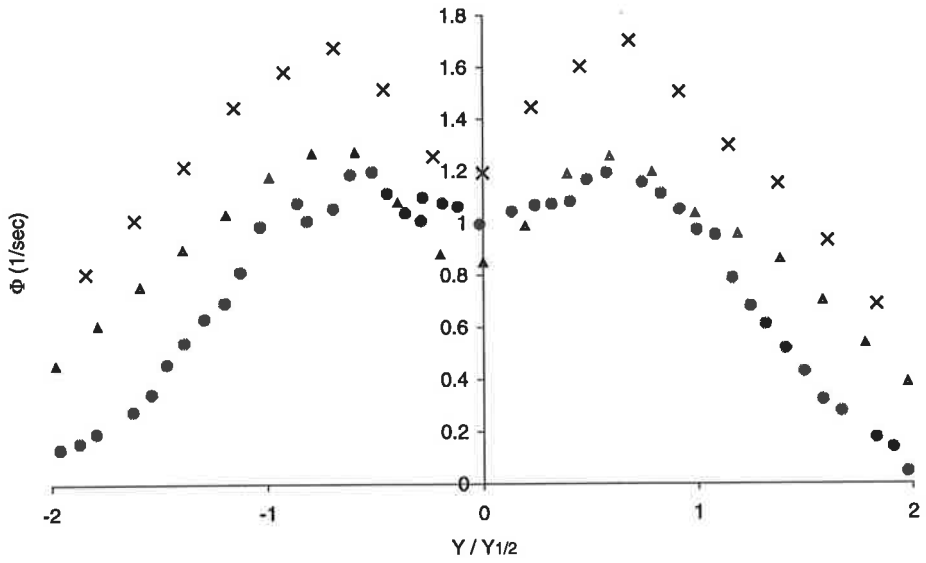

Figure 6.1 A comparison of the radial profiles of scalar dissipation in the near field of a jet. Present data set, Re = 16,400, smooth contraction nozzle: × ; x/d = 9: ▵ ; x/d = 10. • ; Namazian *et al.*(1988), Re = 7,000, pipe nozzle, at x/d = 9.

6.4 INSTANTANEOUS IMAGES OF THE SCALAR GRADIENT

Using Equation 6.4 the total scalar dissipation, the scalar gradient can be calculated for each point in an individual planar image of the concentration field. Instantaneous images of the concentration field and the calculated scalar gradient field are presented in this section for the simple jet and for the high and low MPJ flows that have also been presented in the previous sections.

A randomly selected instantaneous concentration field for the simple jet is presented in Figure 6.2(a). Structures along the edge of the mixing field in the shear region can be clearly identified. Clear examples of an edge structure are the mushroom shaped protrusions on the right side of the mixing field located at 75 millimeters from the exit and the structure at 100 millimeters on the left side of the jet. Structures of the order of the width of the jet are also apparent using the regions of different colour to identify regions of different concentration.

The scalar dissipation field for the instantaneous concentration image of Figure 6.2(a) has been calculated and is presented in Figure 6.2(b). The colour scale is presented logarithmically to allow a broad range of the scalar dissipations to be distinguished. Peaks in the scalar dissipation field in the region near to the potential core are observed along the edge of structures, forming layers. These layers are observed visually to be at an angle of about 45° from the axis of the flow. In the far field the layers are still associated with the edge of some structures but have become more isotropic. This is consistent with the observations of Feikema *et al.* (1996) and Namazian *et al.* (1988). Layers of peak scalar dissipation are also observed at the interface between jet fluid and ambient fluid. This can be clearly seen at the edge of the above mentioned mushroom structures and structures in the shear layer.

An instantaneous image of concentration for the low Strouhal number case is presented in Figure 6.3(a). Note that the colour scale has been changed relative to Figure 6.2(a) to maximize the clarity in each image. Structures of relatively high concentration associated with the helical region in the near field are apparent. Concentration along the centre line contains regions of quite uniform concentration, broken up by structures of the order of the width of the jet. Along the edge of the jet, in the shear layer region, large vortical shaped / mushroom shaped structures are observed (see Chapter 5, for an estimate of the length scale).

The magnitude of scalar dissipation in all parts of the flow produced by the MPJ nozzle, except for the emerging jet, is very much lower than that in the simple jet. As a result the bandwidth of the colour scale for the scalar dissipation images in Figure 6.3(b) and Figure 6.4(b) are adjusted by two orders of magnitude to provide optimum clarity in each image.

Layers of high scalar dissipation are observed on the outer edge of the structures in the helical region of the low Strouhal number jet (Figure 6.3(b)). Layering is also apparent about the outer edge of structures along the edge of the flow. Throughout the central region of the mixing field the magnitude of scalar dissipation is two orders of magnitude lower than occurs in a simple jet, again indicating large regions of uniform concentration and low strain rate. In contrast to the simple jet flow, in which the layers of high scalar dissipation are typically aligned at about 45° to the direction of mean flow, there is no characteristic pattern or direction of the layers in the MPJ flow, other than large wrinkling at the outer edge of structures. This is further indication that there is no prominent direction of shear within a larger central region of the flow, supporting the findings of the isotropic nature of the integral length scale in Chapter 5.

The colour scales quantifying concentration and scalar dissipation are the same for the low (Figure 6.3) and high (Figure 6.4) Strouhal number flows to facilitate direct comparison.

Similar general features can be found for both flows, but magnitudes differ substantially. For example, the proximity of the collapsing helix, containing large structures, is closer to the nozzle for the higher Strouhal number, the concentration is higher and the characteristic width of the mixing field is generally narrower. The higher concentrations throughout the mixing field of the high Strouhal number coincides with generally higher values of scalar dissipation and higher peak dissipation in the layers (Figure 6.4(b)). The presence of layers of scalar dissipation right across the central region of the mixing field can be seen in both Strouhal number flows, but sparsely spaced, consistent with the scale of the dominant motions being very large. Layers of high scalar dissipation correlate with the edge of large structures of uniform concentration spanning the whole mixing field. The presence of ambient or low concentration fluid between the structures is indicative of large-scale vortical motions and increases the magnitude of scalar dissipation in this region. Nevertheless the observed concentration values are relatively low, compared to a simple jet.

The effect of precession on the mixing of the jet of fuel in a combusting system has been observed to be significant, as mentioned in the introduction to this thesis. The importance of mixing and the features of the mixing fields of the described flows can be highlighted with regard to a combusting system utilizing these flows. One important fuel, as discussed in Chapter 5 is natural gas (predominantly CH_4) and the dominant oxidant is air which corresponds to flammability limits over the range of $0.05 < C < 0.15$.

Schneider (1997) observed that the mean velocity decay rate of an MPJ flow is increased for increasing values of Strouhal number, resulting in a mixing field of generally low velocity for high values of Strouhal number. This and the observation that scalar dissipation within the layers throughout the mixing field increases with increasing Strouhal number indicates that molecular diffusion could be a more significant, (possibly even the dominant) mode of scalar transport than occurs in a simple jet. Naturally, the large-scale turbulent motions are

responsible for the large-scale engulfment of "ambient" or low concentration flowed into layers around the jet fluid.

While the concentration at the base of the helix is high, that within the merging region of the helix (the transition region) has a lower concentration than that in the core of a the simple jet at the same axial location. No part of the core region of the simple jet flow reaches a concentration corresponding to a flammable mixture until the top of the imaged area (z = 125mm), which is significantly into the far field from a combustion view point. By contrast, the entire core region of the flow produced by the MPJ flows (Figures 6.3(a) and 6.4(a)) are at or below the upper flammability limit. This highlights that there is high entrainment of air within the developing region of the helix, a result of the high shear present. The concentration in the core of the flow beyond the helix region is lower for the low Strouhal number flow (Figure 6.3(a)) being permanently fuel-lean than for the high Strouhal number flows (Figure 6.4(a)) which is, predominantly fuel-rich. This is consistent with observations of MPJ flames in which the low Strouhal number flames are generally small and blue, while the high Strouhal number flames are yellow and buoyant (Nathan *et al.* 1996).

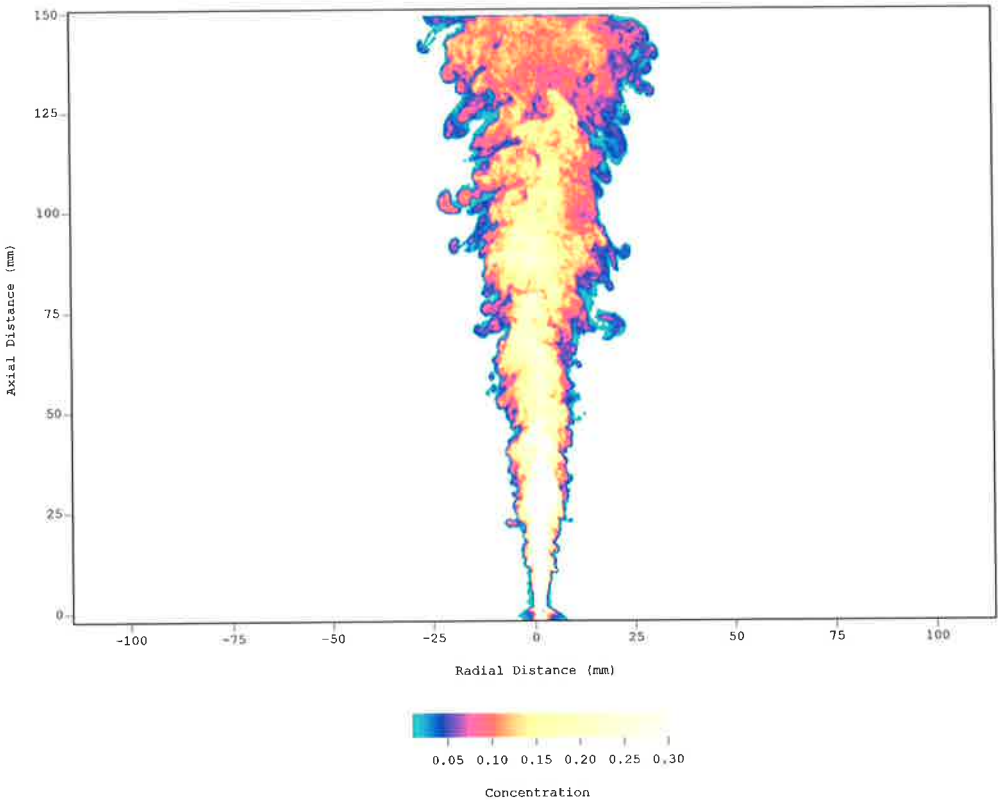

Figure 6.2(a) Simple jet instantaneous concentration field.
Re = 3,800; St = 0, $\phi = 0°$; d = 3mm

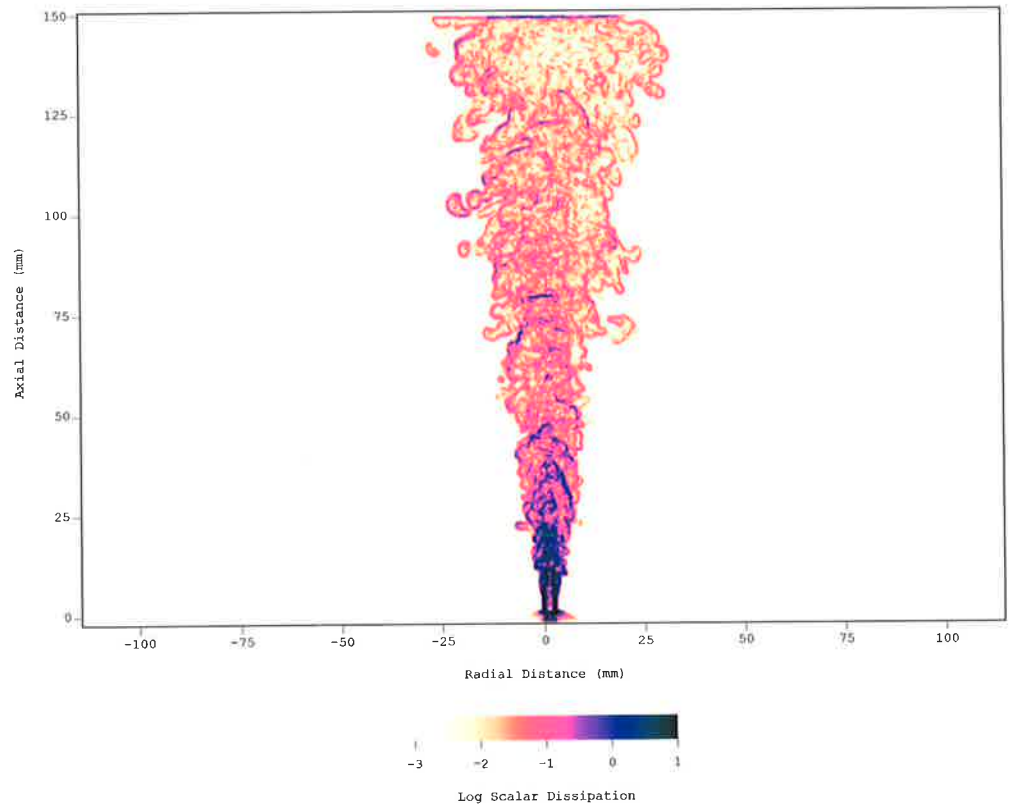

Figure 6.2(b) Simple jet instantaneous scalar dissipation field.
Re = 3,800; St = 0, $\phi = 0°$; d = 3mm

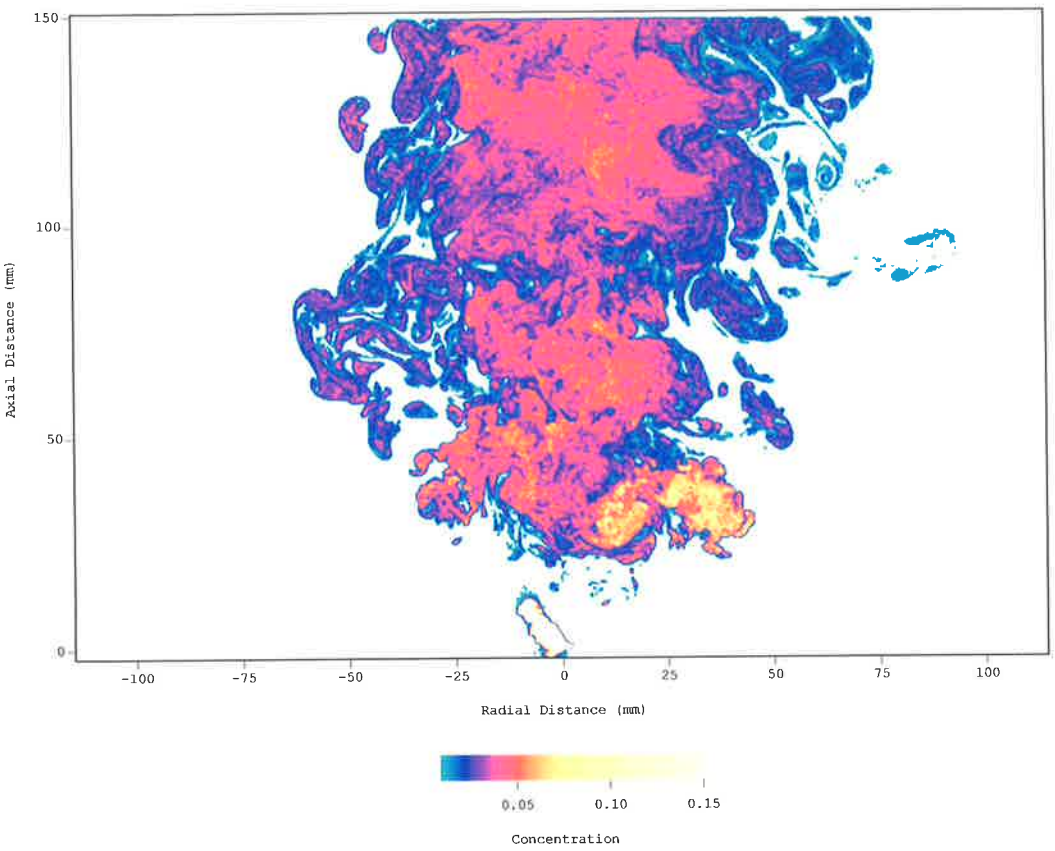

Figure 6.3(a) MPJ instantaneous concentration field – low Strouhal number case. Re = 3,800; St = 0.0063, $\phi = 45°$; d = 3mm

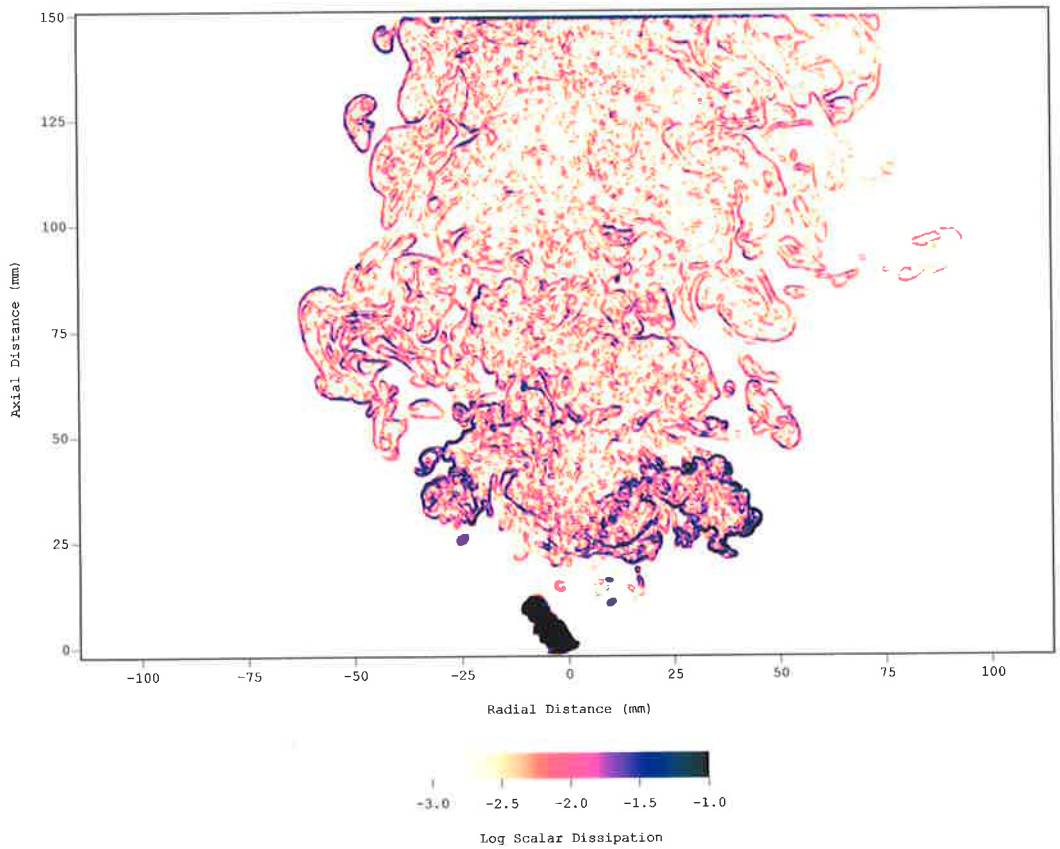

Figure 6.3(b) The instantaneous scalar dissipation field of Figure 6.3(a)– low Strouhal number case. Re = 3,800; St = 0.063, $\phi = 45°$; d = 3mm

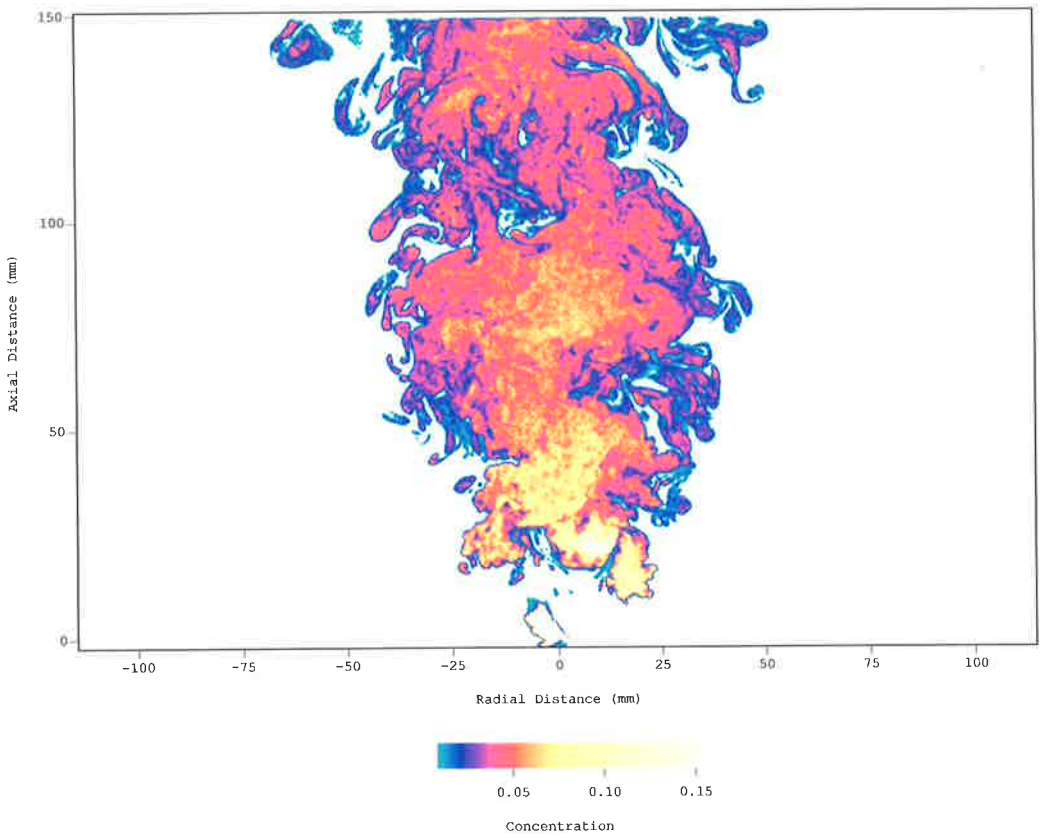

Figure 6.4(a) MPJ instantaneous concentration field – high Strouhal number case. Re = 3,800; St = 0.0126, ϕ = 45°; d = 3mm

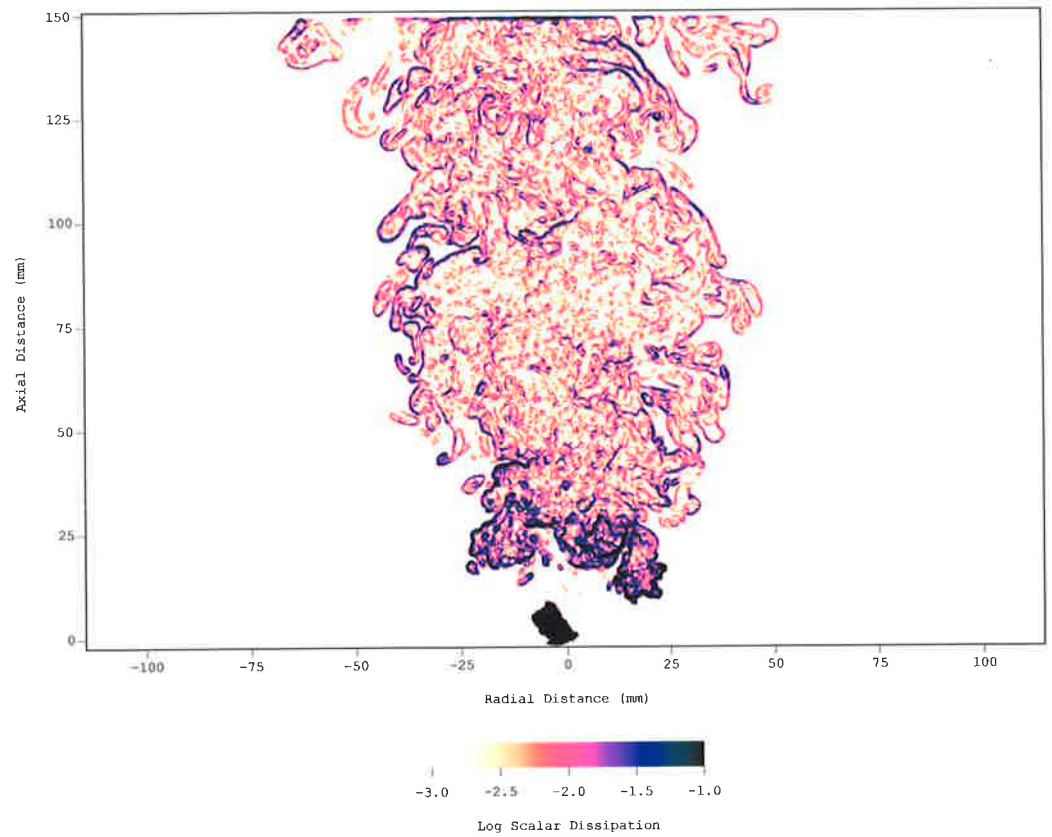

Figure 6.4(b) The instantaneous scalar dissipation field of Figure 6.4(a) – high Strouhal number case. Re = 3,800; St = 0.0126, ϕ = 45°; d = 3mm

6.5 MEASUREMENTS OF MEAN SCALAR DISSIPATION

Planar images of the average scalar dissipation field for the simple jet flow and for various classes of the MPJ flow are presented in Figure 6.5(a-h). The bandwidth of the (logarithmic) colour scale that quantifies scalar dissipation is consistent for all images. All of the mean scalar dissipation images are markedly different from the instantaneous images. In particular, the layers of high scalar dissipation, which are a significant feature of the instantaneous flow field are not present in the average fields.

Maximum values of mean scalar dissipation in the planar field of the simple jet (Figure 6.5(a)) are found in the near field region and are measured to be in the range of $30s^{-1}$. Scalar dissipation decreases with axial distance but does not fall to zero along the centerline of the jet also found by other experimental work (Feikema *et al.* 1996; Namazian *et al.* 1988), in contrast to the predictions of the mixing model of Feikema *et al.* (1996). Although not clearly evident in this image, the maximum values of scalar dissipation at a given axial position are found away from the axis, at radial locations which correspond to the regions of maximum shear in the jet, consistent with the literature (Feikema *et al.* 1996; Namazian *et al.* 1988).

Images of the scalar dissipation field for various Strouhal numbers are presented in Figure 6.5(b-h). All of the images show general features associated with the helical flow, which have been observed in other sections of this thesis. The emerging jet at the angle of deflection and the wide initial spreading of the mixing field are clearly evident. The measured magnitude of mean scalar dissipation for all of the MPJ flows are significantly lower than that measured for the simple jet case at an equivalent axial position, consistent with the lower measured values of concentration within the in the MPJ flow fields. The highest values of scalar dissipation are found to occur around the region of the emerging jet. The far field is

identified with having low values of nearly consistent scalar dissipation across the range of Strouhal number cases presented. The most significant effect of increased Strouhal number is the increase in scalar dissipation around the structures associated with the 0°, 180° and 360° slices through the helical region of the flow. The increased peak scalar dissipation is observed to correlate with the increase in mean concentration, that also occurs with increased Strouhal number.

Plots of scalar dissipation along the jet centerline for each of the flows presented in Figure 6.5 are plotted in Figure 6.6. The plot highlights the significant difference in magnitude of scalar dissipation between the simple jet and the various types of MPJ flow. However it should be noted that the peak values of scalar dissipation for the MPJ flows occur away from the axis, so that this data is most relevant in the far field. Some trends of the effect of Strouhal number of precession on the scalar dissipation field can be observed from this plot. Scalar dissipation throughout the flow field is higher for high values of Strouhal number. With increasing Strouhal number, scalar dissipation decay in the far field appears to approach a lower constant value. The magnitude of the field dissipation decreases with decreased Strouhal number, for the range of Strouhal numbers examined.

A peak of maximum mean centerline scalar dissipation is measured in all of the flows, including the simple jet, in the near field region. For the simple jet case this peak occurs at z/r = 10, just past the end of the potential core. Interestingly, its location coincides closely with the peak in the centerline unmixedness (Figure 4.10) and is therefore deduced to be associated with the high fluctuations at the end of the potential core. The position of the peak also correlates with the concentration of the layers of high scalar dissipation in the instantaneous images of Figure 6.2(a) where high concentration jet fluid is in close proximity to ambient fluid.

For the MPJ cases, the peak in mean centerline scalar dissipation is associated with the merging or collapsing of the helical region where large scale flow structures and the presence of ambient fluid across the centerline are evident in the limit cycle region of the flow. For the low Strouhal number cases the peak is further from the nozzle than for the high Strouhal number cases, following the trend in the position and shape of the collapsing helical region.

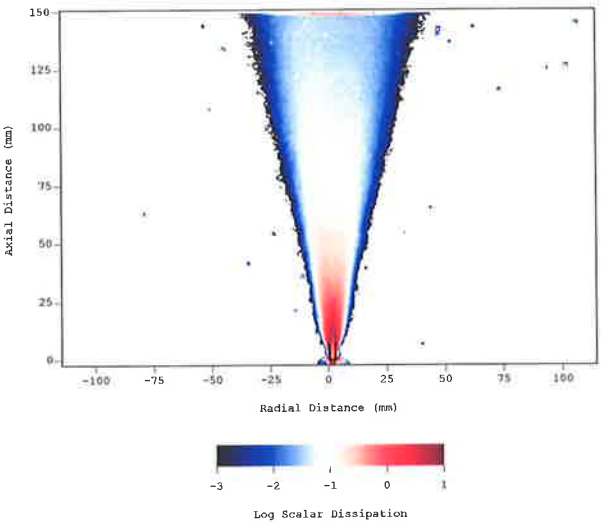

Figure 6.5 (a) Re = 3,800; St = 0; $\phi = 0°$

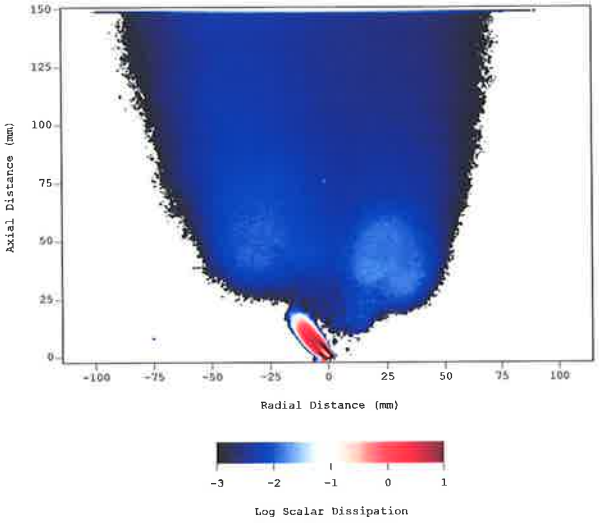

Figure 6.5 (b) Re = 3,800; St = 0.0047; $\phi = 45°$

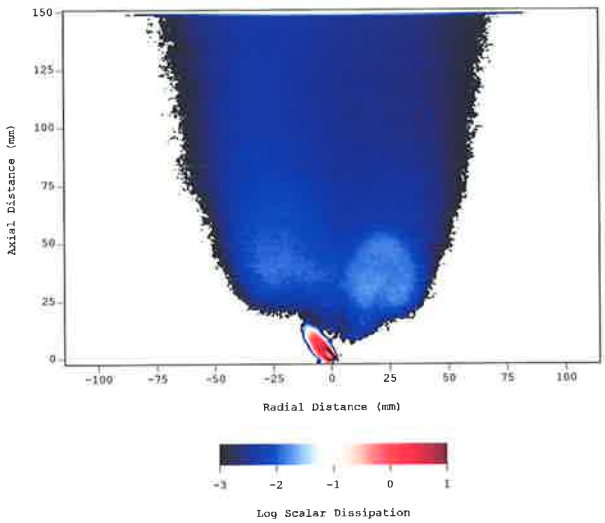

Figure 6.5 (c) Re = 3,800; St = 0.0063; $\phi = 45°$

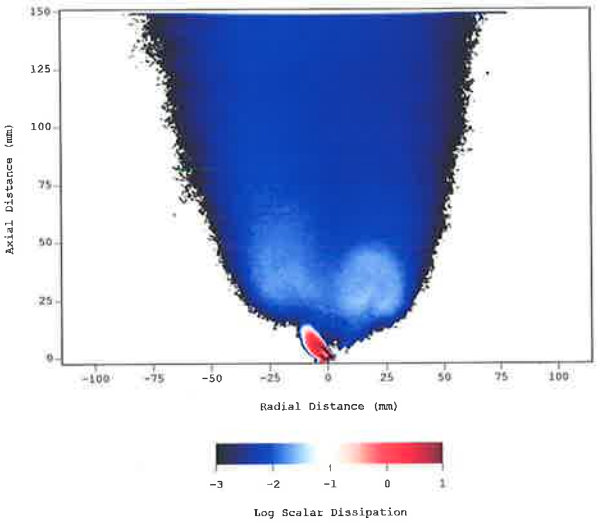

Figure 6.5 (d) Re = 3,800; St = 0.0079; $\phi = 45°$

Figure 6.5 Phase averaged mean scalar dissipation fields

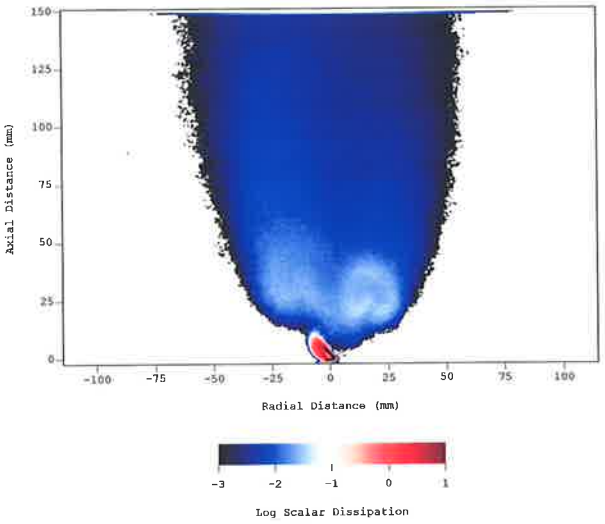

Figure 6.5 (e) Re = 3,800; St = 0.0098; $\phi = 45°$

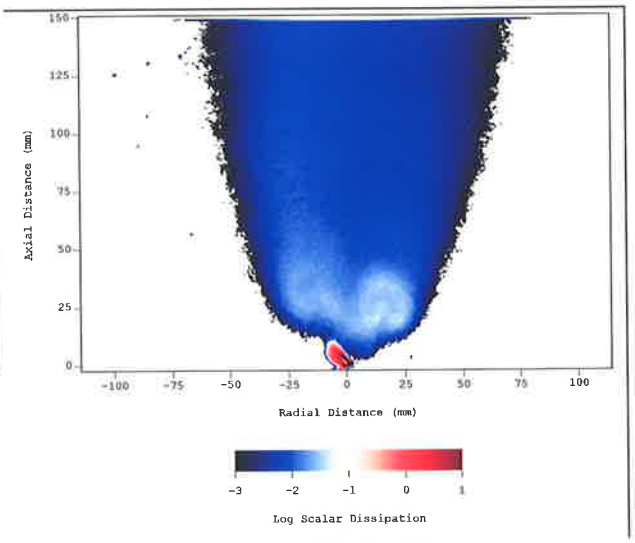

Figure 6.5 (f) Re = 3,800; St = 0.011; $\phi = 45°$

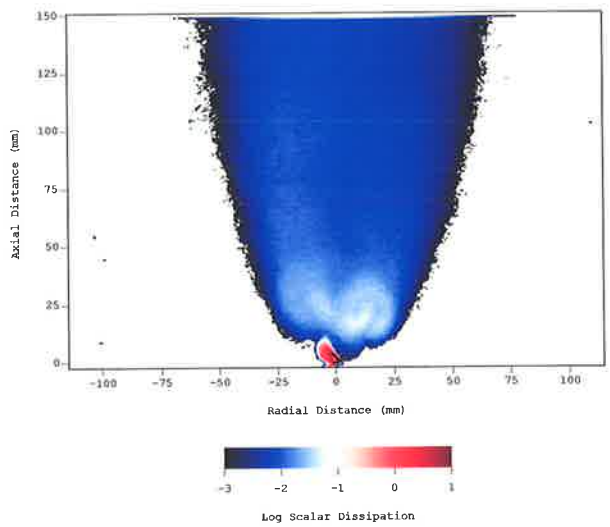

Figure 6.5 (g) Re = 3,800; St = 0.0126; $\phi = 45°$

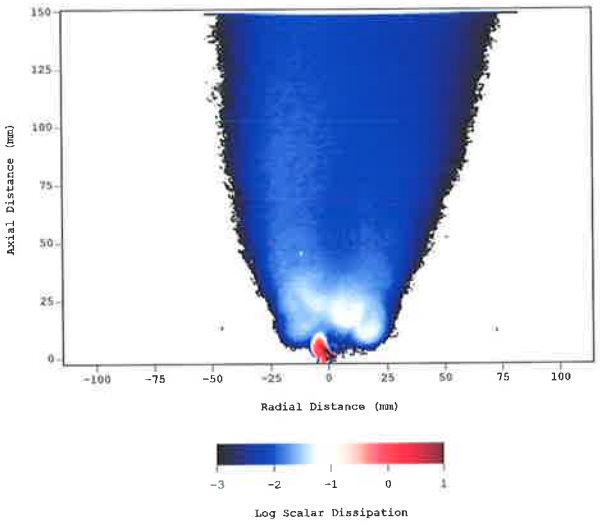

Figure 6.5 (h) Re = 3,800; St = 0.015; $\phi = 45°$

Figure 6.5 Phase averaged mean scalar dissipation fields

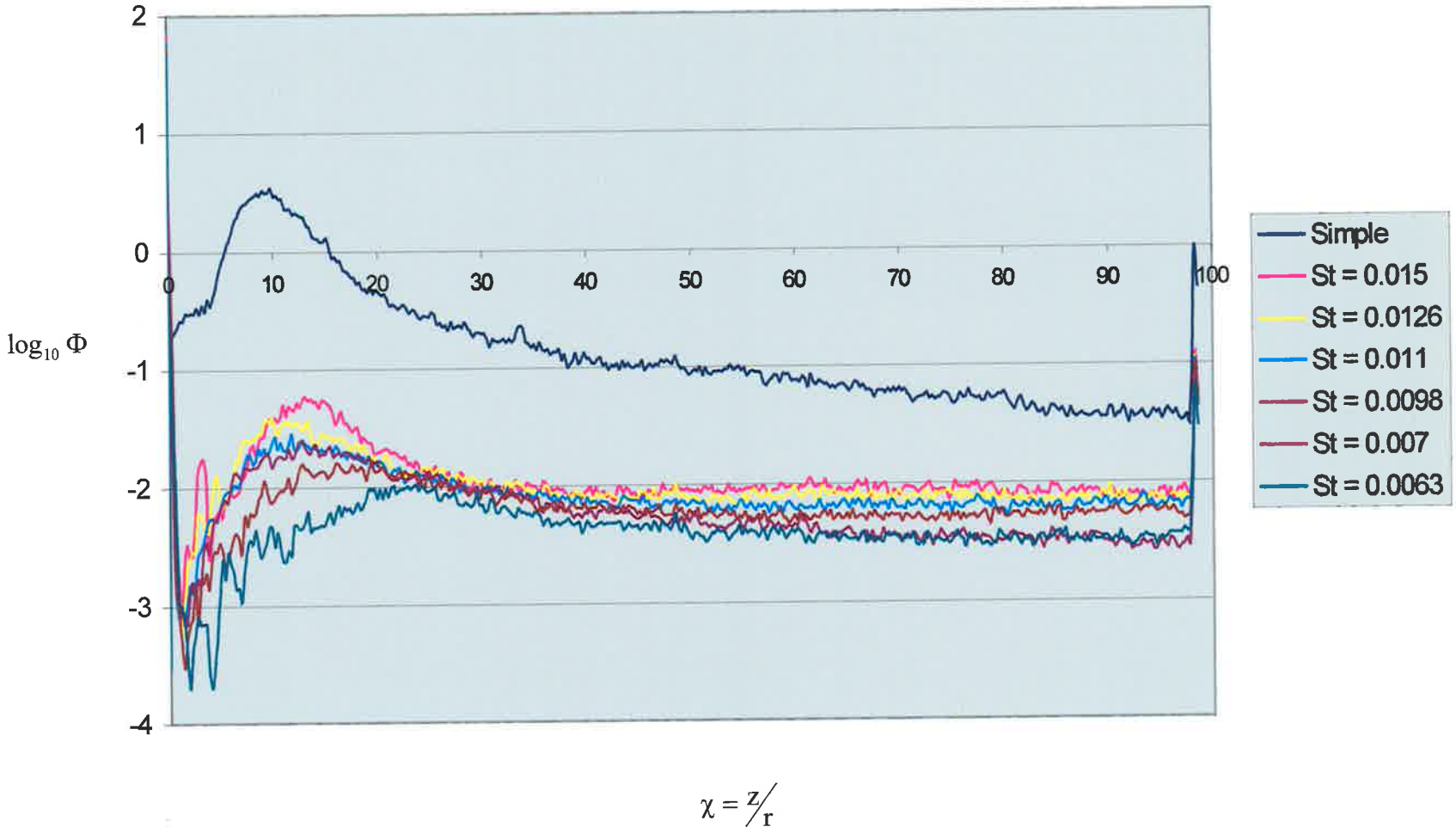

Figure 6.6 Mean scalar dissipation (Φ) along the centre line of the jet flow fields. Re = 3,800 d = 3mm. MPJ; $\phi = 45°$

6.6 FAR FIELD PROBABILITY DENSITY FUNCTION (PDF) OF SCALAR CONCENTRATION

The character of the mixing field can also be investigated through the Probability Distribution Function (PDF) of concentration. A histogram of the instantaneous concentration divided by the local mean concentration, C/ $\overline{C}$, is divided into bins and is normalized so

$$\int_0^\infty \mathrm{PDF}\left(\frac{C}{\overline{C}}\right) d\frac{c}{\overline{C}} = 1. \qquad \text{Equation 6.5}$$

A PDF is usually calculated at a single point in space. However good resolution of the PDF requires a large number of data points. The present data sets contain 400 images of each flow condition. To increase the number of samples used to build the PDF a region of 100 pixels in the far field along the jet centerline corresponding to $70 < z/r < 95$ has been used. The results are presented in Figure 6.7.

The distribution of concentration for the simple jet flow is seen to be symmetrical about the mean value and to have a peak probability of 0.18. This is consistent with the findings of Dowling and Dimotakis (1990). No ambient fluid is found on the centerline, as indicted in Figure 6.6. by the value of $\mathrm{PDF}\left(C/\overline{C}\right) = 0$ for the $C/\overline{C} = 0$ bin.

Precession has a significant influence on the shape of the distribution. There is a general trend of reduced peak concentration and broadening of the shape of the distribution both with increased and decreased Strouhal number about the value of St = 0.067. Note that this follows the general trend found with centerline unmixedness in the far field (see Chapter 4). It is also highly significant that the simple jet flow on the centerline contains no pure ambient fluid while the MPJ flows do show the presence of ambient fluid. The lack of ambient fluid

on the centerline for the simple jet flow is consistent with the finding of Dowling and Dimotakis (1990) for gaseous flows (although it is found in flows where water is used as the working fluid). The presence of pure jet fluid on the centerline of MPJ flows is further evidence that mean structure of turbulence is altered by precession in a manner that enhances large scale engulfment of ambient fluid and suppresses fine scale intimate mixing. This picture is consistent with the structure apparent in the instantaneous concentration images where large regions of relatively uniform concentration are seen, interspaced with the layers of very low concentration fluid drawn right to the axis of the flow. A shift in the scale of turbulent motions is also consistent with the reduced shear measured in the central region of the flow (see measurement of length scales in Chapter 4).

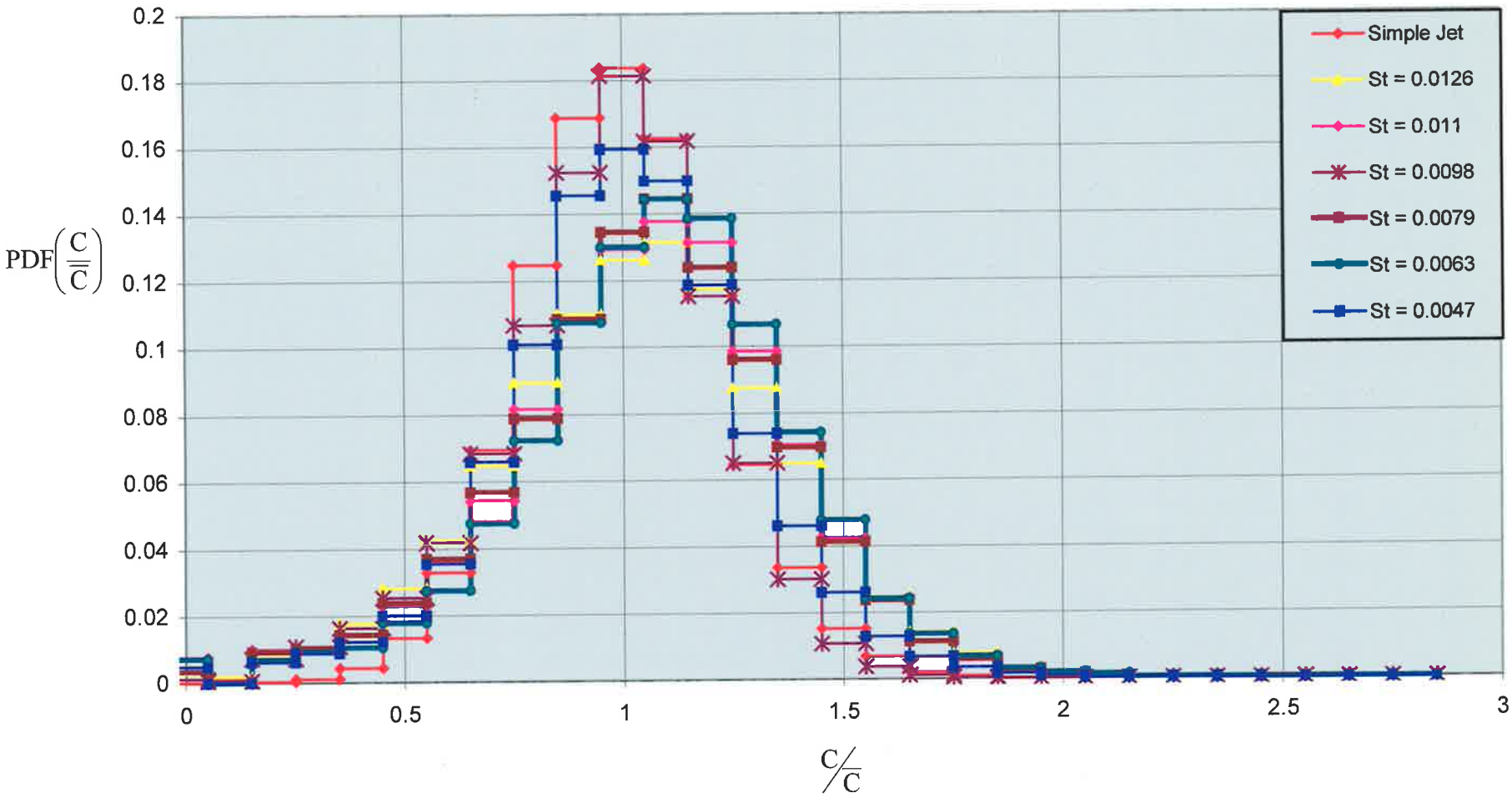

Figure 6.7 Probability Density Function (PDF) of concentration in the far field along the centerline for the different jet mixing fields (different Strouhal numbers), scaled about the mean concentration. Re = 3,800 d = 3mm. $\phi = 45$

6.7 COMMENTS

The measured decrease in velocity (Schneider, 1997) and measured increase in concentration for increasing values of Strouhal number at a given location throughout the mixing field coincides with higher measured values of both instantaneous and mean scalar dissipation. It also results in a broadening of the distribution of the PDF of concentration, to the extent that pure ambient fluid is drawn into the centre of the flow.

Taken together the above factors support the hypothesis that precession acts to enhance large-scale turbulence while fine scale turbulence is suppressed in both the transition region and far field of the flow. The data implies that molecular diffusion processes rather than turbulent diffusion processes dominate fine scale mixing there. These effects become evident in the region corresponding to the collapse of the helical structure of the flow, that is in the region containing features that have limit cycle characteristics. However the region in which the helical footprint of the jet is most evident, corresponding to the greatest rate of decay in mean velocity, is characterized by increased Reynolds stresses (Schneider, 1996) and increased strain rate (see Chapter 3). It is therefore deduced that turbulent diffusion dominates this region of the flow. Although the present experimental technique was not designed to resolve scalar dissipation in this region of the flow (the spatial resolution was optimized for whole field data), the scalar dissipation in the emerging jet is of the same order of magnitude as found in the highest shear dominated regions around the potential core of a simple jet.

7 CONCLUSIONS

7.1 THE RESULTS

It has been found that precession of a jet introduces additional strain, which dominates the near field mixing characteristics and whose effects propagate into the far field. Within the transition and far field regions the characteristic large-scale motions, as deduced from the integral length scale, are enhanced and the characteristic strain rate is reduced. Changes to the structure of the turbulence are revealed both by visualization and by statistical measurements of concentration. At high Strouhal numbers, the asymptotic value of centerline unmixedness is increased, the decay rate of the jet is reduced, the half width of the field is increased, and the shape of the PDF of concentration is broadened and the presence of ambient fluid on the centerline is demonstrated. These measurements are all consistent with an increase in large-scale engulfment and a suppression of fine scale mixing in these flows. Taken together, the findings support the conclusion that the underlying structure of turbulence throughout the field is a function of the precession characteristics.

7.2 THE HYPOTHESES

Four key hypotheses have been examined, as follows:

Hypothesis (1) **That the flow field produced by a Mechanical Precessing Jet (MPJ) nozzle can be divided into three distinct regions and that each region can be characterized by distinctly different flow phenomena which dominate the mixing in that region.**

The Near Field

In the near field, the footprint of the emerging jet forms a three dimensional helix which precesses with the nozzle. The two-dimensional phase averaged images and the reconstructed three-dimensional data sets of planar phase averaged data (Chapter 3) unequivocally confirm this picture. The characteristic mixing phenomena in this region are dominated by the high shear generated by the precession of the jet, which introduces an additional strain rate on the jet fluid in this region. The additional strain rate results in a higher decay rate of the concentration field within this near field region than occurs in a simple jet. A pair of counter rotating vortex structures is formed within the helix region and is deduced to be generated directly by the precession rather than being a consequence of upstream phenomena (Chapter 3).

The Transition Region

The two dimensional phase averaged images of the flow field (Chapter 3) demonstrate that the counter rotating vortex pairs in the helix merge to form a "collapsed spiral". The images demonstrate that the helix is only clearly identifiable for a phase angle in the range $0 < \theta < 2\pi$. The region associated with the "collapsed spiral" is termed the transition region. Mixing in this region is shown to be dominated by "engulfment"

processes, that is, mixing is characterized by the "layering" of jet and ambient fluid across the complete radial extent of the flow field. Scalar gradient measurements (Chapter 6) show that these large-scale structures, which are the remnants of the helical footprint, exist across the full extent of the flow. The high values of the scalar gradient in the layers surrounding the structures and the low magnitude of the mean concentration are further evidence of the engulfment process.

The Far Field.

The far field phase averaged concentration in a precessing jet flow is significantly lower than occurs in a simple jet at the same axial location. The asymptotic centerline unmixedness is of a similar order of magnitude to that of the simple jet but exhibits a strong dependence on the Strouhal number. A clear trend of increasing unmixedness with Strouhal number is found so that at high Strouhal numbers, the centerline unmixedness is some 30% higher than in the simple jet. This suggests that the structure of turbulence in the far field tends toward that of a simple jet, but that it is altered by the residual effects of precession. Scalar gradient measurements (Chapter 6) reveal an anisotropic layering of scalar dissipation in the far field. Measurements of the macro mixing length scale (Chapter 5) in the far field are larger than for a simple jet and are isotropic on the axis. This supports the hypothesis that the large-scale structures in the far field of a precessing jet are larger than those of a simple jet at similar axial locations.

Hypothesis (2) **That precession of a jet introduces an additional strain rate to the emerging jet and to a first order this augmented strain history characterizes the mixing in the precessing helical region.**

A dimensionless strain rate parameter, $f.\sin\phi/(V_o/d)$, is derived (Chapter 3) and found to characterize the features of the helical footprint for a wide range of frequencies, exit angles and Reynolds numbers. The dimensionless strain rate characterizes the axial shape of the helix and its growth in total vector form. However, it does not account for radial pressure gradient described by Schneider (1995) and so does not account for radial collapse of the helix. It represents a significant advance on the traditional Strouhal number used by previous investigators who have ignored the effect of jet exit deflection angle, ϕ on how precession influences the flow. The presence of increased strain rate in this region of the flow is also supported by velocity measurements, which show increased turbulence intensity and Reynolds stresses in the helical region of the flow.

Hypothesis (3) **That the transition region display fundamental characteristics of a "limit cycle".**

A "limit cycle" can be described by a dependent variable that tends toward some constant value, which subsequently determines the character of the flow field. It is shown that the axial pitch and radial diameter of the three dimensional helix in the near field, the concentration found within the helical structure in the near field and the characteristic length scale of the flow along the centerline of the flow within the transition region, each possess the characteristics of a limit cycle. Clear evidence for this is found in the collapse of the helix, described above, and the presence of a region of zero, or near zero, growth of the jet in this region, and in the three-dimensional reconstruction of phase averaged images (Chapters 3 and 5).

Hypothesis (4) **That the spectrum of length scales within the transitional region and far field of the flow field generated by a Mechanical Precessing Jet (MPJ) nozzle is altered through suppression of fine scale mixing and augmentation of large-scale mixing.**

Measurements of the macro mixing length scale (Chapter 5) show that precession has a significant effect on the mixing scales across the transitional and far field regions of the flow field. The effect of precession is to generate a broad central region in the flow where the scales are nearly isotropic, surrounded on the edge of the flow by larger scales which have reduced shear relative to comparable structures in a simple jet. Measurements of the scalar gradient also show the presence of larger scales in the flow by the presence of more extensive "layering" across the flow field than occurs in the non-precessing case. The present work indicates that if the large scales of the flow are increased in size, there is corresponding decrease in fine scales of the flow. This is supported by the increase in centerline unmixedness, the broadening of the PDF of concentration, the presence of increased concentration of unmixed fluid on the centerline and the high values of scalar dissipation on the edge of large, slow moving structures.

7.3 IMPLICATIONS ON COMBUSTION.

The present work adds significant insight into the flames produced by the MPJ nozzles. Flames at low Strouhal number (St ~ 0.005) characteristically are short, blue, have high residual CO and a high ratio of NO_2 to total NO_x, suggesting highly quenched reactions (Nathan *et al.* 1996). Comparison of these findings with the concentration measurements of the present study shows that the fluid, which has mixed to a flammable mixture, in flows at this Strouhal number, is contained within the precessing helix region in which the strain rates are higher than in a simple jet flow. The flames produced by high Strouhal number flows (St > 0.015) are yellow, have high emissivity and low NO_2 to NO_x ratio, suggesting increased residence time of fuel rich fluid and that combustion occurs at low strain. Comparison with the corresponding cold flow measurement in the present work shows that the fluid, which is mixed to a flammable concentration, is found predominantly in the collapsed spiral and far field regions of the flow in which strain rate is relatively low.

Thus, it is clear that the present work demonstrates that modification of the structure of turbulence in jet flows is possible, that it propagates throughout the jet flow field, and can have a profound influence on the combustion characteristics of a flame.

7.4 THE FUTURE WORK

Several lines of investigation are prompted by the present research, not all of which are directly related to the further investigation of precessing jet flows. What follows is an indication of some of the areas not yet addressed and questions to be answered in each. These are divided into two areas: those questions directly related to understanding the precessing jet phenomena and those that are important to the more general fields of fluid mechanics and combustion.

Future work for investigation of precessing jet flows.

- A full analytical investigation of the flow is needed. Present understanding is limited by the small amount of theoretical input into the problem, which can be included by research into the fundamental equations of motion. It is surmised here that this work will be required to focus separately in the three regions of the flow identified by the present work.

- The MPJ is a useful tool for generating reproducible mixing fields for the investigation of combustion phenomena. It allows fine control of turbulence characteristics in the mixing field of a jet, influencing both the region in which a flame is stabilized and the subsequent combustion. However, its role as an analogue to the Fluidic Precessing Jet (FPJ) which is used in industry is limited. Modifications to the basic design of the MPJ are needed to allow better characterization of the flow field of an FPJ. A suggestion, presently in the design phase, is the addition of an FPJ chamber to an MPJ nozzle at the inlet to the nozzle chamber. This will allow control of the precessional frequency of the jet and, importantly, will allow measurements to be taken of the FPJ with reference to the position in the precessional cycle.

- The present finding that the addition of strain to the emerging jet offers potential for improved full characterization of the near flow field of the MPJ. Further investigation of

the addition of strain in this near field region will require detailed measurement of the velocity and pressure field at much greater resolution than has previously been achieved. The present study provides a basis for the selection of the appropriate jet exit conditions for this future work, including a range of precessional frequencies for each of a range of deflection angles and jet Reynolds number. As found both in previous velocity investigations and in the current work, the effect of Reynolds number on the flow is only second order. Thus the prime criterion for the flow velocity is to allow for good experimental resolution.

Future work in the general fluids area.

- The present investigation has highlighted some limitations in the present understanding of jet mixing, specifically related to two-dimensional collection and analysis of the concentration field data. Specific points to be addressed are:
  - The definition of the integral length scale and how it is measured experimentally. The present results show the integral scale, taken literally, is anisotropic in a region of the flow believed to be isotropic and does not follow the trend predicted by theory, namely that the axial two point spatial correlation should fall to zero for some finite separation in the flow field. That the integral scale has a "correlation floor" highlights that present statistical theories of turbulence do not fully take into account the presence of large-scale structures or the influence these structures have on the flow field.
  - Concentration measurements of a jet issuing from an axisymmetric nozzle presented in Chapter 2 indicate features of the flow which are yet to be understood. An example is the behavior of the unmixedness parameter in the "asymptotic" region and especially in the near field transition region. Here the present research and that of So *et al.* (1990) suggests that concentration measurements are more sensitive to flow field fluctuations than are velocity measurements.

- It is obvious that the complex phenomenon of combustion cannot be described fully or modeled by a single dimensionless flow variable or even by a small group of variables. Understanding will only be achieved with relevant knowledge of the velocity, concentration and the temperature fields (as a minimum). Also the influences of the magnitude of the several spatial and time scales need to be taken into account. Thus, investigation of phenomena with multiple diagnostic techniques is required to push forward to theoretical understanding.

8. LIST OF PUBLICATIONS RELATED TO THE CURRENT PROJECT

The following is a list of publications which have been produced from the current work.

8.1 CONFERENCE PAPERS

Nobes, D.S., Newbold, G.J.R., Nathan, G.J., Luxton, R.E., Alwahabi, Z.T. (1996a). A planar imaging technique for measurement of concentration in a jet. First Conference on Laser Diagnostics in Fluid Mechanics and Combustion. Sydney University, Australia, December 5-6, 148-153.

Nobes, D.S., Newbold, G.J.R., Nathan, G.J., Luxton, R.E., Alwahabi, Z.T. and King, K.D. (1996b). Phase average imaging of concentration of a precessing jet flow. First Conference on Laser Diagnostics in Fluid Mechanics and Combustion. Sydney University, Australia, December 5-6, 154-159.

Nobes, D.S., Newbold, G.J.R., Nathan, G.J., Luxton, R.E., Alwahabi, Z.T. and King, K.D. (1997). The mixing field of a simple round jet and a fluidic precessing jet. The First Asia-Pacific Conference on Combustion. Osaka University, Japan, May 12-15, 334-337.

Nobes, D.S., Newbold, G.J.R., Nathan, G.J., Luxton, R.E., Alwahabi, Z.T. and King, K.D. (1997). Measurement of concentration unmixedness in a turbulent round jet. Submitted to Phys. Fluids.

Nobes, D.S., Newbold, G.J.R. and Alwahabi, Z.T. (1997). Quantitative planar imaging of large structures developed through the precession of a jet. IUTAM Symposium on Simulation and Identification of Organized Structures in Flows. Technical University of Denmark, Lyngby, May 25-29.

8.2 CO-AUTHORED PAPERS

Alwahabi, Z.T., King, K.D., Nathan, G.J., **Nobes, D.S.,** Newbold, G.J.R. and Luxton, R.E., (1996). Planar laser induced fluorescence studies of OH and CH radicals in precessing jet flames. First Conference on Laser Diagnostics in Fluid Mechanics and Combustion. Sydney University, Australia, December 5-6, 252.

Alwahabi, Z.T., King, K.D., Nathan, G.J., **Nobes, D.S.,** Newbold, G.J.R., and Luxton, R.E., (1997). Planar laser induced fluorescence studies of radicals in precessing jet flames. Chemeca, Rotorua, New Zealand, September 29-October 1.

Nathan, G.J., **Nobes, D.S.**, Mi. J.C., Schneider, G.M., Newbold, G.J., Alwahabi, Z.T., Luxton, R.E. and King, K.D. (1997). Exploring the relationship between mixing, radiation and NOx emissions from natural gas flames. *Combustion and Emissions Control II*, The Institute of Energy

Newbold, G.J.R., **Nobes, D.S.**, Alwahabi, Z.T., Nathan, G.J., and Luxton, R.E., (1995). The application of PIV to the precessing jet nozzle. Twelfth Australasian Fluid Mechanics Conference, Sydney University, Australia, December 10-15, 395-398.

Newbold, G.J.R., **Nobes, D.S.,** Nathan, G.J., Luxton, R.E., Alwahabi, Z.T., and King, K.D. (1996). Visualisation and mixing in the precessing jet flow. First Conference on Laser Diagnostics in Fluid Mechanics and Combustion. Sydney University, Australia, December 5-6, 253.

Newbold, G.J.R., **Nobes, D.S.**, Nathan, G.J., Luxton, R.E., Alwahabi, Z.T., and King, K.D. (1997). Reaction and flow field in the stabilisation region of a fluidic precessing jet flame. Fifth Flame Days. Sydney University, Australia, November 20-21.

9. REFERENCES

[1] Abramovich, G.N. (1963) "The theory of Turbulent Jets", MIT Press Cambridge. Massachusetts.

[2] Balendra,S.A., Manias,C.G. and Rapson,D.S. (1996),`` Low NO Lime Production Using a GyroTherm Burner"J. Rock Products, in preparation,

[3] Becker, H.A., Hottal, H.C. and Williams, G.C. (1963). Mixing and Flow in Ducted Turbulent Jets, *Ninth Symposium (International) on Combustion,* Pittsburgh: The Combustion Institute pp 7 - 20

[4] Becker, H.A., Hottal, H.C. and Williams, G.C. (1967a) On the Light-scattering Technique for the Study of Turbulence and Mixing, *J. Fluid Mech.* Vol 30 pp 259-284

[5] Becker, H.A., Hottal, H.C. and Williams, G.C. (1967b) The Nozzle-fluid Concentration Field of the Round, Turbulent, Free Jet, *J. Fluid Mech.* Vol 30 pp 285-303

[6] Becker, H.A. (1977). Mixing, Concentration Fluctuations, and Marker Nephelometry. *Studies in Convection*, Vol2, edited by B.E. Launder, Academic Press, New York, pp. 45-139

[7] Beer,J.M., Chigier, N.A., Davies,T.W. and Bassindale,K. (1971) "Laminarization of Turbulent Flames in Rotating Environments", *Combustion and Flame* Vol 16 pp 39-45

[8] Beer,J.M. and Chigier, N.A. (1972) *COMBUSTION AERODYNAMICS* Applied Science Publishers LTD

[9] Birch,A.D., Brown,D.R., Dodson,M.G. and Thomas,J.R. (1978). The turbulent concentration field of a methane jet, *J. Fluid Mech.* Vol 88 pp431-449

[10] Bowman,C.T.(1992) "Control of combustion generated nitrogen oxide emissions: Technology driven by regulation" Twentyfourth Symposium (International) on Combustion, The Combustion Institute, pp859

[11] Bradshaw, P. (1971) "An introduction to turbulence and its measurement", Papamon Press.

[12] Braun, M. (1983) "Differential Equations and Their Applications", Springer-Verlag New York, Inc.

[13] Chao,Y.C., Han,J.M. and Jeng,M.S. (1990) "A quantitative laser sheet image processing method for the study of the coherent structure of a circulate jet flow", *Exp. in Fluids*, Vol 6, pp 323-332

[14] Chao,Y.C., Jeng,M.S., and Han,J.M. (1991) "Visualization and image processing of an acoustically excited jet flow", *Exp. in Fluids*, Vol 12, pp 29-40

[15] Chen, C.J. and Rodi, W. (1980) "Vertical Turbulent Buoyant Jets – a review of experimental data" *Pergamon*

[16] Clemens,N.T. and Mungal,M.G. (1991) "A planar Mie scattering technique for visualizing supersonic mixing flows" *Exp. in Fluids*, Vol 11, pp 175-185

[17] Corrsin,S. and Uberoi, M.S. (1950) "Further experiments on the flow and heat transfer in a heated turbulent jet" *NASA Rep. 998*

[18] Crow,S.C. and Champagne,F.H. (1971) "Orderly structure in jet turbulence", *J. Fluid Mech.* Vol 48 pp 547-591

[19] Dahm, W.J.A. and Dimotakis, P.E. (1990). Mixing at Large Schmidt Number in the Self-Similar Far Field of Turbulent Jets. *J. Fluid Mech* Vol 217, pp. 299-330

[20] Dahm, W.J.A., Southerland, K.B. and Buch,K.A.(1991) "Direct, high resolution, four-dimensional measurements of the fine scale structure of Sc>>1 molecular mixing in turbulent flows", *Physics of Fluids A,* Vol 3, No 5 pp 1115-1127.

[21] Dowling, D.R. (1991) "The estimated scalar dissipation rate in gas-phase turbulent jets", *Phys. Fluids A* Vol3 No9 pp. 2229-2246

[22] Dowling, D.R. and Dimotakis, P.E. (1990). Similarity of the Concentration Field of Gas-Phase Turbulent Jets, *J. Fluid Mech*, Vol 218, pp. 109-141

[23] Dibble,R.W., Kollman, W. and Schefer,R.W. (1984) "Measurements and predictions of scalar dissipation in turbulent jet flames", Twentieth Symposium (International) on Combustion, The Combustion Institute, pp. 345-352

[24] Dimotakis,P.E., Miake-Lye,R.C. and Papantoniou,D.A. (1983) "Structure and dynamice of round turbulent jets" *Phys. Fluids* Vol26 (11), pp. 3185-3192

[25] Eckbreth, A.C. (1988) *Laser Diagnostics for Combustion Temperature and Species* Abacus Press, UK..

[26] Everest,D.A., Driscoll,J.F., Dahm,W.J.A. and Feikema,D.A. (1995) "Images of the Two-Dimentional Field and Temperature Gradients to Quantify Mixing Rates within a Non-Premixed Turbulent Jet Flame", *Comb. and Flame* Vol 101, pp 58-68

[27] Feikema,D.A., Everest,D.A. and Driscoll,J.F. (1996) "Images of Dissipation Layers to Quantify Mixing within a Turbulent Jet", *AIAAJ* Vol 34, No12 pp 2531-2538

[28] Fuel and Combustion Technology Int. (FCT) (1996) "A Combustion Technology and Engineering Course", Adelaide, Australia , Aug 5-7 1996

[29] Greenspan, H.P. (1968) *The Theory of Rotating Fluids,* Cambridge University Press

[30] Gouldin, F.C., Schefer, R.W., Johnson, S.C. and Kollmann, W. (1986) "Nonreacting Turbulent Mixing Flows", *Prog. Energy Combust Sci.* Vol. 12 pp 257-303

[31] Hill,S.J., (1992)``Characterisation of the Flow Fields Produced by the Enhanced MixingNozzle: A Development Towards High Temperature and Multi-Phase Applications",Dept. Mech. Eng., University of Adelaide

[32] Hill,S.J., Nathan,G.J. and Luxton,R.E., (1992),``Precessing and Axial Flows Following a Sudden Expansion in an Axi-symmetric Nozzle ", Eleventh Australasian Fluid Mechanics Conference, December, Hobart, Australia

[33] Hill,S.J., Nathan,G.J. and Luxton,R.E., (1995)``Precession in Axi-symmetric Confined Jets ", Twelfth Australasian Fluid Mechanics Conference, December, Sydney, Australia

[34] Hill,S.J., (1998),``Precessing Flows", PhD thesis, Dept. Mech. Eng., the University of Adelaide, in preparation.

[35] Hinze, J.O. (1959) "Turbulence". McGraw-Hill

[36] Hinze, J.O. (1975) "Turbulence".2nd Ed, McGraw-Hill

[37] Hussain, A.K.M.F. (1986). "Coherent structures and turbulence", *J. Fluid Mech.*, 173, 303-356

[38] Hussain, A.K.M.F. and Clark,A.R. (1981). "On the coherent structure of the axisymmetric mixing layer : a flow-visualisation study", *J. Fluid Mech.*, 104, 263-294

[39] International Panel on Climate Change (IPCC) (1995) "1995 Summary for Policy Makers: Working Group I", Madird, Nov 29, 1995.

[40] S Itoh,S., Narui,H. and Sasaki,T. (1992) Numerical Analysis of Confined Jet Flow Field. *Advances in Finite Element Analysis in Fluid Mechanics*, FED-Vol. 137, pp. 81-85.

[41] Jenkins,B.G., Nathan,G.J. and Manias,C.G., (1994)``Modelling of Precessing Burners and their Application to Rotary Alumina Kilns", Third International Conference on Combustion Technologies for a Clean Environment, 3-6 July, Portugal

[42] Kalghatgi,G.T. (1984) "Lift-off heights and visible lengths of vertical turbulent jet diffusion flames in still air" *Comb Sci and Technol* Vol 41 pp 17-29

[43] Kent, J.H., and Bastin, S.J. (1984). Parametric effects on sooting in turbulent acetylene diffusion flames. *Comb. Flame*, 56, 29-42.

[44] Khodadadi,J.M. and Vlachos,N.S. (1989) "Experimental and Numerical Study of Confined Coaxial Turbulent Jets", *AAIA Journal*, Vol 27 No5 pp532-541

[45] Larsen, T. (1994) Numerical Modelling of Jets and Plumes- a Civil Engineering Perspective. *Recent Advances in the Fluid Mechanics of Turbulent Jets and Plumes*. P.A.Davies and M.J. Valente Neves (eds). Kluwer Academic Publishers, Netherlands.

[46] Launder, B.E. and Spaulding, D.B. (1974) The Numerical Prediction of Turbulent Flows, *Computer Methods in Applied Mechanics and Engineering*, Vol 3 pp 269-289

[47] Lockwood,F.C. and Moneib,H.A. (1980). Fluctuating temperature measurements in a heated round free jet. *Comb. Sci. Tech.* Vol22, 63-81.

[48] Luxton,R.E. (1993) "On Mixing, Cement and the Hot End of Aerodynamics", Advances in Aerodynamics and Astronautics, Prof. Roddam Narasimha FRS *FESTSCHRIFT*, Ed. Preblise,S. and Visheramasth,M. Bangalore, Dec. 1993

[49] Luxton,R.E., Nathan,G.J. and Luminis Pty. Ltd., (1988) "Mixing of Fluids", Australian Patent Office,Patent Application No. 16235/88, International Patent Application No. PCT/AU88/00114.

[50] Luxton,R.E. and Nathan,G.J., (1989),"A Precessing Asymmetric Flow Field in an Abruptly Expanding Axi-symmetric Duct", Tenth Australasian Fluid Mechanics Conference, Vol 2, pp 11.29-11.33, Dec, Melbourne, Australia,

[51] Luxton,R.E., Nathan,G.J. and Zhang,D.K. (1995) "An Historical Perspective and Overview of Combustion Research at the University of Adelaide". The Australian Symposium on Combustion, (November) Adelaide, Australia

[52] Manias,C.G. and Nathan,G.J., (1992)``The Precessing Jet Gas Burner -- A Low NO Burner Providing Process Efficiency and Product Quality Improvements", International Kiln Association Conference, Oct., Toronto, Canada.

[53] Manias,C.G. and Nathan,G.J., (1993),``The Precessing Jet Gas Burner -- A Low NO Burner Providing Process Efficiency and Product Quality Improvements", *World Cement*, (March), 4-11.

[54] Manias,C.G. and Nathan,G.J., (1994),``Low NO Clinker Production", *World Cement*, (May)

[55] Manias,C.G. and Nathan,G.J. (1994) ``Gyro-Therm - The Precessing Jet Burner",C.S.I.R.O./U.N.I.D.O. Conference, Feb., Melbourne, Australia.

[56] Manias,C.G., Nathan,G.J. and Rapson,D.S. (1994)``The `Gyro-Therm' Kiln Burner -- A Leaner and Greener Gas Combustion Technology ", International Clean Air Society, Oct., Perth, Australia.

[57] Manias,C.G., Nathan,G.J. and Rapson,D.S., (1995)'' 'Gyro-Therm': A New Efficient Low NO Gas Burner for Product Quality Improvements", ASEAN Federation of Cement Manufacturers, (April), Kuala Lumpar.

[58] Manohar,S.S (1994) " Large Eddy Simulation of a Precessing Deflected Jet", Pennsalvania State University.

[59] Melling,A. and Whitelaw,J.H. (1975) Optical and Flow aspects of particles. *Proc. Of the LDA-Symposium, The Accuracy of Flow Measurements by Laser Doppler Methods*, Copenhagen, pp 382-402

[60] Moles, F.D. (1986) "The elements of flame control in rotary kilns", *Rock Products* Proc. 22nd Intl. Cement Seminar. Chicago, U.S.A, Dec 8-10, pp 79-102

[61] Monin, A.S. and Yaglom, A.M. (1972) "Statistical Fluid Mechanics", M.I.T Press, Cambridge, Mass.

[62] Namazian, M., Schefer R.W. and Kelly J. (1988) "Scalar Dissipation Measurements in the Development Region of a Jet", *Combustion and Flame* Vol 74, pp. 147-160

[63] Namazian, M., Kelly J., Schefer R.W., Johnston S.C. and Long M.B. (1989). Nonpremixed bluff-body burner and flame imaging study. *Exp. in Fluids.* Vol 8 pp 216-228

[64] Namazian, M., Kelly J., Schefer R.W., Johnston S.C. and Long M.B. (1992). Concentration Imaging Measurements in Turbulent Concentric-Jet Flows. *AAIA J.* Vol 30 No2. pp 384-394

[65] Narasimha,R. and Sreenivasan,K.R. (1979) "Relaminarization of Fluid Flows", *Advances in Applied Mechanics* Vol 19 pp 222-309

[66] Nathan,G.J., (1988)``The Enhanced Mixing Burner", PhD Thesis, Dept. Mech. Eng., the University of Adelaide"

[67] Nathan,G.J., Brumale,S., Proctor,D. and Luxton,R.E., (1993) ``NOx Reduction in Flames by Modification of Turbulence with Jet Precession", `Combustion and Emissions Control', The Institute of Energy, ISBN 0902597434, pp 213-230

[68] Nathan,G.J. and Luxton,R.E., (1988), ``A Stable, Un-Premixed Gas Burner with Infinite Turn-Down Ratio", First European Conf. on Industrial Furnaces and Boilers, (March), Lisbon, Portugal.

[69] Nathan,G.J. and Luxton,R.E., (1989)``Mixing Enhancement by Jet Precession", The Fourth Asian Congress of Fluid Mechanics, (Aug.), Hong Kong, Vol 2, pp A237-A240.

[70] Nathan,G.J. and Luxton,R.E., (1989) ''The Combustion Characteristics of an Enhanced Mixing Nozzle", Joint International Conference of The Combustion Institute (Sept), Sydney, Aust, 248-251.

[71] Nathan,G.J., Luxton,R.E., Balendra,S.A., Williams,G.H. and Manias,C.G. (1990) ''A Preliminary assessment of the Enhanced Mixing Burner in a cement kiln", Internal Report, Dept. Mech. Eng., University of Adelaide.

[72] Nathan,G.J. and Luxton,R.E., (1991a) ''The Stability and Emission Characteristics of the Enhanced Mixing Burner in a 50kW Furnace ", Final Report to the State Energy Research Advisory Committee for the Period 1989/90, Dept. Mech. Eng., University of Adelaide.

[73] Nathan,G.J. and Luxton,R.E. (1991b) ''The Entrainment and Combustion Characteristics of an Axi-symmetric, Self Exciting, Enhanced Mixing Nozzle", Third ASME-JSME Thermal Engineering Joint Conference, (March), Reno, Nevada.

[74] Nathan,G.J. and Luxton,R.E. (1991c) ''Flame Stability and Emission Characteristics of the Enhanced Mixing Burner", Second European Conference on Industrial Furnaces and Boilers, (April), Algarve, Portugal.

[75] Nathan,G.J. and Luxton,R.E. (1991d) ''The Flow Field within an Axi-symmetric Nozzle Utilizing a Large Abrupt Expantion", *International Conference of Experimental Fluid Mechanics*, Chengin, China, June 17-21 1991

[76] Nathan,G.J. and Luxton,R.E., (1992a) ``The Flow field Within an Axi-symmetric Nozzle Utilising a Large Abrupt Expansion", Recent Advances in Experimental Fluid Mechanics, ed. Zhuang, F.G., International Academic Pub., 527-532.

[77] Nathan,G.J. and Luxton,R.E., (1992b)``Mixing Enhancement by a Self-Exciting, Asymmetric Precessing Flow-Field", Transport Phenomena in Heat and Mass Transfer,ed. Reizes,J.A., pub. Elsevier, ISBN 0 444 89851 4,Vol 2, pp 1297-1307.

[78] Nathan,G.J., Manias,C.G. and Luxton,R.E., (1991) ``Potential Increases in the Efficiency of a Rotary Kiln using an Enhanced Mixing Burner", IEAust International Mech Eng Congress, (July), Sydney, Aust., Vol 4, pp 58-61.

[79] Nathan,G.J. and Smart,J.P. (1991) ``A Simple, Unswirled Low NOx Gas Burner", Second Australian Flame Days Conference, Australian Flame Research Committee, IFRF, (Oct.), Sydney, Aust.

[80] Nathan,G.J. and Smart,J.P., (1991),``An Investigation of the Combustion Characteristics of the Enhanced Mixing Burner firing Natural Gas at 2MW", IFRF Doc F90/y/9, International Flame Research Foundation, Ijmuiden, Netherlands.

[81] Nathan,G.J., Luxton,J.P. and Smart,J.P., (1992) ''Reduced NOx Emissions from Enhanced Large Scale Turbulence in an Un-swirled gas burner", Tenth Members' Conference, International Flame Research Foundation, (May), Noordwijkerhout, Netherlands.

[82] Nathan,G.J., Luxton,R.E. and Smart,J.P., (1992) ''Reduced NOx Emissions and Enhanced Large Scale Turbulence from a Precessing Jet Burner", Twentyfourth Symposium (International) on Combustion, The Combustion Institute, pp. 1399-1405.

[83] Nathan,G.J. and Luxton,R.E. (1992) ''A Low NO Gas Burner with a Radiant Flame",Energy Efficiency in Process Technology, Commission of the European Communities, (Oct.), Vouliagmeni, Greece.

[84] Nathan,G.J. and Luxton,R.E., (1992)''Large Scale Turbulence Generated by a Precessing Free Jet", International Union of Theoretical and Applied Mechanics, IUTAM Symposium on Eddy Structure Identification in Free Turbulent Shear Flows, (Oct.), Poiters, France.

[85] Nathan,G.J. and Luxton,R.E." (1993) ''A Low NO Gas Burner with a Radiant Flame", ed. Pilavachi,P.A., Energy Efficiency in Process Technolog", Elsevier, ISBN 1-85861-019-2, pp 883-892.

[86] Nathan,G.J. Luxton,R.E. and Luminis Pty. Ltd., (1992), ''Variable Flame Burner Configuration", Australian Patent Office, Patent Application No. PL4827/92.

[87] Nathan,G.J., Hill,S.J., Luxton,R.E. and Luminis Pty. Ltd. (1992) ''Variable Flame Precessing Jet Nozzle", Australian Patent Office, Provisional Austalian Patent Application, 7/3/95.

[88] Nathan,G.J. and Turns,SR. and Bandaru,R.V., (1995) ''The Effects of Fuel Jet Precession on the Global Properties and Emissions of Free Turbulent Jet Flames", American Flame Research Council International Symposium, (October), Monterey, CA, USA.

[89] Nathan,G.J. and Turns,SR.. and Bandaru,R.V., (1996) ''The Influence of Jet Precession on NO Emmissions and Radiation from Turbulent Flames"", to appear,Combustion Science and Technology.

[90] Nathan,G.J. and Manias,C.G., (1995) ''The Role of Process and Flame Interaction in Reducing NOx Emissions", Combustion and Emissions Control, pp 309-318, ISBN 0 90 259 7493.

[91] Nathan,G.J. and Rapson,D.S. (1995) ''Simultaneous Optimisation of Heat Transfer Profile and NOx Emissions in a Cement Kiln", The Australian Symposium on Combustion, (November), Adelaide, Australia.

[92] Nathan,G.J., Hill,S.J and Luxton,R.E.. (1998), ''An Axi-Symmetric 'Fluidic' Nozzle to Generate Jet Precession", J. Fluid Mech (to appear).

[93] Nathan,G.J., Nobes, D.S., Mi,J., Schnieder,G.M. Newbold,G.J.R., Alwahabi,Z.T., Luxton,R.E. and King,K.D. (1997) "Exploring the relationship between mixing, radiation amd Nox emissions from natural gas flames", *Combustion and Emissions Control II*, The Institute of Energy

[94] Newbold,G.J.R., (1998) "Mixing and Combustion in Precessing Jet Flows" PhD Thesis, Dept. Mech. Eng., the University of Adelaide"

[95] Newbold,G.J.R., Nathan,G.J. and Luxton,R.E., (1993a), ``Large Scale Motions in an Un-Confined Precessing Jet Diffusion Flame", The Australian Symposium on Combustion, (November), The University of Newcastle, Australia.

[96] Newbold,G.J.R., Nathan,G.J. and Luxton,R.E., (1993b) ``Large Scale Dynamics of a Precessing Jet Flame", Fifth Australasian Heat and Mass Transfer Conference, (December), The University of Queensland, Brisbane, Australia.

[97] Newbold,G.J.R., Nobes,D.S., Alwahabi,Z.A., Nathan,G.J. and Luxton,R.E. (1995) ``The Application of PIV to the Precessing Jet Nozzle", Twelfth Australasian Fluid Mechanics Conference, (December), The University of Sydney, Australia.

[98] Newbold,G.J.R., Nathan,G.J. and Luxton,R.E. (1997) ``The Large Scale Dynamic Behavior of an Unconfined Precessing Jet Flame", *Combust. Sci. and Tech.* Vol 126, pp. 71-95.

[99] Ogawa,A. (1992) "Vortex Flow", CRC Press, ISBN 0-8493-5782-9

[100] Patankar,S.V., Basu,D.K. and Alpay,S.A. (1977) Prediction of the three-dimentional velocity field of a deflected turbulent jet. *J. Fluids Engng.*, Trans ASME, Dec 1977, pp758-762.

[101] Pitts, W.M. (1988) Assessment of theories for the behaviour and blowout of lifted turbulent jet diffusion flames. *Twenty-Second Symposium (International) on Combustion*, The Combustion Institute, pp 809-816.

[102] Pitts,W.M. (1991a). Effects of global density ratio on the centerline mixing behavior of axisymmetric turbulent jets. *Exp. in Fluids.* Vol 11 pp.125-134

[103] Pitts,W.M. (1991b). Reynolds number effects on the mixing behavior of axisymmetric turbulent jets. *Exp. in Fluids.* Vol 11 pp.135-141

[104] Proctor,D., Nathan,G.J., Luxton,R.E., Pearson,I.G., Brumale,S.A., Mann,B.A. Schneider,G.M. and Newbold,G.J.R., (1992), "The Efficient Low NO Burning of Gas for Large Scale Industrial Applications", Second International Conference on Combustion Technologies for a Clean Environment, (July), Lisbon, Portugal.

[105] Proctor,D., Nathan,G.J., Pearson,I.G., Brumale,S.A., Mann,B.A., Schneider,G.M. and Luxton,R.E. (1993),"Turbulence and combustion Interaction in a Precessing Jet Flame", The Australian Symposium on Combustion, The University of Newcastle, Australia., (November), pp A6--4.

[106] Rajaratnam, N. (1976) *Turbulent Jets* Elsevier Scientific Publishing Co.

[107] Rapson,D.S., Stokes,B. and Hill,S.J., (1995) "Kiln Flame Shape Optimisation using a Gyro-Therm Gas Burner", J. World Cement, (July).

[108] Rapson,D.S. and Nathan,G.J. (1995) "The Gyro-Therm Burner -- An Environmentally Friendly, Low NOx Burner", RACI, (Sept), Adelaide, Australia.

[109] Richards, C.D. and Pitts, W.M. (1993). Global Density Effects on the Self-Preservation Behaviour of Turbulent Free Jets. *J. Fluid Mech* Vol 254, pp. 417-435

[110] Ricou, F.P. and Spalding, D.B. (1961). Measurements of entrainment by axisymentrical turbulent jets. *J. Fluid Mech.* Vol 11, pp 21- 32

[111] Rhine,J.M. and Tucker,R.J. (1991) "Modelling of Gas Fired Furnaces and Boilers", McGraw-Hill.

[112] Rodi, W., (1984) Turbulent models and their applications in hydraulics, State-of-the-art review, IAHR, Delft, The Netherlands.

[113] Roquemore,W.M., Tankin, R.S., Chiu, H.H. and Lottes,S.A. (1986). A Study of a Bluff-Body Combustor using Laser Sheet. *Exp. in Fluids.* 4 pp.205-213

[114] Rosenweig, R.E., Hottel, H.C. and Williams, G.C. (1961). Smoke-scattering Light Measurements of Turbulent Concentration Fluctuation, *Chem. Eng. Sci*, 15 pp 111-129

[115] Saffman,P.G. (1993) "Vortex Dynamics", Cambridge University Press

[116] Røkke, N.A., Hustad, J.E., and Sønju, O.K. (1994). A study of partially premixed unconfined propane flames. *Comb. Flame*, 97, 88-106.

[117] Sarofim, A.F. (1986) "Radiative Heat Transfer in Combustion: Friend or Foe" Twenty First Symposium (Int) on Combustion, pp1-23.

[118] Schefer,R.W., Namazian,M. and Kelly,J. (1989) "Comparison of Turbulent-Jet and Bluff-Body Stabilized Flames", *Comb. Sci. Tech.* Vol67 pp 123-146

[119] Schefer,R.W., Kerstein,A.R., Namazian,M. and Kelly,J. (1994) "Role of large-scale structure in a nonreacting turbulent CH_4 jet", *Phys. Fluids*, Vol6 (2) pp 652-661

[120] Schneider,G.M. (1997), ''Flow Structures and Turbulence Characteristics in a Precessing Jet", PhD Thesis, Dept. Mech. Eng., the University of Adelaide.

[121] Schneider,G.M., Nathan,G.J. and Luxton,R.E., (1992) ''An Experimental Study of a Precessing Deflected Jet", Eleventh Australasian Fluid Mechanics Conference, (December), Hobart, Australia.

[122] Schneider,G.M., Vidakovic,S.S., Hooper,J.D., Musgrove,A.R., Nathan,G.J. and Luxton,R.E, (1993) ''Theoretical and Experimental Pressure Field Evaluation Downstream of a Mechanically Precessing Jet", Fifth Australasian Heat and Mass Transfer Conference, (December), The University of Queensland, Brisbane, Australia.

[123] Schneider,G.M., Nathan,G.J., Luxton,R.E., Hooper,J.D. and Musgrove,A.R. (1994)''Velocity and Reynolds Stresses in a Precessing, Deflected Jet", Second International Conference Experimental Fluid Mechanics, (July), Torino Italy.

[124] Schneider,G.M., Froud,D., Syred,N., Nathan,G.J. and Luxton,R.E. (1996a) ''Velocity Measurements in a Precessing Jet Flow using a Three Dimensional LDA System", Experiments in Fluids, (to appear)

[125] Schneider,G.M., Nathan,G.J., Luxton,R.E., Hooper,J.D. and Musgrove,A.R., (1996b), ''Velocity and Reynolds Stresses in a Precessing Jet", Experiments in Fluids, (to appear).

[126] Schneider,G.M., Nathan,G.J. and Luxton,R.E., (1994), ''Velocity Contours in a Precessing, Deflected Jet", International Conference on Flow Interaction, (September), Hong Kong.

[127] Schneider,G.M., Nathan,G.J. and Luxton,R.E. (1997a) "Vortical Structures in a Precessing Jet Flow", *Album of Visualisation.* The Visualisation Society of Japan. No14. pp 8

[128] Schneider,G.M., Nathan,G.J. and Luxton,R.E. (1997b) "Structures in a Precessing Jet Flow", *Album of Visualisation.* The Visualisation Society of Japan. No14. pp 8

[129] Schneider,G.M., Nathan,G.J. and Luxton,R.E. (1997c) "Instantaneous Image in a Precessing Jet Flow", *Album of Visualisation.* The Visualisation Society of Japan. No14. pp 9

[130] Schneider,G.M. Newbold,G.J.R. Nathan,G.J. and Luxton,R.E., (1997d), ``Vortical Structures in a Precessing Jet", Fourth World Conference on Heat Transfer and Fluid Mechanics, (June), Brussels.

[131] Smart,J.P. and Weber,R. (1989) "Reduction of NO_x and optimisation of burnout with an aerodynamically air-staged burner and an air staged pre-combustor" *J. Inst. Energy,* Dec. pp 237-245

[132] So,R.M.C., Zhu,J.Y., Otugen,M.V. and Hwang,B.C.(1990) "Some measurements in a binary gas jet" *Exp in Fluids* Vol 9, pp 273-284

[133] Smith,N.L., Nathan,G.J., Megalos,N.P. and Zhang,D.K., (1995) ``The Influence of a Precessing Jet Flow Field on Coal Flame Ignition Patterns", The Australian Symposium on Combustion, (November) Adelaide, Australia.

[134] Syred, N and Beer, J.M. (1974) "Combustion in Swirling Flows: A Review". *Comb and Flame* Vol 23 pp 143-201.

[135] Tan, S.Y. and Lan, C.E. (1997), "Estimation of aeroelastic models in structural limit-cycle oscillations from test data". *AIAA J.*, Vol. 35, No6. pp 1025-1029.

[136] Tritton, D.J. (1988) *Physical Fluid Dynamics* 2nd Ed. Oxford Science Press

[137] TSI (1987) *Model 9306 Six-Jet Atomizer – Instruction Manual* TSI Incorperated.

[138] Turns, S.R. (1996) "*An Introduction to Combustion*", McGraw-Hill, Inc. ISBN 0-07-911812-7

[139] Turns,S.R. and Bandaru,R.V. and Nathan,G.J. (1994) ``Oxides of Nitrogen Emissions from Turbulent Hydrocarbon/Air Jet Diffusion Flames: for the Gas Research Institute", Dept. Mech. Eng., The Pennsylvania State University, 5092-260-2596.

[140] Van Cruynigen,I. Lozano,A. and Hanson,R.K.(1990) "Quantitative imaging of concentration by planar laser-induced fluorescence", *Exp in Fluids* Vol 10 pp 41-49

[141] White, F.M. (1991) *Viscous Fluid Flow* 2nd Ed. M^{c}Graw-Hill.